Cedrick Ansorge

Analyses of Turbulence in the Neutrally and Stably Stratified Planetary Boundary Layer

Springer

Springer Theses

Recognizing Outstanding Ph.D. Research

Aims and Scope

The series "Springer Theses" brings together a selection of the very best Ph.D. theses from around the world and across the physical sciences. Nominated and endorsed by two recognized specialists, each published volume has been selected for its scientific excellence and the high impact of its contents for the pertinent field of research. For greater accessibility to non-specialists, the published versions include an extended introduction, as well as a foreword by the student's supervisor explaining the special relevance of the work for the field. As a whole, the series will provide a valuable resource both for newcomers to the research fields described, and for other scientists seeking detailed background information on special questions. Finally, it provides an accredited documentation of the valuable contributions made by today's younger generation of scientists.

Theses are accepted into the series by invited nomination only and must fulfill all of the following criteria

- They must be written in good English.
- The topic should fall within the confines of Chemistry, Physics, Earth Sciences, Engineering and related interdisciplinary fields such as Materials, Nanoscience, Chemical Engineering, Complex Systems and Biophysics.
- The work reported in the thesis must represent a significant scientific advance.
- If the thesis includes previously published material, permission to reproduce this must be gained from the respective copyright holder.
- They must have been examined and passed during the 12 months prior to nomination.
- Each thesis should include a foreword by the supervisor outlining the significance of its content.
- The theses should have a clearly defined structure including an introduction accessible to scientists not expert in that particular field.

More information about this series at http://www.springer.com/series/8790

Cedrick Ansorge

Analyses of Turbulence in the Neutrally and Stably Stratified Planetary Boundary Layer

Doctoral Thesis accepted by
University of Hamburg, Hamburg, Germany

Springer

Author
Cedrick Ansorge
Atmosphere in the Earth System
Max Planck Institute for Meteorology
Hamburg
Germany

Supervisor
Juan Pedro Mellado
Atmosphere in the Earth System
Max Planck Institute for Meteorology
Hamburg
Germany

Supervisor's Foreword

Atmospheric models rely on turbulence parametrizations to represent the effect of unresolved motions on resolved properties of the planetary boundary layer. According to observations, common parametrizations fail to reproduce the correct effect in conditions of strongly stable stratification, when turbulence collapses and becomes intermittent in space and time. This problem has hampered the advance of our understanding of the planetary boundary layer for decades. In this book, Cedrick Ansorge demonstrates that we can eliminate this problem by simulating turbulence directly, without turbulence parametrizations, which allows him to investigate systematically, for the first time, key properties in conditions ranging from weak to strong stratification.

Direct numerical simulation of the planetary boundary layer has become feasible only recently with the advent of massively parallel supercomputers. Besides the well-established measurement-driven and conceptual approaches, direct numerical simulation opens a new avenue to study the planetary boundary layer. Direct numerical simulation removes the uncertainty of turbulence parametrizations; it does not use any turbulence parametrization, which turns out to be of critical importance in conditions of strongly stable stratification. But direct numerical simulation alone is no guarantee to advance physical understanding—direct numerical simulation serves this purpose only in combination with well-defined, physically sounded physical models that allow experiments in controlled conditions. Cedrick Ansorge employs a stably stratified Ekman layer as a physical model of the stable boundary layer, which he demonstrates to successfully reproduce the three stratification regimes observed in nature: weakly, intermediately and strongly stratified.

By means of this novel technique, the work presented in this book provides new answers to long-standing questions. For example, it shows that both turbulence collapse and the decoupling between the surface and the outer layer, need not be an on–off process in time but can rather occur intermittently in space without the need of external triggers, such as surface heterogeneity. It suffices that wave-like, large-scale structures (with a size of several boundary-layer depths) have enough space and time to develop. This result helps to explain the difficulty to obtain spatial

intermittency in simulations, because we need to retain these large scales and, simultaneously, resolve the small-scale turbulence inside the turbulence regions. Another important question addressed in this book is how this intermittency affects conventional statistics and turbulence parametrizations. A new conditioning method is developed to partition the flow into turbulent and non-turbulent regions in the vicinity of the wall. Systematic application of this conditioning method shows that turbulence properties inside the turbulent regions in the weakly and intermediately stratified cases are similar to turbulence properties in the neutrally stratified case. The order-of-one changes observed in the conventional statistics as stratification increases are mainly caused by the change of the volume fraction occupied by the turbulent regions.

To conclude, this work exemplifies how process-level studies that combine physical set-ups of reduced complexity with direct numerical simulations can yield new insight into relevant atmospheric phenomena. The numerical methods and physical set-up of stratified Ekman flows are presented in great detail, but this work also translates results from this simplified set-up into new physical understanding of the planetary boundary layer. Hence, the research presented in this book is an excellent example of how new computational capabilities are opening new very promising avenues in atmospheric research. As Cedrick's advisor, I enjoyed learning with him about the intricacies of stably stratified turbulence in the planetary boundary layer, and I congratulate him for an outstanding work. I hope this book inspires other scientists to also exploit these new computational capabilities in the study of geophysical turbulence.

Hamburg, Germany   Juan Pedro Mellado
July 2016

Parts of this thesis have been published in the following journal articles:

- **J.P. Mellado and C. Ansorge (2012)**: Factorization of the Fourier transform of the pressure-Poisson equation using finite differences in colocated grids. *Zeitschrift für Angewandte Mathematik und Mechanik/Journal of Applied Mathematics and Mechanics*, **92**(5) pp 380–392

- **C. Ansorge and J.P. Mellado (2014)**: Global intermittency and collapsing turbulence in the stratified planetary boundary layer. *Boundary-Layer Meteorology*, **153**(1) pp 89–116

- **C. Ansorge and J.P. Mellado (2016)**: Analyses of external and global intermittency in the logarithmic layer of Ekman flow. *Accepted for publication in the Journal of Fluid Mechanics*

Acknowledgments

Contents

Symbols and Abbreviations

α	Angle between free-stream velocity G and surface shear stress τ_0
δ	Turbulent Ekman layer depth $\delta = \frac{u_\star}{f}$
δ_v	Viscous layer length scale $\delta_v = \frac{v}{u_\star}$
δ_{95}	Height at which $\sqrt{\overline{uw}^2 + \overline{vw}^2} = 0.05 u_\star^2$
δ_{ij}	Kronecker symbol
ϵ_{ijk}	Lévy-Civita symbol
η	Kolmogorov length scale $\eta = \left(\frac{v^3}{\epsilon}\right)^{1/4}$
κ	Von-Kármán constant
ω	Vorticity $\omega = \nabla \times \mathbf{u}$
Ma	Mach number $Ma = \frac{U_0}{U_{sound}} = \frac{U_0}{1/(1 - R_d/c_p)R_d T_0}$
Pr	Prandtl number $Pr = \frac{v}{v_H}$
L_O^+	Stability-dependent Reynolds number $\frac{L_O u_\star}{v}$
Re	Viscous Reynolds number $Re = \frac{GD}{v}$
Ro	Rossby number $\frac{G}{\lambda f}$
μ	Thermal conductivity of air $\left[\mathrm{Wm^{-1}K^{-1}}\right]$
v	Kinematic viscosity of air $[\mathrm{ms^{-2}}]$
v_H	Thermal diffusivity of air $v = \frac{\mu}{c_p} [\mathrm{ms^{-2}}]$
v_E	Turbulent viscosity of a flow $[\mathrm{ms^{-2}}]$
Ω	Vector of planetary rotation $[\mathrm{s^{-1}}]$
π	Normalized non-hydrostatic pressure $\pi = \frac{p}{\rho_0} [\mathrm{ms^{-2}}]$
ρ	Density of dry air $[\mathrm{kg\,m^{-3}}]$
Λ_{Ro}	Rossby deformation radius $L_0 = \frac{G}{f}$
τ_0	Wall shear stress $\tau_0 = v \frac{\partial U}{\partial z}\big|_{z=0}$
Θ, θ	Reynolds average and fluctuation of potential temperature
b	Buoyancy $b = \frac{\theta'}{\theta_0} g = -\frac{\rho'}{\rho_0(z)} g [\mathrm{ms^{-2}}]$
$b_\star$	Friction buoyancy $b_\star = v\partial_z B/u_\star$

c_p	Specific heat capacity of dry air at constant pressure $c_p = 1.004\,\mathrm{kJ\,kg^{-1}\,K^{-1}}$
D	Viscous Ekman layer depth $D = \sqrt{\frac{2\nu}{f}}$
f	Coriolis parameter $f = 2\Omega \sin\phi_0$, where ϕ_0 is the reference latitude
G	Geostrophic wind $G = f^{-1}\partial_y \pi$
L_O	Obukhov length scale $L_O = -\frac{u_\star^2}{b_\star}$
p	Pressure [Pa]
R_d	Gas constant for dry air $R = 287\,\mathrm{J\,kg^{-1}K}$
R_{ij}	Reynolds stress $R_{ij} = \overline{u_i u_j}\,[\mathrm{ms^{-2}}]$
$u_\star$	Friction velocity at the wall $u_\star = \sqrt{\frac{\tau_0}{\rho}}$
u_1, u	Streamwise component of velocity
$\mathbf{u}$	Velocity vector $\mathbf{u} = (u, v, w)$
U_i, Π, B	Reynolds-averaged instantaneous quantities $X = \overline{\overline{X}}$
u_2, v	Spanwise component of velocity
u_3, w	Vertical component of velocity
z^+	Inner layer normalized height $z^+ = \frac{z}{\nu/u_\star}$
z^-	Outer layer normalized height $z^- = \frac{z}{\delta}$
DNS	Direct numerical simulation
HPC	High-performance computing
K41	Kolmogorov's theory on isotropic turbulence (Kolmogorov, 1941)
LES	Large eddy simulation
PBL	Planetary boundary layer
PSD	Power spectral density
RANS	Reynolds-averaged Navier–Stokes simulation
RHS	Right-hand side
r.m.s.	Root-mean-square
SBL	Stably stratified planetary boundary layer
SIRK3	Semi-implicit third-order–three-stage Runge–Kutta scheme according to Spalart, Moser and Rogers (1991)
TKE	Turbulence kinetic energy

Persons Mentioned in This Work

Science is about advancing the frontiers of knowledge. An important and necessary part in the pursuit of unknown territory within the universe of science is the reproducibility of results and the credit to previous work which is commonly assured by citations. (Some scientists and scientific institutions take this so far that citations are even mistaken as an indicator of quality or impact of a scientific work.) In today's science there are, however, ideas and concepts so pertinent and re-occurring that their inventors or important contributors are commonly not cited but constants, equations or ideas are simply named by them. These people who— some of them centuries ago—paved the ground for this work are acknowledged in the following compilation. References to their occurrence in the main text are found in the index.

Boussinesq, Joseph Valentin
- ⋆ Mar 13 1842 (St-André-de Snagonis, France)
- † Feb 19 1929 (Paris, France)
  Mathematician

Brunt, Sir David
- ⋆ Jun 17 1886 (Staylittle, Wales)
- † Feb 5 1965
  Meteorologist

Buckingham, Edgar
- ⋆ July 8 1867 (Philadelphia, PA, USA)
- † Apr 29 1940 (Washington D.C., MD, USA)
  Mathematician

Burgers, Johannes Martinus
- ⋆ Jan 13 1895 (Arnhem, Netherlands)
- † Jun 7 1981 (Washington D.C., MD, USA)
  Physicist

Chebyshev, Pafnuty
⋆ May 16 1821 (Borovsk, Russia)
† Dec 8 1894 (St. Peterburg, Russia)
Mathematician

Courant, Richard
⋆ Jan 8 1888 (Lublinitz, Germany)
† Jan 27 1972 (New Rochelle, NY, USA)
Mathematician

Coriolis, Gaspard-Gustave de
⋆ May 21 1792 (Paris, France)
† Sep 19 1843 (Paris, France)
Mathematician, Statistician, Engineer

Corrsin, Stanley
⋆ Apr 3 1920 (Philadelphia, PA, USA)
† Jun 2 1986 (Ridderwood, MD, USA)
Fluid Dynamicist

Dirichlet, Peter Gustav Lejeune
⋆ Feb 13 1805 (Düren, Germany)
† May 5 1859 (Göttingen, Germany)
Mathematician

Doppler, Christian
⋆ Nov 29 1803 (Salzburg, Austria)
† Mar 17 1853 (Venice, Italy)
Mathematician, Physicist

Ekman, Vagn-Walfrid
⋆ May 3 1874 (Stockholm, Sweden)
† Mar 9 1954 (Stockaryd, Sweden)
Oceanographer

Fourier, Joseph
⋆ Mar 21, 1768 (Auxerre, France)
† May 16 1830 (Paris, France)
Mathematician

Friedrichs, Kurt
⋆ Sep 28 1901 (Kiel, Germany)
† Dec 31 1982 (New Rochelle, NY, USA)
Applied Mathematician

Gauss, Carl Friedrich
⋆ Apr 30 1777 (Braunschweig, Germany)
† Feb 23 1855 (Göttingen, Germany)
Mathematician

Green, Albert E.
   ⋆ Nov 11 1912 (London, UK)
   † Aug 12 1999
   Applied Mathematician

Heaviside, Oliver
   ⋆ May 18 1850 (London, UK)
   † Feb 3 1925 (Torquay, UK)
   Mathematician

Helmholtz, Hermann von
   ⋆ Aug 31 1821 (Potsdam, Germany)
   † Sep 8 1904 (Berlin, Germany)
   Physicist

Kármán, Theodore von
   ⋆ May 11 1881 (Budapest, Hungary)
   † May 7 1963 (Aachen, Germany)
   Engineer

Kolmogorov, Andrey Nikolajevich
   ⋆ Apr 25 1903 (Tambov, Russia)
   † Oct 20 1987 (Moscow, Russia)
   Mathematician

Kutta, Martin Wilhelm
   ⋆ Nov 3, 1867 (Pitschen, Silesia)
   † Dec 25 1944 (Germany)
   Mathematician, Engineer

Laplace, Pierre-Simon
   ⋆ Mar 23 1749 (Beaumont-en-Auge, France)
   † Mar 5 1827 (France)
   Astronomer, Mathematician

Lewy, Hans
   ⋆ Oct 20 1904 (Breslau, Germany)
   † Aug 23 1988 (Berkeley, CA, USA)
   Mathematician

Mach, Ernst
   ⋆ Feb 18 1838 (Brno, Austria)
   † Feb 19 1916 (Munich, Germany)
   Physicist

Monin, Andrei Sergejevich
   ⋆ Jul 2 1921 (Moscow, Russia)
   † Sep 22, 2007 (Moscow, Russia)
   Meteorologist, Fluid Dynamicist

Navier, Claude-Louis
- ⋆ Feb 10 1785 (Dijon, France)
- † Aug 21 1836 (Paris, France)
- Mathematician, Physicist

Neumann, Carl
- ⋆ May 7 1832 (Königsberg, Germany)
- † Mar 27 1925 (Leipzig, Germany)
- Mathematician

Nyquist, Harry
- ⋆ Feb 7 1889 (Stora Kil, Sweden)
- † Apr 4 1976 (Harlingen, TX, USA)
- Electronic engineer

Obukhov, Alexander Mikhailovich
- ⋆ May 5 1918 (Saratov, Russia)
- † Dec 3 1989 (Moscow, Russia)
- Meteorologist, Fluid Dynamicist

Padé, Henri Eugène
- ⋆ Dec 17 1863 (Abbeville, France)
- † Jul 9 1953 (Aix-en-Provence, France)
- Mathematician

Prandtl, Ludwig
- ⋆ Feb 4 1875 (Freising, Germany)
- † Aug 15 1953 (Göttingen, Germany)
- Engineer, Aerodynamicist

Poicaré, Henri
- ⋆ Apr 29 1854 (Nancy, France)
- † Jul 17 1912 (Paris, France)
- Mathematician

Poisson, Siméon Denis
- ⋆ Jun 21 1781 (Pithiviers, France)
- † Apr 25 1840 (Sceaux, France)
- Mathematician

Rayleigh, John William Strutt, 3rd Baron
- ⋆ 12 Nov 1842 (Essex, England)
- † Jun 30 1919 (Witham, England)
- Physicist

Reynolds, Osborne
- ⋆ Aug 23 1842 (Belfast, Ireland)
- † Feb 21 1912 (Watchet, England)
- Pysicist

Richardson, Lewis Fry
  ⋆ Oct 11 1881 (Newcastle up. Tyne, England)
  † Sep 30 1953 (Kilmun, Scotland)
    Mathematician, Meteorologist, Physicist

Robin, Gustave Victor
  ⋆ May 17 1855 (France)
  † 1897 (Paris, France)
    Applied Mathematician

Runge, Carl David Tolmé
  ⋆ Aug 30 1856 (Bremen, Germany)
  † Jan 3 1927 (Göttingen, Germany)
    Mathematician, Physicist

Stokes, Sir George Bt.
  ⋆ Aug 13 1819 (Skreen, Ireland)
  † Feb 1 1903 (Cambridge, England)
  Mathematician, Physicist

Taylor, Brook
  ⋆ Aug 18 1685 (Edmonton, England)
  † Dec 29 1731 (London, England)
    Mathematician

Taylor, Geoffrey Ingram
  ⋆ Mar 7 1886 (St John's Wodd, England)
  † Jun 27 1975 (Cambridge, England)
  Mathematician, Physicist, Fluid Dynamicist

Townsend, Alan A.
  ⋆ Mar 7 1886 (St John's Wodd, England)
  † Jun 27 1975 (Cambridge, England)
    Fluid Dynamicist

Väisälä, Vilho
  ⋆ Sep 28 1889 (Finnland)
  † Aug 12 1969 (Finnland)
    Mathematician, Meteorologist

Part I
Preliminaries

Chapter 1
Introduction

The planetary boundary layer (PBL) is the bottom layer of the troposphere, i.e. that part in contact with the underlying land or ocean surface. Not only is the PBL the atmosphere's part which humans are primarily exposed to, but also does it govern the exchange of energy, momentum and humidity between the solid earth and the free atmosphere, the troposphere's part located immediately above the PBL. While the upper end of the PBL can be defined in numerous ways (on the earth, it ranges between some tens of meters and few kilometers), its lower limit is the surface itself. There, velocity and temperature of air need to match that of the underlying medium—be it an immovable wall, water or floating ice. At the upper end, the velocity is set by the wind and temperature in the free atmosphere inducing gradients in both the velocity and temperature across the PBL. Due to the huge vertical extent of the boundary layer and the low viscosity of air, even small vertical variations in the velocity deem the flow of air in the PBL turbulent which intensifies the vertical exchange of momentum, mass and energy by orders of magnitude.

Vertical gradients in temperature are mostly a consequence of differential heating or radiative processes, and in the absence of humidity and advection, they are caused by heating or cooling at the surface. Temperature and density variations are linked through the equation of state for air as an ideal gas. Depending on their sign, density variations may enhance or damp turbulence in the PBL, whose characteristics crucially depend on its density stratification. When the surface is relatively cooler than the air in the free atmosphere, density perturbations are damped: the density stratification is stable. The PBL under the impact of stable density stratification (SBL) is the object of research in this work, where fundamental aspects of wall-bounded stably-stratified turbulence are addressed, and their implications for the SBL are laid out.

If the surface cools sufficiently, turbulence is not only damped, but sometimes observed to cease partially or even entirely (Schlichting 1935; van de Wiel et al. 2012). The cessation of turbulence under strong stratification is often accompanied

by the occurrence of laminar patches even close to the surface, a phenomenon called global intermittency (Mahrt 1999). This particular mode of turbulence under strong stratification and the associated decoupling of the PBL from the surface impose challenges for mixing formulations in general circulation models used for numerical weather prediction and climate projections. Enhanced mixing formulations need often to be used in the mixing parameterizations for boundary layers of general circulation models to prevent a decoupling of the atmosphere from the surface (van de Wiel et al. 2012). Being heuristically formulated and tuned for the performance of general circulation models, these enhanced mixing formulations lack a physical basis and cause warm biases at the surface under very cold conditions (Tjernstrom et al. 2005). A better understanding of the underlying dynamics and physical processes, especially in the very stable limit, could hence contribute to alleviate and ultimately overcome these problems of mixing formulations under stable stratification (Mahrt 1999). This work embarks on a new tool in the context of the SBL, namely the direct numerical simulation (DNS) of turbulent flow, to re-establish an old perspective— that of fundamental fluid mechanics. Links between the extensive bodies of work devoted to stably stratified fluids and the SBL are established and exploited to gain new insight into the dynamics of the SBL.

1.1   Turbulence Regimes

Often, SBLs are classified into three regimes (Mahrt et al. 1998; Garg et al. 2000; Sun et al. 2012, sketched in Fig. 1.1). First, in the *weakly stable regime* (black dashed line), temperature behaves almost as a passive scalar, and the PBL's structure is indistinguishable from the neutral reference: weakness of the temperature gradients limits the turbulent heat exchange. Consequently, if stratification is strengthened slightly,
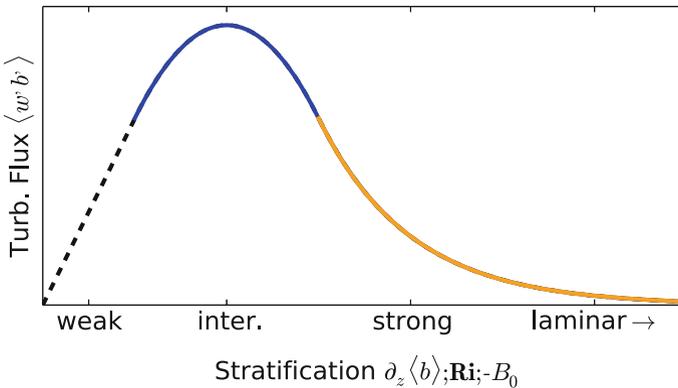
Fig. 1.1   Idealized schematic of the turbulent heat flux in the surface layer under increasing static stability; here, the turbulent heat flux is presented as a boundary-condition problem

the turbulent heat flux increases monotonically as a function of the stratification. Second, in the *intermediately stable regime* (blue line), the turbulent heat flux stagnates if stratification is strengthened; an increased temperature gradient is compensated by a decrease of vertical velocity fluctuations. Third, in the *very stable regime* (orange line), stratification drastically alters the SBL's turbulence structure to the degree that the weakness of turbulent motion limits the vertical heat exchange: The turbulent heat flux decreases with strengthening stratification. If strong enough, stratification can—locally or globally—lead to the absence of turbulence.

Although the very stable regime can be commonly observed in the atmosphere (Mahrt et al. 1998; Ha et al. 2007), there is still a lack of a general framework for the SBL incorporating that very stable regime (van de Wiel and Moene 2012; Mahrt 2014). Monin–Obukhov similarity theory (MOST, Obukhov 1971) lacks the ability to properly reproduce turbulent fluxes under weak-wind conditions (Ha et al. 2007), i.e. in the very stable regime. From atmospheric observations, it is unclear if stratification can become strong enough to suppress turbulent mixing entirely (Mauritsen and Svensson 2007), and it proves problematic to locally classify a very stable PBL as turbulent or non-turbulent. If turbulence is treated as an on–off process, a *runaway cooling* at the surface is often seen in PBL models and large-eddy simulations(LES) applied under very stable conditions (van de Wiel et al. 2012; Huang et al. 2013; Jiménez and Cuxart 2005).

1.2 Global Intermittency

A well-accepted hypothesis is that the cessation of turbulence is not an on–off process but rather a complex transition beginning with global intermittency, the localized absence of turbulence in an otherwise turbulent boundary layer. There exists a well-developed conceptual framework to ascertain whether a laminar flow exposed to a density stratification becomes turbulent: Taylor–Goldstein stability analysis and the Miles–Howard theorem (Di Prima and Swinney 1981; Drazin and Howard 1966) correctly describe both the relative stability of a particular flow and its path to turbulence. A similar framework to determine whether a turbulent flow re-laminarizes is still missing, and the analysis of turbulence in the very stable boundary layer remains challenging (Steeneveld 2014; Mahrt 2014).

The coexistence of locally laminar and locally turbulent flow in a single configuration is already mentioned by Corrsin (1943). He describes external intermittency, i.e. the segregation of a turbulent jet into two disjoint sub-volumes with fully developed turbulence and nearly laminar flow. This concept was termed intermittency and formally introduced by Townsend (1948) in an attempt to generalize Kolmogorov's theory on isotropic turbulence (Kolmogorov 1941, K41), and to apply K41 to a statistically inhomogeneous flow. Intermittency refers here to the concept of *external* intermittency, not to be confused with *internal* intermittency (cf. Tsinober 2014). Townsend (1948) postulates that regions of fully developed turbulence exist for a sufficiently long period of time to allow for the establishment of local isotropy inside

them. When the non-turbulent fraction of the turbulent flow is taken into account, his experimental data agree better with the prediction of K41.

Using an advanced method to determine the intermittency factor in a boundary layer (based on high-frequency velocity oscillations; cf. Townsend (1949)), Corrsin and Kistler (1955) provide physical reasoning and experimental evidence for the hypothesis that the interface between turbulent and non-turbulent motion is one between rotational and irrotational flow. In particular, they show that the root mean square (r.m.s.) of the vorticity varies by orders of magnitude across this interface. Based on such a vorticity-thresholding, a work by Kovasznay et al. (1970) introduces conditional sampling and averaging techniques to study separately the turbulent and non-turbulent flow regions in the intermittent part of a boundary layer.

The aforementioned studies are concerned with the case where non-turbulent flow exists aloft or around some region of turbulent motion. Another variant occurs when stabilizing body forces act on a flow and cause the decay, cessation or absence of turbulence. In stratified channels, re-laminarization was shown not to occur as an on–off process in time but rather as a complex transition from a turbulent to a non-turbulent state (Armenio and Sarkar 2002; Flores and Riley 2011; García-Villalba and del Àlamo 2011). When stratification increases gradually, the transition begins with the localized absence of turbulent eddies in an otherwise turbulent flow. Brethouwer et al. (2012) as well as Deusebio (2015) demonstrate a similar nature of transition for several wall-bounded flows, including both channel and pipe flow, with different stabilizing body forces. In Ekman flow stabilizing effects of both stratification and rotation are present, and a similar transition occurs under strong stratification as found independently in this work and by Deusebio et al. (2014).

To the author's knowledge, occurrence of global intermittency in atmospheric configurations has not yet reflected into an application of the conditioning methods described above to study separately the turbulent and non-turbulent sub-volumes in a rotating and stratified boundary layer. The challenge is twofold: First, small-scale derivatives have to be measured with sufficient accuracy to determine a vorticity-based intermittency factor γ (Kuznetsov et al. 1992). Despite advances in measurement techniques, still approximative methods are commonly employed to determine intermittency factors (Cava et al. 2012). Regarding numerical simulations, sufficiently resolved data in space and time are made available as part of this work and global intermittency is quantified here using direct numerical simulations of Ekman flow. The second challenge is related to the occurrence of global intermittency close to the wall. While a vorticity-based partitioning of the flow detects external intermittency in the outer layer of neutrally stratified flows, there are problems with global intermittency close to wall. There, large gradients in non-turbulent regions may falsely indicate the existence of turbulence. To overcome this second challenge, this work proposes an analysis of the flow combining the intermittency factor with a high-pass filter operation.

A different problem is the origin of global intermittency. It has been shown from observations globally intermittent turbulence can be triggered by a variety of external disturbances including orographic obstacles (Acevedo and Fitzjarrald 2003), solitary and internal gravity waves (Sun et al. 2004) and wind oscillations, such as nocturnal

low-level jets (Sun et al. 2012). Conceptual studies of the very stable boundary layer (McNider et al. 1995; Derbyshire 1999; van de Wiel and Moene 2002, 2012) have led to qualitative models of turbulence collapse and global intermittency. Global intermittency was, however, not investigated, and it remains unclear whether global intermittency can occur in a SBL without these external triggering mechanisms. In this work, evidence is provided that global intermittency is a process intrinsic to the SBL and does not necessarily rely on these triggering mechanisms as a precursor.

1.3   Approaches to Studying the Stable Boundary Layer

A qualitative understanding of strongly stable and globally intermittent turbulence from observations has proven difficult. In particular, accurate flux measurements are hard to obtain with standard methods, and various processes often interact as outlined in the above Sect. 1.2: Under atmospheric conditions, the entire range of scales, orographic complexity, interaction with the surface, and radiative processes are always present and generally not under a researcher's control. Thus, it is hard to isolate the signal of a single process as is sometimes necessary for a basic physical understanding. Ekman flow over a smooth wall—a much simplified configuration— is chosen here as the physical configuration. This choice enables a systematic and quantitative study of the intermediately and very stable regimes of turbulence in a simplified and well-defined set-up (described in detail in Chap. 2).

   While the study of the weakly stratified limit of simplified SBL configurations is well accomplished by LES (Beare et al. 2006; Huang and Bou-Zeid 2013), the study of very stable cases remains a challenge (Jiménez and Cuxart 2005; Saiki et al. 2000). In particular, the treatment of quasi-laminar patches under very stable conditions is problematic within the conceptual framework of LES. Hence, I consider here DNS, which—in comparison to LES—is not subject to uncertainties of sub-grid closures; DNS can deal with local re-laminarization of a flow as intrinsic to its representation by the Navier–Stokes equations. Following the pioneering work by Coleman et al. (1990), neutrally stratified Ekman flow has been subject to a number of studies (Coleman 1999; Shingai and Kawamura 2004; Miyashita et al. 2006; Marlatt et al. 2010; Spalart et al. 2008, 2009). The stably stratified problem was investigated by Coleman et al. (1992) and Shingai and Kawamura (2002), who studied Ekman flow under weak to moderate stratification in rather small domains. More recently, the small-domain set-up of Coleman et al. (1992) was investigated for stronger stratification by Shah and Bou-Zeid (2014) who found turbulent bursts in time.

   Instead of studying the problem of Ekman flow in its full complexity, it is common practice to use stratified channel flow as a surrogate for the stratified Ekman boundary layer, which is possible due to the analogy between the surface layer of channel flow and that of Ekman flow. In channel flow, oscillations on a period that is large when compared with the eddy turn-over time, were observed; but no intermittency was found at moderate Reynolds numbers (Nieuwstadt 2005). More recently, global

intermittency was simulated in channel flow, and it was proven that too-small domains lead to the formation of artificial flow regimes manifest for instance in the low-frequency oscillation of global statistics (García-Villalba and del Àlamo 2011; Flores and Riley 2011). Whereas the former use a fixed-temperature boundary condition, the latter impose a constant buoyancy flux at the surface. Flores and Riley (2011) observe large-scale intermittency linked to the collapse of turbulence. In contrast to channel flows, Ekman flow has no symmetry in the spanwise direction, which is known to cause some large-scale structures in the neutrally stratified limit (Shingai and Kawamura 2004). Whether these structures affect the collapse of turbulence remains unclear. When compared to an open boundary layer, it sticks out that—as a consequence of the rotating reference frame—the Ekman boundary layer is not growing infinitely despite being open at the top. Jiménez et al. (2009) found in a non-rotating configuration that *the outer flow of boundary layers and channel flows are intrinsically different*. Hence, Ekman flow may differ from channel flow as well—I address here the question, How much does it so?

1.4   Research Proposition

The SBL still poses a challenge in terms of both its modelling and fundamental understanding; problems are particularly pertinent where turbulence is globally inter-mittent and assumptions underlying common turbulence closures break down. This thesis, for the first time systematically, employs DNS, a widely-used tool to study canonical problems in fluid mechanics (Moin and Mahesh 1998), to study stratified Ekman flow. Particular emphasis is on very strong stability where other approaches have problems and many open questions remain. As a simplified set-up, turbulent Ekman flow over a smooth flat plate (introduced in Chap. 2) is chosen, and this work complements existing studies of stably stratified flows relevant to the atmospheric boundary layer.

DNS heavily relies on modern approaches to computing: It requires the utiliza-tion of highest-performance computers including massive parallelization of the algo-rithms used to compute the flow. In part II, the computing aspect is discussed. A new time-stepping scheme is implemented (Chap. 3), and efforts are undertaken as part of this work to optimize an algorithm for the solution of the Navier–Stokes equa-tions (Chap. 4). The consistency of the algorithm and its convergence properties are documented in Chap. 5

Using DNS to study the SBL, problems in the limit of strong stratification are evaded since the solution of the entire spectrum of turbulent motion keeps the set-up free of a turbulence closure model. The goal here is to shed light on the mechanisms of turbulence collapse under stable stratification, and to identify the role of global intermittency in this process. The fundamental nature of this approach—it is based on the governing equations of the flow only—will be shown throughout this work to be a great advantage when the flow is globally or externally intermittent. Part III is devoted to the physical aspects and commences with a description of the neutrally

stratified reference state in Chap. 6. In the subsequent chapters on the stably stratified flow, the utility of this approach is demonstrated, and the turbulent flow is simulated successfully in all regimes of static stability. A new method to overcome the above-mentioned problems in detecting global intermittency in the turbulent flow at large stability is developed in Chap. 8. The partitioning of the flow introduced there implies new avenues in understanding and parameterizing turbulence under very strong stability as shown in Chaps. 7–10.

References

Acevedo, O. C., & Fitzjarrald, D. R. (2003). In the core of the night-effects of intermittent mixing on a horizontally heterogeneous surface. *Boundary-Layer Meteorology*, *106*(1), 1–33. doi:10.1023/A:1020824109575.

Armenio, V., & Sarkar, S. (2002). An investigation of stably stratified turbulent channel flow using large-eddy simulation. *Journal of Fluid Mechanics*, *459*, doi:10.1017/S0022112002007851.

Beare, R. J., MacVean, M. K., Holtslag, A. A. M., et al. (2006). An intercomparison of large-eddy simulations of the stable boundary layer. *Boundary-Layer Meteorology*, *118*(2), 247–272. doi:10.1007/s10546-004-2820-6.

Brethouwer, G., Duguet, Y., & Schlatter, P. (2012). Turbulent-laminar coexistence in wall flows with Coriolis, buoyancy or Lorentz forces. *Journal of Fluid Mechanics*, *704*, 137–172.

Cava, D., Katul, G. G., & Molini, A. (2012). The role of surface characteristics on intermittency and zero-crossing properties of atmospheric turbulence—Cava—2012—Journal of Geophysical Research: Atmospheres (1984–2012)–Wiley Online Library. *Journal of Geophysical Research, 117*, doi:10.1029/2011JD016167.

Coleman, G. N. (1999). Similarity statistics from a direct numerical simulation of the neutrally stratified planetary boundary layer. *Journal of the Atmospheric Sciences*, *56*(6), 891–900.

Coleman, G. N., Ferziger, J. H., & Spalart, P. R. (1990). A numerical study of the turbulent ekman layer. *Journal of Fluid Mechanics*, *213*, 313–348.

Coleman, G. N., Ferziger, J. H., & Spalart, P. R. (1992). Direct simulation of the stably stratified turbulent ekman layer. *Journal of Fluid Mechanics*, *244*, 677–712.

Corrsin, S. (1943). Investigations in an axially symmetrical heated jet of air. *Report WR W-94*. Washington, DC: National Advisory Committee for Aeronautics.

Corrsin, S., & Kistler, A. L. (1955). Free-stream boundaries of turbulent flows. *Technical Report TR1244-3133*. Washington, DC: John Hopkins University. doi:10.1088/1468-5248/5/1/013.

Derbyshire, S. H. (1999). Boundary-layer decoupling over cold surfaces as a physical boundary-instability—Springer. *Boundary-Layer Meteorology*, *90*(2), 297–325. doi:10.1023/A:1001710014316.

Deusebio, E. (2015). The intermittency boundary in plane couette flow. *Journal of Fluid Mechanics*, *781*, 298–329. doi:10.1017/jfm.2015.497.

Deusebio, E., Brethouwer, G., Schlatter, P., et al. (2014). A numerical study of the unstratified and stratified Ekman layer. *Journal of Fluid Mechanics*, *755*, 672–704. doi:10.1017/jfm.2014.318.

Di Prima, R. C., & Swinney, H. L. (1981) Instabilities and transition in flow between concentric rotating cylinders. In H. L. Swinney, J. P. Gollub (Eds.), *Hydrodynamic instabilities and the transition to turbulence*. Berlin: Springer.

Drazin, P. G., & Howard, L. N. (1966) *Hydrodynamic stability of parallel flow of inviscid fluid, volume 9 of Advances in applied mathematics*. Elsevier.

Flores, O., & Riley, J. J. (2011). Analysis of turbulence colapse in the stably stratified surface layer using direct numerical simulation. *Boundary-Layer Meteorology*, *139*(2), 241–259. doi:10.1007/s10546-011-9588-2.

García-Villalba, M., & del Àlamo, J. C. (2011). Turbulence modification by stable stratification in channel flow. *Physics of Fluids*, *23*(4), 045104. doi:10.1063/1.3560359.

Garg, R. P., Ferziger, J. H., Monismith, S. G., et al. (2000). Stably stratified turbulent channel flows. I. Stratification regimes and turbulence suppression mechanism. *Physics of Fluids*, *12*(10), 2569–2594. doi:10.1063/1.1288608.

Ha, K.-J., Hyun, Y.-K., Oh, H.-M., et al. (2007). Evaluation of boundary layer similarity theory for stable conditions in CASES-99. *Monthly Weather Review*, *135*(10), 3474–3483. doi:10.1175/MWR3488.1.

Huang, J., & Bou-Zeid, E. (2013). Turbulence and vertical fluxes in the stable atmospheric boundary layer. Part I: A large-eddy simulation study. *Journal of the Atmospheric Sciences*, *70*(6), 1513–1527. doi:10.1175/JAS-D-12-0167.1.

Huang, J., Bou-Zeid, E., & Golaz, J.-C. (2013). Turbulence and vertical fluxes in the stable atmospheric boundary layer. Part II: A novel mixing-length model. *Journal of the Atmospheric Sciences*, *70*(6), 1528–1542. doi:10.1175/JAS-D-12-0168.1.

Jiménez, J., Hoyas, S. F., & Simens, M. P. (2009). Comparison of turbulent boundary layers and channels from direct numerical simulation. *Reason*.

Jiménez, M. A., & Cuxart, J. (2005). Large-eddy simulations of the stable boundary layer using the standard kolmogorov theory: Range of applicability. *Boundary-Layer Meteorology*, *115*(2), 241–261. doi:10.1007/s10546-004-3470-4.

Kolmogorov, A.N. (1941). Dissipation of energy in locally isotropic turbulence. *Dokl Akad Nauk SSSR*, *434*(1890), 15–17.

Kovasznay, L. S., Kibens, V., & Blackwelder, R. F. (1970). Large-scale motion in the intermittent region of a turbulent boundary layer. *Journal of Fluid Mechanics*, *41*(2), 283–325.

Kuznetsov, V. R., Praskovsky, A. A., & Sabelnikov, V. A. (1992). Fine-scale turbulence structure of intermittent hear flows. *Journal of Fluid Mechanics*, *243*, 595–622.

Mahrt, L. (1999). Stratified atmospheric boundary layers. *Boundary-Layer Meteorology*, *90*(3), 375–396.

Mahrt, L. (2014). Stably stratified atmospheric boundary layers. *Annual Review of Fluid Mechanics*, *46*, 23–45.

Mahrt, L., Sun, J., Blumen, W., et al. (1998). Nocturnal boundary-layer regimes. *Boundary-Layer Meteorology*, *88*(2), 255–278. doi:10.1023/A:1001171313493.

Marlatt, S. W., Waggy, S. B., & Biringen, S. (2010). Direct numerical simulation of the turbulent ekman layer: Turbulent energy budgets. *Journal of Thermophysics And Heat Transfer*, *24*(3), 544–555. doi:10.2514/1.45200.

Mauritsen, T., & Svensson, G. (2007). Observations of stably stratified shear-driven atmospheric turbulence at low and high Richardson numbers. *Journal of the Atmospheric Sciences*, *64*(2), 645–655. doi:10.1175/JAS3856.1.

McNider, R. T., England, D. E., & Friedman, M. J. (1995). Predictability of the stable atmospheric boundary layer. *Journal of the Atmospheric Sciences*, *52*(10), 1602–1614.

Miyashita, K., Iwamoto, K., & Kawamura, H. (2006). Direct numerical simulation of the neutrally stratified turbulent ekman boundary layer. *Journal of the Earth Simulator*, *6*, 3–15.

Moin, P., & Mahesh, K. (1998). Direct numerical simulation: A tool in turbulence research. *Annual Review of Fluid Mechanics*, *30*, 539–578.

Nieuwstadt, F. T. (2005). Direct numerical simulation of stable channel flow at large stability. *Boundary-Layer Meteorology*, *116*(2), 277–299. doi:10.1007/s10546-004-2818-0.

Obukhov, A. M. (1971). Turbulence in an atmosphere with a non-uniform temperature. *Boundary-Layer Meteorology*, *2*(1), 7–29.

Saiki, E. M., Moeng, C.-H., & Sullivan, P. P. (2000). Large-eddy simulation of the stably stratified planetary boundary layer. *Boundary-Layer Meteorology*, *95*(1), 1–30. doi:10.1023/A:1002428223156.

Schlichting, H. (1935). Turbulenz bei Wärmeschichtung. *ZAMM—Journal of Applied Mathematics and Mechanics / Zeitschrift für Angewandte Mathematik und Mechanik*, *15*(6), 313–338.

Shah, S. K., & Bou-Zeid, E. (2014). Direct numerical simulations of turbulent Ekman layers with increasing static stability: Modifications to the bulk structure and second-order statistics. *Journal of Fluid Mechanics*, *760*, 494–539.

Shingai, K., & Kawamura, H. (2002): Direct numerical simulation of turbulent heat transfer in the stably stratified ekman layer. *Thermal Science Engineering*, *10*(1), 0–8, 2.

Shingai, K., & Kawamura, H. (2004). A study of turbulence structure and large-scale motion in the Ekman layer through direct numerical simulations. *Journal of Turbulence*, *5*(5), doi:10.1088/1468-5248/5/1/013.

Spalart, P. R., Coleman, G. N., & Johnstone, R. (2008). Direct numerical simulation of the Ekman layer: A step in Reynolds number, and cautious support for a log law with a shifted origin (Retracted article. See, vol. 21, art. no. 109901, 2009). *Physics of Fluids*, *20*(10), 101507. doi:10.1063/1.3005858.

Spalart, P. R., Coleman, G. N., & Johnstone, R. (2009). Retraction: "Direct numerical simulation of the Ekman layer: A step in Reynolds number, and cautious support for a log law with a shifted origin" [Physics of Fluids 20, 101507 (2008)]. *Physics of Fluids*, *21*(10), 109901. doi:10.1063/1.3247176.

Steeneveld, G.-J. (2014). Current challenges in understanding and forecasting stable boundary layers over land and ice. *Frontiers in Environmental Science*, *2*, 1–6. doi:10.3389/fenvs.2014.00041.

Sun, J., Lenschow, D. H., Burns, S. P., et al. (2004). Atmospheric disturbances that generate intermittent turbulence in nocturnal boundary layers. *Boundary-Layer Meteorology*, *110*(2), 255–279.

Sun, J., Mahrt, L., Banta, R. M., et al. (2012). Turbulence regimes and turbulence intermittency in the stable boundary layer during CASES-99. *Journal of the Atmospheric Sciences*, *69*(1), 338–351. doi:10.1175/JAS-D-11-082.1.

Tjernstrom, M., Žagar, M., Svensson, G., et al. (2005). Modelling the arctic boundary layer: An evaluation of six arcmip regional-scale models using data from the sheba project. *Boundary-Layer Meteorology*, *117*(2), 337–381. doi:10.1007/s10546-004-7954-z.

Townsend, A. A. (1948). Local isotropy in the turbulent wake of a cylinder. *Australian Journal of Scientific Research, Series A*, *1*(2), 161–174.

Townsend, A. A. (1949). The fully developed wake of a circular cylinder. *Australian Journal of Chemistry*, *2*, 451–468.

Tsinober, A. (2014). *The essence of turbulence as a physical phenomenon*. Dordrecht: Springer. doi:10.1007/978-94-007-7180-2.

van de Wiel, B. J. H., & Moene, A. F. (2002). Intermittent turbulence and oscillations in the stable boundary layer over land. Part II: A system dynamics approach. *Journal of the Atmospheric Sciences*, *69*, 2567–2581.

van de Wiel, B. J. H., & Moene, A. F. (2012). The cessation of continuous turbulence as precursor of the very stable nocturnal boundary layer. *Journal of the Atmospheric Sciences*, doi:10.1175/JAS-D-12-064.1.

van de Wiel, B. J. H., Moene, A. F., Jonker, H. J. J., et al. (2012). The minimum wind speed for sustainable turbulence in the nocturnal boundary layer. *Journal of the Atmospheric Sciences*, *69*(11), 3116–3127. doi:10.1175/JAS-D-12-0107.1.

Chapter 2
Problem Formulation and Tools

2.1 The Governing Equations

The flow of a Newtonian fluid, such as gaseous air, is governed by the Navier–Stokes equations to within sufficient accuracy (Batchelor 1967). These equations are widely accepted as the appropriate vehicle to study laminar and turbulent flows. In a rotating reference frame, a fictitious force, the Coriolis Force, appears to act on the fluid (Chemin et al. 2006). When combined with the conservation laws of energy and mass and an equation of state of the fluid, these equations form a closed coupled system of partial differential equations for three velocity components $(u_i)_{i=1,2,3}$, the pressure p, density ρ and temperature T (see for instance Batchelor 1967)

$$\frac{d\rho u_i}{dt} = -\frac{\partial p}{\partial x_i} + \frac{\partial}{\partial x_j}\left[\rho v\left(\tau_{ij} - \frac{1}{3}\frac{\partial u_k}{\partial x_k}\delta_{i,j}\right)\right] + 2\rho\epsilon_{ijk}u_j\Omega_k - \rho g\delta_{i,3}$$

(2.1a)

$$\frac{d\rho(c_p - R_d)T}{dt} = +\frac{\partial}{\partial x_j}\left(v_H\rho\frac{\partial T}{\partial x_j}\right) + 2v\rho\left[\tau_{ij}\tau_{ij} - \frac{1}{3}\left(\frac{\partial u_i}{\partial x_i}\right)^2\right] - p\frac{\partial u_i}{\partial x_i}$$

(2.1b)

$$\frac{1}{\rho}\frac{d\rho}{dt} = -\frac{\partial u_j}{\partial x_j}$$

(2.1c)

$$\frac{p}{\rho} = R_d T.$$

(2.1d)

Here, v is the kinematic viscosity of air, and v_H the diffusivity of heat, $(c_p - R_d) = c_v$ is the volumetric heat capacity of air, and

$$\tau_{ij} \equiv \frac{1}{2}\left(\frac{\partial u_i}{\partial x_j} + \frac{\partial u_j}{\partial x_i}\right)$$

is the rate-of-strain tensor. The coordinate directions $i = 1, 2, 3$ are denoted as Ox, Oy and Oz, and Oz points in the vertical (wall-normal) direction. The velocity components are $u = u_1$, $v = u_2$, $w = u_3$.

Hydrostatic balance. In a geophysical context, it is common to use the concept of hydrostatic balance. Using the hydrostatic balance as a background state, density is decomposed into a reference value $\rho_0(z)$ and a fluctuation ρ' such that $\rho(x, y, z, t) = \rho_0 + \rho'(x, y, z, t)$. The density and pressure terms on the right-hand side (RHS) of Eq. (2.1a) for $i = 3$ can be written as

$$-\left(\frac{\partial p}{\partial z} + \rho g\right) = -\left(\frac{\partial p_h}{\partial z} + \rho_0 g + \frac{\partial p'}{\partial z} + \rho' g\right) = -\rho\left(\frac{1}{\rho}\frac{\partial p'}{\partial z} + \frac{\rho'}{\rho}g\right) \quad (2.2)$$

$$\text{with } \frac{\partial p_h}{\partial z} = -\rho_0 g,$$

where p_h is the hydrostatic pressure.

Potential temperature. The potential temperature θ is defined as

$$\theta := T\left(\frac{p_{ref}}{p}\right)^{R_d/c_p} \quad (2.3)$$

with $p_{ref} := 10^5$ Pa. The vertical gradient of θ, $\partial\theta/\partial z$, is a measure of stratification, and in a non-buoyant, i.e. neutrally stratified, atmosphere it is $\partial\theta/\partial z = 0$. θ is a measure of the entropy $s = c_p \ln \theta$, and when the energy Eq. (2.1b) is expressed in terms of θ, the changes of temperature due to density fluctuations $\partial_t(\rho R_d T) = \partial_t(p)$ are absorbed in the potential temperature.

Divergence-free constraint: incompressibility. A total change of pressure can be expressed in terms of potential temperature and density as

$$\frac{dp}{dt} = \frac{\partial p}{\partial \theta}\bigg|_\rho \frac{d\theta}{dt} + \frac{\partial p}{\partial \rho}\bigg|_\theta \frac{d\rho}{dt}, \quad (2.4)$$

with $\sqrt{(\partial p/\partial \rho)|_\theta} =: c$, the speed of sound. Hence, total changes in density ρ are expressed as

$$\frac{d\rho}{dt} = \frac{1}{c^2}\left(\frac{dp}{dt} - \frac{\partial p}{\partial \theta}\bigg|_p \frac{d\theta}{dt}\right). \quad (2.5)$$

If the speed of sound, c, is large in comparison to any velocity in the flow, changes in density become very small. The neglect of the first term is the *incompressibility assumption*; it implies the limit $c \to \infty$ and thus infinitely fast propagation of sound waves. Perturbations in the pressure field propagate at infinite speed. This instantaneous communication of pressure perturbations is manifest in a Helmholtz-type equation for the pressure that results if the divergence of Eq. (2.1a) is forced to zero (Sect. 3.1).

The neglect of the second term in Eq. (2.5) is related to density changes in response to internal dissipative heating and density changes in response to molecular conduction of heat (Batchelor (1967), p.170) which are known to be small under typical atmospheric conditions. Together with the neglect of the first term on the RHS of Eq. (2.5), this implies $d\rho/dt = 0$ which together with mass conservation requires that the momentum field has zero divergence, i.e. $\nabla \cdot \mathbf{u} = 0$.

In terms of non-dimensional parameters, all terms in Eq. (2.5) scale with the square of the Mach number

$$Ma = \frac{U_0}{\left(1/(1 - R_d/c_p)R_d T_0\right)^{1/2}} = \frac{U_0}{c}. \tag{2.6}$$

For consistency one also needs to neglect the anti-symmetric part of the second term on the RHS of Eq. (2.1b), the dissipative heating itself, which is also of the order of Ma^2. A consequence of the divergence-free constraint, is that $d\ln p \ll d\ln\theta$, from which $\rho'/\rho \cong -\theta'/\theta$ follows.

Boussinesq approximation. If $\rho'/\rho \ll 1$, one can approximate $\rho = \rho_0$ in the right-hand side of Eq. (2.2). This neglect of density variations is referred to as Boussinesq approximation (Cushman-Roisin and Beckers 2011, p. 83). Introducing the modified pressure $\pi := p/\rho_0$ along with a reference temperature θ_0 that corresponds to the reference density b_0, Eq. (2.2) becomes

$$-\frac{1}{\rho_0}\left(\frac{\partial p}{\partial z} + \rho g\right) = -\frac{\partial \pi}{\partial z} + \frac{\theta'}{\theta_0}g = -\frac{\partial \pi}{\partial z} + b, \text{ with } b := g\frac{\theta'}{\theta_0} \tag{2.7}$$

where b is the buoyancy and $\theta_0 = const.$ is the non-buoyant hydrostatic background potential temperature profile.

Equation 2.7 can be plugged into Eq. 2.1 when the latter is divided by ρ. In all other terms, the approximation $\rho = \rho_0$ is applied and density effects are covered by the buoyancy b—the remainder of the gravity term—only.

f-plane approximation, geostrophic balance. On a rotating sphere the local vector of angular rotation depends on the latitude ϕ as $\Omega(\phi) = \left|\vec{\Omega}\right|(0, \cos\phi, \sin\phi)$, which makes the Coriolis acceleration

$$-2\vec{\Omega} \times \vec{v} = -2|\vec{\Omega}| \begin{pmatrix} w\cos\phi - v\sin\phi \\ u\sin\phi \\ u\cos\phi \end{pmatrix}. \tag{2.8}$$

At the poles the vector of rotation Ω simplifies to $\Omega = (0, 0, |\Omega|)^T = (0, 0, f/2)^T$ with $f := 2|\Omega|\sin\phi$ the Coriolis parameter, and one may locally consider a horizontal plate rotating around the vertical axis. Hence the name f-plane approximation. Away from the poles this f-plane approximation is a further simplification of Eq. (2.1a), which is justified in particular at high latitudes and for small vertical

velocities. As a consequence of the f-plane approximation, the latitude ϕ drops out as a parameter of the problem.

If a shear-free, homogeneous flow on an f-plane, is exposed to a pressure gradient, the pressure gradient force may only be balanced by the Coriolis force. This balance is the *geostrophic balance*:

$$G_i = f \epsilon_{i3k} \frac{\partial \Pi}{\partial x_k}, \tag{2.9}$$

where $\mathbf{G} = G_i \hat{e}_i$ is the geostrophic wind vector and $\partial \Pi / \partial x_k$ is the mean pressure gradient along $O x_k$. Far away from the wall, this geostrophic balance of the pressure gradient with the mean flow along isobars is a good approximation, and turbulence as well as viscous effects do not play an important role. The physical problem—besides the latitude—also depends on the direction along which the pressure gradient is imposed. Without loss of generality, the coordinate system is aligned such that $\hat{e}_1 = \mathbf{G}/|\mathbf{G}|$ and I refer to the direction of $\mathbf{G}$ as streamwise and to that of $\hat{e}_2 = (\vec{\Omega} \times \mathbf{G})/|\vec{\Omega} \times \mathbf{G}|$ as spanwise direction.

Simplified equations and boundary conditions. Using the simplifications discussed above, Eqs. (2.1a)–(2.1c) become

$$\frac{\partial u_i}{\partial t} = - u_j \frac{\partial u_i}{\partial x_j} - \frac{\partial \pi}{\partial x_i} + \nu \frac{\partial^2 u_i}{\partial x_j^2} + f \epsilon_{ij3} u_j + b \delta_{i,3} \tag{2.10a}$$

$$\frac{\partial b}{\partial t} = - u_j \frac{\partial b}{\partial x_j} + \nu_H \frac{\partial^2 b}{\partial x_j^2} \tag{2.10b}$$

$$\frac{\partial u_i}{\partial x_i} = 0, \tag{2.10c}$$

where the variation of the molecular diffusivities ν and ν_H as a function of the state of the air is ignored. The set of partial differential Equations (2.10a)–(2.10c) is closed, and it describes the time-evolution of the velocity, pressure and buoyancy fields given initial and boundary conditions.

At the lower boundary, a no-slip and no-penetration condition is imposed mimicking a solid wall. At the upper boundary, a free-slip and no-penetration condition is used. This supposes that the upper end of the domain is part of the free stream and as such in geostrophic balance. In the horizontal direction, the domain is doubly-periodic. It needs to be large enough to capture the largest structure relevant for turbulence. Stratification may be imposed via a Dirichlet (fixed-value), Neumann (fixed-gradient) or Robin (mixed) boundary condition. In this work, only Dirichlet boundary conditions are considered.

2.2 Non-dimensionalization and Parameter Space

If a fluid mechanical problem is rescaled, the law of hydrodynamic similarity may be exploited to apply the Buckingham-Π theorem. This allows to draw definite conclusions on classes of flows rather than a single configuration. Therefore it is necessary to identify relevant parameters and group them into non-dimensional combinations.

2.2.1 The Neutrally Stratified Regime

Under neutral stratification, the Ekman-flow dynamics are governed by the quantities $\{G, f, \nu, \nu_H\}$ (we include here the diffusivity of a passive tracer for completeness) once turbulence has fully developed and the flow fields have sufficiently de-correlated from the initial conditions. Following previous studies (Coleman et al. 1992; Spalart et al. 2008, 2009; Marlatt et al. 2010), the Coriolis parameter f is replaced by the laminar Ekman-layer depth $D \equiv \sqrt{2\nu f^{-1}}$ in the dimensional analysis. This yields the Reynolds and Prandtl numbers

$$Re = \frac{GD}{\nu}, \quad Pr = \frac{\nu}{\nu_H}, \tag{2.11}$$

where it is noted that $Re \propto \nu^{-1/2}$. Here, the Prandtl number is fixed as $Pr \equiv 1$. In contrast to the boundary-layer flow over a flat plate, where the shear layer deepens continuously and no steady state is reached, Ekman flow acquires a balance between the production of turbulence due to shear and the suppression of turbulence due to rotation. The neutrally stratified flow has hence a steady-state solution in terms of a statistical description of turbulence which is a function of Re only. This also implies that the definition of an initial condition from a mathematical perspective is irrelevant if the flow is linearly unstable, which is the case for Ekman flow beyond $Re = Re_{\text{crit}} = 115$ (Lilly 1966). For $Re > Re_{\text{crit}}$, the flow transitions to its turbulent statistical equilibrium state.

2.2.2 Uniqueness of the Solution

Given initial and boundary conditions, one might ask the question, Is this equilibrium state deterministic? Despite recent advance (Otelbaev 2014), the general unique solubility of the Navier–Stokes equations still withstands a widely accepted rigid mathematical proof (Gowers 2000; Ladyzhenskaya 2003). So, from a fundamental point of view, it is not clear if there is a single such equilibrium state—multiple such states might exist, and infinitesimal perturbations in the initial condition might determine to which statistical equilibrium the flow transitions. While, in theory,

non-uniqueness of the solution might allow for the existence of multiple relevant equilibria, this is practically not realizable. Not only would additional equilibria be irrelevant for physical realizations of the problem: no more than one equilibrium has been observed both numerically and in laboratory experiment. But also would the existence of two physically realizable equilibria contradict the Navier–Stokes equation's unique solubility for a finite time (Ladyzhenskaya 2003; Chemin et al. 2006). Hence, in the following it is assumed, there exists only one equilibrium.

If such an equilibrium exists, it is inevitably attained by the flow for $Re > Re_{\mathrm{crit}}$. Once the flow is in its turbulent state, the laminar length scale D no longer describes the flow appropriately. Instead, the boundary-layer depth scale $\delta \equiv u_\star/f$ is used, where $u_\star$ is the friction velocity defined below. The following parameters characterize the turbulent flow:

$$u_\star^2 = \nu \frac{\partial \sqrt{\langle u \rangle^2 + \langle v \rangle^2}}{\partial z}\bigg|_{z=0}, \quad \delta = u_\star/f \quad \text{and} \quad Re_\tau = \frac{u_\star \delta}{\nu}. \qquad (2.12)$$

In contrast to channel flows, $u_\star$ in the Ekman layer cannot be known a priori but only a posteriori, and $u_\star$ depends weakly on Re (Spalart 1989). Following common practice, the flow is studied in terms of an inner layer (where molecular viscosity plays an important role) and an outer layer (where turbulent viscosity plays an important role). In the inner layer, i.e. also in the surface layer, the wall unit $\nu/u_\star$ and the friction velocity $u_\star$ are chosen for normalization; normalized quantities are denoted by a superscript $+$. In the outer layer, quantities are normalized by $u_\star$ and δ, and correspondingly normalized quantities are denoted by a superscript $-$. Because of its physical meaning, the inertial period $2\pi f^{-1}$ is used as the outer reference time scale instead of f^{-1}.

2.2.3 Imposing Stratification: Initial and Boundary Conditions

When a stratified flow is considered, in addition to the boundary conditions for the flow and scalar, an initial condition for the active scalar is needed. For the velocity fields, a turbulent initial condition is employed—depending on the case and question either from an equilibrated neutrally stratified simulation or from a quasi-steady stratified simulation.

Here, the problem is studied for a fixed surface buoyancy only; for a discussion of the impact of flux boundary conditions and more complex set-ups, see Flores and Riley (2011) and van de Wiel et al. (2012). The buoyancy difference between the surface and the far field is B_0 (cf. Coleman et al. 1992); this new parameter combines into the Froude number $Fr = G^2/(B_0 D)$. Fr incorporates the laminar length scale D loosing its relevance in turbulent flow. In the turbulent set-up, stratification is expressed more appropriately in terms of the global bulk Richardson number,

$$Ri_B := \frac{B_0 \delta_{\text{neutral}}}{G^2}. \tag{2.13a}$$

Due to the choice of a Dirichlet boundary condition,

$$b(x, y, z = 0, t > 0) = 0 \quad \text{and} \quad b(x, y, z = z_{top}, t > 0) = B_0, \tag{2.13b}$$

Ri_B is an inviscid external parameter, and used in the following to classify simulations according to their stratification.

The Obukhov length L_O (Obukhov 1971) is an alternative measure to characterize stratification. In particular, the ratio of the Obukhov length L_O with the wall unit $\nu/u_\star$,

$$L_O^+ = L_O \frac{u_\star}{\nu} := \left(-\frac{\theta_0}{g} \frac{u_\star^3}{\overline{\theta w}|_{z=z_0}} \right)^+ = \left(\frac{u_\star^3}{u_\star b_\star} \right)^+ \quad \text{with} \quad u_\star b_\star = \nu \left. \frac{\partial \langle b \rangle}{\partial z} \right|_{z=0} \tag{2.13c}$$

determines the character of turbulence (Flores and Riley 2011): L_O^+ measures the biggest possible scale separation in a stratified flow (Flores and Riley 2011), and is therefore an appropriate Reynolds number in a stratified environment. Interestingly, the critical value of $L_0^+ \simeq 100$ estimated by Flores and Riley is very similar to the critical Reynolds number for linear instability of Ekman flow ($Re_{\text{crit}} = 115$). Recent work (Deusebio 2015) indeed suggests this threshold is almost universal.

This is consistent with the research on minimal flow units suggesting that the near-wall cycle of turbulence can only be sustained for scales larger than 100 wall units (Jiménez and Pinelli 1999).

Over a smooth wall, this parameter can also be interpreted in terms of the gradient Richardson number

$$Ri_G := \frac{\partial_z B|_{z=0}}{(\partial_z U)^2|_{z=0}} = \nu \frac{b_\star}{u_\star^3} = \left(L_O^+ \right)^{-1}, \tag{2.13d}$$

where $Pr = 1$, as defined above, is used. Therefore, L_O^+ contains information about the stability character in the near-wall region. Large L_O^+ implies a small Ri_G and hence turbulence can develop in the lower part of the SBL. In Ekman flow over a surface at fixed temperature, both L_O and Ri_G are not external parameters to the problem, but they are time-dependent measures describing the evolution of the system. For that reason Ri_B is used as control parameter.

Besides the strength of stratification, the profile of stratification imposed as the initial condition has a significant impact during the initial phase: the initial profile determines the duration of the initial transient. The focus here is on the cases where almost the entire stratification concentrates initially within the viscous sub-layer of

the flow, mimicking a sudden cooling of the surface. Following Coleman et al. (1992), the initial condition for the buoyancy is

$$b(x, y, z, t_0) = 1 - \text{erf}\left[\frac{z/D}{2a}\right] = 1 - \text{erf}\left[\frac{z}{2a}\left(\frac{\delta_{neutral}}{\sqrt{2Re_\tau}}\right)^{-1}\right], \quad (2.14)$$

where b is the buoyancy normalized with the surface boundary value B_0, Re_τ is defined in Eq. (2.12) and $a = 0.15$ is the non-dimensional thickness. Also, $\delta_{neutral}$ refers to the value of the neutrally stratified case used for the initialization of the velocity fields.

This particular choice of the initial condition through the concentration of the entire buoyancy gradient into the surface layer bears the dilemma that stratification may be very strong close to the surface even if Ri_B, which is expected to control the long-time evolution of the system, is sub-critical. In that case, the initial transient can contain periods of time wherein the turbulence is shut off through a very efficient cut of production in the buffer layer; this initial phase is most appropriately characterized by Ri_G. Ri_G is indicative of the respective stratification in the production region (surface layer) and more appropriate to study the initial transient when a stratification is imposed in an initially very thin layer at the surface. Given the large spread between the two parameters Ri_B and Ri_G ($Ri_G(t = 0)/Ri_B = G^2/u_\star^2$), the range of stratifications over which this might occur is potentially large. Thereafter molecular mixing slowly diminishes the buoyancy gradient until the flow may become unstable again. Although the focus of this work is the long-time evolution of the system, the ratios of these transition time scales to the integral time scale of turbulence, $2\pi f^{-1}$ (or $f^{-1} = \delta/u_\star$, see above), are relevant in the context of the atmosphere. For instance, they determine whether a fully-developed boundary layer has time to reach its quasi-steady state over the course of a night (or other externally set time scales). In Sect. 7.1, I show that the key findings are, at least in the range considered here, independent of the choice of initial condition.

2.2.4 Parameter Space of the Non-dimensionalized Problem

The problem as formulated hereunto depends only on two parameters, a Reynolds and a Richardson number. The Reynolds number measures the separation of scales between the large scales (in this case, these are the scales forcing the system) and the smallest scales contributing to the spectrum of turbulent motion. Some relevant aspects of the flow are commonly expected to scale self-similarly with respect to the Reynolds number—at least in the limit of the (high) Reynolds numbers typical for the PBL. The Richardson number represents stratification, and it is well known that turbulent flow reacts sensitively to changes in the stratification from theoretical considerations, observations and numerical studies (Richardson 1920; Fernando 1991; Peltier and Caulfield 2003; Ivey et al. 2008).
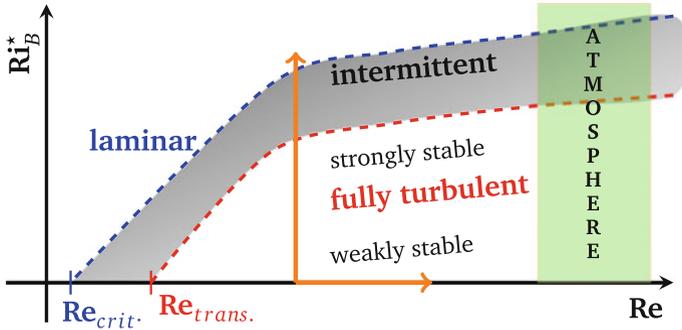
Fig. 2.1 Schematic of the problem's parameter space as introduced in the text

Previous work suggests to partition the problem's parameter space as sketched in Fig. 2.1. Under neutral stratification the only parameter of the problem is the Reynolds number, and once in the fully turbulent regime, low-order statistics are well-known to be to a certain degree independent of the Reynolds number *Re* (Moin and Mahesh 1998). If stratification is increased at fixed *Re*, the regimes of weak, intermediate and strong stratification are covered before the flow laminarizes. While there is no doubt as to the existence of those regimes, the thresholds and dynamics of transitions and their nature are under debate (Tritton and Davies 1981; Manneville 2008); in particular no conclusive statements have been made on the limit and dynamics of stratification for the re-laminarization of a turbulent flow and the associated phenomenon of global intermittency, where laminar patches exist in an otherwise turbulent flow.

2.3 Analysis Tools

The direct numerical simulation of a turbulent flow consists of the solution of Eqs. 2.1a–2.1d, and it may be interpreted as a merely technical problem or numerical exercise (Chaps. 3–5). Once these solutions are available, they may be studied to gain physical insight (Chaps. 6–8). Commonly, this is not achieved via the analysis of a single datum (even though this constitutes a reasonable option for some kind of analyses) but rather by means of analysis methods that have solid theoretical foundations and are widely applied. Besides the very common approach of a spectral decomposition (Finnegan and Kaimal 1994) and the analysis of probability density functions, conditional sampling and virtual tower measurements are used in this work and described in the following sections.

2.3.1 Conditional Sampling

Free turbulent flows are ubiquitous in engineering, and they are even more so in geophysical applications of turbulence research. The possible coexistence of non-turbulent and turbulent fluid in a statistically homogeneous manifold of a turbulent flow domain was already recognized by Corrsin (1943, cf. Chap. 1 of the present work). Phenomena at the turbulent–non-turbulent interface—namely external inter-mittency and entrainment—play a pivotal role in the development of boundary layers with a free stream. The successful (experimental) distinction between turbulent and non-turbulent fluid based on the instantaneous vorticity magnitude allows to separate the flow domain into a turbulent and non-turbulent part (Corrsin and Kistler 1955). If turbulent processes or quantities—such as the turbulent diffusion and the associated turbulent diffusivity—are of interest, one may argue that a consideration of statistics based on the turbulent or non-turbulent subsets alone is useful. A sample is then based on a subset of the domain that suffices a particular condition—hence the term conditional sampling for this procedure that is widely used in the experimental study of turbulent flows (Antonia 1981). The capability to sample a flow conditionally allows a whole new set of analysis methods embraced under the term of conditional statistics; these statistics may be averages or higher moments, but they may also be more complex such as probability density functions or wavelets.

   With respect to atmospheric boundary layers, conditional sampling so far has almost exclusively been used in the context of field measurements in the surface layer under convective conditions (Singh Khalsa 1980; Singh Khalsa and Greenhut 1985; Katul et al. 1994). A weakly intermittent nocturnal surface inversion layer and a Bora flow have been investigated using conditional statistics with respect to the eigen-structure of micro-fronts by Mahrt and Frank (1988).

2.3.2 Temporally Resolved Probes

While the details of an individual realization of a turbulent flow are often not of particular interest when investigating the turbulent dynamics, also the vast number of degrees of freedom in a DNS prohibits to analyze all the data that potentially become available throughout a simulation. For technical reasons, namely the restart of a simulation, fully-resolved three-dimensional fields are saved at fixed iteration points, but otherwise only a predefined set of statistics is extracted and saved. Hence, for an a posteriori analysis there are data at very high spatial but rather coarse temporal resolution. While this is generally sufficient for the study of the bulk turbulence in a statistical sense, i.e. based on ensemble averages, investigation of some processes at high temporal frequency demands higher temporal resolution. Also, observational data in the atmosphere are mostly obtained from fixed-in-space probes (towers) at a high temporal resolution, and generally very coarse spatial resolution—if at all

there is more than one tower available for the analysis of a flow within the spatial separation relevant to turbulent processes.

During this work, I implemented a tower-sampling at high temporal resolution at selected locations. In the largest set-up (at $Re = 1000$ with a horizontal box size $L_{xy}/\delta \simeq 20$), the flow is sampled at the full temporal resolution, i.e. at every iteration at 32×32 locations in each horizontal plane. This corresponds to a spacing of $(0.64\delta \times 0.64\delta)$ or $(1.01\delta_{95} \times 1.01\delta_{95})$ (cf. Chap. 6). This spatial separation allows to consider each tower as an approximately independent realizations of the flow.

Let $\mathbf{x}_i(t, z)$ the instantaneous realization of a flow realization at time t, height z and location $\mathbf{r}_i$. Let further $(t_n)_{n\in\mathbb{N}}$ the discrete series of times through which the flow is integrated, and $(\mathbf{r}_i)_{i\in\{1...1024\}\subset\mathbb{N}}$. Further, let

$$\overline{x_i(z)}^T := \frac{1}{n(T)} \sum_{n=1}^{n(T)} \mathbf{x}_i(t_n, z) \tag{2.15}$$

$$\text{with } n(T) \text{ such that } t_{n(T)-1} < T \le t_{n(T)},$$

that is, $\overline{x_i(z)}^T$ is the average of the tower at $\mathbf{r}_i$ over a period of time of length T.

Ergodicity of the stationary, four-dimensional turbulent field implies

$$\langle \mathbf{x}_i(t, z) \rangle = \lim_{T\to\infty} \overline{x_i(z)}^T. \tag{2.16}$$

Moreover, in the limit of an infinite number of towers, it is $\langle \mathbf{x}(z) \rangle = \langle \mathbf{x}_i(t_n, z) \rangle$.

2.4 Summary

In this chapter, the physical problem is formulated using the governing equations. The Navier–Stokes equations in the Boussinesq limit are identified as the appropriate set of equations to study the flow. These equations are introduced along some common assumptions and simplifications, and their simplified version is subsequently non-dimensionalized. The non-dimensional parameter space of the problem is introduced and qualitatively characterized, and the main analysis methods are presented.

References

Antonia, R. A. (1981). Conditional sampling in turbulence measurement. *Annual Review of Fluid Mechanics*, *13*, 131–156.

Batchelor, G. K. (1967). *An introduction to fluid dynamics*. Cambridge University Press.

Chemin, J.-Y., Desjardins, B., & Gallagher, I. et al. (2006). *Mathematical geophysics, volume 32 of Oxford Lecture Series in Mathematics and its Applications*. Oxford: Clarendon Press.

Corrsin, S. (1943). Investigations in an axially symmetrical heated jet of air. *Report WR W-94*. Washington, DC: National Advisory Committee for Aeronautics.

Corrsin, S., & Kistler, A. L. (1955). Free-stream boundaries of turbulent flows. *Technical Report TR1244-3133*. Washington DC: John Hopkins University. doi:10.1088/1468-5248/5/1/013.

Cushman-Roisin, B., & Beckers, J. M. (2011). *Introduction to geophysical fluid dynamics: physical and numerical aspects, volume 101 of International Geophysical Series*, 2nd edn. Elsevier.

Coleman, G. N., Ferziger, J. H., & Spalart, P. R. (1992). Direct Simulation of the stably stratified turbulent ekman layer. *Journal of Fluid Mechanics*, *244*, 677–712.

Deusebio, E. (2015). The intermittency boundary in plane couette flow. *Journal of Fluid Mechanics, 781*, 298–329. doi:10.1017/jfm.2015.497.

Fernando, H. (1991). Turbulent mixing in stratified fluids. *Annual Review of Fluid Mechanics*, *23*, 455–493.

Finnegan, J., & Kaimal, J. C. (1994). *Atmospheric boundary layer flows: Their structure and measurement.* Oxford University Press.

Flores, O., & Riley, J. J. (2011). Analysis of turbulence colapse in the stably stratified surface layer using direct numerical simulation. *Boundary-Layer Meteorology*, *139*(2), 241–259. doi:10.1007/s10546-011-9588-2.

Gowers, T. W. (2000). The importance of mathematics. In: *Millenium Meeting*. Paris.

Ivey, G. N., Winters, K. B., & Koseff, J. R. (2008). Density stratification, turbulence, but how much mixing? *Annual Review of Fluid Mechanics*, *40*(1), 169–184. doi:10.1146/annurev.fluid.39.050905.110314.

Jiménez, J., & Pinelli, A. (1999). The autonomous cycle of near-wall turbulence. *Journal of Fluid Mechanics*, *389*, 335–359.

Katul, G. G., Albertson, J., Parlange, M., et al. (1994). Conditional sampling, bursting, and the intermittent structure of sensible heat flux. *Journal of Geophysical Research*, *99*(D11), 22869. doi:10.1029/94JD01679.

Ladyzhenskaya, O. A. (2003). Sixth problem of the millennium: Navier-Stokes equations, existence and smoothness. *Russian Mathematical Surveys*, *58*(2), 251.

Lilly, D. K. (1966). On the instability of ekman boundary layer flow. *Journal of the Atmospheric Sciences*, *23*, 481–494.

Mahrt, L., & Frank, H. (1988). Eigenstructure of eddy microfronts. *Tellus A*, *40A*(2), 107–119. doi:10.1111/j.1600-0870.1988.tb00410.x.

Manneville, P. (2008). Understanding the sub-critical transition to turbulence in wall flows. arXiv.org; doi:10.1007/s12043-008-0105-1.

Marlatt, S. W., Waggy, S. B., & Biringen, S. (2010). Direct numerical simulation of the turbulent ekman layer: turbulent energy budgets. *Journal of Thermophysics And Heat Transfer*, *24*(3), 544–555. doi:10.2514/1.45200.

Moin, P., & Mahesh, K. (1998). Direct numerical simulation: A tool in turbulence research. *Annual Review of Fluid Mechanics*, *30*, 539–578.

Obukhov, A. M. (1971). Turbulence in an atmosphere with a non-uniform temperature. *Boundary-Layer Meteorology*, *2*(1), 7–29.

Otelbaev, M. (2014). Existence of a unique solution of the Navier-Stokes equations (in Russian). *Kazakhian Journal of Mathematics*, *13*(4), 5–104.

Peltier, W. R., & Caulfield, C. P. (2003). Mixing efficiency in stratified shear flows. *Annual Review of Fluid Mechanics*, *35*, 135–167. doi:10.1146/annurev.fluid.35.101101.161144.

Richardson, L. F. (1920). The supply of energy from and to atmospheric eddies. *Proceedings of the Royal Society of London Series a-Containing Papers of a Mathematical and Physical Character*, *97*(686), 354–373.

Singh Khalsa, S. J., & Greenhut, G. K. (1985). Conditional sampling of updrafts and downdrafts in the marine atmospheric boundary layer. *Journal of the Atmospheric Sciences*, *42*(23), 2550–2562. doi:10.1175/1520-0469(1985)042<2550:CSOUAD>2.0.CO;2.

Singh Khalsa, J. (1980). Surface-layer intermittency investigated with conditional sampling. *Boundary-Layer Meteorology*, *19*(2), 135–153. doi:10.1007/BF00117216.

Spalart, P. R. (1989). Theoretical and numerical studies of a three-dimensional turbulent boundary layer. *Journal of Fluid Mechanics*, *205*, 319–340.

Spalart, P. R., Coleman, G. N., & Johnstone, R. (2008). Direct numerical simulation of the Ekman layer: A step in Reynolds number, and cautious support for a log law with a shifted origin (Retracted article. See, vol. 21, art. no. 109901, 2009). *Physics of Fluids*, *20*(10), 101507. doi:10. 1063/1.3005858.

Spalart, P. R., Coleman, G. N., & Johnstone, R. (2009). Retraction: "Direct numerical simulation of the Ekman layer: A step in Reynolds number, and cautious support for a log law with a shifted origin" [Phys. Fluids 20, 101507 (2008)]. *Physics of Fluids*, *21*(10), 109901. doi:10.1063/1. 3247176.

Tritton, D. J., & Davies, P. A. (1981). Instabilities in geophysical fluid dynamics. In: H. L. Swinney, & J. P. Gollub (Eds.), *Hydrodynamic instabilities and the transition to turbulence*. Berlin: Springer.

van de Wiel, B. J. H., Moene, A. F., Jonker, H. J. J., et al. (2012). The minimum wind speed for sustainable turbulence in the nocturnal boundary layer. *Journal of the Atmospheric Sciences*, *69*(11), 3116–3127. doi:10.1175/JAS-D-12-0107.1.

Part II
Numerics

Chapter 3
Discretization

DNS of a turbulent flow requires a discretization of the governing Navier–Stokes equations in both time and space. The Navier–Stokes equations are a set of partial differential equations for the temporal evolution of the vector field $u = (\mathbf{u}, p) \in \mathbb{R}^4$, $\mathbf{u} \in \mathbb{R}^3$, and may be written as

$$\frac{\partial u}{\partial t} = F(u). \tag{3.1}$$

Discretization of Eq. (3.1) consists in a discrete representation of the operators ∂_t and F, which appears as two separate problems from a naïve stand point. (They are, of course, related by stability constraints such as the Courant-condition and related constraints originating from the discretizations of the two operators; for a test of the algorithms employed in this work, see Chap. 5.)

In this work, the spatial discretization is based on compact Padé schemes (Sect. 3.2). For the temporal discretization, besides an existing explicit Runge–Kutta time stepping scheme, a semi-implicit Runge–Kutta scheme is implemented. A semi-implicit scheme overcomes the diffusive constraint on the time step expected to arise at very high Reynolds number. This chapter only briefly lays out the general aspects of incompressible flow simulations (Sects. 3.1, 3.2), and thereafter focuses on the time integration. Time stepping schemes available for DNS codes are reviewed, and the selection of an appropriate scheme is detailed (Sect. 3.3). The linear stability region of the selected scheme is calculated (Sect. 3.4), and the actual implementation of the semi-implicit scheme is discussed (Sect. 3.5).

3.1 The Pressure Problem

A key problem when integrating the incompressible equations in the native variable formulation is an implicit coupling of the momentum equations with the divergence-free constraint. This implicit coupling becomes explicit, once the divergence of

the momentum equations is taken: a Poisson-type equation for the pressure results. Hence, a standard explicit formulation for F, where the constraint is not enforced separately, would violate the divergence-free constraint on the flow and lead to accumulating errors while the pressure field is unknown. This can be overcome with the split-step (also known as fractional step) approach, where the integration is split into three parts:

$$\tilde{\mathbf{u}}_{n+1} = \left(1 + \tau F'\right) \mathbf{u}_n \tag{3.2a}$$

$$\phi_{n+1} = \frac{1}{\tau} \Delta^{-1} (\nabla \tilde{\mathbf{u}}_{n+1}) \tag{3.2b}$$

$$\mathbf{u}_{n+1} = \tilde{\mathbf{u}}_{n+1} - \tau \nabla \phi = \left(1 + \tau F'\right) \mathbf{u}_n - \tau \nabla \Delta^{-1} \left[\nabla \left(1 + \tau F'\right) \mathbf{u}_n\right], \quad \tag{3.2c}$$

where τ is the discrete time step and $F'(\mathbf{u}) = F(u) + \nabla p : \mathbb{R}^3 \to \mathbb{R}^3$ operates on the velocities $\mathbf{u}$ only. The pressure ϕ_{n+1} is estimated in the second step (Eq. 3.2b) based on the intermediate velocities $\tilde{\mathbf{u}}_{n+1}$ and used to project these intermediate velocities such that the divergence-free constraint (Sect. 2.1) is fulfilled. This approach has been introduced by Kim and Moin (1985); unfortunately, it is in general only first-order accurate in the pressure (Perot 1993, also Eqs. 3.22b, 3.22c). For periodic boundary conditions, however, second-order accuracy is recovered. Perot (1993) also describes, how the method can be altered to achieve arbitrary orders of accuracy. Therefor, an approximate factorization of the problem is used, in which the discrete Laplacian Δ is replaced by DBG, where D and G are the discrete divergence and gradient operators, and B is chosen such that the desired order of accuracy is achieved.

The problem with the pressure–velocity coupling can be overcome if a non-native variable formulation of the Navier–Stokes equations is used, the ω–w formulation. In this formulation, the pressure is eliminated by taking the curl of the momentum equations, and the temporal integration is carried out in terms of the vertical component of velocity, w, and the vorticity, ω. It was considered here to express the equations in the ω–w formulation. An analysis of their discretized version and the involved computational load, however, shows that this would result in several additional global transpositions of three-dimensional fields. Hence, a primitive–variable formulation of the Navier–Stokes equations is chosen which involves the solution of one Poisson equation for the pressure at each sub-stage of the time integration.

3.2   Spatial Discretization

Compact Padé schemes are used for the spatial discretization. These schemes have favorable resolution properties compared to discretizations based on local stencils such as finite difference methods, also of higher order (Lele 1992). This advantage is illustrated in Fig. 3.1 where the modified wavenumbers of a compact and centered-difference scheme are shown. In comparison with a second-order centered-difference scheme, the compact scheme resolves variability at high wavenumbers much better.
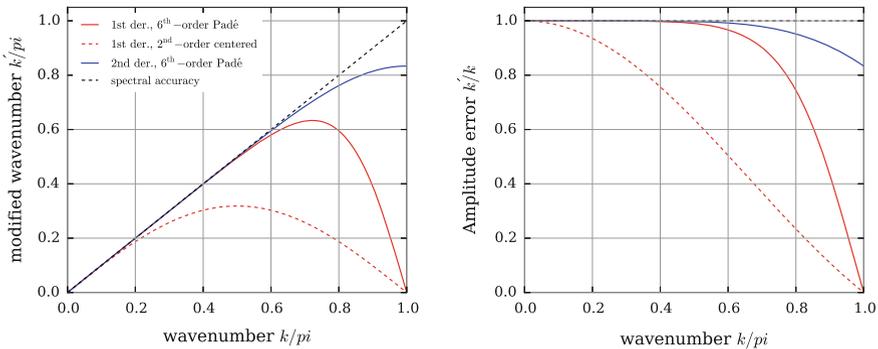
Fig. 3.1 Modified wavenumbers (*left panel*) and amplitude error (*right panel*) according to (Lele 1992). The x-axis shows the wavenumber, where a wavenumber zero corresponds to the mean, and a wavenumber $k/\pi = 1$ to the $2\Delta(Ox)$-fluctuation. *Red lines* are for first derivatives (*solid* Sixth-order compact scheme, *dashed* Second–order centered differences), *blue* ones for second derivatives (sixth-order compact scheme). The *dashed black line* shows the spectral accuracy

The amplitude error becomes significant only at wavenumbers $k/\pi \approx 0.5$, and for common standards, such as an accuracy of 80–90 % at the smallest scale, less than half the number of points in each direction is needed in comparison with a centered difference scheme. This allows for a reduced number of collocation points, and hence enables to study larger domains in terms of physical parameters given fixed computational resources.

Such favorable resolution properties come at a price: For the calculation of a compact derivative, a banded linear system involving all the points in the direction along which a derivative is calculated needs to be solved: Compact Padé schemes require computationally expensive global transpositions when a derivative is calculated (Sect. 4.1.3). Hence, any possible reduction of the number of transpositions, i.e. derivatives to be calculated (no matter if first or second), has precedence over a slight reduction in the number of floating-point operations when choosing a numerical method and optimizing the algorithm.

3.3 Time Stepping Schemes

Time stepping consists of the discretization of the operator ∂_t in Eq. (3.1). It is essentially the approximation of the field u at some time $t + \tau$ in the future $u_{n+1} = u(t_n + \tau)$, as a function of $F(u_n)$, possibly earlier instances ($F(u_{n-\{1,2,3,...\}})$), and a future instance $F(u_{n+1})$. It does not include the discretization of F, which is the spatial discretization discussed above.

It is assumed here that available schemes for the time stepping are consistent, i.e. they converge to an actual solution of the problem under consideration (if an algorithm is checked against an analytical solution, consistency becomes

synonymous to accuracy). The ideal choice of a time stepping scheme then '*fairly*' balances the algorithm's *numerical cost* and *stability* with the result's *accuracy*. Which balance is '*fair*', depends on the questions asked and the problem under consideration and is a complex decision at a researcher's discretion. Stability is a binary requirement: Given a problem, its spatial discretization and a time step τ, an algorithm is either stable (and results are meaningful), or it is unstable (and 'blows up'). Commonly, free parameters of an algorithm are used to optimize, i.e. maximize, its stability region and to allow for larger time steps.

The computational cost function depends on the numerical resources at hand, such as available memory versus computing time and the HPC architecture where the algorithm is to be implemented, i.e. the level of parallelization required (cf. Chap. 4). Based on the available schemes, the decision on the numerical algorithm is detailed in Sect. 3.3.4.

3.3.1   Explicit Runge–Kutta Schemes

A very common approach is to estimate the velocity field u_{n+1} as a function of a single available instant, i.e. $u_{n+1} = f(u_n)$. The simplest of such schemes is the explicit Euler-forward integration where

$$u_{n+1} = u_n + \tau F(u_n). \tag{3.3}$$

Explicit methods may have several sub-stages and involve several evaluations of F; they are generalized in the class of Runge–Kutta schemes. In general, a Runge–Kutta scheme requires enough memory to store the full fields of every sub-stage until the end of the evaluation. Due to the flexibility in defining a Runge–Kutta method, there exist classes which do not require any more memory than the explicit Euler integration in Eq. (3.3). For reasons of memory efficiency, only such *low-storage methods* are considered here.

Low-storage methods were introduced by Williamson (1980), and read as

$$w^{i+1} = w^i + \tau_i \left[F(w^{i-1}) + \sum_{j=1}^{i-1} \alpha^j F(w^j) \right] \tag{3.4a}$$

$$\text{with } w^0 = u_n \text{ and } u_{n+1} = w_{n_{step}},$$

where $i \in \{0, \ldots, n_{step} - 1\} \subset \mathbb{N}$, $\alpha^i \in \mathbb{R}$ and $\tau_i = \tau b_i$ with $b_i \in \mathbb{R}$. Williamson in particular discusses the set of third-order–three-stage Runge–Kutta schemes. In such schemes, $n_{step} = 3$ and coefficients are chosen such that u_{n+1} is a third-order accurate estimate in τ. Here, scheme no.7 from Table 1 in Williamson (1980, α_{33}, b_{33}) and a higher-order version developed by Carpenter et al. (1991, α_{45}, b_{45}) are used:

$$b_{33} = \begin{pmatrix} \frac{1}{3} \\ \frac{15}{16} \\ \frac{8}{15} \end{pmatrix}, \alpha_{33} = \begin{pmatrix} 0 \\ \frac{1}{3} \\ \frac{3}{4} \end{pmatrix}, b_{45} = \begin{pmatrix} \frac{1432997174477}{9575080441755} \\ \frac{5161836677717}{13612068292357} \\ \frac{1720146321549}{2090206949498} \\ \frac{3134564353537}{4481467310338} \\ \frac{2277821191437}{14882151754819} \end{pmatrix}, \alpha_{45} = \begin{pmatrix} 0 \\ \frac{567301805773}{1357537059087} \\ \frac{2404267990393}{2016746695238} \\ \frac{3550918686646}{2091501179385} \\ \frac{1275806237668}{842570457699} \end{pmatrix}.$$

$$(3.4b)$$

This time-stepping scheme has been successfully applied to a number of geophysical problem settings such as cloud-top mixing (Mellado et al. 2009a, b; Mellado 2012) and the convective boundary layer (Garcia and Mellado 2014; van Heerwaarden et al. 2014). Ekman flow under neutral stability (Marlatt et al. 2010; Waggy et al. 2011; Marlatt and Waggy 2012) and in the convective regime (Waggy and Biringen 2011) has also been studied with this method.

Regarding the allowable maximum time step, an explicit Runge–Kutta method employed for the integration of the Navier–Stokes equations is subject to two constraints: First, the Courant–Friedrichs–Lewy (CFL) criterion (Courant et al. 1928) originating from the advection term: it determines the maximum allowable time step τ given the velocity and grid spacing. In honor of Courant's contribution, this criterion is nowadays expressed in terms of a critical Courant number

$$Cr = \tau \left| \frac{U_i}{\Delta x_i} \right|_\infty, \tag{3.5}$$

where $|(\cdot)|_\infty$ is the L-infinity norm returning the maximum of the field $(\cdot)$. (A critical Courant number may not be exceeded in order for a time stepping scheme to be numerically stable, and the reader is referred to Sect. 3.4 for the discussion of the stability region of a Runge–Kutta method.) Second, a similar constraint originating from the stability constraint of the diffusive term; if it becomes limiting, this constraint is very strong as it requires the time step to decrease with the square of the minimum grid spacing $[\min(\Delta x)]^2$. While the CFL can be eliminated using fully implicit methods only, the diffusive constraint alone can be overcome using semi-implicit methods which are discussed next.

3.3.2 Semi-implicit Runge–Kutta Schemes

An alternative to such explicit methods are implicit methods, where

$$u_{n+1} = f(u_n, u_{n+1}). \tag{3.6}$$

If f depends in a non-linear way on u_{n+1}, a time-stepping scheme is called fully implicit. Then, computationally prohibitively expensive algorithms for the inversion of non-linear systems have to be employed. Such fully implicit methods are not

considered here. In contrast to fully implicit methods, semi-implicit methods only involve a linear dependency of f on u_{n+1}. This may be achieved by a linearization of f with respect to u_{n+1} or a splitting of the operator f into a linear and a non-linear part. Since the diffusion constraint originates from a linear term, namely the Laplacian of the velocity field, a splitting of F seems a reasonable option:

$$F(u) = L(u) + N(u), \tag{3.7}$$

where L is a linear operator and N is a non-linear operator. Then one can use computationally relatively cheap implicit integration schemes for L and explicit schemes for N. For high Reynolds numbers this decomposition is equivalent to a decomposition into the stiff (L) and non-stiff (N) part of the operator F. As a consequence, implicit time stepping for L permits larger time steps once the diffusive constraint on the time step dominates the Courant-number constraint.

Third-order–three-stage scheme (SMR91). A semi-implicit scheme for incompressible flow simulations has been applied first by Spalart et al. (1991), hereafter referred to as SMR91. In the literature, there seems to be some confusion about the origin of this scheme since Simens et al. (2009) refer to Akselvoll and Moin (1996); there, however, SMR91 is used as reference. Another reference in this context is Mohan Rai and Moin (1991) who refer to SMR91 as unpublished under a slightly different title. SMR91 suggest the following scheme:

$$w^1 = \left(1 - \beta^1 \tau L\right)^{-1} \left[u_n + \tau \left(\alpha^1 L(u_n) + \gamma^1 N(u_n)\right)\right] \tag{3.8a}$$

$$w^2 = \left(1 - \beta^2 \tau L\right)^{-1} \left[w^1 + \tau \left(\alpha^2 L(w^1) + \gamma^2 N(w^1) + \zeta_2 N(u_n)\right)\right] \tag{3.8b}$$

$$u_{n+1} = \left(1 - \beta^3 \tau L\right)^{-1} \left[w^2 + \tau \left(\alpha^3 L(w^2) + \gamma^3 N(w^2) + \zeta_3 N(w^1)\right)\right] \tag{3.8c}$$

with the physical requirement $\beta^i + \alpha^i = \gamma^i$ for $i \in \{1, 2, 3\}$. They find that there is no combination of parameters $\alpha, \beta, \gamma, \zeta$ which fulfills the requirements for third-order accuracy on both L and N. When the third-order constraint on L is dropped, they find a one-parameter family of solutions to the non-linear problem. A member of this family which they consider optimal is

$$\begin{aligned}
\alpha &= \left(\tfrac{29}{96}, -\tfrac{3}{40}, \tfrac{1}{6}\right) \quad \beta = \left(\tfrac{37}{160}, \tfrac{5}{24}, \tfrac{1}{6}\right) \\
\gamma &= \left(\tfrac{8}{15}, \tfrac{5}{12}, \tfrac{3}{4}\right) \quad \zeta = \left(0, -\tfrac{17}{60}, -\tfrac{5}{12}\right).
\end{aligned} \tag{3.8d}$$

While this formulation formally does not overcome the drop to first-order temporal accuracy in the pressure p due to a split-step approach (Perot 1993), SMR91 state that the drop in accuracy related to the split-step approach does not affect the order of accuracy for the velocities. Moreover, from a practical point of view, the stability constraints on time stepping for the problems studied here are often so strong that the time-integration error is outweighed by the spatial one by several orders of magnitude

(Chap. 5). This scheme is used by a number of groups to study incompressible three-dimensional turbulence:

- Neutrally, stably and unstably stratified Ekman flow was studied by Coleman et al. (1990), Coleman (1999), Coleman et al. (1992), Coleman et al. (1994), Coleman and Ferziger (1996).
- Jiménez et al. (2009) used such a scheme for a comparison between the PBL and channel flow.
- It was also employed in the primitive-variable formulation for the study of neutrally and stably stratified channel flows (Flores and Jiménez 2006; Flores and Riley 2011).
- In a vorticity-based formulation, such a time stepping was used for seminal studies of near-wall dynamics in channel flow under neutral stratification (del Àlamo and Jiménez 2003; del Àlamo et al. 2004; Jiménez et al. 2004; Jiménez and Hoyas 2008) and under stable stratification (García-Villalba and del Àlamo 2011).

Third-order–three-1/3-step scheme (Nikitin 2006). The reason for the drop to second-order accuracy when the time stepping is done explicitly for non-linear terms and implicitly for linear terms is that in a three-stage Runge–Kutta scheme coefficients cannot be chosen such that the error from the implicit terms cancel. One can, however, add a step which corrects for the error in the viscous terms and brings the scheme back to third-order accuracy also for the linear term. Such a scheme is introduced by Nikitin (2006) and reads as

$$w^1 = (1 - \tau \gamma_1 \mathbf{J}_F)^{-1} \left[u_n + \tau \left(\frac{2}{3} F(u_n) - \gamma_1 \mathbf{J}_F(u_n) \right) \right] \quad (3.9a)$$

$$w^2 = (1 - \tau \gamma_2 \mathbf{J}_F)^{-1} \left[u_n + \tau \left(\frac{1}{3} F(u_n) + \frac{1}{3} F(w^1) - \gamma_2 \mathbf{J}_F(w^1) \right) \right] \quad (3.9b)$$

$$\bar{u}_{n+1} = \frac{3}{2} \qquad\qquad (\alpha w^1 + (1-\alpha) w^2) - \frac{1}{2} u_n \quad (3.9c)$$

$$\tilde{u}_{n+1} = (1 - \tau \gamma_3 \mathbf{J}_F)^{-1} \left[u_n + \tau \left(\frac{1}{4} F(u_n) + \frac{3}{4} F(w^1) - \gamma_3 \mathbf{J}_F \bar{u}_{n+1} \right) \right] \quad (3.9d)$$

$$u_{n+1} = (1 - \tau \gamma_4 \mathbf{J}_F)^{-1} \left[u_n + \tau \left(\frac{1}{4} F(u_n) + \frac{3}{4} F(w^1) - \gamma_4 \mathbf{J}_F \tilde{u}_{n+1} \right) \right], \quad (3.9e)$$

where $\mathbf{J}_F$ is a first-order approximation to the Jacobian of the non-linear operator F. Moreover, it is $\alpha \in \mathbb{R}$ and $\{\gamma_i\}_{i=1,\ldots,4} \subset \mathbb{R}$. The additional steps in Eqs. (3.9c) and (3.9d) do not involve an additional evaluation of F and are thus computationally relatively cheap. A straightforward choice is $\mathbf{J_F} = \nabla^2 = L$. In that case, for $\gamma_i = 1$, the diffusion scheme would be purely implicit. For $\gamma_i = 0$ the scheme would be purely explicit, for $\gamma = 0.5$, a Crank-Nicholson like integration is obtained. $\alpha = 3/2$ yields maximum memory efficiency at runtime, and $\gamma \geq 1/3$ follows from stability considerations. In tests $\gamma = 1/3$ has produced the most accurate results (Nikitin 2006).

This scheme has been successfully applied to the study of four-dimensional turbulence (Nikitin 2011) and of the turbulent–non-turbulent interfaces and entrainment across such interfaces (Holzner et al. 2008, 2010).

Additive semi-implicit third-order–three-stage Runge–Kutta scheme. Another approach to retain third-order accuracy is the evaluation of the explicit and implicit terms at different sub-stages as described by Zhong (1996):

$$w_1 = h \left[1 - \alpha_1 \tau \mathbf{J_F} \right]^{-1} (N(u_n) + L(u_n)) \tag{3.10a}$$

$$w_2 = h \left[1 - \alpha_2 \tau \mathbf{J_F} \right]^{-1} (N(u_n + \beta_{21} w_1) + L(u_n + \gamma_{21} w_1)) \tag{3.10b}$$

$$w_3 = h \left[1 - \alpha_3 \tau \mathbf{J_F} \right]^{-1} (N(u_n + \beta_{31} w_1 + \beta_{32} w_2) + L(u_n + \gamma_{31} w_1 + \gamma_{32} w_2)) \tag{3.10c}$$

$$u_{n+1} = u_n + \omega_1 w_1 + \omega_2 w_2 + \omega_3 w_3, \tag{3.10d}$$

where, as before, $\mathbf{J_F}$ is in general a Jacobian of F; in incompressible flows $J_F = L = \Delta$ (as in SMR91) is a reasonable choice. Zhong (1996) fixes $\omega_1 = \omega_2 = 1/8$ and determines the remaining 10 free parameters from the accuracy and strong-stability conditions. This method was derived and applied for the study of reactive flow simulations.

The problem with this method is that only for $\gamma_{ij} = \beta_{ij}$ it could possibly be formulated as a low-storage scheme. Then, however, the scheme reduces to a standard semi-implicit Runge–Kutta scheme. SMR91 have shown that with such a scheme third-order accuracy cannot be obtained.

3.3.3   Multi-level Schemes and Other Methods

Leapfrog with Robert–Asselin filter. The standard Leapfrog method is an explicit three-level scheme:

$$u_{i+1} = u_{i-1} + 2\tau f(u_i). \tag{3.11a}$$

This method is energy-conserving in time and time-reversible (in contrast to Runge–Kutta methods), but unconditionally unstable for all dissipative systems. The instability is caused by a 2τ temporal oscillation, the computational mode. For applications in numerical weather forecasting, the scheme was modified (Robert 1966; Asselin 1972) by a smoothing that damps the computational mode, the so-called Robert–Asselin filter:

$$\bar{u}_{i+1} = u_{i-1} + 2\tau f(u_i) \tag{3.11b}$$

$$u_{i+1} = \bar{u}_{i+1} + \alpha(\bar{u}_{i+1} - 2u_i + u_{i-1}); \qquad 1 \gg \alpha \in \mathbb{R}_+ \tag{3.11c}$$

This scheme is still implemented in most weather and climate models, but also applied in DNS of the nocturnal low-level jet (Shapiro and Fedorovich 2009) and

for the investigation of the Prandtl-number dependence of convection (Shapiro and Fedorovich 2004).

Adams-Bashforth–Cranck-Nicholson (AB–CN) method. This multi-level method has been introduced by Kim and Moin (1985), and formally reads as

$$\tilde{u} = \left[1 - \frac{\tau}{2}L\right]^{-1} \left[\mathbf{u}_n + \frac{\tau}{2}\left(3N'(\mathbf{u}_n) - N'(\mathbf{u}_{n-1}) + L(\mathbf{u}_n)\right)\right] \tag{3.12a}$$

$$\phi_{n+1} = \frac{1}{\tau}\Delta^{-1}\left(\nabla\mathbf{u}\right) \tag{3.12b}$$

$$u_{n+1} = \tilde{u} - \tau\nabla\phi_{n+1}, \tag{3.12c}$$

where, as in Eq. (3.2), $N'(\mathbf{u}) = N(u) + \nabla p$ and L is the discrete Laplacian Δ. Due to the split-step procedure, this method is second-order accurate for periodic domains. This scheme is a three-level scheme and hence requires at least 50 % more memory than low-storage or explicit schemes.

This scheme has been applied successfully to DNS of turbulent channel flow under neutral (Kim et al. 1987; Moser et al. 1999; Abe et al. 2004) and stable (Nieuwstadt 2005) density stratification. Turbulent Ekman layers have been simulated with this scheme by Shingai and Kawamura (2004) as well as (Miyashita et al. 2006).

Others. A predictor–corrector second-order scheme is used by Najm et al. (1998). Kim et al. (2002) develop a time stepping based on an approximate factorization of the second-order linearized equations. These schemes are not considered here in detail since they are of low order while their implementation would require considerable technical effort.

3.3.4   Choice of a Method

Above, several options were presented which are employed successfully in DNS of turbulent flow. Now, a scheme is chosen for implementation.

Given the high accuracy of the spatial discretization (compact Padé schemes, Sect. 3.2), a low-order time stepping such as Euler-forward seems inappropriate. This would also require very small time steps since the stability region of an Euler scheme is rather small. For reasons of memory economy, schemes that require more memory than a low-storage Runge–Kutta scheme (current implementation), do not come into question. Given the options described above, the semi-implicit third-order–three-stage scheme introduced by SMR91 (Eqs. 3.8a–3.8c, henceforth SIRK3) appears as the most appropriate option to the author in the case when the diffusion number constraint on the time step dominates the Courant–Friedrichs–Lewy criterion. This scheme is not well-documented in the literature (SMR91 only devote one paragraph in an appendix to the method). The rest of this chapter is devoted to the description of this scheme's stability properties, some details of the implementation and possible optimizations.

3.4   Stability of the SIRK3 Scheme

The stability properties of the algorithm under consideration are unknown a priori
and have not been discussed in the literature to the author's knowledge. SMR91
mention a theoretical stability limit of $\sqrt{3}$ and routinely used peak Courant numbers
of up to two. Consider the first-order ODE

$$\frac{ds}{dt} = \lambda s, \qquad s \in \mathbb{R}, \lambda \in \mathbb{C}, \quad \widetilde{s}(t) = s_0 \exp \lambda t, \tag{3.13a}$$

where $\widetilde{s}$ is the only non-trivial solution to this initial value problem with $s_0 \in \mathbb{R}$. Let
$s_0 := 1$. The SIRK3 scheme can be used to estimate $\widetilde{s}(\tau)$ where τ is the integration
time step, i.e. the solution after a single iteration is considered. Note, that there are two
possibilities to apply the scheme to this problem: First, one can assume $\{L_e(s) = 0,$
$N_e(s) = \lambda s\}$ which is a purely explicit integration and essentially a standard third-
order Runge–Kutta integration. Second, one can assume $\{L_i(s) = \lambda s, N_i(s) = 0\}$
which is a Runge–Kutta integration in which each sub-step is purely implicit. The
corresponding numerical estimates for $\tilde{s}(\lambda \tau)$ are

$$\widetilde{s}_e(\lambda \tau) = 1 + \lambda \tau + \frac{1}{2}(\lambda \tau)^2 + \frac{1}{6}\lambda \tau^3 \tag{3.13b}$$

$$\widetilde{s}_i(\lambda \tau) = \frac{1 + \tau_e^1 k_{ex}^1 \lambda}{1 - \tau_e^1 k_{im}^1 \lambda} \frac{1 + \tau_e^2 k_{ex}^2 \lambda}{1 - \tau_e^2 k_{im}^2 \lambda} \frac{1 + \tau_e^3 k_{ex}^3 \lambda}{1 - \tau_e^3 k_{im}^3 \lambda}. \tag{3.13c}$$

Knowing the exact amplification factor $\exp \lambda \tau$, the numerical dissipation and disper-
sion are obtained as the amplitude and phase of $\widetilde{s}_{\{i,e\}}(\lambda)/e^{\lambda \tau}$, respectively. The linear
stability region of a fully explicit scheme is defined by $|s_{\{i,e\}}| < 1$ which is shown
as a thick black line in Fig. 3.2. There, also the numerical dissipation and dispersion
for the explicit and semi-implicit integration of the above problem is shown.

The maximum allowable Courant number (CFL) for the advection scheme used in
the estimation of F is the modulus of the non-trivial root of $\widetilde{s}_e(0+bi), b \approx 1.73$ which
has to be normalized with the maximum modified wavenumber for the advection
operators, i.e.

$$CFL_{a,max} = \frac{1.731}{1.989} \simeq 0.87. \tag{3.14}$$

This is required purely for stability of the algorithm. The upper panel of Fig. 3.2
characterizes integration errors of the advection. It shows that for

$$CFL = 0.9 \times CFL_{a,max} \simeq 0.8 \tag{3.15}$$
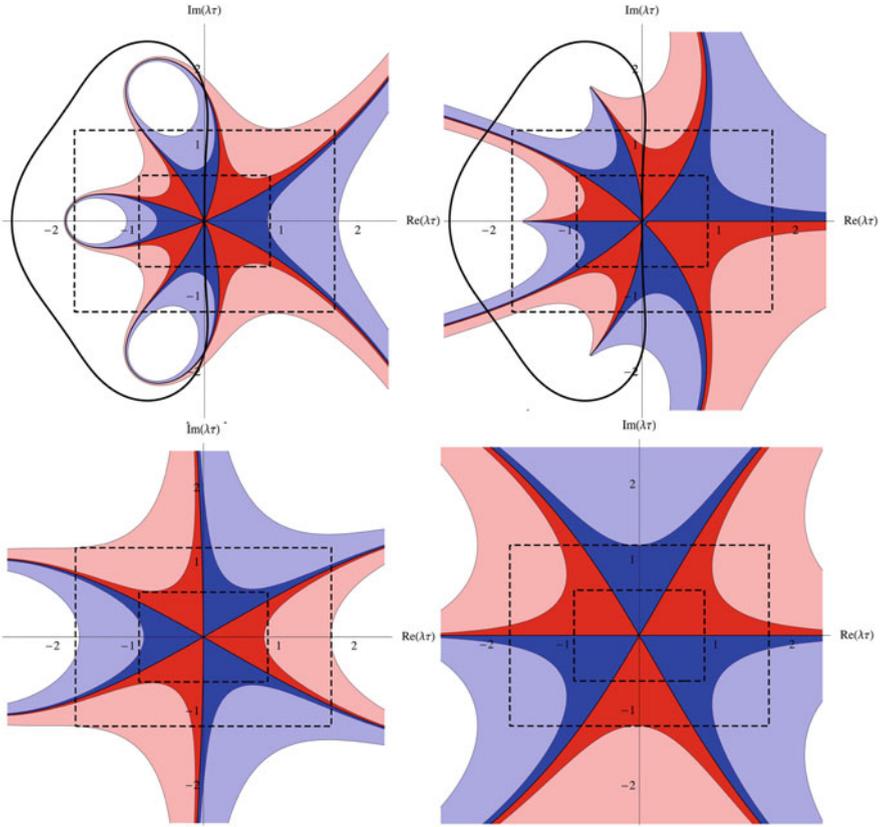
Fig. 3.2 Numerical dissipation (*left*) and dispersion (*right*) per time step τ for the explicit (*upper panel*) and semi-implicit (*lower panel*) integration. The *dark red* and *blue* areas indicate regions in which the errors are less than 1 % (*red* negative/damping, *blue* positive/amplification). Light *colored regions* are correspondingly for 10 % errors. The overall stability envelope of the explicit scheme ($|s_e(\lambda\tau)| = 1$) is shown by a *thick solid black line*. The *outer dashed box* shows precision down to 2Δ, where Δ is the grid spacing. The *inner box* shows the precision if results are considered only down to 4Δ.

(the outer dashed box) the dissipation errors are well below 10 % apart from small fractions of the left end of the box. If only waves down to 4Δ (the inner dashed box) with Δ the grid spacing are considered, the error is below one percent for nearly all wavenumbers possible.

Since the diffusion is calculated with the semi-implicit integration, diffusion errors are characterized by the lower panel in Fig. 3.2. By design of the algorithm the semi-implicit part is unconditionally stable for $Re(\lambda) \leq 0$. Nonetheless, the diffusive CFL can be used to control the maximum error, and for $CFL_d < 1.7$ all λ have both dissipative and diffusive errors below 10 % down to 2Δ and below 1 % down to 4Δ.

3.5 Implementation of the SIRK3 Scheme

3.5.1 Rotation of the Grid: Equations Solved by the DNS

The Navier–Stokes equations for a Boussinesq flow read as

$$\frac{\partial u_i}{\partial t} = -u_j \frac{\partial u_i}{\partial x_j} - \frac{\partial \pi_{tot}}{\partial x} + f \epsilon_{ik3} u_k + \nu \frac{\partial^2 u_i}{\partial x_j^2} \tag{3.16}$$

(cf. Chap. 2). With the large-scale pressure gradient $\partial \pi_{\text{geo}}/\partial x_k$, a parameter external to the problem, the geostrophic balance reads as

$$f G_i = \epsilon_{ik3} \frac{\partial \pi_{\text{geo}}}{\partial x_k}. \tag{3.17}$$

$\nabla \pi_{tot}$ can then be split into an ageostrophic contribution $\nabla \pi$ and a geostrophic contribution $f G_i$ to rewrite Eq. (3.16) as

$$\frac{\partial u_i}{\partial t} = -u_j \frac{\partial u_i}{\partial x_j} - \frac{\partial \pi}{\partial x_i} + f \epsilon_{ik3} (u_k - G_k) + \nu \frac{\partial^2 u_i}{\partial x_j^2}, \tag{3.18}$$

which is valid in a system where the spanwise coordinate coincides with the direction of the pressure gradient.

In the vicinity of the wall, turbulence is manifest in the form of wall-streaks. These streaks are approximately aligned with the mean flow close to the wall, and they have a spanwise extent of tens of wall units while they are very long (up to 1000 wall units) in the streamwise direction (Jiménez and Pinelli 1999). It is hence numerically beneficial to align the coordinate system with the wall-shear stress instead of the geostrophic wind; then, the highest resolution is only required in the spanwise direction where the streaks have the largest gradients. Although the exact turning of the wind is unknown a priori (it is part of the solution), one can attempt to minimize numerical errors by rotating the grid into the direction expected for α. Therefore, Eq. 3.18 are transformed with the rotation matrix (variables in the rotated frame of reference are indicated by a subscript α) such that

$$\begin{pmatrix} u_\alpha \\ v_\alpha \\ w_\alpha \end{pmatrix} = \begin{pmatrix} \cos\alpha & -\sin\alpha & 0 \\ \sin\alpha & \cos\alpha & 0 \\ 0 & 0 & 1 \end{pmatrix} \begin{pmatrix} u \\ v \\ w \end{pmatrix}, \tag{3.19}$$

and the prognostic equations for $\mathbf{u}_\alpha = (u_\alpha, v_\alpha, w_\alpha)^T$ are

$$\frac{\partial u_\alpha}{\partial t} = -\mathbf{u}_\alpha \nabla u_\alpha \; - \; \frac{\partial \pi}{\partial x_\alpha} + \nu \triangle u_\alpha \; -f \left(v_\alpha - G_{2,\alpha}\right)$$

$$\frac{\partial v_\alpha}{\partial t} = -\mathbf{u}_\alpha \nabla v_\alpha \; - \; \frac{\partial \pi}{\partial y_\alpha} + \nu \triangle v_\alpha \; +f \left(u_\alpha - G_{1,\alpha}\right) \qquad (3.20)$$

$$\frac{\partial w_\alpha}{\partial t} = -\mathbf{u}_\alpha \nabla w_\alpha \; - \; \frac{\partial \pi}{\partial z} + \nu \triangle w_\alpha$$

where $G_{1,\alpha} = G \cos \alpha$ and $G_{2,\alpha} = -G \sin \alpha$. This modification allows to increase the grid spacing in the direction approximately aligned with the surface stress by a factor 2. Since this is the direction where the Courant-constraint is strongest, it also allows for larger time steps and has the potential to reduce the amount computing time to about one quarter of its original value—without having to sacrifice accuracy or domain size.

3.5.2 Buffer Zone

The flow is in geostrophic equilibrium at its upper boundary $z = \infty$. In a vertically finite domain, however, boundary effects are expected and deviations from geostrophic equilibrium can occur both due to deviations from the height-dependent laminar solution from the equilibrium and long-lived remnants of turbulent bursts in the outer layer (Chap. 6). A simple no-slip condition would lead to an artificial boundary layer in the vicinity of such structures; a free-slip boundary condition can cause reflections and hence artificial downward-fluxes of turbulent energy obscuring turbulence dynamics in the outer layer of the PBL where turbulent fluxes are generally small. To eliminate those effects, a Rayleigh-damping layer is introduced at the top of the domain. In all simulations, this layer extends over the upper 16 points and has a damping time of 1, i.e. the damping of a turbulent structure at the uppermost level of the domain over the inertial period $2\pi/f$ is $e^{-2\pi} \approx 6.8 \times 10^{-3}$. The damping coefficient $\sigma(z)$ follows the relation:

$$\sigma(z) = \begin{cases} z < z_d; & 0 \\ z_d \leq z \leq z_{top}; & \alpha \left(\frac{z - z_d}{z_{top} - z_d}\right)^\beta \end{cases} . \qquad (3.21)$$

In this work, it is $\alpha := 1$ and $\beta := 2$ such that $\sigma(z)$ is smooth and differentiable with respect to the height z.

3.5.3 Discretization in the Interior of the Domain

One can write the discretized problem as

$$\frac{1}{\tau}(w_i^{m+1} - w_i^m) = -\mathbf{w}^m \nabla w_i^m + 2\epsilon_{ik3}\Omega_j w_k^m + \nu(\alpha \triangle w_i^m + \beta \triangle w_i^{m+1}) - D_i \pi^m \qquad (3.22a)$$

where $\triangle$ is the discrete Laplacian, D_i is the discretized derivative and $\nabla = (D_1, D_2, D_3)$. Further, define $L \equiv \nu\triangle$, and $N_i(\mathbf{w}^m) \equiv -\mathbf{w}^m \cdot \nabla w_i^m + 2\epsilon_{ik3}\Omega_j w_k^m$ with $\mathbf{w}^m = \left(w_1^m, w_2^m, w_3^m\right)$. It follows

$$w_i^{m+1} = (\mathbb{1} - \beta^m\tau L)^{-1}\left[w_i^m + \tau\left(N_i\mathbf{w}^m + \alpha^m L w_i^m - D_i\pi^m\right)\right]$$

$$\Rightarrow w_i^{m+1} = \underbrace{(\mathbb{1} - \beta^m\tau L)^{-1}\left[w_i^m + \tau\left(N_i\mathbf{w}^m + \alpha^m L w_i^m\right)\right]}_{\widetilde{w}_i^m} - \tau\left[\sum_{l=0}^{\infty}(\beta^m\tau L)^l\right]D_i\pi^m.$$

$$(3.22b)$$

Solving for the full Eq. (3.22b) is—due to the series expansion of the Helmholtz operator $(\mathbb{1} - \beta^m\tau L)^{-1}$—a transient problem and numerically prohibitively expensive. Instead one can truncate the Neumann series after the first member ($l = 0$) to arrive at the $O(\tau)$ accurate approximation to the full equation

$$w_i^{m+1} = \widetilde{w}_i^m - \tau D_i\pi^m + O(\tau^2).$$ $$(3.22c)$$

(Higher orders can be retained if desired.) This approximation is equal to a splitting of the problem into two sub-steps as described in Sect. 3.1, and it quantifies the splitting error to be of first order. In a physical sense this means, the pressure term is utilized to enforce the physical constraint of incompressibility (Sect. 3.1). This is done through a projection of an intermediate momentum field—namely that where all the source and sink terms for momentum act but the pressure gradient force—onto an incompressible flow field that fulfills the boundary conditions.

In the set of Eqs. (3.8a–3.8c), the operator L occurs twice. Mathematically, this is correct since part of the linear tendency is integrated explicitly. From a computational perspective this is rather inconvenient. It requires the full Laplacian to be evaluated at each sub-stage, and on top a Helmholtz equation has to be solved. For the calculation of $\widetilde{w}_i^m$ the algebraic identity $L^{-1}\circ L = \mathbb{1}$ can be exploited to save this double-evaluation of the Laplacian:

$$\alpha\tau\left[\mathbb{1} - \beta\tau L\right]^{-1}L = \frac{\alpha}{\beta}\left[\mathbb{1} - \beta\tau L^{-1}\right]\left[-\mathbb{1} + \beta\tau L + \mathbb{1}\right] \qquad (3.22d)$$

$$= \frac{\alpha}{\beta}\left[\mathbb{1} - \beta\tau L\right]^{-1}\left[\beta\tau L - \mathbb{1}\right] + \frac{\alpha}{\beta}\left[\mathbb{1} - \beta\tau L\right]^{-1}\mathbb{1}$$

$$= \frac{\alpha}{\beta}\left[\left[\mathbb{1} - \beta\tau L\right]^{-1}\right] - \frac{\alpha}{\beta}\mathbb{1}. \qquad (3.22e)$$

Hence, the explicit part of the diffusion can be accounted for by operating on a field which is augmented by α/β. The augmentation is then removed after the Helmholtz solver (the term $-\alpha/\beta\mathbb{1}$ in Eq. (3.22e)). This algebraic modification eliminates all $(3+n_{scalar})\cdot 3$ second derivatives to be calculated and thus decreases the computational cost for the integration of the equations by about 50 %. Defining

$$\widetilde{w'}_i^m \equiv \widetilde{w}_i^m\left(1 + \frac{\alpha^m}{\beta^m}\right),$$

Eq. (3.22c) reads as

$$w_i^{m+1} = (\mathbb{1} - \beta^m \tau L)^{-1} \underbrace{\underbrace{\left[w_i^m \left(1 + \frac{\alpha^m}{\beta^m} \right) + \tau N_i(w^m) \right]}_{w_i^m\text{ explicit}} - \frac{\alpha^m}{\beta^m} w_i^m - \tau D_i \pi^m}_{\widetilde{w}'^m_i}. \quad (3.22f)$$

3.5.4 Dirichlet Boundary Conditions for the Semi-implicit Solver

Due to the split-step approach for the time integration, numerical boundary conditions for the intermediate velocity $\widetilde{w}_i^m$ and the pressure π^m are needed which are consistent with the discretization of the problem. In the case where Dirichlet boundary conditions are prescribed, it is assumed that they are not time-dependent and hence $w_i^{m+1}|\Gamma = w_i^m|\Gamma$ where Γ is the boundary of the computational box. Extending Eq. (3.22b) to the boundaries where $\partial_t = 0$ in the case of Dirichlet boundary conditions, this yields

$$\left\{ N_i \mathbf{w}^m + \alpha^m L w_i^m + \beta^m L w_i^{m+1} = D_i \pi^m \right\} |_\Gamma$$
$$\Rightarrow \left\{ N_i \mathbf{w}^m + L w_i^m + O(\tau) = D_i \pi^m \right\} |_\Gamma \quad (3.23a)$$

where the constraint $\alpha^m + \beta^m = 1$ is used. Substituting (3.23a)—only valid on Γ—to Eq. (3.22c) yields the following Dirichlet boundary conditions on $\widetilde{w}_i^m$ and Neumann boundary conditions on π^m:

$$\widetilde{w}_i^m|_\Gamma = w_i^{m+1}|_\Gamma + \tau \left[(N_i \mathbf{w}^m)|_\Gamma + (L w_i^m)_\Gamma \right] + O(\tau^2) \quad (3.23b)$$
$$D_3 \pi^m = N_3 \mathbf{w}^m + L w_3^m + O(\tau). \quad (3.23c)$$

The Helmholtz-type Eq. (3.23b) is, however, not solved for $\widetilde{w}_i^m$ but $\widetilde{w}'^m_i = \widetilde{w}_i^m + \frac{\alpha}{\beta} w_i^m$. In the particular case of a turbulent Ekman boundary layer, the Dirichlet boundary conditions do not depend on time. Eq. (3.23b) to first order in τ reduce to

$$\widetilde{w}'^m_1|_\Gamma = w_1|_\Gamma \left(1 + \tfrac{\alpha}{\beta} \right) + \tau \left(\nu D_1^{(2)} w_1^m + N_1(\mathbf{w}^m) \right) |_\Gamma$$
$$\widetilde{w}'^m_2|_\Gamma = w_2|_\Gamma \left(1 + \tfrac{\alpha}{\beta} \right) + \tau \left(\nu D_2^{(2)} w_2^m + N_2(\mathbf{w}^m) \right) |_\Gamma \quad (3.23d)$$
$$\widetilde{w}'^m_3|_\Gamma = w_3|_\Gamma \left(1 + \tfrac{\alpha}{\beta} \right) + \tau \left(\nu D_3^{(2)} w_3^m + N_3(\mathbf{w}^m) \right) |_\Gamma$$

where $D_i^{(j)}$ is the jth discrete derivative in the direction of i. At the bottom boundary, $\widetilde{w}'_1|_{\Gamma,\text{bottom}} = \widetilde{w}'_2|_{\Gamma,\text{bottom}} = 0$ (no-slip condition), and $\widetilde{w}'_3|_{\Gamma,bottom} = 0$ (no-penetration

condition). At the top boundary, Neumann boundary conditions are used for the horizontal velocity components, i.e. $\partial_z \widetilde{w'_1}^m|_{\Gamma,\mathrm{top}} = \partial_z \widetilde{w'_2}^m|_{\Gamma,\mathrm{top}}$, and for the vertical component also the no-penetration condition $\partial_z \widetilde{w'_3}^m|_{\Gamma,\mathrm{top}}$ is employed.

Due to the neglect of the implicit tendency at the boundary, the sub-step Eq. (3.23d) in which the boundary conditions for the Helmholtz solver are obtained, is purely explicit. Hence, formally, this scheme has the same stability bounds as the fully explicit scheme. The diffusion in the interior of the domain, however, aids stability such that in practice the scheme is stable up to diffusion numbers on the order of 10^3—orders of magnitude larger than the value of 0.25 for the fully explicit scheme. It was decided nonetheless to circumvent this boundary-instability by resorting to the leading-order accurate estimate of the boundaries consisting only in the first term on the RHS of Eq. (3.23d) since in tests it does not impact on the overall accuracy.

3.5.5 Integration of a Scalar Variable

Any scalar s can be discretized in the exact same way as the velocities:

$$(s^{m+1} - s^m)/\Delta t = -\mathbf{w}^m \nabla s^m + \nu(\alpha \triangle s^m + \beta \triangle s^{m+1}). \tag{3.24}$$

In that case, due to the absence of pressure forces $\widetilde{s}^m = s^{m+1}$, where $\widetilde{s}$ is defined analogously to $\widetilde{w}^m$. Hence, no additional numerical boundary conditions are needed on $\widetilde{s}^m$ as $\widetilde{s}^m|_\Gamma = s^{m+1}|_\Gamma$.

3.5.6 Description of the Implementation

Let $\tau_e^i \equiv \tau \gamma^i$ be an effective sub-step, and let $w^0 = u_n$ and $u_{n+1} = w^3$. The scheme in Eqs. (3.8a)–(3.8c) then becomes

$$
\begin{aligned}
w^1 &= \left(1 - k_{im}^1 \tau_e^1 L\right)^{-1} && \left[u_n + \tau_e^1 \left(k_{ex}^1 L(u_n) + N(w^0)\right)\right] \\
w^2 &= \left(1 - k_{im}^2 \tau_e^2 L\right)^{-1} && \left[w^1 + \tau_e^2 \left(k_{ex}^2 L(w^1) + N(w^1) + k_{co}^2 N(w^0)\right)\right] \\
w^3 &= \left(1 - k_{im}^3 \tau_e^3 L\right)^{-1} && \left[w^2 + \tau_e^3 \left(k_{ex}^3 L(w^2) + N(w^2) + k_{co}^3 N(w^1)\right)\right]
\end{aligned}
\tag{3.25}
$$

with $k_{ex} = \alpha/\gamma$, $k_{im} = \beta/\gamma$, $k_{co} = \zeta/\gamma$. This modification allows to pre-calculate α/γ, β/γ and ζ/γ and thus saves one floating point operation per grid point and Runge–Kutta sub-stage.

Figure 3.3 shows how these equations are translated to the present algorithm. When integrating the equations, all velocities and active scalars cannot be updated until the end of the explicit part since they are used for the advection and buoyancy terms respectively. Also, the old tendency cannot be overwritten since it is needed

```
1    DO i=1,n_step
       ! save old tendencies
3       tmp4=h1; tmp5=h2; tmp6=h3;
       ! save boundary conditions if Dirichlet is used
5       ...

7       ! EXPLICIT PART OF FLOW INTEGRATION (advection and buoyancy)
       dte = kdt(i) * dt
9
       h1 = N1(u,v,w,s); ! direction Ox
11      h2 = N2(u,v,w,s); ! direction Oy
       h3 = N3(u,v,w,s); ! direction Oz
13
       ! apply Buffer to tendencies h1,h2,h3
15      ! ... important to do this here for 3rd order convergence of the
            buffer terms

17      tmp1 = u*(1+kex/kim) + dte*( h1 + kco(i)*tmp4)!cannot overwrite u,v,w
       tmp2 = v*(1+kex/kim) + dte*( h2 + kco(i)*tmp5)!needed for scalar
19      tmp3 = w*(1+kex/kim) + dte*( h3 + kco(i)*tmp6)!kco(1) = C_0_R

21      ! Full integration of scalar variables (if any) needs to be done here

23      ! IMPLICIT PART OF FLOW INTEGRATION
       alpha= dte*kim(i)*visc; beta=-1/alpha
25
       ! apply BCs (Dirichlet or Neumann, depending on simulation)
27      ...
       ! setup BCs for helmholtz (always Dirichlet)
29      ! account for factor 1+kex/kim in dirichlet bcs_<1,2,3>
       ...
31      CALL HELMHOLTZ_FXZ(tmp1, beta, bcs_1)    ! use dirichlet BCs
       CALL HELMHOLTZ_FXZ(tmp2, beta, bcs_2)    !
33      CALL HELMHOLTZ_FXZ(tmp3, beta, bcs_3)    !

35      u = tmp1*beta - kex/kim*u
       v = tmp2*beta - kex/kim*v
37      w = tmp3*beta - kex/kim*w

39      ! PRESSURE PROJECTION STEP (remove residual divergence)
       tmp1 = (du/dx + dv/dy + dw/dz)/dte
41      CALL POISSON_FXZ(tmp1)

43      tmp2 = DERIVATIVE_X(tmp1);
       tmp3 = DERIVATIVE_Y(tmp1);
45      tmp4 = DERIVATIVE_Z(tmp1);

47      u = u-dte*tmp2;   h1=h1-tmp2    ! calculated with PARTIAL_X
       v = v-dte*tmp3;   h2=h2-tmp3    ! comes from FDE_BVP solver in poisson
49      w = w-dte*tmp4;   h3=h3-tmp4    ! calculated with PARTIAL_Z

51      ! enforce boundary conditions (again!)
       ...
53    ENDDO
```

Fig. 3.3   Pseudo Code listing for the implementation of the semi-implicit Runge–Kutta solver

for the explicit update (lines 17–19). The old tendencies are hence stored to tempo-
rary arrays at the beginning of the sub-stage (line 3, `tmp4`, `tmp5`, `tmp6` for u, v, w
respectively). The explicit terms (operator N) of the right-hand side are calculated in
lines 10–12. In lines 17–19, the intermediate velocities containing explicit tendencies
(w_{explicit}, Eq. 3.22f) are obtained and stored to the temporary arrays `tmp1`, `tmp2`,
and `tmp3`. Next, the boundary conditions for the Helmholtz equations are prepared;
due to the augmentation of the velocity fields (and similarly the scalar fields) by
$1 + k_{ex}/k_{im}$, the boundary conditions of the Helmholtz-solver have to be adapted
accordingly (not shown). The Helmholtz-solver always uses Dirichlet boundary
conditions at both the bottom and the top of the computational domain, i.e. *values
at the boundary are not affected by diffusion*, also in the case of Neumann boundary
conditions. The three Helmholtz equations for the augmented velocities

$$\widetilde{w}'^m_i = (1 - \beta^i \tau L)^{-1} w_{i,\text{explicit}} \tag{3.26}$$

(cf. Eq. 3.22f) are solved in lines 31–33. The intermediate velocities $\widetilde{w}^m_i$ are obtained
in lines 35–37. Now, the pressure projection step is carried out (lines 40–49). At
the end of the sub-stage the velocities (u, v, and w) are updated with the explicit
tendency, implicit diffusion and the pressure-tendency. The explicit tendencies are
saved in arrays `h1-3`; they constitute the old tendencies which have, multiplied by
k^i_{co}, to be added after the explicit part of the next sub-stage if there is one (lines
17–19). If $i = n_{step}$, the velocity fields contain the estimate u_{n+1}, and the iteration
step is finished. Note that, as shown in Fig. 3.3, boundary conditions are enforced
before the implicit solver and at the end (after incorporation of the pressure terms) of
each sub-stage again. It is found here that this additional enforcement of boundary
condition increases the overall accuracy of the code for a case in which diffusive
errors dominate from second order to third order in space (Sect. 5.3).

References

Abe, H., Kawamura, H., & Matsuo, Y. (2004). Surface heat-flux fluctuations in a turbulent channel
    flow up to Re $\tau = 1020$ with Pr $= 0.025$ and 0.71. *International Journal Of Heat And Fluid Flow*,
    25(3), 404–419.
Akselvoll, K., & Moin, P. (1996). An efficient method for temporal integration of the Navier-Stokes
    equations in confined axisymmetric geometries. *Journal of Computational Physics*, *125*(2), 454–
    463.
Asselin, R. (1972). Frequency filter for time integrations. *Monthly Weather Review*, *100*, 487–490.
Carpenter, M. H., Gottlieb, D., & Abarbanel, S. (1991): The stability of numerical boundary treat-
    ments for compact high-order finite-difference schemes. *Technical Report ICASE 91-71*, Institute
    for Computer Applications in Science and Engineering NASA Langley Research Center Hamp-
    ton, Virginia 23665-5225, Langley, VG.
Coleman, G. N. (1999). Similarity statistics from a direct numerical simulation of the neutrally
    stratified planetary boundary layer. *Journal of the Atmospheric Sciences*, *56*(6), 891–900.
Coleman, G. N., & Ferziger, J. H. (1996). Direct numerical simulation of a vigorously heated low
    Reynolds number convective boundary layer. *Dynamics Of Atmospheres And Oceans*, *24*(1–4),
    85–94.

Coleman, G. N., Ferziger, J. H., & Spalart, P. R. (1990). A numerical study of the turbulent ekman layer. *Journal of Fluid Mechanics*, *213*, 313–348.

Coleman, G. N., Ferziger, J. H., & Spalart, P. R. (1992). Direct simulation of the stably stratified turbulent ekman layer. *Journal of Fluid Mechanics*, *244*, 677–712.

Coleman, G. N., Ferziger, J. H., & Spalart, P. R. (1994). A numerical study of the convective boundary layer. *Boundary-Layer Meteorology*, *70*(3), 247–272.

Courant, R., Friedrichs, K., & Lewy, H. (1928). Über die partiellen Differenzengleichungen der mathematischen Physik. *Mathematische Annalen*, *100*(1), 32–74. doi:10.1007/BF01448839.

del Àlamo, J. C., & Jiménez, J. (2003). Spectra of the very large anisotropic scales in turbulent channels. *Physics of Fluids*, *15*(6), L41–L44.

del Àlamo, J. C., Jiménez, J., Zandonade, P., et al. (2004). Scaling of the energy spectra of turbulent channels. *Journal of Fluid Mechanics*, *500*, 135–144. doi:10.1017/S002211200300733X.

Flores, O., & Jiménez, J. (2006). Effect of wall-boundary disturbances on turbulent channel flows. *Journal of Fluid Mechanics*, *566*, 357–376.

Flores, O., & Riley, J. J. (2011). Analysis of turbulence colapse in the stably stratified surface layer using direct numerical simulation. *Boundary-Layer Meteorology*, *139*(2), 241–259. doi:10.1007/s10546-011-9588-2.

Garcia, J. R., & Mellado, J.-P. (2014). The two-layer structure of the entrainment zone in the convective boundary layer. *Journal of the Atmospheric Sciences*, *71*(6), 1935–1955. doi:10.1175/JAS-D-13-0148.1.

García-Villalba, M., & del Àlamo, J. C. (2011). Turbulence modification by stable stratification in channel flow. *Physics of Fluids*, *23*(4), 045104. doi:10.1063/1.3560359.

Holzner, M., Liberzon, A., & Nikitin, N. (2008). A Lagrangian investigation of the small-scale features of turbulent entrainment through particle tracking and direct numerical simulation. *Journal of Fluid Mechanics*, *598*, 465–475. doi:10.1017/S0022112008000141.

Holzner, M., Lüthi, B., & Tsinober, A. (2010). Acceleration, pressure and related quantities in the proximity of the turbulent/non-turbulent interface. *Journal of Fluid Mechanics*, *639*, 153–165.

Jiménez, J., & Hoyas, S. F. (2008). Turbulent fluctuations above the buffer layer of wall-bounded flows. *Journal of Fluid Mechanics*, *611*. doi:10.1017/S0022112008002747.

Jiménez, J., del Àlamo, J. C., & Flores, O. (2004). The large-scale dynamics of near-wall turbulence. *Journal of Fluid Mechanics*, *505(-1)*, 179–199. doi:10.1017/S0022112004008389.

Jiménez, J., Hoyas, S. F., & Simens, M. P. (2009). Comparison of turbulent boundary layers and channels from direct numerical simulation. *Sixth International Symposium on Turbulence and Shear Flow Phenomena, Seoul, Korea*, 289–294.

Jiménez, J., & Pinelli, A. (1999). The autonomous cycle of near-wall turbulence. *Journal of Fluid Mechanics*, *389*, 335–359.

Kim, J., Moin, P., & Moser, R. D. (1987). Turbulence statistics in fully developed channel flow at low Reynolds number. *Journal of Fluid Mechanics*, *177(-1)*, 133–166. doi:10.1017/S0022112087000892.

Kim, K., Baek, S.-J., & Sung, H. J. J. (2002). An implicit velocity decoupling procedure for the incompressible Navier-Stokes equations. *International Journal for Numerical Methods in Fluids*, *38*, 125–138. doi:10.1016/j.ijheatfluidflow.2009.08.002.

Kim, J., & Moin, P. (1985). Application of a fractional-step method to incompressible navier-stokes equations. *Journal of Computational Physics*, *59*(2), 308–323.

Lele, S. K. (1992). Compact finite difference schemes with spectral-like resolution. *Journal of Computational Physics*, *103*(1), 16–42.

Marlatt, S. W., & Waggy, S. B. (2012). Direct numerical simulation of the turbulent ekman layer: Evaluation of closure models. *Journal of the Atmospheric Sciences*, *69*, 1106–1117.

Marlatt, S. W., Waggy, S. B., & Biringen, S. (2010). Direct numerical simulation of the turbulent ekman layer: Turbulent energy budgets. *Journal of Thermophysics And Heat Transfer*, *24*(3), 544–555. doi:10.2514/1.45200.

Mellado, J.-P. (2012). Direct numerical simulation of free convection over a heated plate. *Journal of Fluid Mechanics*, *712*, 418–450. doi:10.1017/jfm.2012.428.

Mellado, J.-P., Stevens, B., Schmidt, H., et al. (2009a). Bouyancy reversal in cloud top mixing layers. *Quarterly Journal of the Royal Meteorological Society*, *135*(641), 963–978. doi:10.1002/qj.417.

Mellado, J.-P., Wang, L., & Peters, N. (2009b). Gradient trajectory analysis of a scalar field with external intermittency. *Journal of Fluid Mechanics*, *626*, 333–365. doi:10.1017/S0022112009005886.

Miyashita, K., Iwamoto, K., & Kawamura, H. (2006). Direct numerical simulation of the neutrally stratified turbulent ekman boundary layer. *Journal of the Earth Simulator*, *6*, 3–15.

Mohan Rai, M., & Moin, P. (1991). Direct simulations of turbulent flow using finite-difference schemes. *Journal of Computational Physics*, *96*(1), 15–53.

Moser, R. D., Kim, J., & Mansour, N. N. (1999). Direct numerical simulation of turbulent channel flow up to Re[sub τ]=590. *Physics of Fluids*, *11*(4), 943. doi:10.1063/1.869966.

Najm, H. N., Wyckoff, P. S., & Knio, O. M. (1998). A semi-implicit numerical scheme for reacting flow. *Journal of Computational Physics*, *143*(2), 381–402. doi:10.1006/jcph.1997.5856.

Nieuwstadt, F. T. (2005). Direct numerical simulation of stable channel flow at large stability. *Boundary-Layer Meteorology*, *116*(2), 277–299. doi:10.1007/s10546-004-2818-0.

Nikitin, N. (2006). Third-order-accurate semi-implicit Runge-Kutta scheme for incompressible Navier-Stokes equations. *International Journal for Numerical Methods in Fluids*, *51*(2), 221–233. doi:10.1002/fld.1122.

Nikitin, N. (2011). Four-dimensional turbulence in a plane channel. *Journal of Fluid Mechanics*, *680*, 67–79. doi:10.1017/jfm.2011.148.

Perot, J. (1993). An analysis of the fractional step method. *Journal of Computational Physics*, *108*(1), 51–58.

Robert, A. J. (1966). The integration of a low order spectral form of the primitive meteorological equations. *Journal of the Meteorological Society of Japan*, *44*(5), 237–245.

Shapiro, A., & Fedorovich, E. (2004). Prandtl number dependence of unsteady natural convection along a vertical plate in a stably stratified fluid. *International Journal of Heat and Mass Transfer*, *47*(22), 4911–4927.

Shapiro, A., & Fedorovich, E. (2009). Nocturnal low-level jet over a shallow slope. *Acta Geophysica*, *57*(4), 950–980. doi:10.2478/s11600-009-0026-5.

Shingai, K., & Kawamura, H. (2004). A study of turbulence structure and large-scale motion in the Ekman layer through direct numerical simulations. *Journal of Turbulence*, *5*(5), doi:10.1088/1468-5248/5/1/013.

Simens, M. P., Jiménez, J., Hoyas, S. F., et al. (2009). A high-resolution code for turbulent boundary layers. *Journal of Computational Physics*, *228*(11), 4218–4231. doi:10.1016/j.jcp.2009.02.031.

Spalart, P. R., Moser, R. D., & Rogers, M. M. (1991). Spectral methods for the Navier-Stokes equations with one infinite and two periodic directions. *Journal of Computational Physics*, *96*, 297–324.

van Heerwaarden, C. C., Mellado, J.-P., & de Lozar, A. (2014). Scaling laws for the heterogeneously heated free convective boundary layer. *Journal of Atmospheric Sciences*, *71*(11), 3975–4000.

Waggy, S. B., & Biringen, S. (2011). Direct numerical simulation of top-down and bottom-up scalar diffusion in the convective Ekman layer. *Bulletin of the American Physical Society*, *56*(18).

Waggy, S. B., Marlatt, S. W., & Biringen, S. (2011). Direct numerical simulation of the turbulent ekman layer: Instantaneous flow structures. *Journal of Thermophysics And Heat Transfer*, *25*(2), 309.

Williamson, J. (1980). Low-storage runge-kutta schemes. *Journal of Computational Physics*, *35*, 48–56.

Zhong, X. (1996). Additive semi-implicit Runge-Kutta methods for computing high-speed non-equilibrium reactive flows. *Journal of Computational Physics*, *128*(1), 19–31.

Chapter 4
Overlapping Communication and Computation

From a computational perspective direct numerical simulation (DNS) of turbulent flows is enormously challenging (Sect. 4.1). In fact, the computing power needed for turbulence resolving simulation at Reynolds numbers well within the turbulent regime became available only recently with the advent of massively parallel super-computer systems (http://top500.org). And this is the main reason why the work presented in this thesis is carried out right now—even though the scientific questions are pertinent since many years, sometimes even since decades (Chap. 1).

A utilization of current high-performance computing (HPC) resources demands a distribution of the problem to a large number of independently acting computing entities which requires communication in between those entities. With increasing problem size and number of computing entities, the share of time that is needed to communicate in between the computing entities increases. While data are being sent and received over the network, the computing entities are often idle, i.e. they do not process data. For reasons hidden deep in the implementation of the Message Passing Interface, this is also the case if so-called non-blocking versions of send and receive operators are used. A library called `NB3DFFT` that works around this issue has been developed by J. H. Göbbert at RWTH Aachen University/FZ Jülich.

In Sects. 4.2 and 4.3 I demonstrate how this library is adopted by the algorithm used in this work to efficiently overlap the communication and computation of data at a rather high level in the code. For the configurations used in this work, this saves about 10 % of computing time. For even larger simulations, this optimization pushes the threshold of feasible simulations since the savings increase with simulation size. It also allows to obtain results—spending the same amount of computing time as a standard implementation—in less real time since it makes parallelization more efficient. Given the current trend in HPC to ever more distributed system, this approach is expected to also be useful for upcoming generations of HPC systems.

4.1 Motivation—A Rough Estimate of the Computational Demand

4.1.1 Memory Demand

The direct numerical simulation of a turbulent flow is very computing intense: The resolution of all relevant degrees of freedom in a turbulent flow—including the Kolmogorov scale η where viscosity acts—requires enormous computational power. The transitional Reynolds number Re_{trans}, i.e. that Re at which a flow becomes unstable to perturbations and transitions to turbulence, gives a rough estimate for the degrees of freedom that are at least needed for the direct simulation of a turbulent flow. Fixing a large scale L_0, it is $\eta \propto L_0 Re^{-3/4}$, and one can assume that—independent of L_0—the number of degrees of freedom necessary per direction is $Re^{3/4}$. It is $\mathcal{O}(Re_{\text{trans}}) = 2^8 - 2^{12}$ (Moin and Mahesh 1998; Moody 1944; Lilly 1966) implying a minimum of $2^{18} - 2^{27}$ degrees of freedom in a turbulence-resolving simulation. To be well within the turbulent regime, it is required that $Re > Re_{\text{trans}}$, and a reasonable estimate for the degrees of freedom is 2^{27}. The resolution properties of compact schemes demand around $8 \times 2^{27} = 2^{30}$ collocation points for an accurate enough representation of the relevant scales (Fig. 3.1). Here a three-dimensional turbulent flow with three velocity components and one scalar (4 prognostic variables) is considered. The fields and their tendencies have to be stored separately in double precision and at least 6 arrays are needed as working storage (Sect. 3.5.6, Fig. 3.3). The amount of random-access memory (RAM) required in bytes is then at least $(8 + 6) \times 8 \approx 2^7$ times the number of collocation points, which amounts to

$$
\left[\underbrace{2^4}_{\text{arrays}} \times \underbrace{2^3}_{\text{double precision}} \times \underbrace{\left(\underbrace{2^3}_{\text{resolution}} \times \underbrace{2^{27}}_{\text{dof}} \right)}_{\text{number of collocation points}} \right] \text{Bytes} \approx 134 \, \text{Giga Byte} \qquad (4.1)
$$

(For notational convenience, the definitions of Giga and Terra in terms of powers of two are used here, i.e. Mega refers to 2^{20}, Giga to 2^{30} and Tera to 2^{40}.) Such an amount of memory is not available as RAM on any modern computer, and it requires the utilization of high-performance computing (HPC) resources. The problem has to be distributed over many computing entities that—altogether—possess the desired amount of memory.

4.1.2   Computational Demand

The operation count per time-integration sub-step is a large ($\mathcal{O}(10^2)$) integer multiple of the number of collocation points such that the order of the number of floating point operations (FLOPs) is similar to the number of bytes utilized in the RAM. For the 4th order explicit Runge–Kutta scheme, five sub-steps are carried out per iteration. I estimate the computational demand per iteration step to be of the order of 1 Terra FLOP. On modern architectures, heavily optimized computer codes dealing with the simulation of turbulence utilize no more than 2–5 % of the theoretical maximum performance of a computer which increases this estimate in terms of the CPU cycles necessary to perform the calculations to around 2^6 Terra FLOP.

   The number of time steps required to resolve an eddy-turnover time is due to the Courant-criterion also approximately inversely proportional to the Kolmogorov scale η, and may be estimated by $2^{12 \cdot 3/4} = 2^9$ (2^{12} degrees of freedom have been estimated above as necessary for a flow well within the turbulent regime). It is, however, not enough to calculate one eddy-turnover time since a simulation starts from a non-turbulent initial condition, and the flow initially transitions to a turbulent state. This transient takes several eddy-turnover times where its particular properties and duration depend on the initial conditions applied. Once a flow is in its turbulent state, usually a simulation is continued for several eddy turnover times either to accumulate statistics and improve convergence (in the case of a stationary problem) or to check the self-similarity hypotheses or convergence to quasi-equilibrium states (in a temporally evolving problem). Assuming, a flow is integrated over 2^5 eddy-turnover time scales (2^4 for the initial transient and another 2^4 for the statistical convergence), a need for at least

$$\left[\underbrace{2^5}_{\text{eddy−turnover times}} \times \underbrace{2^6}_{\text{iterations}} \times \underbrace{2^9}_{\text{operation count}} \right] \text{Terra FLOP} = 2^{20} \text{ Terra FLOP} \quad (4.2)$$

is obtained.

   Even if the problem would fit into the memory of a modern computer—this amount of operations cannot be calculated in a reasonable period of time. With modern CPU operating at clock rates of around 2^3 Giga FLOP FLOP per second, such an endeavor would take

$$1000 \times 2^{17} \text{ seconds} \approx 4 \text{ years} \quad (4.3)$$

and require a sufficient extension of funding for this work that is not compatible with the MPG's guidelines and recommendations for the education of doctoral students by the national German science council (Wissenschaftsrat 2002). Consequently, HPC resources have to be utilized not only for reasons of memory utilization but also due to high computational demand.

4.1.3 The Link Between Spatial Discretization and Communication

Turbulence simulation is a global task in the sense of distributed computing, i.e. the problem cannot be split into independent sub-problems whose solution is computationally demanding. On the contrary to some applications in genetics or quantum physics, where this is the case, in turbulence simulations the need for computation and data exchange is strongly intertwined. In the governing equations of an incompressible flow, this need for communication is manifest in two ways: the derivatives and the Poisson equation for the pressure (Chap. 2, Sect. 3.1). Both of these operators rely on non-local information that may reside in a different computing entity. These two operators—the horizontal derivative and the Poisson equation—can be treated separately: The intermediate flow fields contain all source and sink terms for momentum but the pressure and only require derivatives to be calculated; the Poisson equation is then solved in a second step to project the equations to an incompressible flow field (cf. Sect. 3.1, Eqs. 3.2, 3.22b, 3.22c).

In the particular case of the present DNS algorithm, more than two thirds of the computer time is spent in calculating derivatives and transferring the associated information in between the computing entities. Hence, the focus here is on the optimization of a Runge–Kutta sub-stage without the calculation of the pressure term. Besides a few additions and multiplications, this consists mostly in the calculation of derivatives. The specific amount of communication that is necessary to calculate a single derivative, the stencil, depends on the spatial discretization that is chosen.

Spectral schemes. If a fully spectral method is employed, the whole (three-dimensional) flow field is needed to determine the value of any derivative; a spectral method has a global stencil; the calculation of derivatives in that case is rather expensive since two Fourier transformations are solved to obtain a derivative in physical space. Optimized implementations of the Fourier transformation achieve an operation count of $\mathcal{O}\left\{(N \log N)^3\right\}$ for a three-dimensional problem where N is the problem size in one direction. This effort comes with the benefit of a mathematically perfect derivative, i.e. no spatial resolution is lost in the discretization of the derivatives. A measure for the performance of the discretization of a derivative is the modified wavenumber (Fig. 3.1), and spectral methods have an optimal modified wavenumber $k' = k$.

The major drawback of a Fourier spectral scheme is that it can only handle equidistant grids in all three spatial directions. In particular in the vertical direction, where often points are clustered in the viscous sub-layer near the wall, this may be problematic. A possible solution is to solve vertical derivatives using a Chebyshev transformation or one of the two schemes discussed next—centered differences or compact Padé schemes.

Centered-difference schemes. On the contrary to a fully spectral method, centered difference schemes have local stencils. They commonly employ between three and seven collocation points, and are rather cheap in terms of their operation count.

The operation count goes in all cases as $\mathcal{O}\left\{N^3\right\}$, and in the case of a second-order centered derivative is $(2N)^3$ with a three-point stencil. In terms of their resolution properties, centered-difference schemes are inferior to spectral methods: While, similar to spectral schemes, they cannot resolve any feature with a wavelength smaller than 2Δ, the modified wavenumber deviates from the ideal one already for much larger features. In fact, Fig. 3.1 shows that even at a wavelength of 4Δ the amplitude error is already around 40 %. There are higher-order centered difference schemes with wider stencils that perform much better. A common property of centered difference schemes (no matter at what order) is that they are numerically diffusive. This means, the small wavelengths where normally diffusion extracts energy from the turbulent cascade are systematically damped stronger than the equations require. While this aids physical stability, it might affect the turbulence dynamics at the small scales which is undesired when simulating turbulence directly. This can lead to an only apparent resolution of the turbulent cascade where numerical diffusion breaks the cascade on scale much larger than the Kolmogorov scale.

Compact Padé schemes. A possibility to work around this problem of numerical diffusion are compact schemes. Not only do they have a smaller amplitude error in the modified wavenumber analysis (Fig. 3.1) but also are they less diffusive at high wavenumbers (Lele 1992, Fig. 5). For a compact scheme, all data along the line over which the derivative is calculated are necessary; a compact method has a global stencil, separately along each direction; the calculation is—compared with Fourier transformations—rather cheap since only banded matrices have to be inverted, which is possible in an operation count of $\mathcal{O}\left\{N^3\right\}$.

4.2 Approach and Implementation

4.2.1 Why Overlap Communication and Computation?

In the present implementation of the algorithm the communication of data is carried out whenever it is needed (and once an array is available in transposed form it is saved until it is not needed any more to save transpositions). While calls to the Message-Passing Interface are active, no calculation happens and the data are globally transposed as desired. Let these non-local transpositions occupy a fraction f_{comm} and all the other calculation a fraction f_{calc} of the computing time such that

$$f_{\text{calc}} + f_{\text{comm}} = 1. \tag{4.4}$$

This situation is sketched in part (A) Fig. 4.1: The local-in-memory calculation of body forces and derivatives with available data—either because they have been transposed before or because they do not need to be transposed—only utilizes the floating point unit (FPU) of each computing entity separately. The transposition consists in the send and receive operations of data as well as a local transposition,
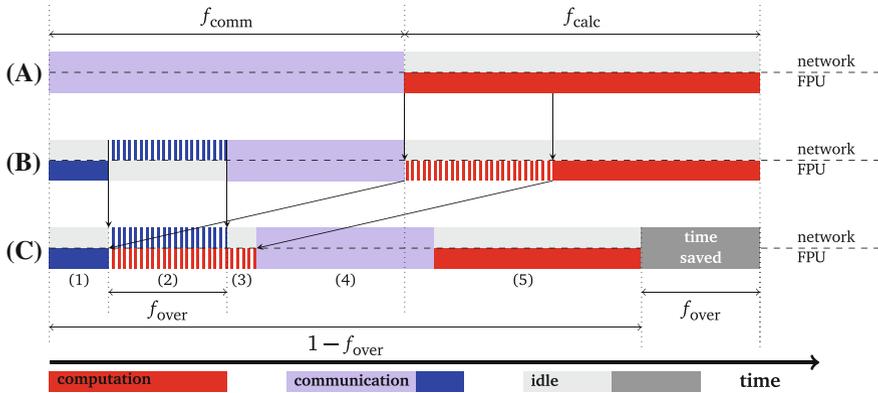
Fig. 4.1 Schematic of re-organization of the algorithm for non-blocking communication. *Part A* shows a standard implementation where data is first transposed and then a derivative is calculated. In *Part B*, a possible re-organization of the code is shown where the communication is organized in such a way that in a first step, data are packed locally, and the communication is initiated (*dark blue part*); While the data is sent in a second step, the FPU is idle. An isolated part of calculations can be identified that (optimally) occupies a similar period of time as the communication over the network. The final layout where a part of the computation is done simultaneous to the computation is shown in *Part C*

and as such it generally utilizes both the network and the local FPU. It is, however, possible to re-organize the communication such that over significant parts of the process mainly the network is utilized as outlined in part (B) of Fig. 4.1. Then, a suitable part of local calculations which can be done on data that do not need to be transposed (or are already available in transposed form) can be performed while the communication utilizes the network. The overlapped version of the algorithm has five (instead of two) phases as sketched in part (C):

(1) The communication is initialized and the data are packed for the network-send operation.
(2) The network-send operation takes place, which utilizes the network card. Con-comitantly, calculations are performed on the FPUs.
(3) The calculations might take longer or shorter than the network send operations. In the case sketched here, the part of the communication that again needs to utilize the FPUs has to wait until the calculations are finished. It might as well be the case that the network part takes longer (this is not sketched here).
(4) The transpositions are finished.
(5) The remaining calculations with transposed data are carried out.

Ideally, the time needed to perform the calculations is similar to the time that the send and receive operations over the network require. In a real-world set-up, this is hard to achieve, and one or the other will take longer. The saved time fraction f_{over}, is the minimum of the two periods.

4.2.2 *Design of the* **NB3DFFT** *Library*

The implementation of a framework to overlap communication and computation has been carried out by J. H. Göbbert at RWTH Aachen University and is available through a library called NB3DFFT. To achieve the goal of an overlap between communication and computation which is sketched in a very simple variant in Fig. 4.1, this library takes an approach based on two threads implemented via openMP. The two threads are a worker and a scheduler thread—where the scheduler thread takes over the communication. This happens on demand by the worker thread.

At the beginning of a code region suitable for nonblocking communication, the scheduler thread is started in parallel with the worker thread; the scheduler now waits for a communication call by the worker thread. (This is particularly efficient on systems which have more logical than physical processors which is the case at the Jülich Supercomputing Centre where simulations for this work have mainly been carried out.) Once the worker thread needs data from another computing entity or has data ready to be sent, it issues a call to the NB3DFFT library. The library through shared OpenMP variables ensures that the scheduler thread learns about the communication that needs to be done and does it. This thread-based approach utilizes modern CPU features in a convenient way. Owing to the widespread availability of multi-tasking on personal PCs and Laptops, they are designed to minimize the computational cost that a context switch causes, and often have more logical cores than FPUs. This allows for efficient switching between threads or even applications. While not desirable for the actual calculation of fluid dynamical problems, the multi threading can efficiently utilize these features available at no cost.

Similarly, arriving at a position where data from another computing entity are needed to continue, the call to the Message-Passing Interface is replaced by a status-request call to the NB3DFFT library. If the data is not ready to be transposed, the code can continue doing other things and come back to the status request later. This is a major advantage of the queue-based approach of the library which allows to minimize phase (3) in Fig. 4.1.

4.2.3 *Re-Organization of the Algorithm*

The algorithm's order of execution is reorganized here to optimally benefit from the NB3DFFT library. Given that the scheduler thread runs in the background and carries out transpositions, the aim of this re-organization is clear: The algorithm needs to be split in parts that only do *either* communication *or* computation. A derivative's calculation consists of four steps:

(a) The data are globally transposed such that data belonging to a single line along which the derivative is being calculated reside in a single computing entity.
(b) The derivative is being calculated.

(c) The data are being transposed back such that every computing entity holds the data for the physical part of space that it is assigned to.
(d) The update of the tendency in physical space—the actual reason for which the derivative is being calculated.

While steps (a) and (c) contain transpositions that are carried out by the scheduler thread in the background, steps (b) and (d) are purely local calculation steps relying on the instantaneous availability of the transposed data. An order of execution is desirable in which steps (a) and (c) are initiated as early as possible and steps (b) and (d) as late as possible.

The starting point here was a scheme in which all of the three are done right after each other. An alternative is to first start all global transpositions, then do all calculations that do not require global transpositions, and finally do the calculations that require transposed data. This would require a severe increase of the RAM since a field that is being transposed while the calculations continue needs two or more fields in the RAM—one for the original field (it may not be modified until the operation is completely finished) and one for the result. I present here a more memory-efficient method that overlaps calculations of a few but not all derivatives.

Such a memory-efficient layout for the computation of advection and diffusion for the four prognostic variables u, v, w and a scalar is shown in Fig. 4.2. The equations evaluated are

$$
\begin{aligned}
u_{\text{tendency}} &= & O_1(u)+ & O_3(u)+ & O_2(u) \\
v_{\text{tendency}} &= & O_1(v)+ & O_3(v)+ & O_2(v) \\
w_{\text{tendency}} &= & O_1(w)+ & O_3(w)+ & O_2(w) \\
s1_{\text{tendency}} &= & O_1(s_1)+ & O_3(s_1)+ & O_2(s_1) \\
\text{transposition :} & & y \leftrightarrow x & y \leftrightarrow z & \text{none}
\end{aligned}
\tag{4.5}
$$

where $O_i(\xi) = u_i D_i^{(1)} \xi + D_i^{(2)} \xi$ is the Burgers operator. The Coriolis and Buoyancy terms can be evaluated before, as part of the sketched operations, or immediately afterwards. The pressure gradient term can only be calculated once the intermediate velocity field is known, i.e. after the tendencies for u, v and w have been updated.

4.3 Performance Measurements

The scheme described in the previous section was developed on the 2048-core intel cluster `thunder` at the *Max Planck Institute for Meteorology* and then ported to the 294, 912-core Tier-0 supercomputer `juqueen` at *Jülich Supercomputing Centre*. On both systems the scaling of the non-blocking communication (NBC) scheme and a fully blocking communication (FBC) scheme was evaluated. I present here a comprehensive scaling study that has been undertaken to demonstrate the value of this scheme to current and future turbulence simulations on the supercomputer `juqueen`.
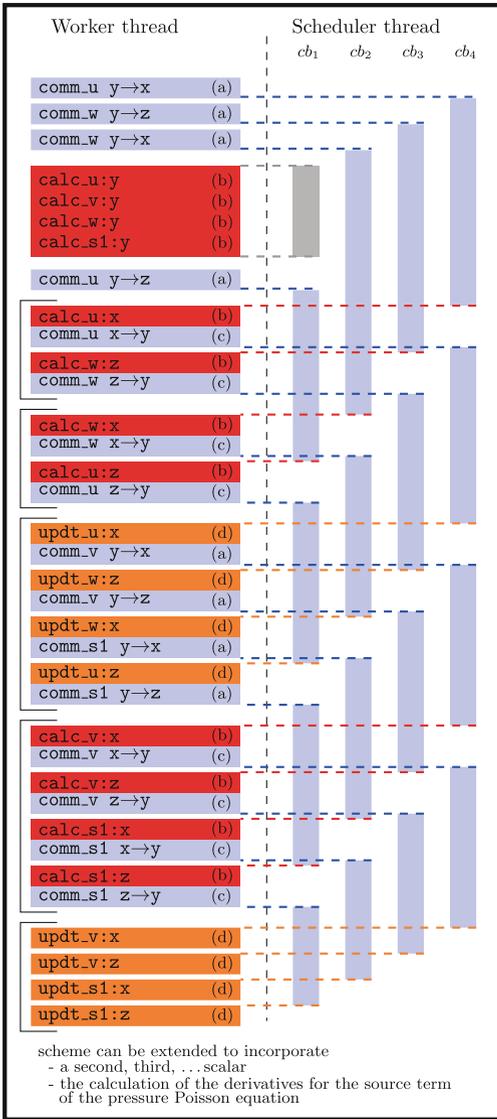
Fig. 4.2 Schematic illustrating an efficient design for an algorithm that overlaps communication and computation with a reasonable amount of memory-overhead (here, the four buffers cb_1–cb_4 for the communication have to be made available on *top* of the memory needed by the the worker thread). A *dashed horizontal line* signalizes a call to the NB3DFFT library. The buffer cb_1 is utilized for a more efficient calculation of the vertical (Oy) derivatives. Initialization of the threads and library is not shown

4.3.1 Performance Metrics: Strong and Weak Scaling

Let T_n^s be the time to once calculate the right-hand side (i.e. advection, diffusion, pressure, buoyancy and Coriolis terms) for a problem of size s with n computing entities. There are two measures to assess quantitatively the parallel performance of a computer code, strong and weak scaling.

For a strong-scaling study, the number of computing entities n is increased to tackle a problem at given size s_0. Ideally, a scaling study is carried out with respect to a serial case. This is not possible here: simulations have sizes that do not fit into a single CPU (Sect. 4.1). Consequently, the smallest amount of computational resources n_0 that provides enough memory for the respective case, is used as a reference for the strong-scaling studies.

The speed-up S_{strong} and parallel efficiency ϵ_{strong} are then calculated as

$$S_{\text{strong},n_0,s_0}(a) = \frac{T_{n_0}^{s_0}}{T_{a \cdot n_0}^{s_0}}, \qquad \epsilon_{\text{strong},n_0,s_0}(a) = \frac{T_{n_0}^{s_0}}{T_{a \cdot n_0}^{s_0}} \frac{1}{a}. \tag{4.6}$$

Optimal strong scaling is achieved if $S_{\text{strong},n_0,s_0}(a) = a \Rightarrow \epsilon_{\text{strong},n_0,s_0}(a) = 1$. In some cases, it may even occur that $S_{\text{strong}} > a$ and consequently $\epsilon_{\text{strong}} > 1$. This is the case when the code, mostly due to better utilization of memory and caches, runs more efficiently on a larger number of cores.

For a weak scaling study, commonly the number of computing entities is increased proportionally to the problem size such that the computational load per computing entity stays approximately constant. Once the constraint of solving identical problems within a scaling study is dropped, one can, however, take the concept a step further and calculate the weak scaling with respect to the smallest simulation available. This makes data across weak and strong-scaling studies comparable, and is still a kind of weak scaling. This approach is used here to provide a performance reference based on the single-node-board performance for those cases which—due to memory constraints—cannot be run in a single node board. The speed-up S_{weak} and parallel efficiency ϵ_{weak} are calculated as

$$S_{\text{weak},n_0,s_0}(a,b) = \frac{bT_{n_0}^{s_0}}{T_{a \cdot n_0}^{b \cdot s_0}}, \qquad \epsilon_{\text{weak},n_0,s_0}(a,b) \frac{bT_{n_0}^{s_0}}{aT_{a \cdot n_0}^{b \cdot s_0}}. \tag{4.7}$$

A classical weak scaling is recovered if $a = b$.

Generally, weak scaling is considered to be achieved easier than strong scaling. This may be explained with the number of computing entities involved in a communication increasing as n^2 and the amount of data which has to be sent—commonly also increasing as n^2, or sometimes even stronger. When global transpositions of full fields are involved, this is not the case: Given a particular problem size, the amount of information that has to be sent per core decreases approximately as n_0/n. If the global communication time is not bound by the latency (set-up of communication channels, initial calls to library, etc.) but by the actual sending of data over the

network, the time spent in communication might decrease with increasing number of computing entities. In particular, this is the case when the computational load per core is very large, which is the case for the strong-scaling reference cases.

4.3.2   Performance on the Supercomputer `juqueen`

Overhead of the NBC scheme. The initialization of threads, calls to the `NB3DFFT` library and synchronization between the scheduler and worker threads require computational time; this time is an overhead specific to the NBC scheme. While the absolute measurement of this time fraction requires substantial modification of the computer code, the performance degradation in the smallest case gives an indication. The NBC scheme overall runs 19 % slower than the FBC scheme for the case with $2^{20} = 1$ G collocation points (Table 4.1). This configuration does not benefit a lot from the overlap, which is likely due to the relatively short time needed to communicate data: If a simulation fits in a single node board ($n = 1$) no 'expensive' hops to different node boards or even mid-planes/racks are necessary which makes the communication rather cheap.

This degradation of performance in connection with the NBC scheme only occurs for simulations within one or two node boards. In all other cases, the NBC scheme speeds up the simulations—by up to 40 % depending on the configuration (lowest part of Table 4.1). Given that simulations of sizes smaller than 4 G are commonly not carried out on `juqueen`, the FBC scheme is disregarded for future work on this supercomputer.

Strong scaling. The strong scaling for four cases ranging from 1×2^{30} (1 G) to 64×2^{30} (64 G) collocation points is shown in Fig. 4.3 and Table 4.1 for both the NBC and FBC schemes. For the cases with a size of 1 G and 4 G the strong scaling is significantly improved by the NBC scheme. From 2 to 8 node boards, the scaling is super-linear for the smallest case. This is likely due to cache-effects and gives a double benefit: On the one hand, simulations require less real time to finish; on the other hand, they require less computing time and electricity to be calculated. (It is reminded that the reference for this strong scaling is slower by about 20 %. Nonetheless, this provides evidence for a very efficient implementation of the `NB3DFFT` library and its interplay with the current algorithm.)

For the larger cases 4 and 16 G the strong scaling efficiency (but not the actual wall-clock-time) of the FBC scheme is better. This is, however, mainly due to the very bad performance of the reference simulations which run 11 % respectively 30 % slower (Table 4.1). Here, the benefit of the NBC scheme is already hidden in the reference case and deems the inferior scheme to appear more efficient which is a general problem of strong scaling investigation: optimized reference cases are always penalized by a worse scaling. Nonetheless, in absolute terms, the NBC scheme is faster for all simulations beyond a size of 2 G.

Table 4.1 Scaling and performance metrics on the supercomputer `juqueen`

		NBC							FBC						
Problem size [2^30]		1	2	4	8	16	32	64	1	2	4	8	16	32	64
Time per RHS [s]															
32 Nodes	1	10,55							8,9						
2 NodeBoards	2	5,19	10,40						4,70	9,50					
4 NodeBoards	4	2,42	4,81	9,46					2,57	4,92	9,56				
8 Nodeboards	8	1,28	2,61	5,11	9,86				1,43	2,94	5,77	11,16			
1 Midplane	16	0,64	1,37	2,63	5,32	10,57			0,64	1,52	2,95	5,91	11,84		
1 Rack	32	0,37	0,69	1,68	3,80	6,97	11,8		0,40	0,83	1,84	3,92	8,84	12,7	
2 Racks	64	0,26	0,51	0,78	1,72	3,76	7,20	16,72	0,31	0,67	0,96	2,04	4,14	8,1	24,04
4 Racks	128	0,23	0,38	0,47	0,85	1,96	3,98	7,61	0,31	0,64	0,61	1,08	2,06	4,53	9,03
8 Racks	256							4,72							5,52
Strong Scaling Efficiency															
32 Nodes	1	1,00							1,00			efficiency < 66 %			
2 NodeBoards	2	1,02	1,00						0,95	1,00		66% < efficiency < 95%			
4 NodeBoards	4	1,09	1,08	1,00					0,87	0,97	1,00	95% < efficiency			
8 Nodeboards	8	1,03	1,00	0,93	1,00				0,78	0,81	0,83	1,00			
1 Midplane	16	1,03	0,95	0,90	0,93	1,00			0,87	0,81	0,81	0,94	1,00		
1 Rack	32	0,89	0,94	0,70	0,65	0,76	1,00		0,70	0,72	0,65	0,71	0,67	1,00	
2 Racks	64	0,63	0,64	0,76	0,72	0,70	0,82	1,00	0,45	0,44	0,62	0,68	0,71	0,78	1,00
4 Racks	128	0,36	0,43	0,63	0,73	0,67	0,74	1,10	0,22	0,23	0,49	0,65	0,72	0,70	1,33
8 Racks	256							0,89							1,09
Weak Scaling Efficiency															
32 Nodes	1	1,00							1,00						
2 NodeBoards	2	1,02	1,01						0,95	0,94					
4 NodeBoards	4	1,09	1,10	1,12					0,87	0,90	0,93				
8 Nodeboards	8	1,03	1,01	1,03	1,07				0,78	0,76	0,77	0,80			
1 Midplane	16	1,03	0,96	1,00	0,99	1,00			0,87	0,73	0,75	0,75	0,75		
1 Rack	32	0,89	0,96	0,78	0,69	0,76	0,89		0,70	0,67	0,60	0,57	0,50	0,70	
2 Racks	64	0,63	0,65	0,85	0,77	0,70	0,73	0,63	0,45	0,42	0,58	0,55	0,54	0,55	0,37
4 Racks	128	0,36	0,43	0,70	0,78	0,67	0,66	0,69	0,22	0,22	0,46	0,52	0,54	0,49	0,49
8 Racks	256							0,56							0,40
Speed-up by NBC															
32 Nodes	1	-19%													
2 NodeBoards	2	-10%	-9%												
4 NodeBoards	4	6%	2%	1%											
8 Nodeboards	8	**10%**	**11%**	**11%**	**12%**										
1 Midplane	16	0%	10%	**11%**	10%	**11%**									
1 Rack	32	8%	**17%**	9%	3%	**21%**	7%								
2 Racks	64	**16%**	**24%**	**19%**	**16%**	9%	**11%**	**30%**							
4 Racks	128	**26%**	**41%**	**23%**	**21%**	5%	**12%**	**16%**							
8 Racks	256							**17%**							

Upper table lists the computing time used for the evaluation of one Runge–Kutta sub-stage (right-hand-side routine) in seconds. The two colored tables shows the strong-scaling and weak-scaling efficiencies. Coloring of the data indicates performance; blue stands for a near-perfect or super-linear scaling defined as $\epsilon > 95\%$; green stands for acceptable scaling ($\epsilon > 66\%$); red stands for unacceptable scaling ($\epsilon < 66\%$). The lower table lists the computing time saved by the NBC scheme. Bold numbers indicate saving $>10\%$. The problem size in the header is given in Giga (2^{30}) points
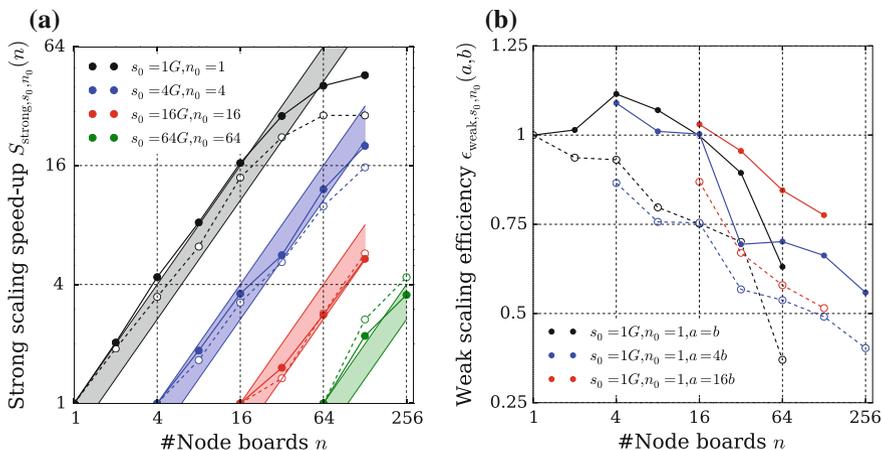
Fig. 4.3 **a** Strong-scaling speed-up S_{strong} for the NBC (*solid, filled dots*) and FBC (*dashed, open dots*) schemes. The range of acceptable performance degradation (strong scaling efficiency larger than 2/3) is shaded by the respective color for each case. **b** Weak-scaling efficiency ϵ_{weak} with respect to the case 1 G run in 1 node board (512 `MPI` tasks, 1,024 `OpenMP` threads). The scaling data are shown for four cases, ranging in size from 2^{30} (`1G`) to 64×2^{30} collocation points. The data here cover set-ups from 512 `MPI` tasks (1,024 `OpenMP` threads) to 131,072 `MPI` tasks (262,144 `OpenMP` threads)

A drop in the strong scaling efficiency is observed when the number of node boards increases from 16 to 32. The layout of an IBM Blue Gene/Q rack explains this: 16 node boards are always located within a single mid plane. On such a mid-plane, communication among node boards does not go over the central network switches. 32 node boards are located within a single rack, and communication goes over the central switches requiring more time.

Weak scaling. The weak scaling with respect to a reference case within a single node obscures the comparison of performance less. It has only one reference case and allows for fair comparison of the performance of simulations at different sizes and using a different number of node boards. The weak scaling of the NBC scheme is better for all cases that are considered here (Fig. 4.3b). The largest difference occurs for the big simulations (>2 G) on more than one rack. In fact, simulations on 2 and 4 racks are now so efficient that they are feasible. This was not the case with the FBC scheme which has weak-scaling efficiencies around 50 % for such big simulations and is in absolute terms around 20–30 % slower.

The biggest case (64 G) was also tested on 8 racks (131,072 MPI tasks). While the efficiency of both the NBC and FBC schemes is unacceptable for operational simulations, it provides a prove of concept that the algorithm is suitable for problems of this size. Optimizations regarding the mapping of processes and arrangement of mid planes which are part of the job submission procedure on the `juqueen` system, might yield significant performance improvements for the NBC scheme. Assuming,

one could utilize the whole `juqueen` system, this would allow simulations with as many as 256×2^{30} collocation points which is a factor 25 more than in the current largest set-up presented here. This would allow to increase the physical scale separation by approximately a factor three to four with respect to the present highest Reynolds number $Re = 1000$.

References

Lele, S. K. (1992). Compact finite difference schemes with spectral-like resolution. *Journal of Computational Physics*, *103*(1), 16–42.

Lilly, D. K. (1966). On the instability of ekman boundary layer flow. *Journal of the Atmospheric Sciences*, *23*, 481–494.

Moin, P., & Mahesh, K. (1998). Direct numerical simulation: A tool in turbulence research. *Annual Review of Fluid Mechanics*, *30*, 539–578.

Moody, L. F. (1944). Friction factors for pipe flow. *Transactions of the American Society of Mechanical Engineers*, *66*(8), 671–684.

Wissenschaftsrat (2002). Empfehlungen zur Doktorandenausbildung. http://www.wissenschaftsrat. de/download/archiv/5459-02.pdf

Chapter 5
A Test Bed for the Numerical Tool

When simulating flows numerically, a validation of the tools is a necessary step. Coleman and Sandberg (2010) suggest various ways to check a DNS code. To ensure a correct implementation of the flow solver implemented here, it has been tested using problems at various stages of complexity ranging from an ordinary differential equation via one- and two-dimensional laminar flow solutions to fully three-dimensionally turbulent flows:

- an ordinary differential equation with known analytical solution (Sect. 5.1)
- a laminar solution for a non-stationary Ekman layer in one dimension (Sect. 5.2.2)
- a Taylor–Green vortex in two dimensions (Sect. 5.3)
- a turbulent solution for the Ekman layer in three dimensions (Sect. 5.4).

If available, solutions are compared against analytical ones or those of the explicit solver which has been extensively tested for a number of flows ranging from wall-bounded turbulence to free-shear flows and jets in two and three dimensions. In this section, the tests of the SIRK3 scheme (cf. Chap. 3) are described. Similar tests have been carried out for the explicit fourth-order, five-stage Runge–Kutta scheme but for brevity are not discussed at the same level of detail here.

5.1 Behavior of the Semi-implicit Scheme When Solving a Non-linear ODE

To study the behavior of the SIRK3 scheme, the non-linear ordinary differential equation (ODE)

$$\frac{du}{dt} = au + bu^2; \quad u, t \in \mathbb{R} \tag{5.1}$$
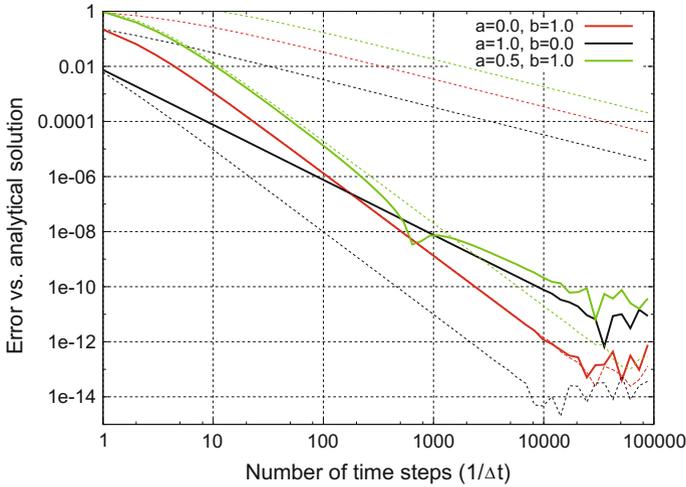
Fig. 5.1 Errors of numerical solutions when compared to the analytical one. *Thick solid lines* show the SIRK3 scheme. *The dashed lines* are a fully explicit three-stage Runge–Kutta scheme after Williamson (1980). *The thin dotted lines* result from a first-order Euler-forward integration of the equation. *The red lines* are for a purely non-linear problem ($a = 0, \ b = 1$), *the black lines* for a purely linear one ($a = 1, \ b = 0$), and *the green lines* for the full equation with $a = 0.5$ and $b = 1$

is employed. For $a, b = \text{constant} \in \mathbb{R}$, it has a known analytical solution. The linear and non-linear contributions can be adjusted to the needs, to investigate the errors for the explicit and implicit integration procedure separately (Fig. 5.1).

For the integration of Eq. (5.1), the SIRK3 scheme behaves as expected. For a purely non-linear problem (red lines) the SIRK3 scheme behaves very similar to the fully explicit Runge–Kutta scheme and time stepping errors decrease with order three until machine precision is reached (around 20,000 time steps); it is only beyond 20,000 time steps—where the errors are of the order of machine precision—that the errors differ; in this range, the error is quasi-random as it depends on the order of execution (and potentially the machine and compilers if the implementation is not fully conformal with the IEEE standard). For a purely linear integration, the order of time integration drops to two (thick black line). When the full equation is integrated, the errors from the integration of the non-linear part of Eq. (5.1) dominate for larger time steps (number of time steps smaller than $\simeq 500$); the convergence of the time stepping scheme is of third order in τ. For smaller time steps (number of time steps larger than $\simeq 1000$), the error from integration of the linear part of Eq. (5.1) dominates, and the order in τ drops to two. The dip in error around 500 time steps results from a change of the sign of the error.

5.2 Analytical Solution of Ekman Flow

5.2.1 The Stationary Laminar Solution

The solution of the stationary case presented here was originally derived by Ekman (1905). He considered the following set of simplified equations for a two-dimensional flow

$$\frac{\partial U}{\partial t} = -\frac{\partial \overline{\pi}}{\partial x} + f V + \nu \frac{\partial^2 U}{\partial z^2} - \frac{\partial \overline{uw}}{\partial z}$$
$$\frac{\partial V}{\partial t} = -\frac{\partial \overline{\pi}}{\partial y} - f U + \nu \frac{\partial^2 V}{\partial z^2} - \frac{\partial \overline{vw}}{\partial z}. \tag{5.2}$$

The turbulent flux of momentum $\overline{uw}$—in analogy to molecular diffusion—can be written as

$$\overline{u_i u_j} = -\nu_T \left(\frac{\partial U_i}{\partial x_j} + \frac{\partial U_j}{\partial x_i} \right). \tag{5.3}$$

While in general ν_T is a function of the flow state and height above ground, Ekman assumed $\nu + \nu_T =: \nu_E$, where ν_E is a constant eddy viscosity. This assumption which is the key to Ekman's laminar solution, is the reason why—if appropriately non-dimensionalized—this solution does not differ from the laminar one. The idealized solution is then referred to as quasi-laminar flow. If the geostrophic balance (Eq. 2.9) and stationarity are introduced, and one lets $\xi := U - G_1 + i(V - G_2)$, the problem reduces to the second-order complex linear boundary-value problem for ξ:

$$\frac{\partial^2 \xi}{\partial z^2} - \frac{if}{\nu_E} \xi = 0 \tag{5.4a}$$

$$\xi|_{z=0} = 0, \qquad \lim_{z \to \infty} \xi = G + i \cdot 0 \tag{5.4b}$$

where the boundary conditions represent a no-slip surface and geostrophic equilibrium in the free atmosphere. With $U = \mathscr{R}(\xi)$ and $V = \mathscr{I}(\xi)$, it follows

$$U_E(\tilde{z})/G = \mathscr{R}(\xi) = (1 - e^{-\tilde{z}} \cos(\tilde{z}))$$
$$V_E(\tilde{z})/G = \mathscr{I}(\xi) = e^{-\tilde{z}} \sin(\tilde{z}), \tag{5.5}$$

where $\tilde{z} := z/D$, and $D := \sqrt{2\nu/f}$. The solution $(U_E, V_E) = (U(\tilde{z}), V(\tilde{z}))$ (Fig. 5.2) is self-similar, i.e. it does not depend on any of the parameters D, f, ν or their non-dimensional combination Re_D.

(a)

(b)
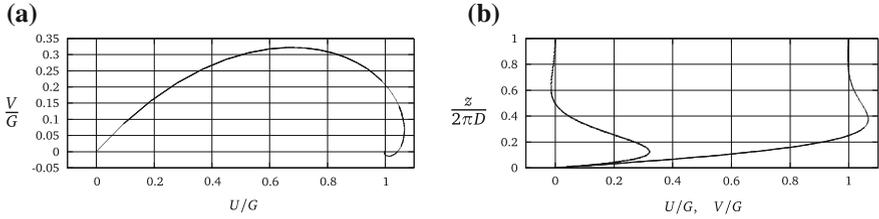
Fig. 5.2 Hodograph (*left panel*) and wind components (*right panel*) for the quasi-laminar Ekman-layer solution Eq. (5.5). In the right panel, the *thick line* depicts the spanwise velocity $V_E(z)$ and the thin one the streamwise velocity component $U_E(z)$

5.2.2 Temporally Evolving Solution

Once the Ekman solution (Eq. 5.5) is known, one can write any horizontally homogeneous velocity field as $V(z, t) = V_E(z) + V'(z, t)$ with $V_E(z)$ a solution of Eq. (5.5).

Applying this decomposition to ξ leads to the linear partial differential equation

$$\frac{\partial \xi'}{\partial t} = -if\xi' + \nu \frac{\partial^2 \xi'}{\partial z^2}. \tag{5.6}$$

with boundary conditions $\xi'|_{z=0} = \xi'|_{z\to\infty} = 0$ and an initial condition to be specified. The linearity of the system (5.6) implies

$$\hat{\xi}' \text{ solves (Equation (5.6))} \Rightarrow \frac{\partial \hat{\xi}'}{\partial z} \text{ solves Equation (5.6)}. \tag{5.7}$$

Hence, a family of non-trivial solutions $(\Xi_n)_{n\in\mathbb{N}_0}$ to the boundary value problem Eq. (5.6) is given by

$$\Xi_n(z, t) = \frac{\partial^{(2n+1)}}{\partial z^{(2n+1)}} \left[e^{-\frac{z^2}{4\sigma(t)^2}} \sqrt{\frac{1}{\sigma_n(t)^2}} \right], n \in \mathbb{N}_0 \tag{5.8}$$

for an appropriate choice of σ. Even though any derivative of Ξ_0 is a solution to Eq. (5.6), only the odd ones fulfill the boundary conditions. The first three members of the family of solutions Ξ_n are shown in the left panel of Fig. 5.3 at $t = 0$ with the initial condition $\sigma_i(0) = 1$.

For $n = 0$, σ is defined through

$$(z^2 - 2\sigma_0^2) \left[\frac{\nu}{\delta^2} - \frac{\partial \sigma_0^2}{\partial t} \right] = 0 \Rightarrow \sigma_0^2(t) = \frac{f}{2}t + \sigma_{0,0}, \tag{5.9}$$
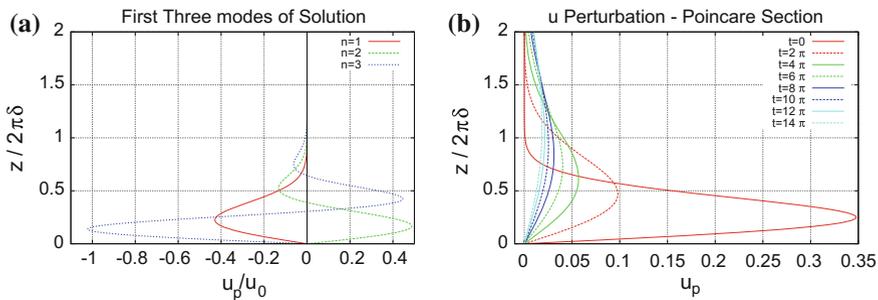
Fig. 5.3 **a** First three members Ξ_1, Ξ_2, Ξ_3 of family of solutions for $\hat{\xi}$; **b** Poincaré sections of the $U'(z, 2\pi n)$ for various $n \in \mathbb{N}$

where $\sigma_{0,0} \equiv \sigma_0(t = 0)$ has to be specified. Hence, the solutions for the temporal development of perturbations of the form $\Xi_0(z, 0)$ to a quasi-laminar Ekman-flow are

$$U'(\tilde{z}, t) = -\frac{A_0\sqrt{2}}{\delta(4\sigma_0 + ft)^{3/2}} \, \tilde{z} \exp\left[-\frac{\tilde{z}^2}{2(\sigma_0 + 4ft)}\right] \cos(ft)$$
$$V'(\tilde{z}, t) = +\frac{A_0\sqrt{2}}{\delta(4\sigma_0 + ft)^{3/2}} \, \tilde{z} \exp\left[-\frac{\tilde{z}^2}{2(\sigma_0 + 4ft)}\right] \sin(ft)$$
(5.10)

where $A_0 \in \mathbb{R}$. For $\sigma_0 > 0$ in the limit $t \to \infty$ the first member of the family of solutions approaches the quasi-laminar steady-state solution (U_E, V_E). Once σ_0 is specified, the level of maximum initial perturbation depends on time as $\tilde{z}_{max}(t) = \sqrt{ft + 4\sigma_0}$. Perturbations propagate upwards and their magnitude is damped with increasing time. This behavior is illustrated by the Poincaré sections taken at $V'(z) = 0 \; (\Leftrightarrow t \mod 2\pi = 0)$ that are shown in the right panel of Fig. 5.3. σ_0 determines the width of the initial perturbation: if $\sigma_0 = 0$, it is singular in the sense that it collapses to a Dirac-δ function.

5.2.3 Convergence of the Errors

The computer code has been set-up to solve the problem Eq. (5.6) in a horizontally very small domain and using a vertical resolution that allows for the error in spatial schemes to be close to roundoff. Around 10,000 mesh points in the vertical direction are necessary to fulfill this requirement. The convergence of the r.m.s. error of the solution when compared to the analytical solution derived above is shown in Fig. 5.4. Due to the very low Reynolds number ($Re = 2$), the viscous error in this case is the dominant source of inaccuracy and the convergence of the numerical scheme is second-order down to machine accuracy. Due to the extremely fine vertical mesh in the vertical direction, the stability criterion for the explicit solver is too strong to compare this convergence order to that of the explicit scheme as all of the time steps
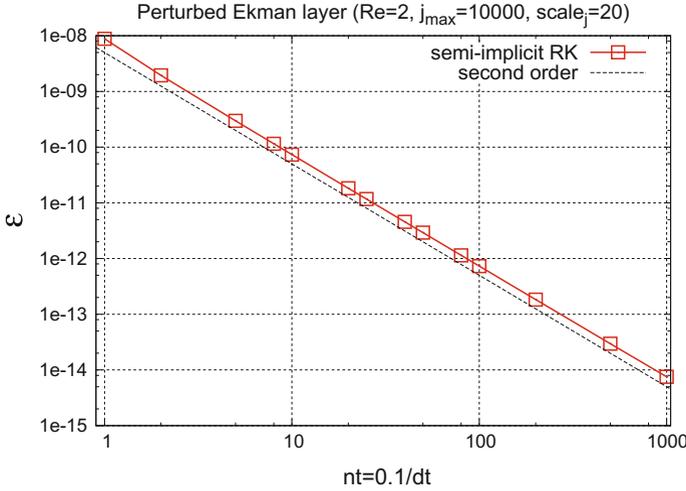
Fig. 5.4 R.m.s. error of the numerical solution for the system (5.6) after $t = 0.1$ when compared to the exact (analytical) solution (5.10)

used here are beyond the stability range of both the third-order–three-step and the fourth-order–five-step Runge–Kutta schemes.

5.3 Two-Dimensional Taylor–Green Vortex

The Taylor–Green vortex is studied at the two Reynolds numbers $8\pi/10$ and $8\pi \times 100$. The results obtained in Mellado and Ansorge (2012) are reproduced using semi-implicit time-stepping. Therefore, the Taylor–Green vortex in the two-dimensional domain $[0, 1] \times [0, 0.5]$ is considered:

$$u_1(x_1, x_2, t) = \sin(2\pi x_1)\cos(2\pi x_2)f(t), \quad u_2 = -\cos(2\pi x_1)\sin(2\pi x_2)f(t),$$

$$p(x_1, x_2, t) = \frac{1}{4}\left[\cos(4\pi x_1) + \cos(4\pi x_2)\right]\left[f(t)\right]^2$$

$$f(t) = \exp\left(-8\pi^2 Re^{-1}t\right).$$

At the higher Reynolds number $Re = 8\pi^2 \times 100$, the overall spatial accuracy of the code is 4th order (Fig. 5.5). When the Reynolds number is decreased by a factor of 1000 to $Re = 8\pi^2/10$, diffusive errors come into play at the boundaries, and the overall spatial accuracy reduces to 3rd order.

The overall convergence order in time is first order (Fig. 5.5b). The relative error in pressure fields is two orders of magnitude larger than in the velocities u and v (Fig. 5.5). The larger error in the pressure fields indicates that this degradation of
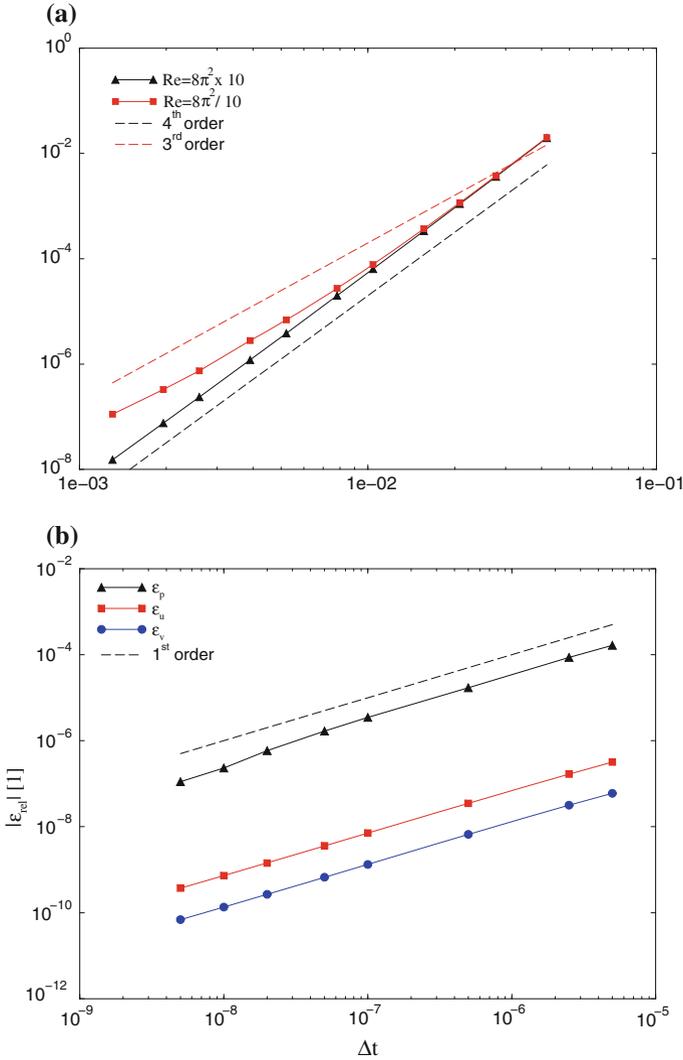
Fig. 5.5 Convergence of the integration errors for the Taylor–Green vortex after $t = 5 \times 10^{-6}$ when changing the grid spacing (**a**) and the time step for a grid spacing of $h = 1/768 \approx 1.3 \times 10^{-3}$ (**b**)

order is a consequence of the series truncation in Eq. (3.22b) and does not contradict results of the previous test in temporally evolving quasi-laminar Ekman flow. In this laminar case, the dynamic pressure is constant throughout the entire flow, and errors do not propagate.

5.4   Three-Dimensional Turbulent Ekman Layer

For turbulent flow, no analytical solution—as it is the case with the previous test cases—is known. To assess the correctness of the simulations consistency in themselves is checked, and they are compared with previous work. Data from simulations with the explicit time stepping scheme at three different Reynolds numbers is used here for a comparison with previous work.

Explicit 4th-order–5-stage Runge–Kutta scheme The hodographs in Fig. 5.6 are for the series of simulations N500L, N750L and N1000L (Table 6.1) which corresponds to a 75 % reduction in viscosity. For case N500L it is shown in Mellado and Ansorge (2012) that the agreement of the hodographs with data obtained from Coleman et al. (1990) is very good. The dependency on Re is small, and it decreases with increasing Re. In particular, the change from $Re = 750$ to $Re = 1000$ is much smaller than that from $Re = 500$ to $Re = 750$. Concomitantly, a logarithmic layer emerges as the scale separation between the outer and inner scales, i.e. the Reynolds number, is increased. This dependency on the Reynolds number is also observed in other studies (Coleman 1999; Spalart et al. 2008) and indicates the consistency of the numerical method.

A more quantitative criterion is the wall friction velocity $u_\star$ and its turning at the surface α with respect to the geostrophic wind—a consequence of the interaction between rotation and friction in Ekman flow. Since the seminal work of Coleman et al. (1990), these observables (they are unknown a priori and hence not a parameter) are commonly used to compare simulations of neutrally stratified Ekman flow; besides,
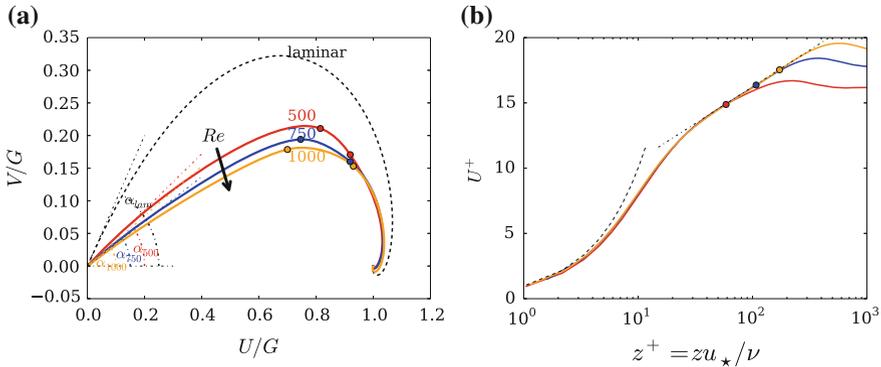

Fig. 5.6   a Hodograph. **b** Streamwise wind speed profile in semi-log space. Figure is for the neutrally stratified cases N500L (*red*), N750L (*blue*) and N1000L (*orange*) according to Table 6.1. In (**a**), the laminar case is shown as a *black dashed line*. The levels $z^+ = 15$ and $z^- = 0.12$ are marked by dots in the hodographs to illustrate the increase of scale separation from $Re = 500$ to $Re = 1000$. In (**b**), the viscous law of the wall ($u^+ = y^+$) and the logarithmic law $u^+ = \kappa^{-1} log(y^+) + A$ with $\kappa = 0.41$ and $A = 5.0$ are shown as *dashed black lines*. As in the hodograph, the level $z^- = 0.12$ is marked by a dot in the corresponding wind speed profile
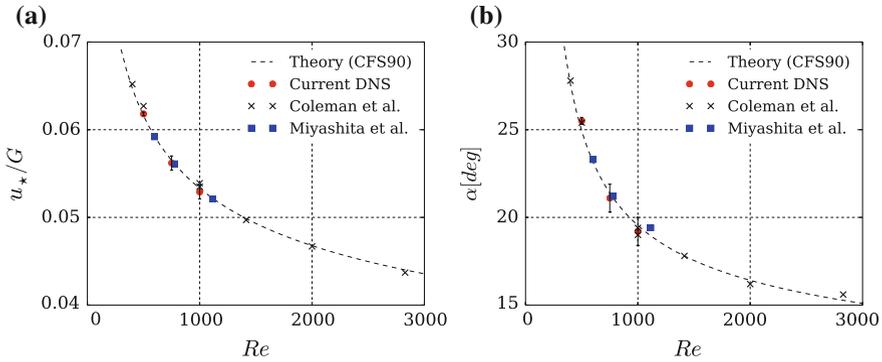
Fig. 5.7 Dependency on Re of the wall friction velocity $u_\star$ (**a**) and the turning angle α of the surface wind with respect to **G** (**b**) for the neutrally stratified configuration. Data is also compared with that available from other groups (Miyashita et al. refers to Miyashita et al. (2006); Coleman et al. and CFS90 refers to Coleman et al. (1990); Coleman (1999); Spalart et al. (2008)). The *dashed lines* show *curves* according to the higher-order theory derived in Spalart (1989). The best fit for the available data is obtained with $A = 5.9$, $B = 0.1$ and $C_5 = -30$ following the nomenclature of Coleman et al. (1990). Statistical uncertainty is estimated for the 'current DNS' from the variance in the time series of the respective quantities

they also give a first estimate of dependency on the Reynolds number. Figure 5.7 compares the values of $u_\star$ and α in the simulations with the semi-empirical 'prediction' as well as previous work, and shows that the three cases are within the uncertainty range of the data. For the current data (*current DNS*), the statistical uncertainties in estimates of $u_\star$ and α are estimated from the respective variance of their time series and shown as error bars in Fig. 5.7.

SIRK3 scheme The SIRK3 scheme was tested successfully for idealized cases (Sects. 5.1–5.3). For the turbulent case, the simulations with this scheme produce an offset in the direction of the friction velocity of about 4°. The reasons for this offset were not investigated further since it turned out that—even for the highest Reynolds number considered here, that is $Re = GD/\nu = 1000$—it is not economic to employ the SIRK3 scheme: The diffusion number is a less strong constraint on the time step than the Courant number.

References

Coleman, G. N., & Sandberg, R. D. (2010). A primer on direct numertical simulation of turbulence—Methods, Procedures and Guidelines. *Technical Report AFM-09/01b*, Aerodynamics & Flight Mechanics Research Group (School of Engineering Sciences, University of Southampton, SO17 1BJ UK), Southampton.

Coleman, G. N. (1999). Similarity statistics from a direct numerical simulation of the neutrally stratified planetary boundary layer. *Journal of the Atmospheric Sciences*, *56*(6), 891–900.

Coleman, G. N., Ferziger, J. H., & Spalart, P. R. (1990). A numerical study of the turbulent ekman layer. *Journal of Fluid Mechanics*, *213*, 313–348.

Ekman, V. W. (1905). On the influence of the earth's rotation on ocean currents. *Arkiv for Matematik, Astronomi Och Fysik*, *2*, 1–53.

Mellado, J.-P., & Ansorge, C. (2012). Factorization of the Fourier transform of the pressure-Poisson equation using finite differences in colocated grids. *ZAMM—Journal of Applied Mathematics and Mechanics / Zeitschrift für Angewandte Mathematik und Mechanik*, *92*(5), 380–392. doi:10.1002/zamm.201100078.

Miyashita, K., Iwamoto, K., & Kawamura, H. (2006). Direct numerical simulation of the neutrally stratified turbulent ekman boundary layer. *Journal of the Earth Simulator*, *6*, 3–15.

Spalart, P. R. (1989). Theoretical and numerical studies of a three-dimensional turbulent boundary layer. *Journal of Fluid Mechanics*, *205*, 319–340.

Spalart, P. R., Coleman, G. N., & Johnstone, R. (2008). Direct numerical simulation of the Ekman layer: A step in Reynolds number, and cautious support for a log law with a shifted origin (Retracted article. See, vol. 21, art. no. 109901, 2009). *Physics of Fluids*, *20*(10), 101507. doi:10.1063/1.3005858.

Williamson, J. (1980). Low-storage runge-kutta schemes. *Journal of Computational Physics*, *35*, 48–56.

Part III
Physics

Chapter 6
The Neutrally Stratified Ekman Layer
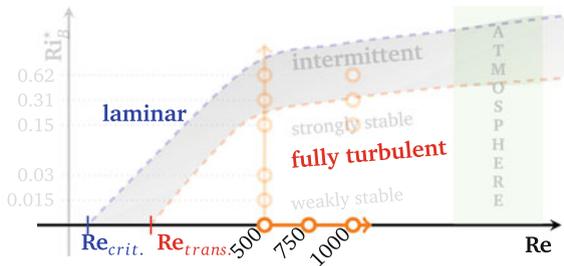
The neutrally stratified Ekman layer—used as initial condition and reference when studying effects of stratification (Chaps. 7 and 8)—is discussed in this chapter. To better differentiate the effect of stratification, the degree of Reynolds-number independence is ascertained in Sect. 6.1 with simulations at $Re = \{500, 750, 1000\}$ (Table 6.1; non-dimensional quantities are defined in Eqs. 2.11, 2.13a on pp. 17, 19). I demonstrate that these Reynolds numbers are well within the turbulent regime and sufficiently high to clearly distinguish between an inner and outer layer. The duality of available high-resolution data in time *and* space allows an estimate of the convergence of measurements with single-point probes (Sect. 6.2). This investigation unveils the presence of motions on large time scales in accordance with recent work on channel flow simulations.

A particular mode of large-scale organization in Ekman flow is external intermittency in the outer layer. This external intermittency, a property intrinsic to open boundary layers and a key difference of Ekman flow when compared to channel flows, is quantified in Sect. 6.3. The lower part of the externally intermittent region coincides with the logarithmic layer, and it is demonstrated here that external intermittency impacts on the logarithmic profile for the mean velocity (Sect. 6.3.3). When this impact is taken into account, a logarithmic profile for the mean velocity fits the

Table 6.1 Set-up of the simulations; L_{xy} is the domain size in the horizontal directions, L_z in the vertical direction, $\Delta(x, y)^+$ is the resolution in the streamwise and spanwise directions Ox and Oy

interval			$A_0(\mathbf{U})$	$\kappa(\mathbf{U})$	$A_0(\mathbf{U}|_{\text{turb}})$	$\kappa(\mathbf{U}|_{\text{turb}})$
40	$< z^+ <$	80	4.89	0.410	5.07	0.420
50	$< z^+ <$	100	4.95	0.413	5.15	0.423
60	$< z^+ <$	120	4.81	0.407	5.08	0.420
80	$< z^+ <$	160	4.46	0.400	4.89	0.413
100	$< z^+ <$	200	4.27	0.389	4.89	0.413

data over a three-times deeper range compared to when it is not taken into account. In this overlap region where the velocity profile conditioned to turbulent patches is logarithmic, spectral analysis and visual inspection (Sect. 6.4) of the flow fields unveil both a large-scale structure originating from the outer layer and small-scale hairpin vortices stemming from the buffer layer.

6.1 Conventional Statistics

6.1.1 Global Measures

Since the seminal work of Coleman et al. (1990), the wall friction velocity $u_\star$ as well as the turning angle α of the surface stress with respect to the geostrophic wind $\mathbf{G}$ are commonly used to compare simulations of neutrally stratified Ekman flows and provide a first estimate of their dependency on Re. Figure 5.7 compares the values of $u_\star$ and α with the semi-empirical theory of Spalart (1989) as well as previous work, and shows that they are within the uncertainty range of the data for the three cases considered here. It illustrates an $\mathcal{O}(1)$ variation in those global parameters with respect to an $\mathcal{O}(10)$ change in viscosity.

Further support for the relatively weak dependency on Re is obtained by the values of the vertically integrated turbulence kinetic energy (TKE, e) and the viscous dissipation rate (ε) shown in Table 6.2 for three Reynolds numbers, where e and ε are defined as follows:

Table 6.2 Global statistics as a function of the Reynolds numbers for the neutrally stratified configuration

Case:	N500L	N750L	N1000L
$u_\star/G$	0.0618	0.0561	0.0531
α	25.5	21.0	19.2
δ_{95}/δ	0.668	0.650	0.631
Re_t	203	407	655
$Re_\tau = \delta^+$	478	898	1399
$fG^{-3}\int_0^\infty e\,dz$	2.18×10^{-4}	1.64×10^{-4}	1.44×10^{-4}
$fu_\star^{-3}\int_0^\infty e\,dz$	0.0570	0.0521	0.0511
$G^{-3}\int_0^\infty \varepsilon\,dz$	1.31×10^{-3}	1.34×10^{-3}	1.32×10^{-3}
$u_\star^{-3}\int_0^\infty \varepsilon\,dz$	5.53	7.58	8.85

The integrals are performed over the entire vertical range of each case. δ_{95} refers to the level at which $\sqrt{\overline{\langle uw \rangle}^2 + \overline{\langle vw \rangle}^2} = 0.05u_\star^2$, e and ε as defined in Eq. (6.1). $Re_t := \max_z \{e^2/(\nu\epsilon)\}$ is a Reynolds number introduced for isotropic turbulence and Re_τ as defined in Eq. (2.12)

$$e := \overline{\left\langle \frac{u_i' u_i'}{2} \right\rangle} \tag{6.1a}$$

$$\varepsilon := \nu \overline{\left\langle \frac{\partial u_i'}{\partial x_j}\left(\frac{\partial u_i'}{\partial x_j} + \frac{\partial u_j'}{\partial x_i}\right) \right\rangle}. \tag{6.1b}$$

The reader is reminded that $\langle \cdot \rangle$ and $\overline{(\cdot)}$ denote the average over a horizontal plane and the time respectively. The viscous dissipation rate is found here to scale independently of Re when normalized with the geostrophic forcing G whereas the energy does so approximately when normalized with $u_\star^2$. This further illustrates only slight changes in the organization of the flow while the viscosity varies by a factor of four. In summary, these statistics indicate that despite the comparatively low Re, the system is well within the turbulent regime.

6.1.2 Vertical Profiles

Velocity hodographs (Fig. 5.6a) also illustrate that the dependency on Re is relatively small; in particular the change from $Re = 750$ to $Re = 1000$ is much smaller than the change from $Re = 500$ to $Re = 750$. At the wall and in the inner layer (below $z^+ = 100$) the inviscid scaling of ε is recovered (Fig. 6.1b). In the outer layer, the dissipation decreases as $(z^+)^{-0.5}$, and when expressed in wall-units the layer over which this happens grows as δ^+. Beyond the inner layer, $\varepsilon^+(z^+)$ is not quite self-similar—the inner scaling is inappropriate. If instead the outer scaling $\varepsilon^-(z^-)$ is used, self-similarity independent of Re is also observed in the outer layer ($0.1 < z^- < 1$, Fig. 6.1).

(a)   **(b)**
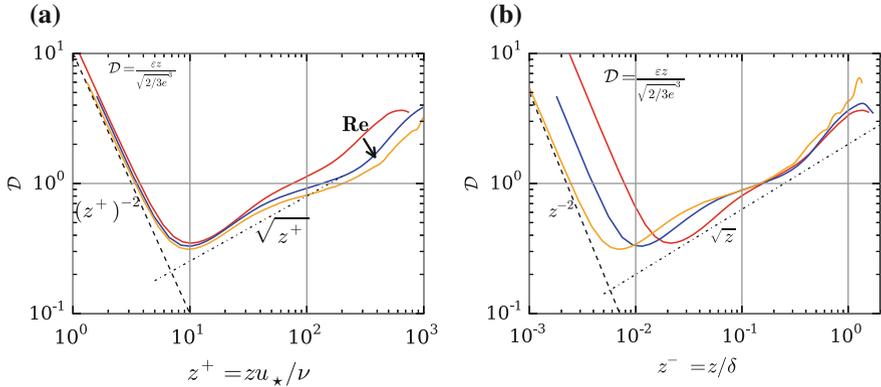
Fig. 6.1 Normalized dissipation for the series of simulations N500L (*red*), N750L (*blue*) N1000L (*orange*). **Panel a** shows the height z^+ normalized with the wall unit, **panel b** shows the height z^- normalized with the boundary layer depth scale δ

From scaling arguments it was concluded that the rotation of wind does not impact properties in the surface layer other than by constant, i.e. height-independent, shift of direction with respect to the free atmosphere (Blackadar and Tennekes 1968; Tennekes 1973). Hence, provided a high enough Re, the surface layer of an Ekman flow can be treated as that of a channel flow, and a logarithmic wind profile develops.

Attempts have been undertaken to obtain the logarithmic law and associated constants for Ekman flow at Reynolds numbers as high as $Re = 2828$ (Spalart et al. 2008, 2009). The slope of the velocity U^+ is approximately constant around $z^+ = 30$ for the three Reynolds numbers considered here (Fig. 5.6b); this agrees with Coleman (1999) and Miyashita et al. (2006). In accordance with Tennekes (1973), the height of departure from the logarithmic law for the three cases coincides with the height at which the velocity begins to turn significantly (see markers at $z^- = 0.12$ in Fig. 5.6b). This logarithmic variation supports the analogy with channel flows, which have been studied in great detail. I will show later how and to what extent the rotation and vertical asymmetry of the flow nonetheless impact on statistics inside the logarithmic layer (Sect. 6.3.3).

Beyond the mean profiles, similarity with channel flow in the inner layer is also found in the TKE budget terms as confirmed by Fig. 6.2a. Irrespective of Re, the production of TKE peaks in the buffer layer, around $z^+ = 12$, and so does the removal by turbulent transport. At the wall, all energy is provided by diffusive downward transport of energy that dissipates locally. The upward transport of TKE away from the production region is caused by turbulent convection. Above $z^+ = 30$, the TKE budget is dominated by a balance between production and dissipation. Contributions to the TKE budget in the outer layer, normalized such that at any level the sum of their squares equals one, are shown in Fig. 6.2b. The change from the production-dominated to the transport- dominated regime, both balanced by viscous dissipation, occurs at $z^- \simeq 0.5$. This is about 20 % lower than in a non-rotating boundary layer
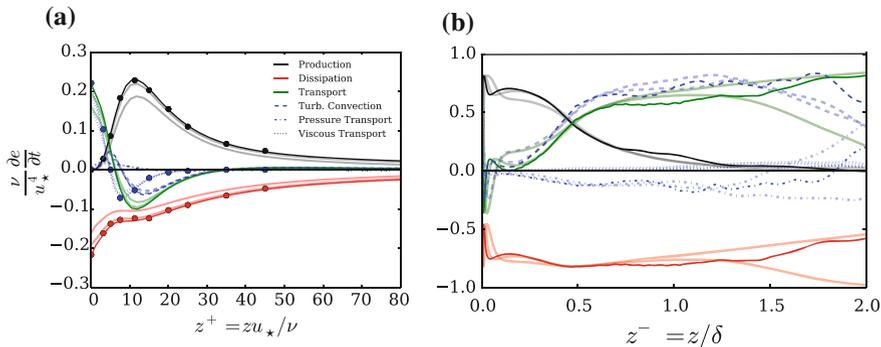
Fig. 6.2 **a** Budgets of the evolution equation for e in the inner layer of the cases `N1000` (*solid*) and `N500`, `N750` (*opaque*). Circles show data from channel flow (Pope 2000, Fig. 7.34, p. 314). **b** Relative contribution in the outer layer. The terms are normalized with their sum of squares at each height

(Pope 2000, Fig. 7.34), and might hint at the fact that the outer scale δ has to be adapted by an order-unity constant (possibly $\delta_{95}/\delta \approx 2/3$) when quantitatively comparing Ekman flow to non-rotating flows.

6.2 Local Versus Ensemble Statistics

In the above sections of this chapter, only data averaged horizontally over the whole computational box have been discussed. Not only are such data conveniently obtained from numerical simulations (the storage of the full computational domain is necessary for technical reasons) but also does the ergodicity assumption imply that these averages converge to the ensemble average in a sufficiently large box. On the contrary, in field observations, it is hardly possible to obtain spatially resolved data with an accuracy sufficient to process turbulence quantities. (Significant advances have been made very recently in obtaining spatially resolved data at a quality that is sufficient for the investigation of turbulence properties (Träumner et al. 2014).) Instead, virtually all studies on physical aspects of the planetary boundary layer resort to the processing of time signals mostly obtained from towers at fixed locations. The interpretation of turbulence signals from such tower-data relies on the stationarity of the time signal and Taylor's hypothesis (Taylor 1938).

Taylor's hypothesis is essential if length scales are estimated from single-point probes. It postulates: In flows where the turbulence intensity is small in comparison with the mean flow, the signal obtained from a fixed-in-space probe can be converted to a spatial measurement via a convection velocity. The presence of large-scale turbulent motion calls this into question (del Àlamo and Jiménez 2009; Moin 2009).

A second problem with relation to measurements at fixed locations is the non-stationarity of external parameters; external in this context refers to *external to turbulence as described by the Navier–Stokes equations* in Chap. 2—for example a daily cycle, synoptic perturbations or micro-physical processes. A convenient way around the problem of non-stationarity is the idea of a scale separation between external scales and internal ones. This concept of a scale separation between temporal and spatial scales of external parameters and the turbulence itself was introduced by Van der Hoven (1957) as the *spectral gap*. While this concept is of indubitable utility for theoretical and conceptual work, both high-resolution measurements and also recent LES (Schalkwijk et al. 2015) call into question to what degree this scale separation actually exists. A whole research community is investigating the so-called meso-scale or gray-zone regime where turbulence and large scales are expected to interact (Wyngaard 2004). While the motivation of this research is mainly a quenching of the *spectral gap* from its large-scale end, one may ask the question: What about the lower end of this gap? In fact, recent work in fluid dynamics has proven the existence of very-large-scale motions in turbulence (del Àlamo and Jiménez 2003, also Sect. 6.4). Also in the planetary boundary layer, low-frequency signals in the vertical velocity have been observed (Ouwersloot et al. 2009). These scales are inherent to turbulence, and as such do not depend on external forcing.

A time-resolved probing as introduced in Sect. 2.3.2 is employed here to estimate how these large-scale motions impact the turbulence signal of a single-point probe and its convergence to the ensemble average. While it does not eliminate problems of the understanding of phenomena at the large-scale end of the *spectral gap*, this analysis is potentially useful in the interpretation of turbulence measurements: It may give quantitative hints as to how much turbulent flux is actually lost by the common time-slicing of field measurements. The subsequent analysis is tightly related to a spectral analysis of the flow and also structure functions of the turbulent flow (Finnegan and Kaimal 1994); the way of presenting data here is chosen as in the author's opinion it represents data in a very accessible way and can facilitate a discussion on these issues between fundamental turbulence research and applied meteorology.

6.2.1 Data Analysis Procedure

I investigate in the following, how well the average over a finite time at a fixed location converges to the ensemble average.[1] That is: Under what circumstances, and to what degree of accuracy, is

$$\langle \mathbf{x}(z) \rangle \sim \overline{x_i(z)}^T \tag{6.2}$$

---

[1]The same notation is used for spatial and ensemble averages. In general, this only holds for the expected value, but not for individual realizations. For large computational boxes, however, the ensemble and horizontal averages are identical as a consequence of the ergodicity of the flow.

true? Here, $\mathbf{x}(z)$ is some local observable, and $\overline{\mathbf{x}_i(z)}^T$ denotes the average over a period of time T of a single-point probe at height z above the horizontal location r_i (Sect. 2.3.2). While the expected value of the right-hand side of Eq. (6.2) is identical to the ensemble average, individual realizations of this right-hand side need not coincide with the ensemble average. The spatial separation of individual realizations by approximately one boundary-layer depth scale δ_{95} allows us to consider them independent realizations such that a standard deviation among the towers can be computed:

$$\sigma_{\mathbf{x(z)}}(T) = \sqrt{\sum_{i=1}^{M} \left(\overline{\mathbf{x}_i(z)}^T - \langle \mathbf{x}(z) \rangle \right)^2} \tag{6.3}$$

where $T \in \mathbb{R}$ is the averaging period, and $M \in \mathbb{N}$ is the number of towers available. Assuming M is large enough, and individual samples are sufficiently de-correlated, in space $\sigma_{\mathbf{x}(z)}(T)$ is the expected error of $\overline{\mathbf{x}_i(z)}^T$ as a representation of $\langle \mathbf{x}(z) \rangle$. For any time-discrete random process R over $\mathbb{N}$, it is $\sigma_R(T) \propto T^{-1/2}$.

6.2.2 Convergence of local estimates to the ensemble mean

The present data indicate a rather slow cessation of the standard error in single-probe estimates when the averaging period increases, pointing at the necessity for
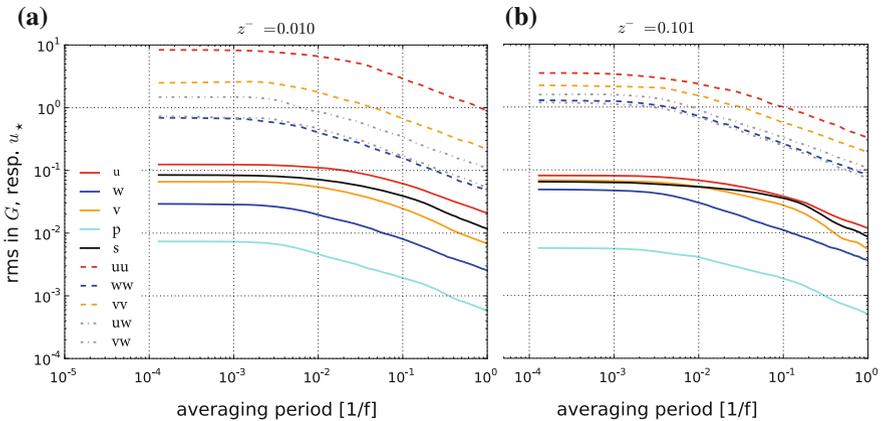
Fig. 6.3 Expected error in an estimate from a single-point probe as a function of the averaging period (case N1000L). Fluxes are normalized by $u_\star^2$ such that the error is relative to the surface friction; U, V, W are normalized by the geostrophic wind, the (passive) scalar is normalized by the bulk difference, and the pressure by the geostrophic pressure gradient. **Panel a** shows convergence at the lower end of the surface layer ($z^- = 0.01$ with δ the boundary layer depth). **Panel b**, ($z^- = 0.10$) shows the overlap (logarithmic) region between inner and outer layer
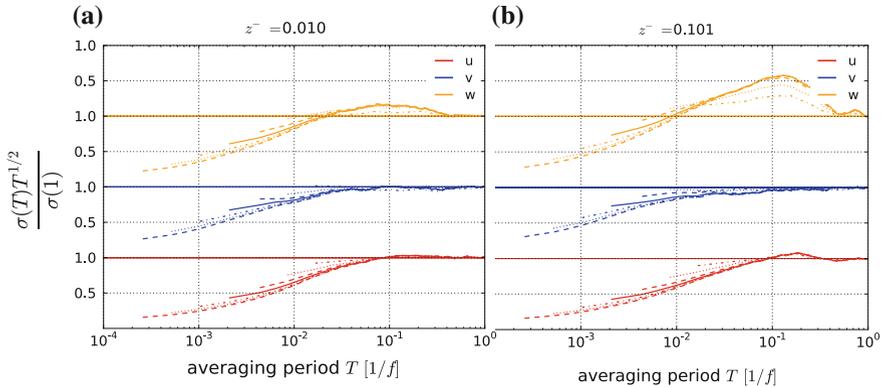
Fig. 6.4 Standard deviation multiplied by the square root of the averaging time and normalized by the standard deviation at $T = f^{-1}$: $\sqrt{T}\sigma(T)/\sigma(1)$. **Panel a** shows convergence at the lower end of the surface layer ($z^- = 0.01$), **panel b**, ($z^- = 0.101$) the overlap (logarithmic) region between inner and outer layer. Data are shifted along the vertical axis for better visibility. *Solid straight colored lines* correspond to a hypothetic and densely sampled random process with variance $\sigma(1) = 1$. Different line styles correspond to a different sampling rate in time where the first value of each *line* is twice the sampling rate in time

long averaging intervals—even very close to the surface (Fig. 6.3). When the averaging period approaches one eddy-turnover time (which is easily on the order of 20 min to an hour under atmospheric conditions) the error in the mean velocity in the lower surface layer ($z^- = 0.01$) is 2 % of the free-stream velocity magnitude. While this is acceptable given the precision of flux measurements in field conditions, short averaging periods, for instance when only a quarter of the eddy-turnover is covered, can easily yield errors of 10 %. Also for the vertical velocity, it is on the order of 1 % which is interesting with respect to tilt corrections commonly carried out for SONIC anemometers where the local coordinate system is oriented so as to obtain zero vertical velocity on average; such errors propagate strongly into other velocity components. At the larger end of sampling intervals, it is $\sigma \propto T^{-1/2}$ (for $T > 0.5/f$, Fig. 6.3), i.e. the process behaves like a random process, that is, decorrelated in time. These deviations from the square-root decay of the standard error stick out more clearly when the data is plotted to compensate for this decay as in Fig. 6.4. Deviations from a random signal for $Tf < 0.5$ illustrate the memory of the turbulence signal. As such, these deviations are a means to quantify the memory's impact on measurements in the surface layer. This structure occurs at a time scale $Tf \simeq 0.1 - 0.3$ corresponding to a wave length (using Taylor's hypothesis with a convection velocity of $G = u_\star/0.0529$ for the case N1000L) around $2 - 6\delta$.

While errors in the mean variables are random, the estimation of fluxes suffers systematically—they are underestimated since an error in the mean profile due to fluctuations always decreases the fluctuation estimate based on the erroneous mean value. The fluxes have shorter de-correlation times than the mean values as seen from an earlier change to the power-law decay in Fig. 6.3, which sets in already for
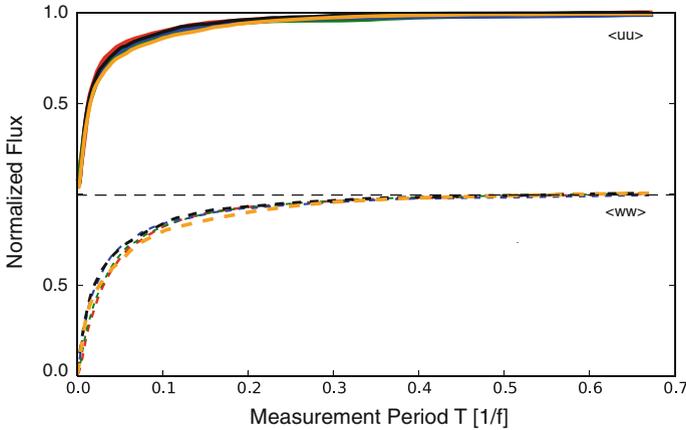
Fig. 6.5 Expected value of the turbulent flux estimated from a single-point probe as a fraction of the ensemble mean turbulent flux at various heights. *Upper part* shows streamwise Reynolds stress, *lower part* shows vertical Reynolds stress

averaging periods $Tf \simeq 2 \times 10^{-3}$ compared to $Tf \simeq 2 \times 10^{-2}$ for the streamwise and spanwise velocities. The bias in the fluxes behaves very similar to the error in the mean values such that the flux estimate from a single-point probe increases with the length of the averaging interval (Fig. 6.5). The bias is on the order of 10 % when averaging over one tenth of the inertial period, and it decreases to around 1 % for an averaging period of length $Tf \approx 1$.

6.3 External Intermittency and Its Impact in the Surface Layer

6.3.1 Definition of external intermittency

The occurrence of large-(time)-scale motions demonstrated in the above Sect. 6.2 is another similarity of the surface layer of Ekman flow with that of channel flow. Despite the qualitative and quantitative agreement with channel flows in many other statistics (Sects. 6.1.1 and 6.1.2), Ekman flow is not bound by an upper solid wall, i.e. it is an external flow. For the non-rotating configuration, Jiménez et al. (2009) find that *the outer flows of boundary layers and channels are intrinsically different*. It is hence expected here that the outer layer of Ekman flow differs from that of both channel flow and a non-rotating boundary layer. In the outer layer of Ekman flow, the wind rotates with height, and non-turbulent fluid is entrained into the boundary layer. This entrainment causes the coexistence of strongly vortical patches adjacent

to much less vortical ones in the outer layer, a property termed external intermittency (Chap. 1).

External intermittency is widely studied for non-rotating boundary layers since the seminal work by Corrsin and Kistler (1955). They introduce the intermittency function

$$\gamma(z) := \overline{\langle H(\omega^2 - \omega_0^2)\rangle}, \tag{6.4}$$

where ω is the vorticity, H is the Heaviside function, and $\overline{\langle \cdot \rangle}$ denotes averaging along planes and in time. $\gamma(z)$ is the fraction of the domain at a given height z exceeding a threshold of enstrophy ω_0, and $\gamma(z)$ is known to be a useful measure of the turbulent area fraction in the outer part of external flows (Kovasznay et al. 1970).

6.3.2   A Vorticity Source in the Outer Layer

In Fig. 6.6a the intermittency function $\gamma(z)$ is shown varying the threshold ω_{thresh} from 0.2 to 10 % of the maximum enstrophy within the domain. In other external flows, the enstrophy often drops by three or more orders of magnitude at the turbulent–non-turbulent interface (Kovasznay et al. 1970; Bisset et al. 2002; Mellado et al. 2009), which deems $\gamma(z)$ independent of the choice of the threshold ω_{thresh} within a certain range. In the present case of Ekman flow, however, γ strongly depends on this threshold. The much less pronounced drop in enstrophy at the turbulent–non-turbulent interface is not a low-Reynolds-number effect, but rather a fundamental property of Ekman flow caused by the rotation of the reference frame and distinguishing it from non-rotating configurations.

The vorticity equation for Ekman flow reads as

$$\frac{\partial \boldsymbol{\omega}}{\partial t} + (\mathbf{u} \cdot \nabla)\boldsymbol{\omega} = (\boldsymbol{\omega} \cdot \nabla)\mathbf{u} + \nu \nabla^2 \mathbf{u} + 2(\boldsymbol{\Omega} \cdot \nabla)\mathbf{u} + 2(\mathbf{u} \cdot \nabla)\boldsymbol{\Omega} \tag{6.5}$$

where $\boldsymbol{\omega} := \nabla \times \mathbf{u}$ and $\boldsymbol{\Omega}$ is the planetary rotation. It is readily seen that the planetary rotation $\boldsymbol{\Omega}$ constitutes a source term in this budget, and rewriting Eq. (6.5) in tensor notation, one can use the f-plane approximation to replace $2\boldsymbol{\Omega} \equiv 2f\hat{e}_z$:

$$\frac{\partial \omega_i}{\partial t} + u_j \frac{\partial \omega_i}{\partial x_j} = \omega_j \frac{\partial u_i}{\partial x_j} + \nu \frac{\partial^2 \omega_i}{\partial x_j^2} + f \frac{\partial u_i}{\partial z}. \tag{6.6}$$

Compared with the non-rotating reference frame, there is the additional source $f\partial_z u_i$ representing vortex stretching of planetary vorticity by a vertical gradient of streamwise velocity. This term is also present in the enstrophy equation:

$$\frac{1}{2}\frac{d\omega_i^2}{dt} = \omega_i\frac{\partial u_j\omega_i}{\partial x_j} + \frac{1}{2}\nu\left[\frac{\partial^2\omega_i^2}{\partial x_j^2} - 2\left(\frac{\partial\omega_i}{\partial x_j}\right)^2\right] + f\omega_i\frac{\partial u_i}{\partial z}. \quad (6.7)$$

In the absence of vorticity, according to Eq. (6.6), the sign of ω_i becomes that of $f\partial_z u_i$ making the last term of the right-hand side of Eq. (6.7) a source of enstrophy. This means that in the presence of even weak velocity gradients in the irrotational region of Ekman flow, the stretching and tilting of planetary vorticity generate mean vorticity and vorticity r.m.s. at a rate proportional to the velocity gradient $\partial_z u_i$ and the Coriolis parameter f. At some level of vorticity this process is balanced by dissipation; until this happens, vorticity is accumulated in the non-turbulent part of the boundary layer causing a background enstrophy that smears out the jump in enstrophy magnitude between turbulent and non-turbulent parts when compared to other (non-rotating) flows. The Re-independence of $\langle u(z)\rangle$ (cf. Sect. 6.1.2) in the outer layer suggests that the term $f\langle\omega_x\rangle\partial_z\langle u\rangle$ scales inviscid, and this mechanism is independent of the Reynolds number. The inviscid scaling is indeed manifest in the small sensitivity of $\gamma(z)$ to Re shown in Fig. 6.6b. It is concluded that this vortex tilting, irrespective of Re, is a fundamental mechanism in Ekman flow rendering the outer, non-turbulent layer different from non-rotating external flows.

Even though the vortex-tilting mechanism discussed above scales inviscid, it deems the choice of a vorticity threshold delicate. $\omega_0 = \omega_{rms}(\delta)$, the r.m.s. of vorticity $\sqrt{\langle\omega'^2\rangle}$ at $z = \delta$ is chosen here as reference vorticity for the turbulent–non-turbulent distinction for three reasons. First, this level—according to classical definitions of the boundary-layer height such as δ_{95} (Table 6.2)—is well outside the part that is considered turbulent. Second, it is $\overline{\langle u_i u_i\rangle} \propto z^{-4}$ for $0.75 \lesssim z^- \lesssim 2$ (not shown), which is a signature of potential flow aloft a turbulent boundary layer (Phillips 1955). Third,
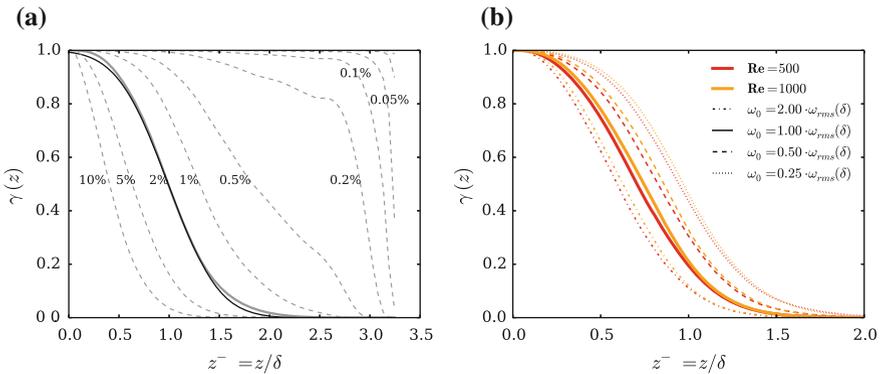

Fig. 6.6 **a** Intermittency factor versus height varying the intermittency threshold by several orders of magnitude (case N1000L) **b** Intermittency factor versus height for (case N500L–*red* and N1000L–*orange*) where the threshold ω_0 expressed in terms of the vorticity r.m.s. at $z = \delta$ is varied by a factor of 4 (note that the variation in Re from 500 to 1000 also corresponds to a variation of ν by a factor of 4)

the resulting profile $\gamma(z)$ (Fig. 6.6) is similar to that found in non-rotating boundary layers (Kovasznay et al. 1970).

6.3.3 A Modified Logarithmic Law for the Mean Velocity

The definition of a discriminator between turbulent and non-turbulent regions of the flow allows for the use of conditional statistics (Sect. 2.3.1). It enables a separation of turbulent from non-turbulent contributions to bulk quantities of the flow which is useful for a process-oriented study of the flow based on fundamental principles. Such a separation is important, in particular in the outer layer where the variation of mean properties between turbulent and non-turbulent patches can contribute significantly to the variances (Pope 2000, Eq. (5.306)). (The case where the non-turbulent partition of the flow extends down to the surface layer is considered in Chap. 8.)

The logarithmic law is based on a similarity argument for the vertical gradient of stream-wise velocity in the surface layer which is often expressed as

$$\frac{\partial U^+}{\partial z^+} = \frac{1}{\kappa z^+} \tag{6.8a}$$

(cf. Prandtl 1961; Von Kármán 1930; Zanoun et al. 2003). Given a velocity profile, κ can be estimated as

$$\hat{\kappa}_{\text{diff}} = \frac{\partial \ln z^+}{\partial U^+}. \tag{6.8b}$$

Such an estimation of κ poses challenges beyond the availability of data at only moderate Reynolds number (Spalart et al. 2009). The main issue when estimating κ directly is a strong decline from $\kappa(z^+ \simeq 50) \simeq 0.42$ to $\kappa \simeq 0.38$ at the upper end of the logarithmic layer. Spalart et al. (2008) proposed that a shifted origin for the logarithmic law yields a much better fit, but rejected this hypothesis later (Spalart et al. 2009). A possible physical interpretation of this dip is the effect of the super-geostrophic wind maximum in Ekman flow located around $z^- \sim 0.2$ (cf. Fig. 5.6), which corresponds to $z^+ \approx 300$ for the Re achieved here. Another possible reason is that in this range of heights, the flow is externally intermittent—a fundamental difference to channel flow for which the law was originally derived. Within non-turbulent sub-volumes of the flow, the application of a logarithmic law is not meaningful.

In a laboratory context, with regard to atmospheric measurements, and when it comes to the parameterization of mean-velocity profiles, the integrated form of Eq. (6.8a) is often more practical: Integration of Eq. (6.8a) over z^+ yields

$$U^+ = \frac{1}{\kappa} \ln z^+ + \mathscr{A}_0, \tag{6.9a}$$

and allows to locally estimate κ as
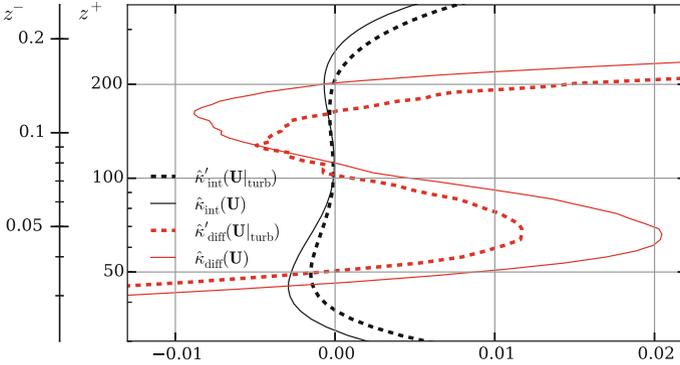
Fig. 6.7 Deviation of the estimates for the von-Kármán constant based on the optimal value for the range $80 < z^+ < 160$ (cf. Table 6.3). Estimates $\hat{\kappa}_{\text{int}}$ based on the integral formulation (Eq. 6.9a) are shown in *black*, estimates $\hat{\kappa}_{\text{diff}}$ based on the differential formulation in *red*. Thick, dashed lines are based on averages conditioned to turbulent patches $(U|_{\text{turb}})$ and *thin solid lines* show conventional averages (U)

$$\hat{\kappa}_{\text{int}} = \frac{\ln z^+}{U^+ - \mathscr{A}_0}. \tag{6.9b}$$

As a consequence of the integration, Eq. (6.9b) includes the additional unknown parameter $\mathscr{A}_0$ representing the lower boundary condition for the logarithmic layer. While $\mathscr{A}_0$ is a physically relevant and geometry-related parameter for the mean velocity profile, it is unrelated to the fundamental problem of determining the von-Kármán constant. We estimate here $\mathscr{A}_0$ together with κ from a least-square fit of the velocity profiles versus the ideal logarithmic profile (Eq. (6.9a)). By construction, this approach also yields an estimate for the optimal value of κ which is consistent with the differential formulation (Eq. 6.8a).

Taking into account external intermittency. The effect of external intermittency on the logarithmic law can be taken into account by conditioning the mean velocity profile to the turbulent sub-volumes only. As a threshold to discern turbulent from non-turbulent regions within the logarithmic layer, we use here $\omega_0 = 2\,\omega_{\text{rms}}(\delta_{95})$, but in a qualitative way, the findings put forward also hold for ω_0 in the range $1/8 < \omega_0/\widetilde{\omega} < 1$. When considering the conditioned profiles, both estimates for κ (Eqs. 6.9b and 6.8b) vary less with height in the region $50 < z^+ < 200$ as seen in Fig. 6.7. In particular, the problematic decline of the estimate for $\hat{\kappa}_{\text{diff}}$ is reduced by about 50 % when only the turbulent fraction of the domain is considered. We propose hence the modified logarithmic law

$$U_{\text{turb}}^+ = \frac{1}{\kappa} \ln z^+ + \mathscr{A}_0. \tag{6.10}$$

Using the velocity conditioned to the turbulent regions of the flow, this formulation takes into account effects of external intermittency in the logarithmic layer of the flow. The considerable improvement of the estimator for the von-Kármán constant,

κ_{diff}, provides strong evidence that the failure to establish a plateau in $\kappa_{\text{diff}}(z^+)$ is, at least partly, an effect of the entrainment of non-turbulent fluid into the logarithmic layer. As such, this effect is intrinsic to Ekman flow however high the Reynolds number and, contrary to possible other mechanisms with impact on the logarithmic law at intermediate Reynolds numbers, cannot be expected to cede when Re is further increased. [In fact, the shifted-origin hypothesis for the logarithmic law put forward by Spalart et al. (2008) seems now again a lot more attractive than it appeared in the light of the findings in Spalart et al. (2009)].

While actually a consequence of external intermittency, this modification can be interpreted in analogy to a wake-law, but it extends deep into the logarithmic layer. When rewritten in terms of the actual velocity profile, i.e. including the non-turbulent regions, our findings suggest the formulation

$$U^+ = \frac{1}{\kappa} \ln z^+ + \mathscr{A}_0 + f_{\text{ext. int.}}(z^-, z^+), \qquad (6.11)$$

where $f_{\text{ext. int.}}$ can be interpreted as a wake function representing the effect of external intermittency and is exactly prescribed by the difference $U^+ - U^+_{\text{turb}}$ of the average wind speed in the conditioned and unconditioned fields. Similarity properties and the exact dependency of the function $f_{\text{ext. int.}}$ on the non-dimensional heights z^- and z^+ need to be identified. [Given the findings presented in this work, parameterizing $f_{\text{ext. int.}}$ through a universal intermittency function γ seems an attractive approach.]

With regards to absolute values of the parameters related to the logarithmic law, our conventional mean velocity profiles support values for κ in the range [0.39, 0.41]—depending on the height range from which they are estimated (Table 6.3). When the

Table 6.3 Estimates from conventional and conditioned velocity profiles for A_0 and κ based on a least-squares fit

Case:	N500L	N750L	N1000L
$u_\star/G$	0.0618	0.0561	0.0531
α	25.5	21.0	19.2
δ_{95}/δ	0.668	0.650	0.631
Re_t	203	407	655
$Re_\tau = \delta^+$	478	898	1399
$f G^{-3} \int_0^\infty e\,dz$	2.18×10^{-4}	1.64×10^{-4}	1.44×10^{-4}
$f u_\star^{-3} \int_0^\infty e\,dz$	0.0570	0.0521	0.0511
$G^{-3} \int_0^\infty \varepsilon\,dz$	1.31×10^{-3}	1.34×10^{-3}	1.32×10^{-3}
$u_\star^{-3} \int_0^\infty \varepsilon\,dz$	5.53	7.58	8.85

The fitted region varies according to the column 'interval'. The column with reference values to Fig. 6.7 is colored gray

non-turbulent patches are excluded from the field, the estimate of κ increases as a consequence of the lower velocity $U_{\text{turb}}^+ < U^+$ appearing in the denominator of the estimators for κ. Along with an increasing effect of external intermittency, this impact increases with height: The impact on κ of using the conditioned profile instead of the conventional averages is a 2 % increase when estimated for $50 < z^+ < 100$, but already a 6 % increase when estimated for $120 < z^+ < 240$. When using the conditioned profile, dependency of both $\mathscr{A}_0$ and κ on the height range from which they are estimated decreases and the data only support the reduced range $[0.41, 0.42]$ for the von-Kármán constant. We interpret this reduced uncertainty in κ as a consequence considering an additional relevant physical mechanism in the logarithmic layer of the flow.

The error in estimating the von-Kármán constant. Given the high degree of accuracy in recent boundary layer measurement techniques such as particle-image velocimetry and volume-resolved laser–Doppler anemometry, it is rather surprising that there is still an uncertainty of the order of 10 % in the actual value of κ (Bailey et al. 2014). Analysis of both the partitioned and unpartitioned data allows to quantify the correlation between the boundary constant $\mathscr{A}_0$ and the estimate of the von-Kármán constant κ from a velocity profile. The strong dependency found below shows that an estimation of κ alone is probably not meaningful, and that the wide range of estimates for the value in κ can be explained through the correlation between κ and $\mathscr{A}_0$.

The logarithmic law for the mean velocity

$$U^+ = \frac{1}{\kappa} \ln z^+ + \mathscr{A}_0 = \frac{1}{\kappa} \ln \left(\frac{z^+}{e^{-\kappa \mathscr{A}_0}} \right) \tag{6.12}$$

is only valid over a finite layer, which means, besides the non-dimensionalized velocity gradient κ, a second unknown, $\mathscr{A}_0$, the lower integration bound comes into play. As seen in Eq. (6.12), $\mathscr{A}_0$ can be recast to a non-dimensionalized scale height z_0 for the logarithmic layer, and it is $z_0^+ = e^{-\kappa A_0} \approx 1/8$.
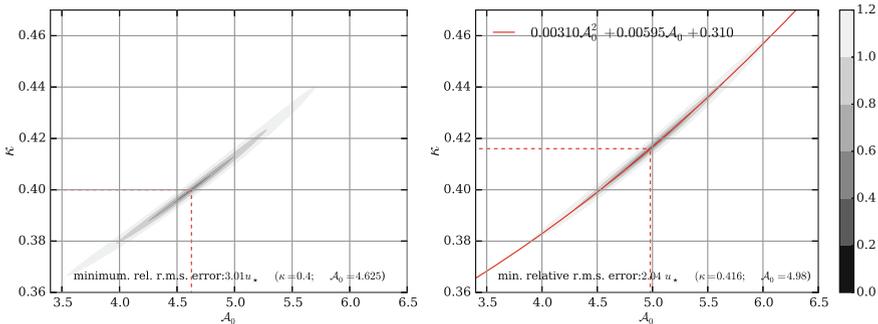
Fig. 6.8 Shading of relative L_2 error as defined in Eq. (6.13) of the logarithmic fit for $40 < z^+ < 200$ with respect to the conventional mean velocity (*left panel*) and the mean velocity U_{turb} conditioned to the turbulent sub-volumes (*right panel*)
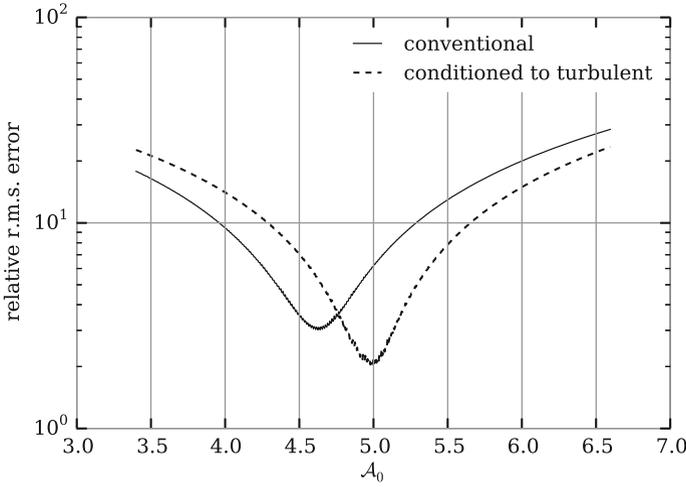
Fig. 6.9 Error $\epsilon_{L_2}(\hat{U})$ for the optimal in the value of κ as a function of $\mathscr{A}_0$. The very narrow but elongated region of small errors indicates a strong correlation between the two fundamentally independent parameters

The L_2 error in Figs. 6.8 and 6.9 is calculated as

$$\epsilon_{L_2}(\hat{U}^+)|_{\kappa,\mathscr{A}_0} = \frac{||\hat{U}^+ - (\kappa^{-1}\ln z^+ + \mathscr{A}_0)||_{L_2}}{||\hat{U}^+||_{L_2}} = \frac{\int_{z_{\min}}^{z_{\max}}\left[\hat{U}^+ - \left(\frac{\ln z^+}{\kappa} + \mathscr{A}_0\right)\right]^2 \mathrm{d}z^+}{\int_{z_{\min}}^{z_{\max}}(\hat{U}^+)^2\mathrm{d}z^+},$$

(6.13)

where $\hat{U}$ is a profile obtained from the simulation `N1000L`. A very strong correlation between the optimal κ and $\mathscr{A}_0$ is evident in Fig. 6.8. This correlation is a consequence of the logarithmic law itself since κ and $\mathscr{A}_0$ are not uncorrelated in the estimate for the von-Kármán-constant κ:

$$\hat{\kappa}(z^+) = \frac{\ln z^+ + \mathscr{A}_0}{U^+}.$$

(6.14)

This persistent correlation may be one reason for the spread of estimates for the von-Kármán constant. When estimated from a profile $U^+(z^+)$ (instead of the derivative $\partial U^+/\partial z^+$), it cannot be estimated alone, but has always to be measured in conjunction with the lower boundary condition for the logarithmic layer, $\mathscr{A}_0$. It is

$$\frac{A_0}{\kappa}\frac{\partial \kappa}{\partial A_0} \approx 0.5$$

(6.15)

around $A_0 = 5.0$, a common value for $\mathscr{A}_0$. This means, a 10 % change in $\mathscr{A}_0$ imposes a 5 % change on estimates of κ.
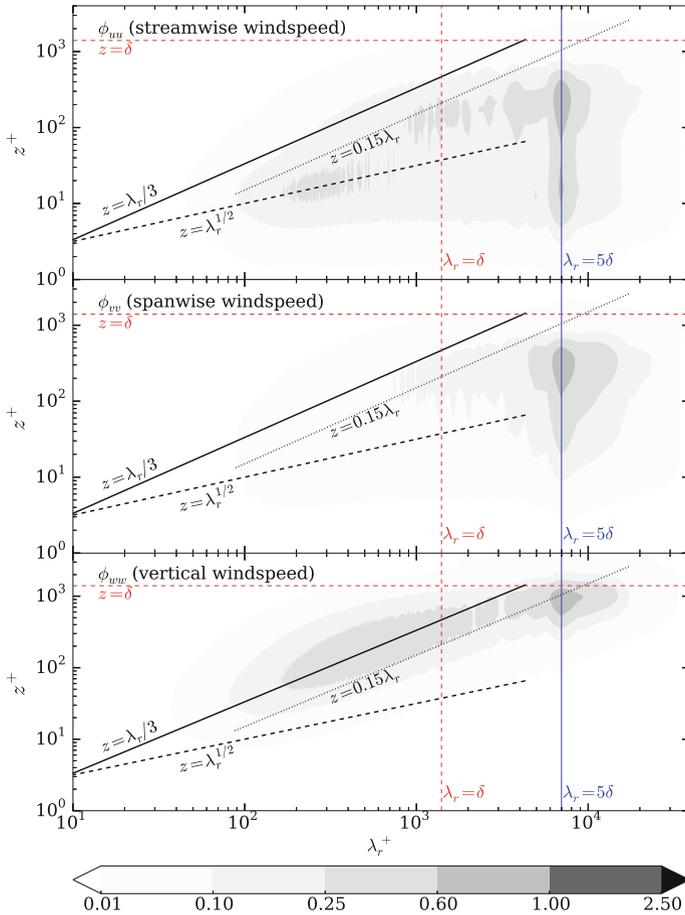
Fig. 6.10 Radial power spectral density of the neutrally stratified case $N1000L$; *upper panel* shows streamwise velocity component, *central panel* spanwise and *lower panel* the *vertical* component

6.4 Flow Synopsis

This chapter concludes with a visual description of the flow in terms of spectra of the three velocity components and slices of the enstrophy. Altogether those encompass many of the aspects discussed throughout this chapter.

The vertical structure suggested by the intermittency factor $\gamma(z)$ is consistent with a visual inspection of the flow enstrophy fields (Fig. 6.11). The strongly vortical regions adjacent to the surface (Fig. 6.11a, b) are typical of wall-bounded flows and indicate the level of the buffer layer. In the buffer layer, vorticity is mainly associated with so-called surface streaks (Fig. 6.11c). Ejections of turbulent fluid
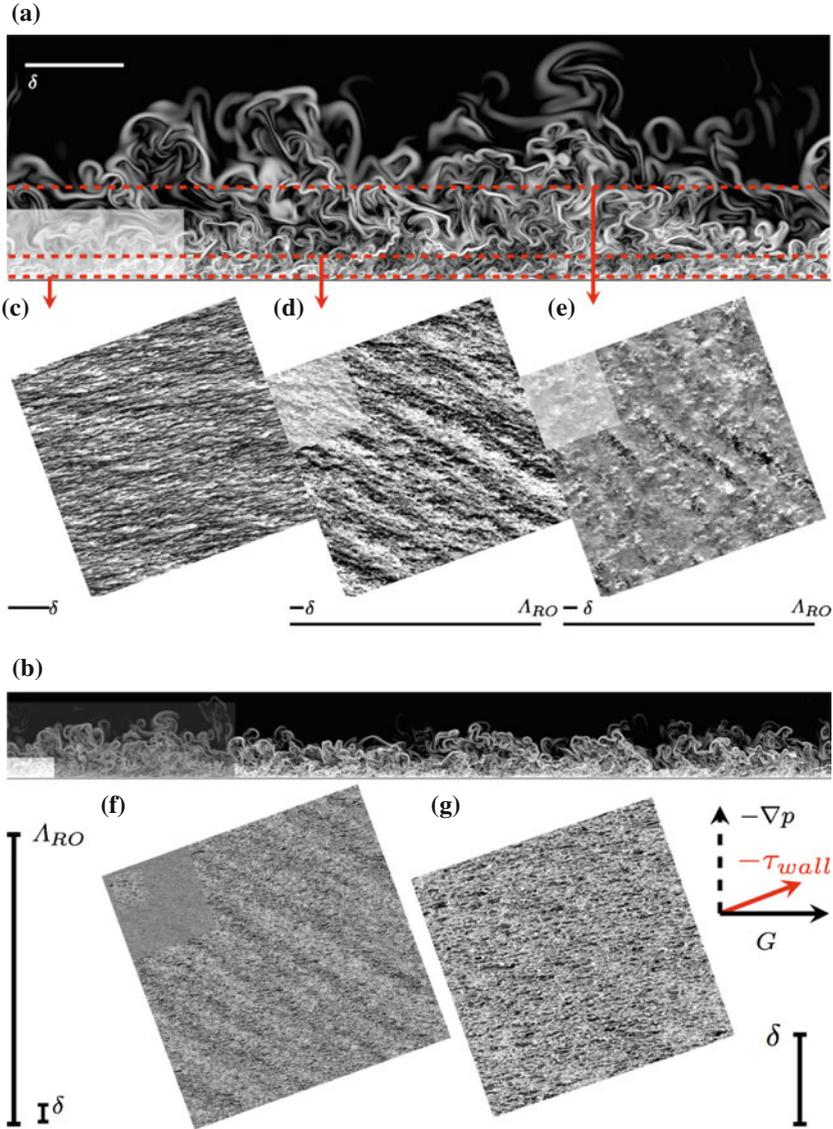
Fig. 6.11 a, b Streamwise–*vertical* cross sections showing the magnitude of the gradient of concentration of a passive scalar originating from the surface. *Grey* scale varies from $10^3 \Lambda_{RO}^{-1}$ (white) to $10^{-1} \Lambda_{RO}^{-1}$ (*black*) where $\Lambda_{RO} = G/f$. Block grey-shading in (**b**) indicates the region shown (**a**). **c–g** *Horizontal* cross-sections. Wind magnitude in the buffer layer ($z^+ \simeq 15$ (**c**)), in the *upper part* of the logarithmic layer ($z^+ \simeq 100$, $z^- \simeq 0.11$ (**d**)), and the outer layer ($z^- \simeq 0.75$, (**e**)). (**c**) shows only the subset marked by *white shading* in (**d**) and (**e**). **f, g** plot the scalar gradient at $z^+ \simeq 40$ in the whole domain (**f**) and for the *grey shaded* square from (**f**) illustrating the hairpin vortices (**g**). Shown in this figure is case N1000L, which has been carried out in computational domain rotated by approximately $-\alpha$: The *horizontal planes* in part figures (**c**)–(**g**) are rotated such that the geostrophic velocity is pointing from left to right as shown in the sketch

are seen as excursions of the white colors into higher levels of the boundary layer (Fig. 6.11a, b).

The change of organization in the turbulent flow when moving upwards is illustrated by horizontal cross-sections of wind magnitude (Fig. 6.11c–e) and an increase of the dominant length scales with height in the power spectra of the velocity variances (Fig. 6.10): In the buffer layer (Fig. 6.11c), the flow is dominated by surface streaks aligned with the mean wind at that level which is anti-parallel to the force exerted on the fluid by surface shear stress τ_{wall}; a clear signature of these streaks is found in the spectra of u along the line $z = \lambda^{1/2}$. In the fully turbulent part of the outer layer (Fig. 6.11d), the turbulence is modulated at large scale that is rotated by about $20°-30°$ clockwise with respect to the geostrophic wind. This large-scale modulation has a dominant length scale of $\lambda_r \approx 5\delta$ which leaves the strongest signature around $z = \delta$; a downward penetration of this dominant mode is found in all three components though it is strongest in the streamwise component (Fig. 6.10). In thi outer layer (Fig. 6.11d), the small-scale structure appears as noise. At higher levels (Fig. 6.11e), the boundary layer is externally intermittent, because turbulence at those levels is mainly provided by strong ejections from lower levels happening only sporadically. Such generated turbulent structures in the outer layer of the flow are long-lived because of their relatively large extent and the weakness of turbulent dissipation at these large scales.

Horizontal planes in the quasi-logarithmic layer of the flow (at $z^+ \simeq 40$, Fig. 6.11f, g) show that the field is homogeneously turbulent, and that the dominant small-scale structures are hairpin vortices typical of the logarithmic layer (Adrian 2007). Their intensity is modulated at a large scale as discussed above. This large-scale is rotated about $20°–30°$ clockwise with respect to the geostrophic wind, and this is the same orientation as that of the modulating structures in the logarithmic layer. This large-scale organization is typical of wall-bounded flows (Marusic et al. 2010; Adrian 2007), and there remains considerable controversy about the role of these large-scale structures in the inner layer (Jiménez 2013). In the present case, they have a clear organization that can be attributed to some large-scale instability inherent to the flow (Barnard 2001); spectral analysis suggests these structures originate from the far outer layer of the flow. The existence of such large-scale structures is hence a fundamental property of turbulent Ekman flow and I expect that they are crucial when the flow is exposed to stable stratification, as discussed in Chap. 8.

6.5 Summary

In this chapter, the neutrally stratified Ekman flow is discussed. For the Reynolds numbers $Re \in \{500, 750, 1000\}$, the set-up is well within the turbulent regime, and the scale separation is large enough for a logarithmic layer to develop.

The impact of the averaging period on flux measurements based on single-point probes is quantified. For averaging intervals of the order of the eddy-turnover time, fluxes are underestimated by about 1%, an acceptable error given the precision

achieved by boundary-layer measurements in the field. The eddy-turnover time may, however, be much longer than commonly used averaging intervals on the order of 5–10 min.

The analogy of the surface layer of Ekman flow with that of channel flow is investigated. In agreement with previous work, a quasi-logarithmic layer above $z^+ \simeq 20$ is found that extends up to $z^+ \simeq 100$ at $Re = 1000$. This well-established analogy of the mean-flow profiles is extended here, and shown to also apply to the turbulence-energy budget. In the outer layer, the flow is externally intermittent, an important difference with channel flow where deviations from the logarithmic law for the mean velocity are caused, at least in part, by the effect of external intermittency. The external intermittency is quantified here by means of the enstrophy allowing to partition the flow to turbulent and non-turbulent regions. Using conditional statistics the impact of external intermittency on the logarithmic law for the mean velocities is quantified: A prominent dip in $U^+/(\ln z^+ + \mathscr{A}_0)$ in the upper part of the logarithmic layer that was observed before, is shown to be a consequence of external intermittency. This dip is largely reduced by considering only the turbulent sub-volumes of the flow, and the data fit then the formulation $U^+_{\text{turb}} = \kappa^{-1} \ln z^+ + \mathscr{A}_0$ with $\kappa = 0.413$ and $\mathscr{A}_0 = 4.46$.

References

Adrian, R. J. (2007). Hairpin vortex organization in wall turbulence. *Physics of Fluids*, *19*, 041301–1–041301-16. doi:10.1063/1.2717527.

Bailey, S., Vallikivi, M., & Hultmark, M. (2014). Estimating the value of von Kármán's constant in turbulent pipe flow. *Journal of Fluid Mechanics*, *749*, 79–98. doi:10.1017/jfm.2014.208.

Barnard, J. C. (2001). *Intermittent turbulence in the very stable ekman layer*. Ph.D. thesis, Washington: University of Washington

Bisset, D. K., Hunt, J. C., & Rogers, M. M. (2002). The turbulent/non-turbulent interface bounding a far wake. *Journal of Fluid Mechanics*, *451*, 383–410.

Blackadar, A. K., & Tennekes, H. (1968). Asymptotic similarity in neutral barotropic planetary boundary layers. *Journal of Atmospheric Sciences*, *25*, 1015–1020. doi:10.1175/1520-0469(1968)025<1015:ASINBP>2.0.CO;2.

Coleman, G. N. (1999). Similarity statistics from a direct numerical simulation of the neutrally stratified planetary boundary layer. *Journal of the Atmospheric Sciences*, *56*(6), 891–900.

Coleman, G. N., Ferziger, J. H., & Spalart, P. R. (1990). A numerical study of the turbulent ekman layer. *Journal of Fluid Mechanics*, *213*, 313–348.

Corrsin, S., & Kistler, A. L. (1955). Free-stream boundaries of turbulent flows. *Technical Report TR1244-3133*. Washington, DC: John Hopkins University. doi:10.1088/1468-5248/5/1/013.

del Àlamo, J. C., & Jiménez, J. (2003). Spectra of the very large anisotropic scales in turbulent channels. *Physics of Fluids*, *15*(6), L41–L44.

del Àlamo, J. C., & Jiménez, J. (2009). Estimation of turbulent convection velocities and corrections to Taylor's approximation. *Journal of Fluid Mechanics*, *640*, 5–26. doi:10.1017/S0022112009991029.

Finnegan, J., & Kaimal, J. C. (1994). *Atmospheric boundary layer flows: Their structure and measurement*. Oxford University Press.

Jiménez, J., Hoyas, S. F., & Simens, M. P. (2009). Comparison of turbulent boundary layers and channels from direct numerical simulation. *Reason*.

Jiménez, J. (2013). Near-wall turbulence. *Physics of Fluids*, *25*, 101302–1–101302-28. doi:10.1063/1.4824988.

Kovasznay, L. S., Kibens, V., & Blackwelder, R. F. (1970). Large-scale motion in the intermittent region of a turbulent boundary layer. *Journal of Fluid Mechanics*, *41*(2), 283–325.

Marusic, I., McKeon, B. J., Monkewitz, P. A., et al. (2010). Wall-bounded turbulent flows at high Reynolds numbers: Recent advances and key issues. *Physics of Fluids*, *22*(6), 065103. doi:10.1063/1.3453711.

Mellado, J.-P., Wang, L., & Peters, N. (2009). Gradient trajectory analysis of a scalar field with external intermittency. *Journal of Fluid Mechanics*, *626*, 333–365. doi:10.1017/S0022112009005886.

Miyashita, K., Iwamoto, K., & Kawamura, H. (2006). Direct numerical simulation of the neutrally stratified turbulent ekman boundary layer. *Journal of the Earth Simulator*, *6*, 3–15.

Moin, P. (2009). Revisiting Taylor's hypothesis. *Journal of Fluid Mechanics*, *640*, 1. doi:10.1017/S0022112009992126.

Ouwersloot, H. G., de Roode, S. R., & Bosveld, F. C., et al. (2009). Vertical wind velocity observations from the Cabauw Tower. In: *19th Symposium on Boundary Layers and Turbulence*, (pp. 1–4). Keystone, CO.

Phillips, O. M. (1955). The irrotational motion outside a free turbulent boundary. *Mathematical Proceedings of the Cambridge Philosophical Society*, *51*(01), 220–229. doi:10.1017/S0305004100030073.

Pope, S. B. (2000). *Turbulent flows*. New York: Cambridge Univ Press.

Prandtl, L. (1961) Zur turbulenten Strömung in Rohren und längs Platten. In: W. Tollmien, H. Schlichting, H. Görtler, & F. W. Riegels (Eds.), *Ludwig prandtl gesammelte abhandlungen*, (pp. 632–648). Berlin, Heidelberg; Springer.

Schalkwijk, J., Jonker, H. J. J., Siebesma, A. P., et al. (2015). A year-long large-eddy simulation of the weather over cabauw: An overview. *Monthly Weather Review*, *143*(3), 828–844. doi:10.1175/MWR-D-14-00293.1.

Spalart, P. R. (1989). Theoretical and numerical studies of a three-dimensional turbulent boundary layer. *Journal of Fluid Mechanics*, *205*, 319–340.

Spalart, P. R., Coleman, G. N., & Johnstone, R. (2008). Direct numerical simulation of the Ekman layer: A step in Reynolds number, and cautious support for a log law with a shifted origin (Retracted article. See, vol. 21, art. no. 109901, 2009). *Physics of Fluids*, *20*(10), 101507. doi:10.1063/1.3005858.

Spalart, P. R., Coleman, G. N., & Johnstone, R. (2009). Retraction: "Direct numerical simulation of the Ekman layer: A step in Reynolds number, and cautious support for a log law with a shifted origin" [Phys. Fluids 20, 101507 (2008)]. *Physics of Fluids*, *21*(10), 109901. doi:10.1063/1.3247176.

Taylor, G. I. (1938). The spectrum of turbulence. In: *Proceedings of the Royal Society of London*, (pp. 476–490).

Tennekes, H. (1973). The logarithmic wind profile. *Journal of Atmospheric Sciences*, *30*, 234–238. doi:10.1175/1520-0469(1973)030<0234:TLWP>2.0.CO;2.

Träumner, K., Damian, T., Stawiarski, C., et al. (2014). Turbulent structures and coherence in the atmospheric surface layer. *Boundary-Layer Meteorology*, *154*(1), 1–25. doi:10.1007/s10546-014-9967-6.

Van der Hoven, I. (1957). Power spectrum of horizontal wind speed in the frequency range from 0.0007 to 900 Cycles per H. *Journal of Meteorology*, *14*, 160–164.

Von Kármán, T. (1930). Mechanische änlichkeit und turbulenz. *Nachrichten von der Gesellschaft der Wissenschaften zu Göttingen, Mathematisch-Physikalische Klasse*, *1924*, 58–76.

Wyngaard, J. C. (2004). Toward numerical modeling in the "Terra Incognita". *Journal of the Atmospheric Sciences*, *61*(14), 1816–1826.

Zanoun, E. S., Durst, F., & Nagib, H. (2003). Evaluating the law of the wall in two-dimensional fully developed turbulent channel flows. *Physics of Fluids*, *15*(10), 3079–3089.

Chapter 7
Turbulence Regimes and Stability
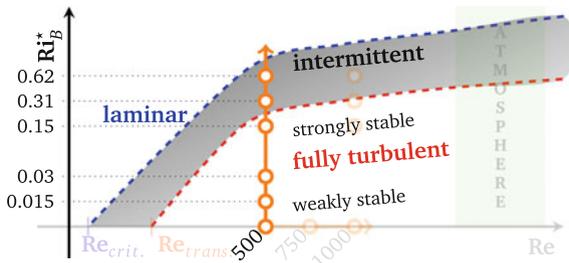
Under the impact of stable stratification, the dynamics of turbulence are multifarious, and they depend on the degree of stratification; a division of the flow into stability regimes proves useful. Stability regimes are discerned in terms of the qualitative impact of static stability on the flow dynamics as discussed in Chap. 1, and they are conveniently described in terms of the buoyancy flux (Fig. 7.1; repeated here from Chap. 1 for reference).

Despite studies of the planetary boundary layer with conceptual models, LES as well as observations, the progress toward a general framework for the stable boundary layer has been limited (Sandu et al. 2013; Steeneveld 2014; Mahrt 2014). Limitations are particularly pertinent with respect to an approach comprising all regimes of stability—from the near-neutral limit of weak stability to the extreme limit where the flow laminarizes, at least partly. While there is progress with regards to conceptual models at the very stable end (van de Wiel et al. 2012), LES and RANS simulations have severe problems in this regime (Jiménez and Cuxart 2005; Mauritsen and Svensson 2007; Huang and Bou-Zeid 2013). Problems of LES and RANS are caused by a break in the underlying paradigms when simulating a stably stratified turbulent flow at large stability: if a flow is not turbulent-throughout, concepts commonly employed for the turbulence closure in such simulations do not hold.

Fig. 7.1 Schematic of the
turbulent buoyancy flux in
the surface layer as the bulk
stratification in a boundary
layer increases
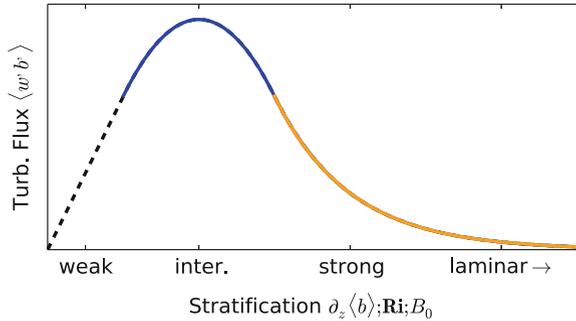
Unfortunately, insight into the nature of and thresholds for transition from the turbulent to the laminar state of a flow—necessary for a physically-based parameterization of turbulent fluxes beyond weak stability—is still small.

In contrast to LES and RANS, the current DNS approach does not rely on a turbulence closure: It evades above mentioned paradigm breaks by resolving the full spectrum of turbulent motion. The set-up introduced in Chap. 2 with parameters shown in Table 7.1 allows—for the first time—to study all regimes of turbulence in the SBL under well-controlled conditions. This is achieved varying only a single parameter, namely the bulk stratification Ri_B. In absence of a turbulence closure, the underlying assumptions consist only in the Boussinesq approximation of the Navier–Stokes equations, and they remain valid in the extreme limit of stratification when the flow re-laminarizes; the non-linear dynamics of re-laminarization are explicitly resolved in the DNS. This chapter begins with a discussion of the impact of initial conditions and time scales for the flow evolution. Subsequently, the regimes of stably stratified turbulence are identified (Sect. 7.2), and the flow in each of the regimes is described (Sects. 7.2.1–7.2.3).

7.1 Initial Conditions and Time Scales Under Stable Stratification

Time enters the set of parameters on which the statistical state of the flow depends once the flow is exposed to a stable density stratification; the turbulent state of the flow at a particular time then may depend on the initial condition. In the present set-up with fixed Ri_B, the energy extraction by surface heat flux is a priori unknown, and so is the evolution of total energy of the flow. While the long-term quasi-steady evolution of the system is governed by Ri_B, the state of turbulence during an initial period is mainly determined by the initial condition—and not by the external parameters alone. Hence, the bulk stratification, Ri_B, not necessarily indicates appropriately the

Table 7.1 Overview of simulations; the set covering all stability regimes is shaded in red

Case	Grid	Ri_B	L_{xy}/δ	IC Case	IC time	len
N500	A	0	8.8	n/a	n/a	1.0
N500L	B	0	17.5	N500	n/a	1.0
N1000L	C	0	17.5	N500L	n/a	1.0
W001	A	$1.5\cdot10^{-3}$	8.8	N500	0.0	0.5
W015	A	$1.5\cdot10^{-2}$	8.8	N500	0.0	1.4
W030	A	$3.1\cdot10^{-2}$	8.8	N500	0.0	9.0
I150	A	0.15	8.8	N500	0.0	1.8
I310	A	0.31	8.8	N500	0.0	4.8
S620	A	0.62	8.8	N500	0.0	1.7
I150-2	A	0.15	8.8	N500	0.0	3.5
IC038	A	$3.8\cdot10^{-2}$	8.8	W030	2.0	9.0
IC050	A	$5\cdot10^{-2}$	8.8	IC038	4.0	9.0
IC075	A	$7.5\cdot10^{-2}$	8.8	IC075	6.0	9.0
IC150	A	0.15	8.8	W030	2.0	4.0
I150L	B	0.15	17.5	N500L	0.0	3.65
S620L	B	0.62	17.5	N500L	0.0	2.9
I150LH	C	0.15	17.5	N1000L	0.0	1.65
I310LH	C	0.31	17.5	N1000L	0.0	0.5
S620LH	C	0.62	17.5	I150LH	1.65	0.5

Grid	Nx	Ny	Nz	L_{xy}/δ	L_z/δ	$(\Delta x)^+$	$(\Delta z)^+|_{z=0}$
A	1024	1024	192	8.8	2.8	4.1	1.05
B	2048	2048	192	17.5	2.8	4.1	1.05
C	3072	6144	512	20.4	3.5	4.6	1.32
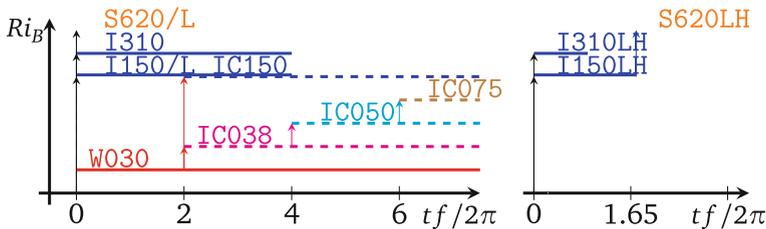
These simulations have been initialized using a neutrally stratified initial condition together with a horizontally homogeneous buoyancy profile as described in Chap. 2 (Eq. 2.14). The simulations at $Re = 500$ are complemented by a set of simulations at $Re = 1000$ to investigate the Reynolds-number effect on the findings presented here. The set labeled IC investigates the impact of the initial conditions; in these simulations, the bulk stratification increases gradually, and initial conditions from the preceding stratification (column IC Case) are used as shown in the sketch. The grids A–C are described in the lower table

turbulence regime which is primarily governed by the surface energy flux (Sect. 2.2.3; for a discussion of the critical stability threshold in the surface layer, see Sect. 8.2).[1]

The associated transition time scales are fundamental properties of the flow. The question, How do these time scales depend on the initial condition? is addressed through an additional set of simulations labeled with the prefix IC (Table 7.1). This set investigates whether transition time scales are determined by the strength of stratification only or also by the way in which it is imposed. The simulations listed in Table 7.1 vary on multiple time scales (Fig. 7.2): first an initial adaptation, second—in the case of a breakdown of turbulence—a turbulence recovery, third the inertial oscillation, and fourth a buoyancy oscillation. Through analytical and numerical study of the flow and the governing equations, I associate here physical processes to variations on these time scales. This understanding of processes and associated time scales provides a basis for the subsequent study of stability regimes under stable stratification (Sect. 7.2).

7.1.1 Initial Adaptation

When the neutrally stratified flow is suddenly exposed to a cooler surface, there is a period of time over which the flow does not respond to the density perturbation and buoyancy mixes as passive scalar into the buffer layer—a thin strongly stratified layer develops in the vicinity of the surface. The system responds to this strong perturbation from the surface with a reduced turbulence intensity and enstrophy magnitude in all cases (Figs. 7.2 and 7.8). The strength of this initial response is stronger for stronger stratification and varies monotonically with the Brunt–Väisälä frequency at the surface, which is strictly seen expressed by L_O^+, but as a consequence of our set-up varies linearly with $\sqrt{Ri_B}$. In the simulations it is found for this initial transient that

$$\frac{1}{E_{\text{neutral}}\sqrt{Ri_B}}\frac{\partial E}{\partial t^-} \simeq -4, \tag{7.1}$$

where the derivative is approximated as $(E(t') - E(0))/t'$ for $t'^- = 0.2$ and $E(t') = \int e(t', z)dz$ and $t^- = tf/2\pi$. This transient is observed for cases in which the stratification concentrates in the viscous sub-layer, and in the cases IC150S and S620LH, where the stratification is increased by a factor of four, respectively five. When compared to the inertial period, this initial transient is short—it ends at $t^- \simeq 0.2$—and is followed by a much slower recovery (Figs. 7.2 and 7.8).

---

[1]Note that a Neumann boundary condition on the scalar, i.e. a fixed surface heat flux does not solve this issue in terms of the total energy as the rate of extraction of (kinetic) energy from the mean flow by the turbulence dynamics would remain elusive.
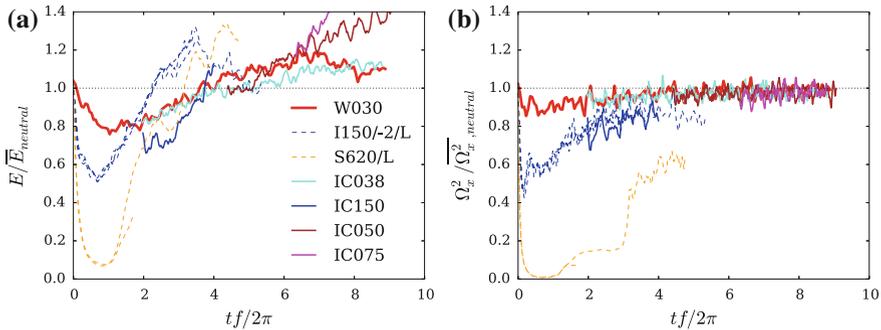
Fig. 7.2 **a** Vertically integrated TKE for the series of cases (IC038S, IC050S, IC075S, IC150S) described in Table 7.1. **b** Same as (**b**) but for vertically integrated spanwise vorticity RMS Ω_x^2

7.1.2 Recovery After Initial Turbulence-Breakdown

The recovery of TKE after an initial breakdown of turbulence is found to occur on a time scale of several inertial periods. The starting point of this recovery depends on the difference between the dynamic impact of the local stratification at the surface (quantified by L_O or $Ri_f(z=0) = \left(L_O^+\right)^{-1}$) on the one hand and the bulk stratification (quantified by Ri_B) on the other; for the simulations done here, it starts between $t^- = 0.5$ and $t^- = 1$. [One may think of set-ups with $Ri_B \simeq 1 > 0.62$ that would allow for globally intermittent turbulence also for large t^-; in the beginning the turbulence would, however, be eliminated by killing its main source in the buffer layer. Before the recovery can start, buoyancy concentrated into the buffer layer needs to be distributed over a larger fraction of the boundary layer which can only happen by viscous mixing once turbulence has ceased.] During the turbulence-recovery, the enstrophy fluctuation (Fig. 7.2a) grows until it reaches an equilibrium at a level close to but smaller than the neutral reference. The time scale of this enstrophy recovery is about two inertial periods independent of stratification strength.

While enstrophy approaches the level of the neutral reference from below, TKE exceeds the reference level in all simulations (Fig. 7.2). The time scale of the TKE recovery—when considered in terms of the eddy-turnover time $1/f$—is similar to that observed by Nieuwstadt (2005) in DNS of stratified open channel flow. This growth in TKE but not the enstrophy indicates significant contributions from weakly or non-vortical motions related to the excitation of waves which efficiently extract energy from the mean flow (this effect is quantified in Sect. 8.3.3). In the present cases, the significant contribution of wave energy is independent of the way in which the initial condition is imposed, but the growth rates of TKE during its recovery are larger for stronger stratification.

7.1.3 Inertial Oscillation

Numerical evidence. The inertial oscillation is pervasive in perturbed rotating systems, and all simulations vary at the inertial time scale $2\pi/f$. Under neutral stratification, the flow is run for a long time to achieve a fully turbulent state and forget the initial condition such that the inertial oscillation—due to an unbalanced initial condition is very small—, i.e. the flow is in its equilibrium with respect to the inertial oscillation. When stratification is imposed on the flow, the equilibrium velocity profile—which the flow hypothetically attains in the long run—changes, and the flow is out-of-equilibrium. This is most prominently seen in an oscillation of the mean velocity profiles as visualized by means of the flow hodographs in Fig. 7.3. When the hodograph is tracked at a certain height (thin lines in Fig. 7.3), the damped nature of the inertial oscillation becomes apparent.

Analytical study. In Chap. 5, a solution for a perturbed case of the quasi-laminar Ekman layer is derived in a non-dimensional framework. This model is employed here to understand aspects of the inertial oscillation in vertically integrated form, in particular its damping. For details of the analysis, see Appendix A; in this section only, all variables are non-dimensionalized by G, D and ν as outlined in Appendix A. In the stratified case, this damping is important as it sets the time scale for transition from the initial to the equilibrium velocity profile.

The streamwise momentum deficit $\mathscr{U}$ and spanwise momentum $\mathscr{V}$ are defined as

$$\mathscr{U} := \int_0^\infty (U-1)\mathrm{d}z \quad \text{and} \quad \mathscr{V} := \int_0^\infty V\,\mathrm{d}z, \tag{7.2}$$
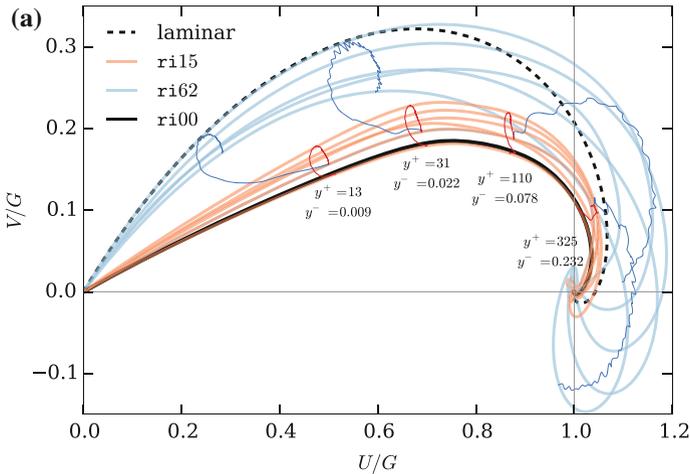
Fig. 7.3 Hodographs of the cases `N1000LH` (*black*), `I150LH` (*red*), and `S620LH` (*blue*) at the time instants marked by vertical lines in Fig. 7.5a.

and I obtain the system of coupled ordinary differential equations

$$\partial_t \mathscr{U} = \mathscr{V} - u_\star^2 \cos \alpha \quad \text{and} \quad \partial_t \mathscr{V} = -\mathscr{U} - u_\star^2 \sin \alpha \quad (7.3)$$

with the equilibrium

$$\mathscr{U}_\infty = -u_{\star,\infty}^2 \sin \alpha_\infty \quad \text{and} \quad \mathscr{V}_\infty = u_{\star,\infty}^2 \cos \alpha_\infty. \quad (7.4)$$

This stationary problem may be closed using the semi-empirical approach of Coleman et al. (1990). In Chaps. 5 and 6 it is shown that an evaluation of the associated constants satisfactorily agrees with this closure. It remains, however, unclear how the perturbed system (7.3) behaves. In particular, it is unclear what determines the damping of the inertial oscillation. When discussing inertial oscillations, it is often assumed, that the terms $u_\star^2 \cos \alpha$ and $u_\star^2 \sin \alpha$ act as linear damping term of the above oscillator. While this is in accordance with observations and the physical intuition that inertial oscillations are damped, it is not clear from this formulation of the equations. In Eq. (7.3), it is only the deviation of the flux from its equilibrium $\left(u_\star^2 \cos \alpha - \mathscr{V}_\infty, -u_\star^2 \sin \alpha - \mathscr{U}_\infty \right)$ which is responsible for deviations from an undamped harmonic oscillator.

Numerical investigations suggest that the oscillation in the momentum fluxes may decouple from the surface shear stress under certain conditions (Evgeni Fedorovich, 2014, personal communication). This is a major problem for the parameterization of the surface shear stress based on boundary-layer parameters such as integrated momentum flux or the momentum at a particular height, and I do believe that a better understanding of the inertial oscillation can help to alleviate and overcome these problems. Under stable conditions, the role of the surface shear stress is even more important: if the prognostic equations for $\mathscr{U}$ and $\mathscr{V}$ are considered, then it is not only the turbulence-closure problem which is dumped in the prescription of the surface shear stress but also is the surface shear stress the only quantity through which buoyancy effects may enter in the momentum budget.

Let $\mathscr{U} = \mathscr{U}' + \mathscr{U}_\infty$ (and analogous for the perturbations of the surface shear stress $\mathscr{V}$, f_x and f_y defined in Appendix A) to obtain

$$\frac{\partial^2 \mathscr{U}'}{\partial t^2} = -\mathscr{U}' + f_y' + \frac{\partial f_x'}{\partial t} \quad (7.5a)$$

$$\frac{\partial^2 \mathscr{V}'}{\partial t^2} = -\mathscr{V}' - f_x' + \frac{\partial f_y'}{\partial t}, \quad (7.5b)$$

which is an exact integral form of the Navier–Stokes–Coriolis equations. In the context of the analytical model, Eq. (7.5) can be rewritten as

$$\frac{\partial^2 \mathscr{U}'}{\partial t^2} = -\left(1 + \frac{1}{4 Re_E^2 \tau^2} \right) \mathscr{U}' + \frac{1}{Re_E \tau} \frac{\partial \mathscr{U}'}{\partial t}$$
$$\frac{\partial^2 \mathscr{V}'}{\partial t^2} = -\left(1 + \frac{1}{4 Re_E^2 \tau^2} \right) \mathscr{V}' + \frac{1}{Re_E \tau} \frac{\partial \mathscr{V}'}{\partial t} \quad (7.6)$$

Fig. 7.4 Illustration of the
perturbation ansatz and the
analytical solution for the
study of the inertial
oscillation
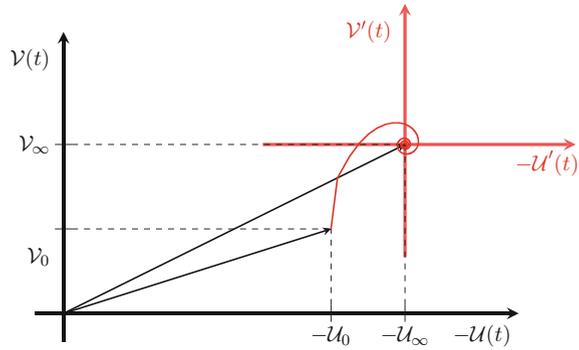
with $\tau = \mu_0 + t/Re_E$ (Appendix A).[2]

Interpretation. Solutions for the perturbed Ekman-layer problem have been presented previously (Ekman 1905; Shapiro and Fedorovich 2010). The present approach is special in that the solution does not involve the (numerical) evaluation of integrals or the like. A solution to the equations is shown in Fig. 7.4. The damping term $1/(Re_E\tau)$ is time-dependent as $\tau = \tau_0 + t/Re_E$, and the strength of the non-linear effects in the damping depends on $\tau_0/(t/Re_E)$ assuming that time is only varying on the order of 1. If large times are permitted, non-linear effects matter for any combination of τ_0 and Re_E. Beyond this non-linearity in the damping, the frequency is shifted to a value slightly larger than the inertial period. This illustrates an interesting behavior of the inertial-oscillator model; in the context of a linear equation, the oscillator does not exactly behave as a linearly damped harmonic oscillator when exposed to perturbations of a Gaussian type. While the exact result presented here only holds for the first mode of the family of possible perturbations, any odd derivative of the Gaussian implies a similar analysis that will yield similar corrections to the frequency and damping terms. These derivatives might form a complete basis of the functional space of the solutions fulfilling the boundary conditions and their relevance goes beyond the analytical study of the first mode.

Strictly seen, this analysis is valid for laminar flows at low Reynolds number. In the turbulent flow, Re is so high that non-linear corrections to the frequency and damping terms in Eq. (7.6) barely matter. One can, however—in the spirit of Ekman—resort to constant-eddy turbulence implying $Re_E \ll Re$. In that case, while the viscous corrections alone are small, the modifications based on Re_E may be substantial. This interpretation is supported by the DNS data which qualitatively confirm the suggested correction terms.

---

[2]The subscript E to the Reynolds number is used here to indicates that this is *not* the Reynolds number of the turbulent flow, but a Reynolds-number based on the eddy-viscosity, i.e. $Re_E := GD/(\nu_E + \nu)$ where $\nu_E \gg \nu$ and hence $Re_E \simeq GD/\nu_E$.

7.1.4 Buoyancy Oscillation

Numerical evidence. A high-frequency oscillation in the outer layer is found in the case S620LH which is spun of the case I150LH at $t^- \simeq 1.65$. While there is significant fluctuation energy in the vertical component of velocity, the turbulence source in the buffer layer is eliminated as indicated by the drastic decrease of $\langle ww \rangle$ near the wall (Fig. 7.5b) as well as the absence of turbulent motion throughout most of the near-wall region. This high-frequency oscillation dominates the time series of turbulence kinetic energy ($\langle u_i u_i \rangle$, TKE), streamwise vorticity r.m.s. Ω_x (Fig. 7.5a) and buoyancy flux ($\langle bw \rangle$, Fig. 7.5c), and its magnitude explains to a large extent the time signal in the integral of both the TKE and the r.m.s. of the stream-wise vorticity Ω_x. This vigorous oscillation is absent if a non-turbulent scalar profile is imposed as initial condition (Fig. 7.8). The initial energy for this oscillation becomes available through the sudden increase of stratification imposed by a multiplication of the buoyancy profile from $Ri_B = 0.15$ to generate the initial condition for the case ri62.

Analytical study. In Appendix B, I show by an analytical study constrained to a fixed height that this oscillation is the manifestation of a conversion of kinetic perturbation energy $\langle w'w' \rangle$ to potential perturbation energy $\langle b'b' \rangle$. Mathematically, the total energy of this oscillator is

$$e := \left(\frac{3}{2} N^2 \langle w'w' \rangle + \langle b'b' \rangle \right), \tag{7.7}$$

and a linear diffusion closure for the kinetic and potential energies implies that $\partial_t e = -e/\tau_e$ where τ_e is the local-in-height dissipation time scale. When the return-to-isotropy term is neglected, the equations for $\langle w'w' \rangle$, $\langle b'b' \rangle$ and $\langle w'b' \rangle$ decouple from the rest, and read as

$$\frac{1}{2} \frac{\partial \langle w'w' \rangle}{\partial t} = \langle b'w' \rangle - \frac{1}{\tau_\epsilon} \langle w'w' \rangle \tag{7.8a}$$

$$\frac{1}{2} \frac{\partial \langle b'b' \rangle}{\partial t} = -\langle b'w' \rangle N^2 \left(1 + \frac{1}{2} \right) - \frac{1}{\tau_\epsilon} \langle b'b' \rangle \tag{7.8b}$$

$$\frac{\partial \langle b'w' \rangle}{\partial t} = \left[\langle b'b' \rangle - \langle w'w' \rangle N^2 \left(1 + \frac{1}{2} \right) \right] - \frac{1}{\tau_\epsilon} \langle b'w' \rangle \tag{7.8c}$$

At a particular instant in time, there is a dominant balance between the time-rate of change and the turbulent transport terms (the dashed and solid lines in Fig. 7.6 collapse). Only over the course of many oscillations, the dissipation of the perturbations becomes significant, and the simulation data suggest $\tau_\epsilon^- \simeq 0.23$ at $z^- \simeq 0.4$. The frequency ω_{bw} and damping α_{bw} of this oscillation in $\langle bw \rangle$ are

$$\omega_{bw}^2 = \frac{5}{2} N^2 - \frac{2}{\tau_{\text{eff}} \tau_\epsilon} \quad \text{and} \quad \alpha_{bw} = \left(\frac{1}{\tau_{\text{eff}}} - \frac{4}{\tau_\epsilon} \right) \tag{7.9}$$
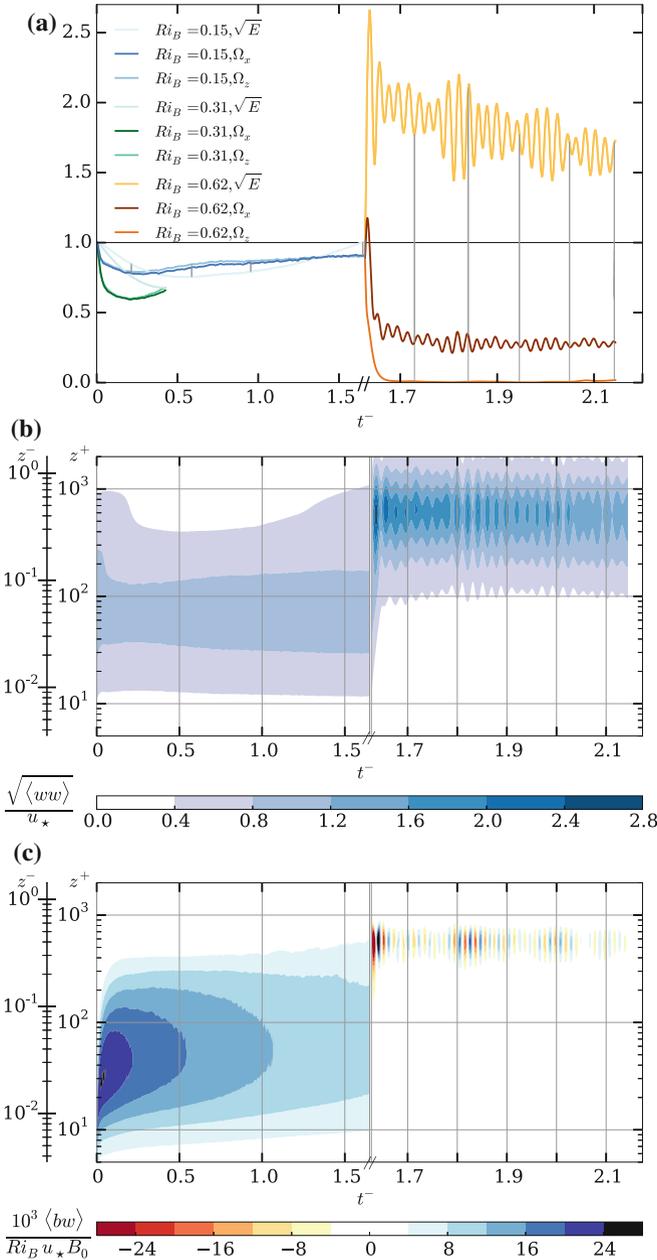
Fig. 7.5 **a** Square root of domain-integrated TKE ($\sqrt{E}$), domain-integrated r.m.s. of the stream-wise component of vorticity Ω_x, and domain-integrated r.m.s. of the wall-normal component of vorticity Ω_z, normalized by the corresponding values from case `ri00`. *Lines* in *red tones* in panel (**a**) correspond to $Ri_B = 0.15$; thereafter $Ri_B = 0.62$ (*blue tones*). **b** Contour plot of $\sqrt{\langle ww \rangle}$, **c** Contour plot of $\langle bw \rangle$. In panels (**b**) and (**c**) the time axis changes scale around $t^- \approx 1.6$, i.e. when the stratification is increased, to better illustrate high-frequency variability
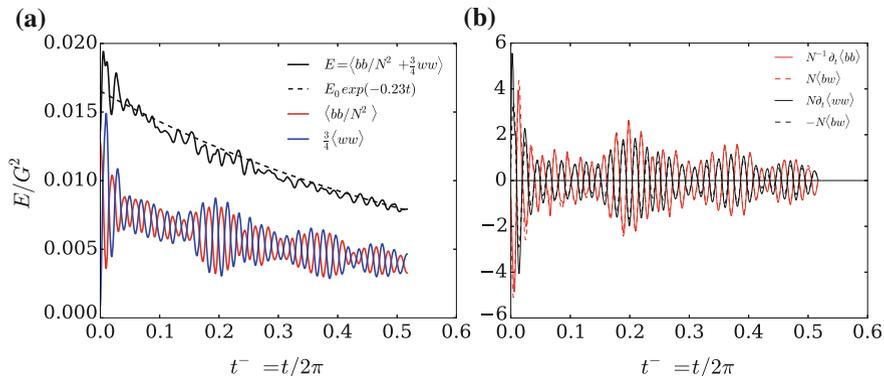
Fig. 7.6 a Time series of vertical velocity variance and scalar variance and the sum of the two (Eq. B.5). **b** LHS (*solid*) and RHS (*dashed*) of Eqs. 7.8a and 7.8b. Data are plotted at $z^- \simeq 0.4$

where $N = \sqrt{\partial_z B}$ is the Brunt–Väisälä frequency at that height where the oscillation is studied, and τ_{eff}, τ_ϵ are the return-to-isotropy and diffusion time scales.

Interpretation. It is important to note that the frequency of this oscillator is not the Brunt–Väisälä frequency, but $2N^2$ when the triple correlation terms are neglected, and $(5/2)N^2$ if the triple-correlation terms are closed through a second-order down-gradient closure. This frequency is also found in the data plotted in Fig. 7.6 where one can count 51 oscillations per inertial period. At the level where the data is plotted, the buoyancy frequency is $(N^-)^2 = 21$ which gives an estimated frequency of $\omega_{bw}^- \simeq 52.5$—very close to the above estimate $\omega_{bw}^- \simeq 51$ from the DNS data. It is surprising that such a simple model can capture the dynamics after turbulence collapse in the outer layer rather well, and it might be worth to consider this mechanism further.

Equation (7.9) defines the transition from the oscillation-dominated to the dissipation-dominated regime: The marginal stratification for damping of the oscillation is $N_{\mathrm{crit}}^2 = 4/(5\tau_{\mathrm{eff}}\tau_\epsilon)$.

- If $N^2 < N_{\mathrm{crit}}^2$, the frequency ω_{bw} is purely imaginary and the system is over-damped. In this case, the inertia-buoyancy oscillation of second-order quantities plays a minor role: turbulent dissipation and return to isotropy are the dominant terms. In this regime, the models applied for the turbulence closure are very important.
- If the stratification is increased such that $N^2 \approx N_{\mathrm{crit}}^2$, the oscillation is dominated by N^2 and the terms involving τ_ϵ and τ_{eff} constitute (i) a modification to the frequency of the oscillator and (ii) a damping of the oscillation.
- For $N^2 \gg N_{\mathrm{crit}}^2$ the stratification imposes an under-damped oscillation, and the conversion mechanism between buoyancy and velocity perturbations dominates the turbulent mechanisms in the flow. In the limit of high stratification, the system becomes a buoyancy oscillator that permanently converts energy from kinetic velocity perturbations $\langle w'w' \rangle$ to buoyancy variance $\langle b'b' \rangle$ and vice versa. Vertical velocity variance $\langle w'w' \rangle$ is created through buoyancy flux at the rate $\langle b'w' \rangle$. At the

same time, this production of vertical velocity variance consumes energy contained in the buoyancy perturbations $\langle b'b' \rangle$ at a rate $(3/2)\,N^2 \langle b'w' \rangle$. In this regime, the turbulence parameterizations merely provide a weak damping and do not have a large effect on the evolution of the system.

Despite its vigorous nature, this oscillation does not create three-dimensional small-scale turbulence as can be inferred from the large contrast between Ω_z and Ω_x (Fig. 7.5a). In the case studied here, the time-signal in Ω_x is governed by the high-frequency oscillation, whereas Ω_z is close to zero and does not exhibit an oscillation of similar magnitude. This indicates the absence of an effective return-to-isotropy term (this term would work on time scales on the order of the integral time scale of the turbulence, f^{-1}, longer than the period of this oscillation on the order of N^{-1}). Further, this demonstrates the absence of so-called pancake vortices—often hypothesized as a source of vorticity under strong stratification (Mahrt 2014).

7.2 Classification of the Stability Regimes

The focus here is on the time after the initial adaptation of the system to the stratification, and simulations are classified according to their dynamics in this time span as weakly, intermediately, or very stable (Sects. 7.2.1–7.2.3). During this slow evolution, turbulence in the vertical column does not immediately adapt to changes in surface friction, and both $u_\star$ and δ evolve on a time scale $\delta/u_\star = 1/f$—a consequence of the non-stationarity of the problem. It is hence problematic to use $u_\star(t)$ as a velocity scale; instead, $u_{\star,\mathrm{neutral}}$ and $\delta_{\mathrm{neutral}}$ are used in this chapter as the reference scales to normalize the results and compare with the neutral case. An analysis of the TKE budgets (Fig. 7.7) in comparison with Fig. 7.1 illustrates that the set of cases introduced in Table 7.1 covers all stability regimes. The time evolution of vertically integrated TKE (Fig. 7.8a) corroborates this finding and suggests the following classification of the simulations:

1. **Weakly stable:**   integrated TKE changes slightly (10–20 %, cases W015S, W031S) with respect to the neutral configuration
2. **Intermediately stable:**   integrated TKE significantly (50 %) decreases and subsequently recovers (case I150, S310S)
3. **Very stable:**   integrated TKE is diminished nearly entirely, and subsequently recovers (case S620).

Time series of integrated enstrophy as well as the vertically integrated budget of TKE at $t^- = 0.5$ support this classification (Figs. 7.7 and 7.8b): The buoyancy flux reaches its maximum among all cases in case I150 supporting its identification as intermediately stable. Both the shear production (blue bars) and the buoyancy flux (black bars) change drastically when the most stable case S620, attributed to the very stable regime, is considered. In this case the terms in the TKE budget as well as the TKE itself reduce to $\simeq 5\%$ of the neutral reference. This reduction of order

one in both the turbulence production and buoyancy flux with respect to the neutral reference illustrates that the buoyancy flux is limited by the absence or weakness of turbulent motion, and not by the pure strength of buoyancy destruction $\int \langle bw \rangle dz$.

7.2.1 Weak Stability

The boundary layer forming in the weakly stable regime ($Ri_B \lesssim 0.05$; W015S, W031S) is very similar to that found under neutral conditions (Fig. 7.10a, d and Chap. 6). Turbulent mixing efficiently weakens the stratification and a quasi-neutral weakly-stable boundary layer forms. As expected and found elsewhere (Sun et al. 2012; Ha et al. 2007; Monin 1970), the weakly stable boundary layer is well described when considered as a perturbation of the neutrally stratified one. TKE alters most strongly in the outer layer (not shown) as also found by Coleman et al. (1992) as well as García-Villalba and del Àlamo (2011), and the hodograph is barely distinguishable from that of the corresponding neutral case N500 (Fig. 7.9c, red line).

7.2.2 Intermediate Stability

In the intermediately stable regime, at $Ri_B = 0.15$, TKE reduces by $\simeq 50\%$ during the initial adaptation period, and the integrated buoyancy flux at $t^- = 1$ is the maximum of all simulations carried out (Fig. 7.7). The relative increase of the integrated buoyancy flux is one order of magnitude smaller than the reduction of TKE and shear production with respect to the neutral reference (Fig. 7.7). This illustrates that the main impact of buoyancy on the flow is not the direct destruction of TKE but a

Fig. 7.7 Vertically integrated terms of the TKE budget equation at $Re = 500$ and $t^- = 0.5$ for cases W015S, W030S, I150, S310S and S620 normalized with the shear production rate of the neutral reference
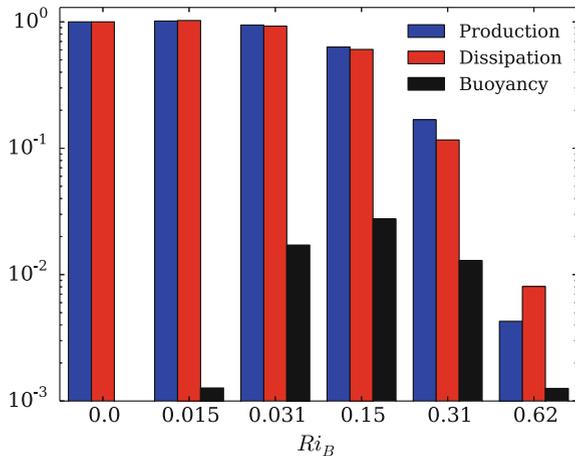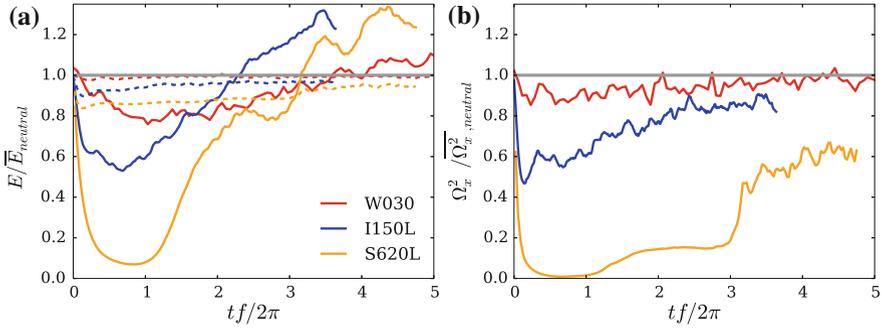
Fig. 7.8 **a** Temporal evolution of vertically integrated turbulent kinetic energy $E(t)$ (*solid*) and averaged wall friction velocity $u_\star(t)$ (*dashed*) normalized with the corresponding neutral reference $E_{neutral}$ and $u_{\star,neutral}$, respectively. **b** Same as **a**, but for the streamwise enstrophy $\langle \Omega_x^2 \rangle(t)$

decrease in the shear-induced production, in particular of the stress $\langle u'w' \rangle$ (Jacobitz et al. 1997 p. 243). Profiles of shear production (not shown) indeed confirm this explanation, in agreement with Jacobitz et al.'s study of stably stratified shear flow. In contrast to the simulations attributed to the weakly stable regime, the hodograph in the intermediately stable regime ($Ri_B = 0.15$, case I150) departs significantly from the neutral reference; it lies in between the hodographs from the neutrally stratified case and a laminar one (Fig. 7.9c).

After an initial decay, the TKE recovers slowly on a time scale of a few inertial periods (Sect. 7.1.2; blue curve in Fig. 7.9a). When expressed in terms of f^{-1}, the time scale of this slow oscillation matches the time scale for recovery observed by Nieuwstadt (2005) in a stably stratified channel flow. Turbulence intensity recovers across the entire boundary layer, and concomitantly the depth of the stratified layer increases (sequence of blue lines in Fig. 7.9b). Given a fixed bulk gradient, this increase in depth of the stratified layer is compensated by weakening stratification in the surface layer ($z^- \lesssim 0.1$). Eventually, during this recovery, the TKE increases beyond the neutral reference both above $z^- \simeq 0.5$ and in the production region (Fig. 7.8a) as also observed by Nieuwstadt (2005).

In agreement with recent work on channel and Couette flow (Flores and Riley 2011; Deusebio 2015) and in contrast to the findings of Nieuwstadt (2005), the simulated boundary layer is globally intermittent. A local break-down of turbulence is evident from Fig. 7.10 showing quasi-laminar patches in a turbulent environment. These quasi-laminar patches extend through the entire vertical fluid column in an otherwise turbulent flow, and hence this state is identified as global intermittency in the sense of Mahrt (1999). Note that Ri_B defined in terms of $\delta_{neutral}$ as an external control parameter is smaller than the Richardson number defined in terms of the depth $\delta(t)$ of the SBL ($\delta(t) \simeq 0.5\delta_{neutral}$ at $tf/2\pi = 1$; see Fig. 7.9b). Hence, the occurrence of global intermittency in this particular case at $Ri_B = 0.15$ agrees with the observation that global intermittency often occurs if

$$\frac{\delta B_0}{G^2} = \frac{\delta}{\delta_{neutral}} Ri_B \simeq 0.25. \tag{7.10}$$
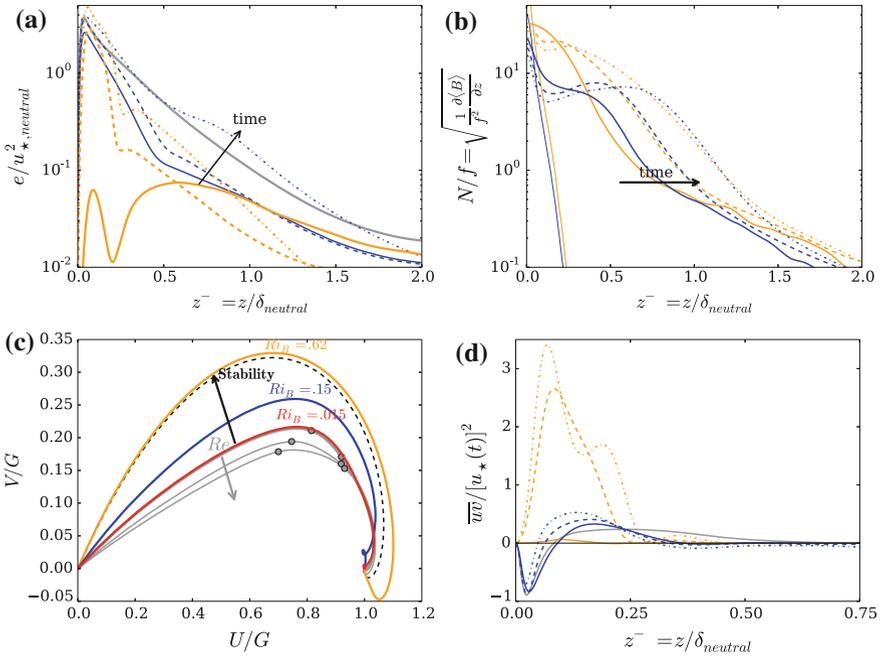
**Fig. 7.9** Vertical profiles of e **a** and normalized buoyancy frequency N/f **b** *blue*—case I150, *orange*—case S620. **d** Shows the in-plane Reynolds stress (*solid* $t^- = 1$; dashed: $t^- = 2.0$; *dash-dotted* $t^- = 3.0$). Thin *solid lines* show the initial condition for the respective case. **c** Hodographs after one inertial period ($t^- = 1$) and those from the neutral cases repeated from Fig. 5.6a

7.2.3 Very Strong Stability

Under very strong stability (cases S620, S620LH), turbulence in the surface layer initially dies out nearly completely since the region of shear production in the buffer layer is eliminated. The hodograph (Fig. 7.9a) is close to that of the corresponding laminar Ekman flow; in fact, the eddy diffusivity estimated from the laminar fit to the velocity profiles (not shown) is 1.01ν. This re-laminarization in the inner layer is seen in Fig. 7.10: the turbulence with relatively high enstrophy magnitudes in panel (a) is replaced in panel (c) by large-scale roll-like structures aligned parallel to the wall-shear stress, i.e. rotated 45° counter-clockwise with respect to the geostrophic wind. The initial re-laminarization is followed by a recovery of turbulence as seen in the time-series of TKE and enstrophy (Fig. 7.8a, b). The recovery of turbulence is similar to that observed in the intermediately stable case. This recovery, however, takes longer, and while the rapid growth of enstrophy levels off around 60 % of the neutral value, the TKE grows beyond its neutral reference.

At the beginning of the recovery of TKE, the maximum of TKE associated with the peak shear production in the buffer layer is eroded (Fig. 7.9a), that is, the production region of turbulent stress is eliminated. Around $z^- = 0.25$, the turbulence intensity
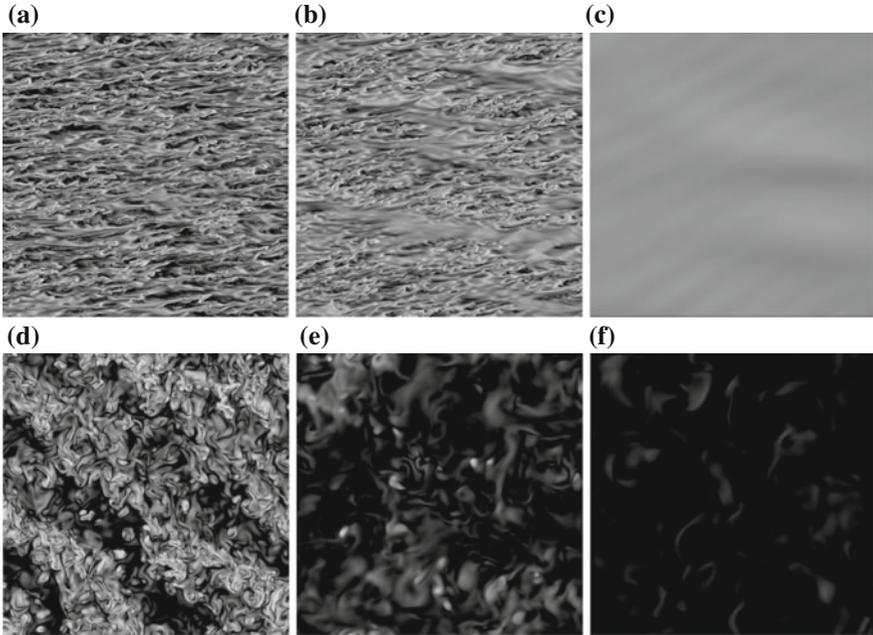
Fig. 7.10 Horizontal planes of enstrophy (coloring from low [*black*] to high [*white*] values) in a domain $\approx (10 \times 10)\delta_{neutral}^2$ at $tf/2\pi \simeq 1$. **a, d**: $Ri_B = 0.015$, case W015S; **b, e**: $Ri_B = 0.15$, case I150; **c, f**: $Ri_B = 0.62$, case S620. **a–c** show the inner layer $z^+ \simeq 15$, **d–f** the outer layer around $z^- = 0.56$.

is reduced even more than at the peak of production; this illustrates the absence of vertical turbulent exchange across the buffer layer and a decoupling of the flow inside this surface layer from higher layers of the flow. Above the decoupled surface layer ($z^- \gtrsim 0.5$), turbulence is affected less strongly by stratification and decays slowly from its fully-turbulent initial state between $t^- \simeq 1$ and $t^- \simeq 2$. Such slowly-decaying residual turbulence is common to night-time boundary layers cooled from below (Stull 1988), illustrating the appropriateness and relevance of the present simulations for the study of such cases.

7.3 Summary

This chapter demonstrates that the DNS set-up introduced in Chap. 2 and used throughout this work is suitable to study all regimes of stratified turbulence without the need to tweak underlying assumptions when stratification is increased to the extreme limit. While the qualitative behavior of the flow agrees well with theory and observations, the present approach allows insight into the dynamics of turbu-

lence based on fundamental principles only, and it evades uncertainties related to the application of turbulence closures. A finding of particular relevance is that global intermittency—in both the time and space dimensions—occurs in absence of external triggers.

A framework is developed here to analytically study the inertial oscillation and a conversion mechanism between $\langle b'b' \rangle$ and $\langle w'w' \rangle$, and it is found that relatively simple models cover the impact of these mechanisms in the flow. The simple analytical model for the inertial oscillation in Ekman flow is based on the assumption of a constant eddy viscosity, and it delivers a closed analytical solution for the quasi-laminar case of an Ekman boundary layer. These dynamics are, however, also relevant in fully turbulent flow as demonstrated by a comparison of the analytical model with data from a turbulent DNS of Ekman flow. The derivation of an explicit drag-law for Ekman flow when it is strongly out of equilibrium remains a problem. Present results suggest that a parameterization of the surface flux based on instantaneous properties of the flow only is not possible in a temporally evolving case such as a low-level-jet boundary layer. If, however, the asymptotic equilibrium state of the boundary layer is known, instantaneous profiles might allow for conjectures about the history and potential evolution of the system which might give some hope for the existence of a quasi-local drag law based on an instantaneous and an equilibrium velocity profile. Such asymptotic equilibrium states may be obtained from future DNS studies once it becomes feasible from a computational perspective to calculate the flow over many inertial periods in sufficiently large domains.

An analysis of the impact of initial conditions (Sect. 7.1) unveils coexistence of motions on various time scales, and is in agreement with the results from analytical study of the flow. It is found that transients on the order of some inertial periods are present in the SBL, even under weak stratification. To the extent covered by the simulations, this finding does not depend on the way in which the initial conditions are imposed. Hence, it is expected that the SBL generally does not equilibrate over the course of a night.

Under very strong stratification the outer layer decouples from the surface layer. In the past, there has been debate on whether such a decoupling produced by boundary-layer schemes in numerical weather prediction (Derbyshire 1999; Acevedo et al. 2012) and LES (Saiki et al. 2000; Jiménez and Cuxart 2005) is an artifact of the subgrid-turbulence model. From the data, it is concluded that, at bulk Richardson numbers of order one ($Ri_B = 0.62$ for this particular case), a decoupling is possible —at least for an intermediate Reynolds number. This is in accordance with van de Wiel and Moene (2012). In contrast to estimates from numerical weather prediction or LES, this estimate is not subject to uncertainties in subgrid schemes, but—similar to stratified shear flow (Jacobitz et al. 1997; Deusebio 2015)—the particular value of a critical Richardson number for decoupling might depend on Re.

References

Acevedo, O. C., Costa, F. D., & Degrazia, G. A. (2012). The coupling state of an idealized stable boundary layer. *Boundary-Layer Meteorology*, *145*(1), 211–228. doi:10.1007/s10546-011-9676-3.

Coleman, G. N., Ferziger, J. H., & Spalart, P. R. (1990). A numerical study of the turbulent ekman layer. *Journal of Fluid Mechanics*, *213*, 313–348.

Coleman, G. N., Ferziger, J. H., & Spalart, P. R. (1992). Direct simulation of the stably stratified turbulent ekman layer. *Journal of Fluid Mechanics*, *244*, 677–712.

Derbyshire, S. H. (1999). Boundary-layer decoupling over cold surfaces as a physical boundary-instability—Springer. *Boundary-Layer Meteorology*, *90*(2), 297–325. doi:10.1023/A:1001710014316.

Deusebio, E. (2015). The intermittency boundary in plane couette flow. *Journal of Fluid Mechanics*, *781*, 298–329. doi:10.1017/jfm.2015.497.

Ekman, V. W. (1905). On the influence of the earth's rotation on ocean currents. *Arkiv for Matematik, Astronomi Och Fysik*, *2*, 1–53.

Flores, O., & Riley, J. J. (2011). Analysis of turbulence colapse in the stably stratified surface layer using direct numerical simulation. *Boundary-Layer Meteorology*, *139*(2), 241–259. doi:10.1007/s10546-011-9588-2.

García-Villalba, M., & del Àlamo, J. C. (2011). Turbulence modification by stable stratification in channel flow. *Physics of Fluids*, *23*(4), 045104. doi:10.1063/1.3560359.

Ha, K.-J., Hyun, Y.-K., Oh, H.-M., et al. (2007). Evaluation of boundary layer similarity theory for stable conditions in CASES-99. *Monthly Weather Review*, *135*(10), 3474–3483. doi:10.1175/MWR3488.1.

Huang, J., & Bou-Zeid, E. (2013). Turbulence and vertical fluxes in the stable atmospheric boundary layer. Part I: A large-eddy simulation study. *Journal of the Atmospheric Sciences*, *70*(6), 1513–1527. doi:10.1175/JAS-D-12-0167.1.

Jacobitz, F. G., Sarkar, S., & van Atta, C. W. (1997). Direct numerical simulations of the turbulence evolution in a uniformly sheared and stably stratified flow. *Journal of Fluid Mechanics*, *342*, 231–261. doi:10.1017/S0022112097005478.

Jiménez, M. A., & Cuxart, J. (2005). Large-eddy simulations of the stable boundary layer using the standard kolmogorov theory: Range of applicability. *Boundary-Layer Meteorology*, *115*(2), 241–261. doi:10.1007/s10546-004-3470-4.

Mahrt, L. (1999). Stratified atmospheric boundary layers. *Boundary-Layer Meteorology*, *90*(3), 375–396.

Mahrt, L. (2014). Stably stratified atmospheric boundary layers. *Annual Review of Fluid Mechanics*, *46*, 23–45.

Mauritsen, T., & Svensson, G. (2007). Observations of stably stratified shear-driven atmospheric turbulence at low and high Richardson numbers. *Journal of the Atmospheric Sciences*, *64*(2), 645–655. doi:10.1175/JAS3856.1.

Monin, A. S. (1970). The atmospheric boundary layer. *Annual Review of Fluid Mechanics*, *225–250*.

Nieuwstadt, F. T. (2005). Direct numerical simulation of stable channel flow at large stability. *Boundary-Layer Meteorology*, *116*(2), 277–299. doi:10.1007/s10546-004-2818-0.

Saiki, E. M., Moeng, C.-H., & Sullivan, P. P. (2000). Large-eddy simulation of the stably stratified planetary boundary layer. *Boundary-Layer Meteorology*, *95*(1), 1–30. doi:10.1023/A:1002428223156.

Sandu, I., Beljaars, A. C. M., Bechtold, P., et al. (2013). Why is it so difficult to represent stably stratified conditions in numerical weather prediction (NWP) models? *Journal of Advances in Modeling Earth Systems*, *5*(2), 117–133. doi:10.1002/jame.20013.

Shapiro, A., & Fedorovich, E. (2010). Analytical description of a nocturnal low-level jet. *Quarterly Journal Of The Royal Meteorological Society*, *136*, 1255–1262. doi:10.1002/qj.628.

Steeneveld, G.-J. (2014). Current challenges in understanding and forecasting stable boundary layers over land and ice. *Frontiers in Environmental Science*, *2*, 1–6. doi:10.3389/fenvs.2014.00041.

Stull, R. B. (1988). *An introduction to boundary layer meteorology*. Dordrecht: Kluwer Academic Publishers.

Sun, J., Mahrt, L., Banta, R. M., et al. (2012). Turbulence regimes and turbulence intermittency in the stable boundary layer during CASES-99. *Journal of the Atmospheric Sciences*, *69*(1), 338–351. doi:10.1175/JAS-D-11-082.1.

van de Wiel, B. J. H., Moene, A. F., Jonker, H. J. J., et al. (2012). The Minimum Wind Speed for Sustainable Turbulence in the Nocturnal Boundary Layer. *Journal of the Atmospheric Sciences*, *69*(11), 3116–3127. doi:10.1175/JAS-D-12-0107.1.

van de Wiel, B. J. H., & Moene, A. F. (2012). The cessation of continuous turbulence as precursor of the very stable nocturnal boundary layer. *Journal of the Atmospheric Sciences*, doi:10.1175/JAS-D-12-064.1.

Chapter 8
Flow Organization and Global Intermittency Under Strong Stratification
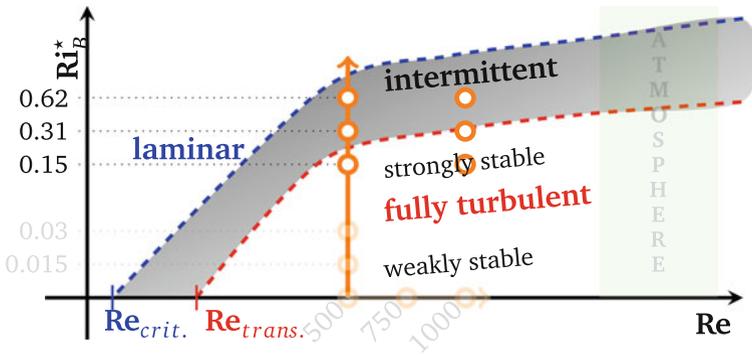
In previous chapters, a set-up to study the SBL is laid out, and I demonstrate how this set-up is utilized to study turbulence in all regimes of static stability. Under strong stratification, a collapse of turbulence and global intermittency are observed. In fact, the potential absence of turbulence under the impact of stratification is long recognized, and the transition of laminar flow to a turbulent state is subject to the field of hydrodynamic instability. Following seminal works by Rayleigh (1880) and Taylor (1923), stability analyses, both linear and nonlinear (Tollmien-Schlichting instability, Taylor–Goldstein stability analysis, Orr–Sommerfeld equation, Miles–Howard theorem), where carried out and a number of related instabilities relevant to atmospheric flows have been identified (Kelvin–Helmholtz waves, Holmboe waves, Di Prima and Swinney (1981), Maslowe (1981), Tritton and Davies (1981), Fernando (1991)). While an accurate prediction and description of the transition phenomena from the laminar to the turbulent state of the SBL is beyond the capability of linear and—as of yet—also non-linear theory, such theory correctly describes the onset of transition. There is hence a well-developed conceptual framework to answer the question if a laminar flow exposed to a density stratification becomes turbulent, or if it does not so.

The transition of laminar flow to its turbulent state which is considered in the hydrodynamic stability analyses, is, however, of limited relevance to the re-laminarization of a turbulent flow. Hence–notwithstanding progress in research on hydrodynamic instability–the lack of a consistent framework to treat turbulence in the very stable boundary layer is still identified as a current challenge in understanding the SBL (Steeneveld 2014; Mahrt 2014; van de Wiel et al. 2012). Recently, thresholds based on outer scalings (Nieuwstadt 2005; van de Wiel et al. 2012) and inner scalings (Flores and Riley 2011; Deusebio 2015) were proposed—another manifestation of the lack of understanding of collapsing turbulence: a threshold for a physical process may not be constant in terms of the outer and inner scaling since their separation increases with the Reynolds number. The present results (Sect. 8.2) suggest that the Obukhov length expressed in wall units, a measure of the scale range unaffected by stability, governs the turbulence intensity in the buffer layer. This layer is central in the range of strong stability since it is the main production region of turbulence.

In Chap. 7, the transition from the fully turbulent state to the laminar state is shown to be accompanied by the occurrence of laminar patches in an otherwise turbulent flow. This partial re-laminarization in an otherwise turbulent flow is referred to as global intermittency and makes global averages and statistics inappropriate. Global intermittency thus calls for the use of conditional statistics, but the vorticity-based conditioning of statistical properties to turbulent and non-turbulent sub-volumes of wall-bounded flow remains challenging. In Sect. 8.3, a new measure to quantify this global intermittency is presented. For that purpose, I apply the classical concept of external intermittency, i.e. the alternation of turbulent and non-turbulent patches of fluid in the outer layer, to the surface layer: If there are laminar patches of fluid extending from the outer layer down to the surface layer, the flow is identified as globally intermittent. To accomplish an identification of global intermittency in the surface layer, the vorticity-based conditioning of a wall-bounded flow is extended by a high-pass filter operation prior to the conditioning. This filter removes background enstrophy impeding the identification of a laminar patch as non-turbulent. Such a procedure is shown here to be appropriate for the detection of global intermittency in the surface layer, and—despite its simplicity—it gives reasonable estimates for intermittency factors in all regimes of static stability.

The capability to detect laminar patches based on a quasi-local[1] measure allows a mutually exclusive partition of the globally intermittent flow to turbulent and non-turbulent. In a subsequent step, these turbulent and non-turbulent partitions of the flow are separately analyzed (Sect. 2.3.1). This procedure unveils intriguing dynamics inside both the turbulent and non-turbulent flow regions (Sect. 8.4), and it suggests a separate treatment of the turbulent and the non-turbulent flow partitions when parameterizing turbulence under strongly stable stratification. Before I commence analyzing the critical stability and introducing conditional statistics alongside

---

[1]The spectral filter is a global operation, but the actual calculation of the intermittency factors is carried out by means of local enstrophy. This is different from other methods proposed recently such as the one by Deusebio (2015).

Table 8.1 Overview of simulations; the grid for all cases in this table has `3072x6144x512` collocation points

Case	*Re*	*Ri*$_B$	IC case	IC time	Analysis time
N1000L	1000	0	N500L	n/a	n/a
I150LH	1000	0.15	N1000L	0.0	1.5
I310LH	1000	0.31	N1000L	0.0	0.25
I620LH	1000	0.62	I150LH	1.65	$1.65 + 0.45 \simeq$ 2.1

For details of the cases, see Table 7.1 in Chap. 7. The column *analysis time* lists the time that is used for the computation of power spectra, probability density functions and flow visualizations in this chapter

the novel filter procedure, the flow's large-scale organization flow is discussed by means of visualizations and a spectral analysis. The simulations used for this discussion throughout the present chapter are summarized in Table 8.1.

8.1 Scaling of the Very-Large-Scale Structures

The vertical structure of a globally intermittent flow realization (case I150LH around $t^- \simeq 0.25$) is shown in Fig. 8.1. There are stripes with relatively low enstrophy[2] in the buffer layer. These regions (enclosed by contour lines in Fig. 8.1) are characterized by a higher buoyancy and the absence of turbulent fluctuations in the vertical and streamwise components of velocity; they are seen as diagonally elongated smooth orange patches in Fig. 8.2. In those regions, turbulence is locally absent—the flow as a whole is globally intermittent though turbulent. The other regions of the flow where the vorticity is higher and also fluctuates much more (dark colors in Fig. 8.1d; the iso-contour of $\ln \zeta^- = 9.65$ is shown in panels (a)–(c)) are turbulent in the usual sense. Inside these turbulent regions, turbulence appears morphologically similar to that under neutral stratification (Chap. 6, Fig. 6.11).

A segregation of the flow into two partitions with similar characteristics inside each of them, but a strongly different appearance of the flow among the two partitions is also manifest in the probability density functions (Fig. 8.3). Close to the surface, high probability densities occur for velocities (u/G and v/G) close to zero. These extend further into the buffer and surface layers when the flow is exposed to such strong stability that it becomes globally intermittent and laminar patches occur ($Ri_B = 0.31$ vs. $Ri_B = 0.15$). Concomitantly, the probability density of the buoyancy widens, and becomes close to bimodal. One mode originates from high

---

[2]Here, already the enstrophy of the high-pass-filtered field introduced in Sect. 8.3.1 is used. The unfiltered enstrophy would illustrate the absence of turbulence by a smoother structure, but not by a reduced level of enstrophy.
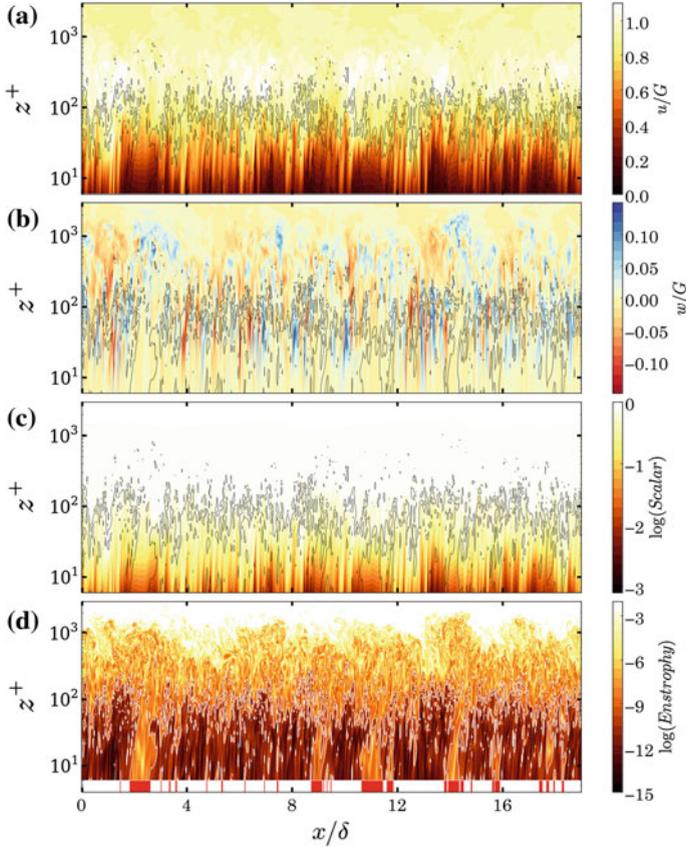
Fig. 8.1 Vertical cross-section of case I310LH ($Ri_B = 0.31$) at $t^- \simeq 0.25$ along the streamwise direction. Shown are **a** streamwise velocity u/G, **b** vertical velocity w/G, **c** logarithm of buoyancy, $\ln[(1 - b)/B_0]$, **d** logarithm of enstrophy of a high-pass-filtered field $-\ln \zeta_{hi}^-$ (cf. Sect. 8.3.1). Contour lines (*black* in panels **a**–**c**, *white* in panel **d**) enclose turbulent regions as detected by the method developed in Sect. 8.3. *Red bars* in (**d**) are the result of a two-dimensional partitioning where a whole flow column is detected to contain a laminar patch when an enstrophy threshold in the buffer layer is not exceeded

buoyancy originating from the surface, and the other is a result of downward mixing of fluid with low buoyancy from above.

The power spectral density (PSD) confirms the above mentioned morphological similarity of the small-scale structure under stable stratification (Fig. 8.4). The spectral distribution of energy density in the stratified and unstratified flows is very similar for wavelengths $\lambda^+ \lesssim 200$. In the range $200 \lesssim \lambda^+ \lesssim 1000$, the PSD is reduced, as seen for instance in the PSD of w, ϕ_{ww} along $z = \lambda_r/3$: The area with ϕ_{ww} is completely eliminated in the stratified case for $\lambda^+ \lesssim 700$. Above $\lambda^+ \simeq 700$ the extent of spectral space with ϕ_{ww} is reduced when only length scales belonging to the

(a)
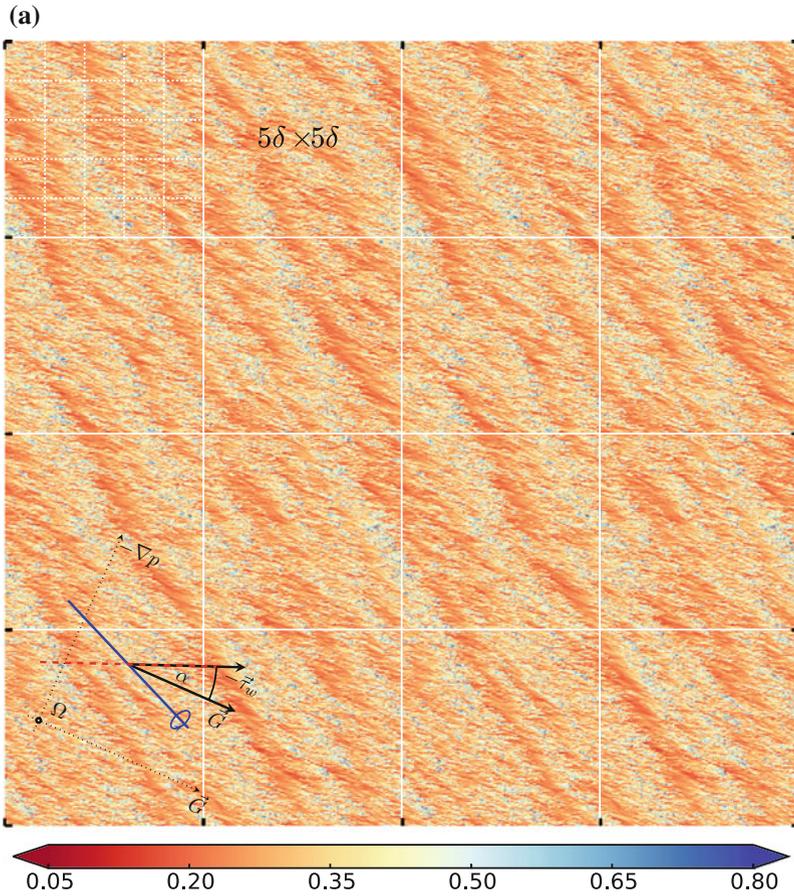
Fig. 8.2 **a, b** Streamwise velocity U/G in a horizontal plane in the buffer layer ($z^+ \simeq 20$, case $\text{I}310$ at $t^- \simeq 0.25$). Panel (**a**) shows the full domain, where panel (**b**) zooms on the section ($1/4 \times 1/4$) on the upper right of panel (**a**). **c** Enstrophy iso-surface of $\omega^2 \simeq (20\omega_{rms}(\delta))^2$ colored by horizontal wind speed in the range $0.4 < \sqrt{u^2 + v^2}/G < 1.15$. A schematic of flow organization as discussed in the main text is overlaid on panels (**a**) and (**b**). Streaks aligned with the surface shear stress are represented by the *red dashed line*. The orientation of the large-scale structures in the outer layer is shown by the *blue line*, and the directions of geostrophic wind and wall shear stress are indicated by *black arrows*. Tick-marks are spaced by 5δ in panel (**a**) and by δ in panel (**b**)

spectrum of motions smaller than $\delta^+ \simeq 1500$ are considered. This agrees with the prediction of linear theory, and confirms the role of the Obukhov length which for the data plotted here is $L_O^+ \simeq 250$

(b)

$$\delta \times \delta$$

(c)
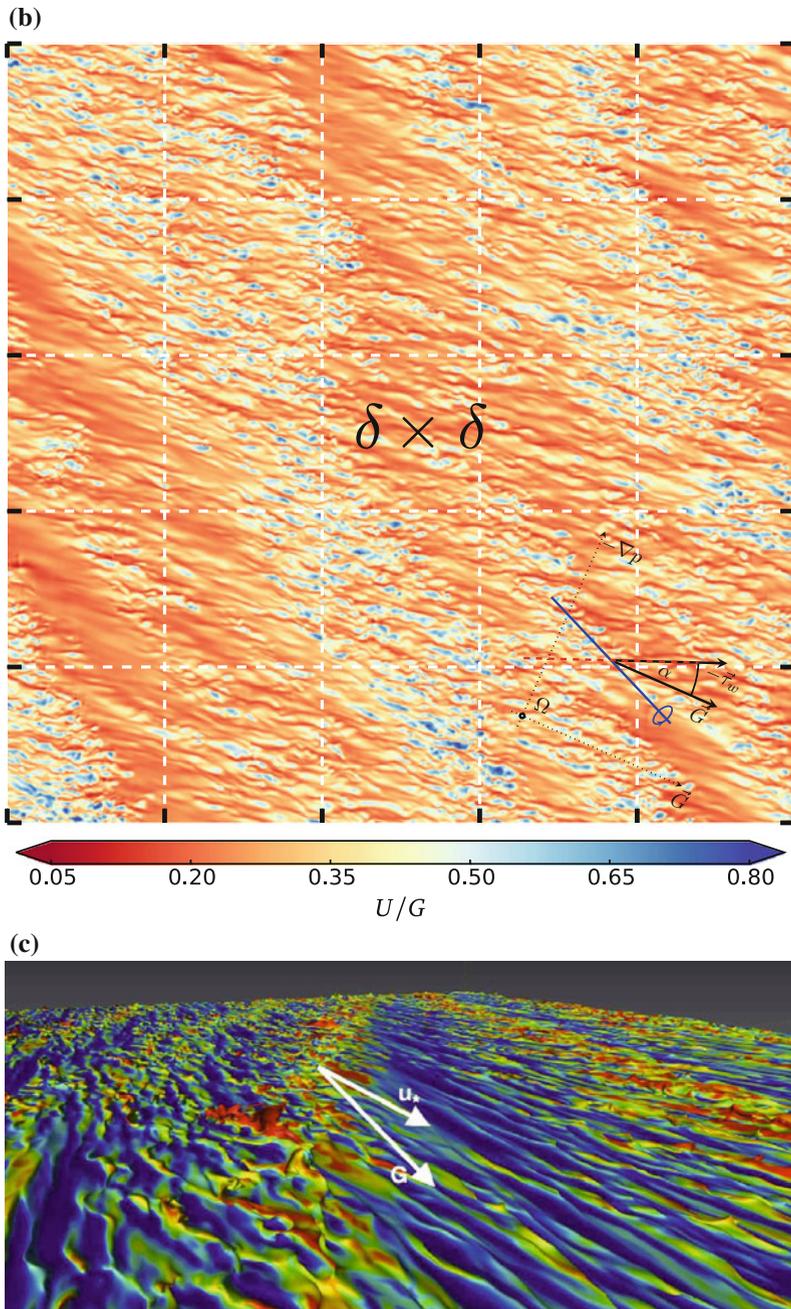
Fig. 8.2 (continued)

While linear theory predicts a larger impact of stratification at larger wavelength, a decrease of PSD at the very large scales is not be found here. Already under neutral stratification, the spatial organization of the outer layer leaves a footprint in the logarithmic layer (Chap. 6, Sect. 6.3.3 and Fig. 6.11). This is even more so for the intermediately stable case I310LH, where around $z^+ \simeq 10$ the PSD of the streamwise velocity increases beyond that in the neutrally stratified case for particular modes at wavelengths larger than δ (Fig. 8.4). This intensification of the large-scale structure in the surface layer is not present in ϕ_{ww} insinuating a non-turbulent mechanism is at play here. The angle along which the laminar and turbulent patches are oriented is estimated to be around 23° clockwise with respect to the geostrophic wind. This is the same orientation that is observed for the large-scale outer-layer structures under neutral stratification (Chap. 6, Fig. 6.11). The dominant wavelength λ of these smooth patches is also seen in the flow visualizations (Fig. 8.2) where the smooth low-velocity regions are spaced by 2–5δ.

What sets the scale of these dominant large-scale structures? The power spectra in Fig. 8.4 show that—when expressed in inner scalings (λ^+)—the position of the large-scale modes in the spectrum shifts whereas the position of these modes expressed in terms of δ, the boundary layer depth scale (vertical blue lines), does not change. This behavior shows that these modes are set by outer scales, and do not scale with the wall unit. When expressed in wall units based on the local-in-time $u_\star(t)$, the length scale of these large-scale motions is independent of the Reynolds number (spectra at $Re = 500$ also exhibit a maximum of the power spectral density at $\lambda \simeq 5\delta$; not shown). This illustrates the two-dimensionality of the problem in the parameter space: With respect to changes of stratification (Ri_B), the flow is self-similar when considered with respect ot outer scales. With respect to changes in the Reynolds number Re, the flow is self-similar when considered with respect to wall scales.

The independence of the large-scale motions of the Reynolds number gives relevant clues about the instability mechanism at work in the present flow under strong stratification. Given the flow's globally intermittent nature in the cases with $Re = 500$, one might have argued that global intermittency is a transitional-Reynolds-number effect and as such not relevant at arbitrary Reynolds number. This argumentation is invalidated by the Re-independent scaling of the mechanism and illustrates the present work's relevance for atmospheric applications. A paradoxon in this mechanism is the increased importance under strong stratification of an outer length scale originating from an inviscid mechanism (where commonly it is argued that vertically distant layers decouple under increasing stratification). This paradoxon is manifest in the power spectra which exhibit an increased energy content at wavenumbers $\lambda > \delta$ due to the very-large-scale mechanism. A substantially decreased energy density is observed in the intermediate range of wave numbers $200 \lesssim \lambda^+ \lesssim 700$ where the stratification acts, and we find only very small impact of stability for $\lambda^+ \lesssim 100$.[3]

---

[3]To draw these conclusions, a scale separation of at least three orders of magnitude in the flow is necessary.
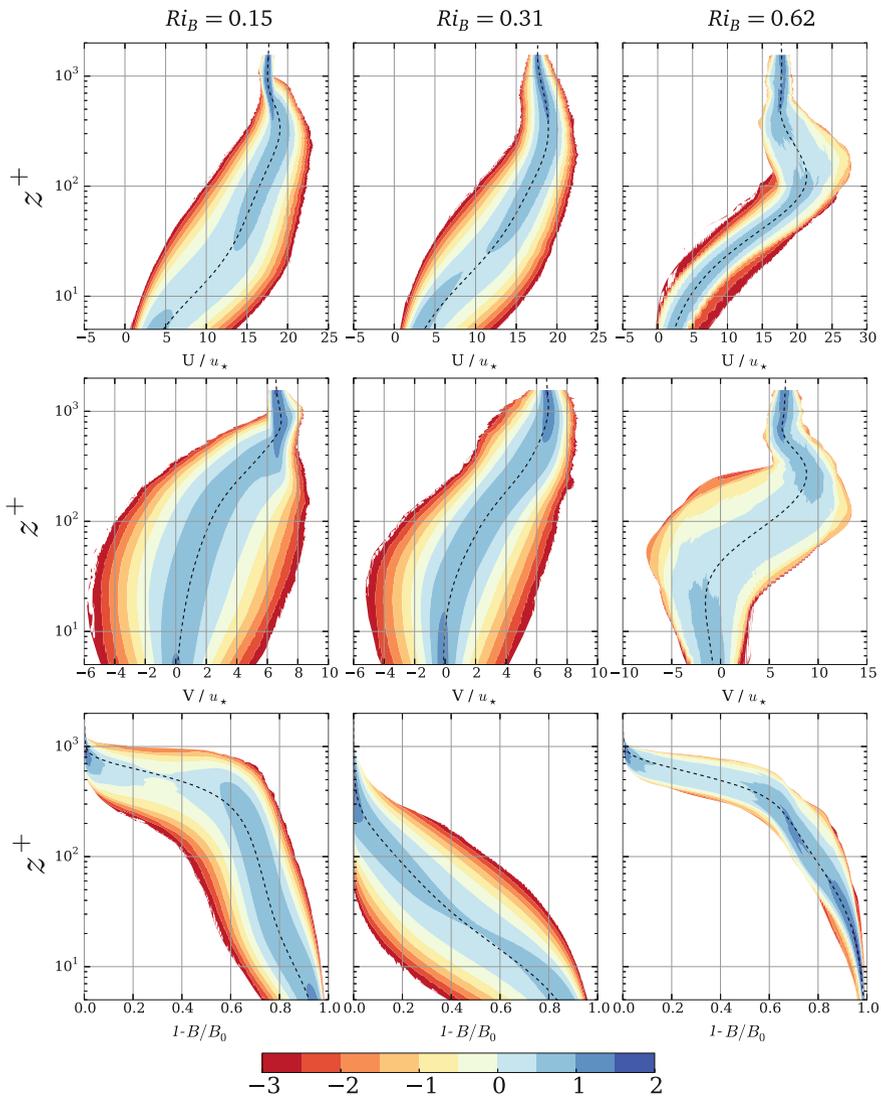
Fig. 8.3 Contours of decadic logarithm of probability density for the streamwise velocity component u (*upper Panel*), the spanwise velocity component v (*central panel*) and the buoyancy normalized between 0 and 1 (*lower panel*); the mean is shown as *black dashed line*. *Left column* shows case I150LH, *central column* I310LH, *right column* I620LH
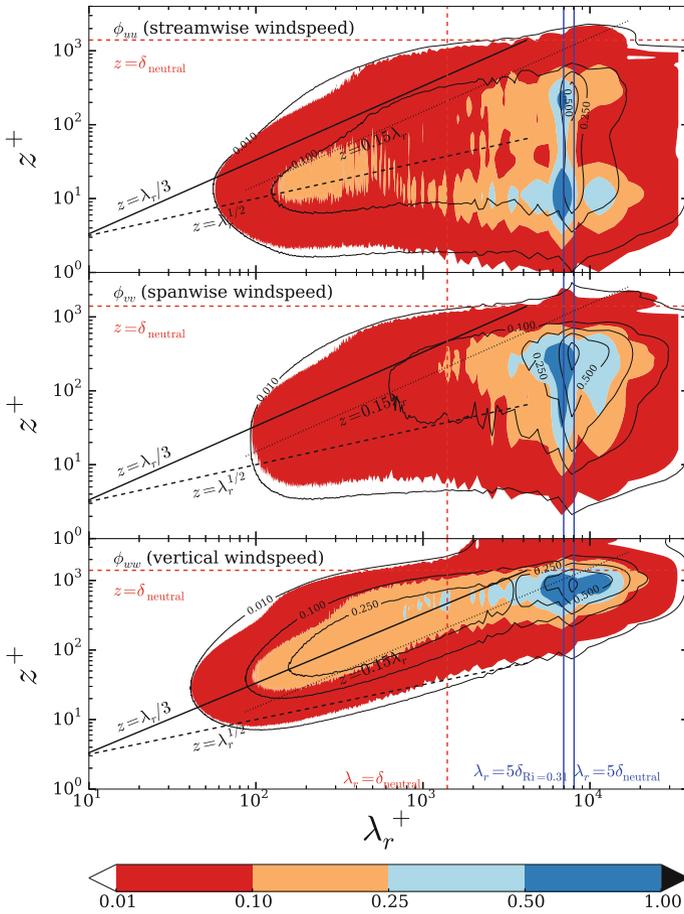
Fig. 8.4 Power spectral density of u, v and w normalized with the maximum of the neutral reference over all wavenumbers *and* heights. *Shading* is for case I310LH at $t^- \simeq 0.25$, contours show the neutral case N1000. All wavenumbers and heights are normalized by the local-in-time wall unit $\nu/u_\star$

8.2   Critical Stability

When discussing the impact of stability in an atmospheric context, the Obukhov length L_O (Eq. 2.13c) is a ubiquitous measure. It can be interpreted as a length scale above which stratification exerts substantial damping forces to an eddy; hence, L_O^+, the inverse of the gradient Richardson number, Ri_G, at the surface, is a measure of the biggest possible scale separation in a stratified flow. Introducing $L_O^+ := L_O u_\star/\nu$, Flores and Riley (2011) indeed suggest that L_O^+ is the relevant large scale when a Reynolds number is sought that takes into account the effect of stratification. The time series of L_O^+ presented in Fig. 8.5a illustrate once more that the set of simu-
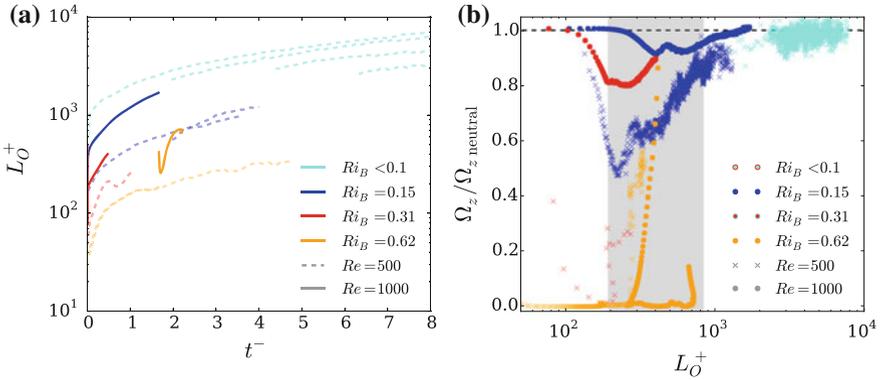
Fig. 8.5 **a** Temporal evolution of the Obukhov length L_O^+ for all simulations listed in Table 7.1. Cases with $Re = 500$ are shown as dashed opaque lines, cases with $Re = 1000$ as full lines. The time axis measures time since the flow is exposed to any kind of stratification, i.e. the cases started from a stratified initial condition do not start at $t = 0$ but at the IC time listed in Table 8.1. **b** Scatter plot of Ω_z (Eq. 8.1) normalized with $\Omega_{z,\text{neutral}}$ versus L_O^+

lations carried out spans a wide range of stratification from L_O^+ on the order of 10 to L_O^+ on the order of several thousand, commensurate with several boundary layer depths δ^+. The Obukhov length depends on both changes in the friction velocity and changes in the surface gradient. In case I620LH—due to a sudden increase of the stratification—, turbulence collapses rapidly, and $u_\star$ drops by about 50 % before the viscous weakening of the surface gradient sets in, which results in an anomalous drop of L_O^+. In all the other cases, L_O^+ increases monotonically with time which is mainly due to a decrease in the surface buoyancy gradient, but supported by a small increase in the wall friction $u_\star$ when the stratification weakens.

The vertical component of vorticity r.m.s. integrated over the buffer layer

$$\Omega_z := \int_{10}^{30} \langle \omega_z^+ \omega_z^+ \rangle \mathrm{d}z^+ \tag{8.1}$$

is normalized with the corresponding value of neutral stratification and plotted versus the Obukhov length L_O^+ in panel (b) of Fig. 8.5. Ω_z is a very sensitive measure of turbulent mixing, and it is less sensitive to large-scale non-turbulent motions under very strong stratification than for instance the TKE as shown in Chap. 7. The behavior of Ω_z may be discussed in terms of three ranges of L_O^+ as indicated by the shading in Fig. 8.5b:

- Below $L_O^+ \simeq 200$, turbulence may not be sustained, and Ω_z decreases until it has reached zero or passed the threshold.
- In the range $200 < L_O^+ < 800$ the trajectory that a simulation takes in the $L_O^+ \times \Omega_z$ space depends on its initial condition, i.e. it is not determined by L_O^+ and Ω_z alone and trajectories may cross. If the level of turbulence is sufficiently high, and the background stratification is sufficiently small, the flow may recover as in the

cases with $Ri_B < 0.62$. If the level of turbulence in the boundary layer is already significantly reduced and the boundary layer is stratified as in the case I620LH, the turbulence collapses. Once the turbulence has collapsed, the flow stays laminar until L_O^+ has grown beyond some threshold much larger than 200.

- Above $L_O^+ \simeq 800$ the flow recovers irrespective of the initial condition, at least for the cases considered here.

The hysteresis in the intermediate range of L_O^+ described above is indicative of a non-linear instability mechanism: a perturbation beyond a threshold magnitude is necessary to keep the flow turbulent while it is linearly stable, and this threshold magnitude depends on the value of L_O^+. The intermediate range of L_O^+ is precisely the range in which the flow is globally intermittent. A morphologically similar type of intermittency is also observed in a number of other flows including plane Couette flow (Deusebio 2015), channel flow under the impact of stabilizing rotation, buoyancy and magnetic forces (Brethouwer et al. 2012) but also pipe flows (Hof et al. 2010). In the latter, the occurrence of laminar patches has been linked successfully to a non-linear stability mechanism in alinearly stable flow, which hints at a very general mechanism behind what is now called *weak turbulence* (Mahrt 2014) in the atmospheric context.

Since a collapse of turbulence is caused by the absence of production in the buffer layer, Ω_z is indicative of such a collapse, and the finding that it is governed by L_O^+ is supportive of recent claims by Flores and Riley (2011) and Deusebio (2015) that the collapse of turbulence is governed by L_O^+. The clear distinction of three ranges of L_O is only possible here due to the use of $\nu/u_\star$ for normalization. When plotted against L_O^-, the data from cases with $Re = 500$ would shift to the right by a ratio $\delta^+(Re = 1000)/\delta^+(Re = 500) \simeq 1399/487$ with respect to that from the cases with $Re = 1000$; a clear distinction of the behavior of Ω_z based on L_O is then impossible. The critical range of L_O^+ can be interpreted as a critical range of heights (it would be that range of heights below which the Obukhov length must not fall for the flow to remain turbulent). When expressed in outer scalings, this critical range of heights depends on the Reynolds number, and it is $0.4 \lesssim z^- \lesssim 2.0$ for $Re = 500$ and $0.15 \lesssim z^- \lesssim 0.5$ at $Re = 1000$. While this does not contradict the findings of Nieuwstadt (2005) and van de Wiel et al. (2012), the sensitivity of this range to the Reynolds number illustrates that a scaling in terms of inner units is appropriate here.

The data in Fig. 8.5a also demonstrate that the bulk Richardson number is not an appropriate parameter to study the collapse of turbulence in the vicinity of the surface as anticipated in Sect. 2.2.3: it does not capture effects of changes in the Reynolds number appropriately. For similar bulk Richardson numbers, a very different evolution of L_O^+ is found. In the present set-up, L_O^+ is a more appropriate parameter to retain the strength of the effect of stratification on turbulence in the surface layer when changing the Reynolds number. In our set-up, the initial condition for the simulations where the buoyancy is initialized from a synthetic field (cf. Chap. 2) is such that the buoyancy gradient $\partial_z b/B_0$ at the surface is directly proportional to Ri_B. To keep L_O^+ constant when the Reynolds number changes, this requires

$$Ri_B \propto \nu^{-1} \tag{8.2}$$

Such a dependency on the viscosity is not a low-Re-effect, but consequence of a set-up where the stratification is concentrated into a very thin layer close to the surface. Physically, this means that the collapse of turbulence is a near-surface process and as such governed by near-surface parameters and scalings. While the scale-separation across the boundary layer (as indicated by Ri_B and Re) might be large, it is the stratification at the surface, i.e. L_O^+, to which the flow responds on a short time scale and which governs the turbulence dynamics in the buffer layer. The buffer layer is the major source region of turbulence in a wall-bounded flow. Hence, L_O^+ can be interpreted in terms of a critical Reynolds number, and it is not surprising that $L_O^+ \simeq 200$ is a limit for the existence of turbulence—similar in magnitude to the critical Reynolds number in neutrally stratified Ekman flow $Re_{crit} = 115$ (Lilly 1966). Another possible interpretation is that in terms of a minimal flow unit, where the critical box size is also of the order of 10^2 wall units.

8.3 Quantification of Intermittency

In the above sections, I show that the flow may become globally intermittent, and that this global intermittency is not a transitional-Re effect, but a phenomenon intrinsic to the flow at large stability. The above investigation of critical stability in terms of L_O^+ reveals that global intermittency may be relevant over a significant fraction of the $Re \times Ri_B$ parameter space, namely that fraction where L_O^+ may be in the range $200 \lesssim L_O^+ \lesssim 800$. The coexistence of turbulent and laminar patches of fluid in this part of the parameter space poses limitations to a conventional statistics approach as is already demonstrated in the limit of neutral stratification where external intermittency impacts on statistics in the surface layer. In a globally intermittent flow, a substantial fraction of the flow is non-turbulent, even in the vicinity of the surface. Global intermittency can hence be quantified in terms of the extent of laminar patches in the vicinity of the surface where in absence of strong stabilizing body forces a wall-bounded flow is turbulent-throughout. The flow is then understood to be composed of two partitions, a laminar and a turbulent one. If the laminar partition has non-zero extent, statistics may be strongly influenced by the alternation of means between the turbulent and non-turbulent flow partition. As demonstrated below, the separate study of statistics in the turbulent and non-turbulent partitions of the flow improves understanding of re-laminarization and subsequent recovery.

A distinction between regions of turbulent and non-turbulent flow based on vorticity has proven difficult for a flow where turbulence is absent even close to the surface. This is due to high values of background enstrophy and may be overcome by a filter approach. Here, the filters (Eq. 8.4) are introduced, and statistics are compared between unfiltered as well as high-pass and low-pass filtered fields. Based on the high-pass filtered fields, intermittency factors are presented. A comparison of high- versus low-pass filtered fields suggests that the filter operation at length scale δ constitutes a spectral decomposition of the flow field into turbulence and wave modes of the flow.

8.3.1 Definition of Flow Filters

The flow is partitioned based on the vorticity, using the intermittency function

$$\gamma(z) = \langle H(\omega - \omega_{\text{threshold}}) \rangle, \tag{8.3}$$

where H (cf. Sect. 6.3.1, Eq. 6.4) is the Heaviside function, ω is the local vorticity magnitude, and $\langle \cdot \rangle$ denotes a horizontal average (Pope 2000). As a threshold $6.9\omega_{\text{rms}}(\delta_{95})$ is used, where $\omega_{\text{rms}}(\delta_{95})$ is the r.m.s. of the vorticity at $z = \delta_{95} \simeq 0.66\delta$. As demonstrated by a comprehensive body of work following Corrsin and Kistler (1955), this approach is well-suited to detect external intermittency (Pope 2000). Section 6.3 demonstrates that the approach is also well-suited to detect external intermittency in neutrally stratified Ekman flow. The same section also investigates how $\gamma(z)$ depends $\omega_{\text{threshold}}$. The detection of global intermittency under stable stratification based on this method is, however, difficult: The contribution of the mean velocity gradient to the total vorticity of the flow field dominates the turbulence contribution to the vorticity close to the wall (Fig. 8.7b). To overcome the problem of partitioning the flow, a horizontal high-pass filter of the velocity fields in Fourier space is used. The filter transfer function is

$$F_\delta(k_h) = \frac{1}{2} \left\{ \text{erf} \left[\ln \left(\frac{k_h}{k_\delta} \right) \right] + 1 \right\}, \quad \text{with} \quad k_h = \sqrt{k_x^2 + k_y^2}, \tag{8.4}$$

which is illustrated in Fig. 8.6. Here k_x and k_y are wavenumbers in the stream- and span-wise directions and the filter wavelength is set as $k_\delta = 2\pi/\delta$. The filters $\mathscr{F}_\delta^\pm$ are then defined by the filter transfer function $\pm(F_\delta - 0.5) + 0.5$. That is, the spectral decomposition of the flow fields into

$$\mathbf{u}_{\text{hi}} = \mathscr{F}_\delta^+ \{\mathbf{u}\} \text{ and } \mathbf{u}_{\text{lo}} = \mathscr{F}_\delta^- \{\mathbf{u}\} = \mathbf{u} - \mathbf{u}_{\text{hi}} \tag{8.5}$$

Fig. 8.6 Filter transfer function versus normalized wavenumber k^-

is considered. When the filter $\mathscr{F}^+$ is applied to the field, the enstrophy in the quiescent patches is reduced to a much lower level than inside turbulent patches (Fig. 8.7c vs. d). The structure inside the turbulent patches is not affected by the filter (the panels (a) and (b) are visually identical); hence this filter is in principle suitable to overcome the problem of partitioning the globally intermittent flow close to the surface. A second even simpler filter is the *Reynolds* decomposition where upper-case letters denote averages and lower case letters fluctuations.
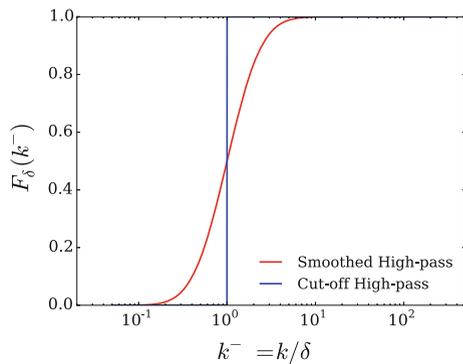
8.3.2 Detection of Global Intermittency

When attempting to quantify global intermittency, vorticity appears as an attractive quantity because of its pivotal role in locally defining turbulence. In the neutrally stratified flow, contributions from the high-pass filtered field $\mathbf{u}_{hi}$ dominate the r.m.s. of the vorticity fluctuations ω_{rms} at all heights (Fig. 8.8a). The vorticity r.m.s. residing in the low-pass filtered field $\mathbf{u}_{lo}$ is less than one third of that contained in $\mathbf{u}_{hi}$. The same holds for the weakly stratified case, supporting further the aforementioned and well-established similarity between the neutral and weakly stably stratified flow regimes. When stratification is increased to $Ri_B = 0.62$, much less vorticity r.m.s. is contained in $\mathbf{u}_{hi}$, in particular close to the wall ($z^- < 0.2$). There, vorticity r.m.s. is largely explained by the low-pass-filter contribution. A contributor to this vorticity r.m.s. are large-scale coherent motions. These large-scale modes belong to the spectrum of turbulent motions in the sense that the flow as a whole is turbulent. Within laminar patches, the flow does, however, not seem quite turbulent. This situation is not any different from the turbulent jets considered in the works of Townsend and Corrsin & Kistler, but the standard indicator function of turbulence—based on the vorticity of the flow field $\mathbf{u}$—does not work because 'external' intermittency occurs in the vicinity of the wall. Here, turbulent sub-volumes are not the only contributor to vorticity, but also the non-turbulent sub-volumes possess substantial vorticity which determines the vorticity of the full field $\mathbf{u}$ inappropriate to locally indicate small-scale activity.

Profiles of TKE (Fig. 8.8b) also show the change from fluctuations dominated by small-scale activity in the neutrally and weakly stratified cases to fluctuations dominated by large-scale activity under strong stability. TKE, however shows a strong buoyancy oscillation (Chap. 7) and concomitantly is less sensitive to the absence of small-scale turbulent motion close to the wall. Therefore, intermittency factors presented in the following are based on the vorticity.

When the flow is partitioned based on unfiltered fields most of the flow is turbulent, even in the strongly stable regime (Fig. 8.9). This classical method of measuring external intermittency thus not only fails to detect the localized absence of turbulence close to the wall evident in Fig. 8.7b, d, but also gives it a higher turbulent area fraction close to the wall (up to $z^- = 0.1$ in Fig. 8.9) when compared to the neutral reference. When a Reynolds decomposition is used (Fig. 8.9), the intermittency factor is reduced slightly in the buffer layer (to ≈0.95 for the case I310LH and to ≈0.9 for the case
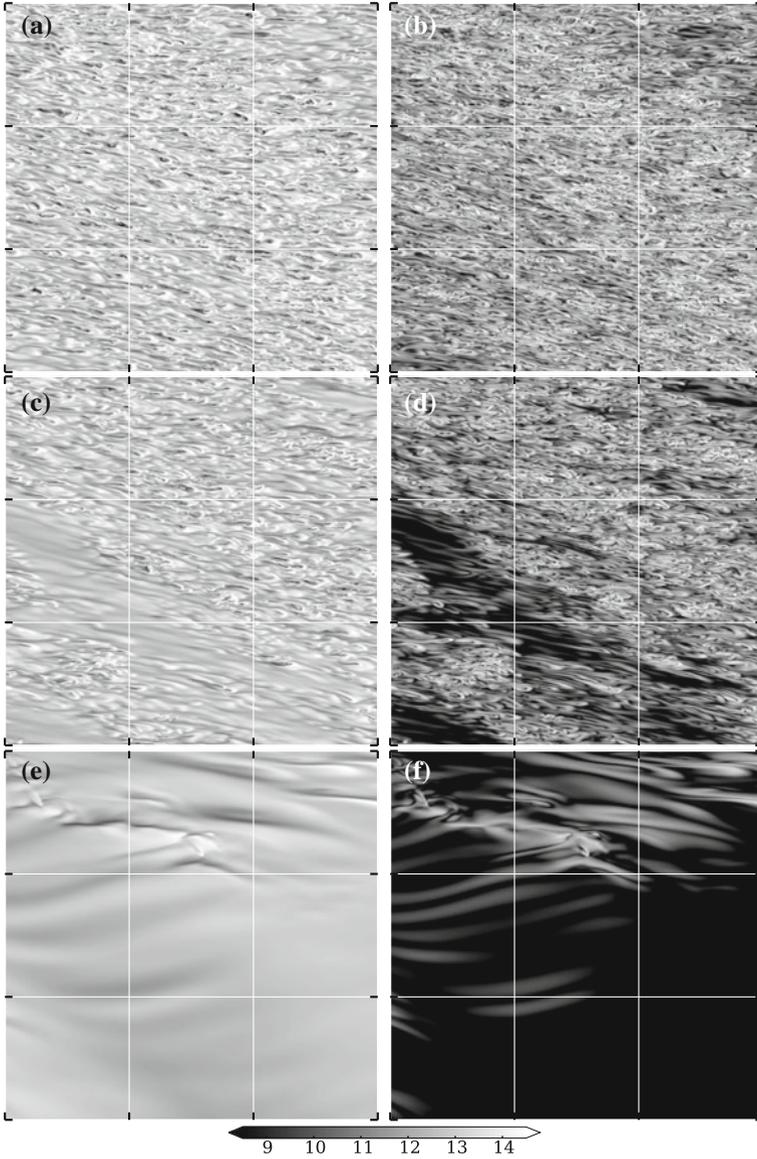
Fig. 8.7 Logarithm of vorticity modulus, $\ln \zeta^-$, at $z^+ = 15$; *Left column* shows $\ln \zeta^-$ of the field u, *right column* of the field u_{hi}. Only a subset of size $3\delta_{\text{neutral}} \times 3\delta_{\text{neutral}}$ ($\approx 1/36$ of the total box) is shown. Tick marks are spaced by δ_{neutral}. *Upper panel* $Ri_B = 0.15$, ($t^- \simeq 1.50$, $L_O^+ \simeq 1500$) *Central panel* $Ri_B = 0.31$, ($t^- \simeq 0.25$, $L_O^+ \simeq 200$), *Lower panel* $Ri_B = 0.62$, ($t^- \simeq 2.10$, $L_O^+ \simeq 400$)
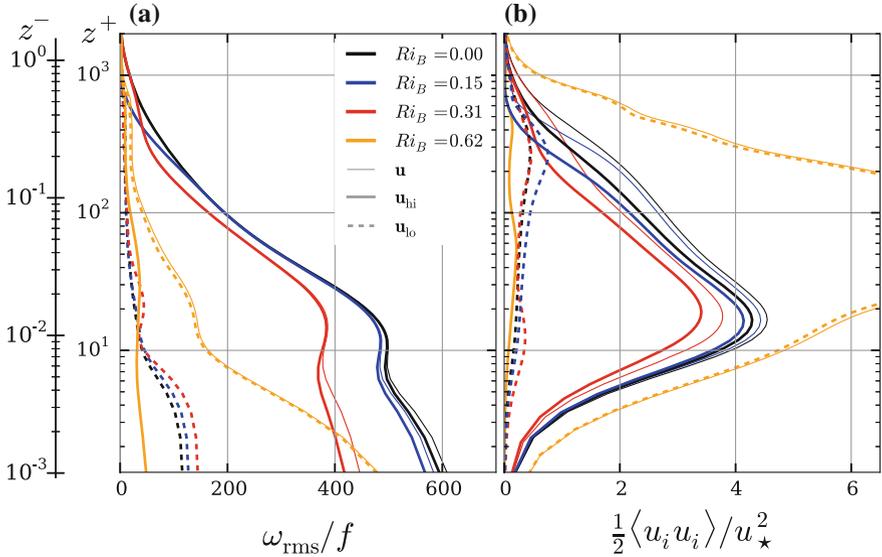
Fig. 8.8 Vertical profiles of the vorticity r.m.s. (**a**) and TKE (**b**) of the unfiltered (*thin*, *solid*), high-pass filtered (*thick*, *solid*) and low-pass filtered (*dashed*) field. The second vertical axis (z^-) is valid for the neutrally stratified case only

I620LH). This small reduction of the turbulent area fraction by only 10 % does not represent an appropriate measure of global intermittency in the flow, which reflects the large-scale contribution to vorticity r.m.s. in the surface layer. If high-pass filtered fields are used to partition the flow, the localized absence of turbulent motion in a vast part of the inner layer in case I620LH is correctly detected. Similarly, a non-turbulent fraction around 15 % in the case I310LH is consistent with the fields presented in Figs. 8.1, 8.2 and 8.7. At the same time, for the neutrally stratified case, the consideration of filtered fields has no impact on $\gamma(z)$ (Figs. 8.7b and 8.9).

The details of the curves $\gamma(z)$ are sensitive to the choice of $\omega_{\text{threshold}}$ because of a vorticity source in the outer-flow region due to rotation of the reference frame (Chap. 6, Sect. 6.3). This vorticity source makes the interface between turbulent and non-turbulent flow in terms of vorticity less sharp than commonly observed in flows without this source. The effect of this vorticity source is a shift of $\gamma(z)$ along the direction Oz when $\omega_{\text{threshold}}$ is varied. A Reynolds-number-dependency study in Chap. 6 shows that the profiles $\gamma(z)$ are independent of Re when $\omega_{\text{threshold}}$ is defined in terms of the vorticity r.m.s. at some fixed height in outer scales z^-, i.e.

$$\omega_{\text{threshold}} = C_0 \omega_{\text{r.m.s.}}(z_{\text{ref}});$$
$$\text{with } z_{\text{ref}}^- = C_1; \quad C_0, C_1 \in \mathbb{R}$$

(8.6)
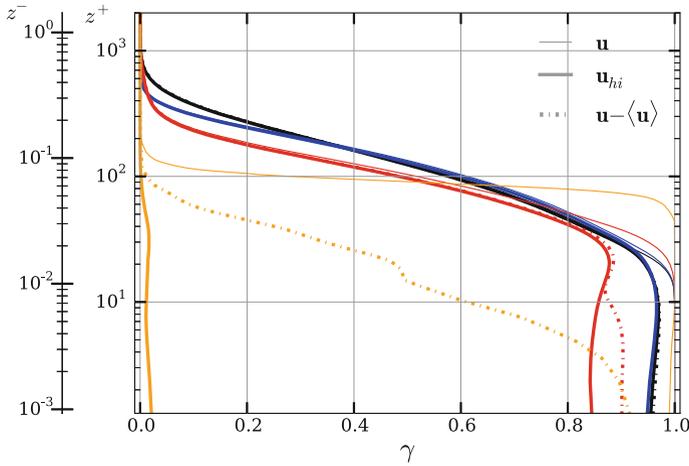
Fig. 8.9 Intermittency factor γ with a threshold vorticity $6.9\omega_{rms}(\delta_{95})$ calculated from a filtered (*solid thick*–$\mathscr{F}_\delta^+$, *dash-dotted*–Reynolds decomposition) and unfiltered (*solid*, *thin*) field. Coloring is as indicated in the previous Fig. 8.8. The second vertical axis (z^-) is valid for the neutrally stratified case only

The choice of C_1 and C_2 is to some degree arbitrary. Thresholds C_0 and C_1 are chosen here such that the intermittent patches which are clearly visible in flow visualizations are detected in the enstrophy fields:

$$C_0 = 6.9; \quad C_1 = \delta_{95}/\delta \simeq 0.66 \Rightarrow \omega_{\text{threshold}} = 6.9\omega_{\text{r.m.s.}}(\delta_{95}) \tag{8.7}$$

(this corresponds to a value of 9.39 in Fig. 8.7). As for any conditioning method, care must be taken with the choice of the threshold, and the height at which γ drops and the particular value of γ in the surface layer depends on $\omega_{\text{threshold}}$. Independently of the threshold, a realistic reduction of the intermittency factor in the vicinity of the wall is—among the options considered here—only achieved with the high-pass filter operation $\mathscr{F}^+$.

8.3.3 Wave-Like Motions

The high-pass filter operation constitutes a spectral decomposition of the flow into large-scale wave-like motions and small-scale mixing eddies. This allows to quantify effects of waves on the statistics to a certain extent. In particular under stable stratification this aids the understanding of small-scale processes whose footprint in the statistics is otherwise obscured by wave effects or coherent large-scale motions.

By means of the buoyancy flux, the above decomposition into turbulent and wavy modes of the fields is now demonstrated. Neglecting contributions from the mixed terms, it is
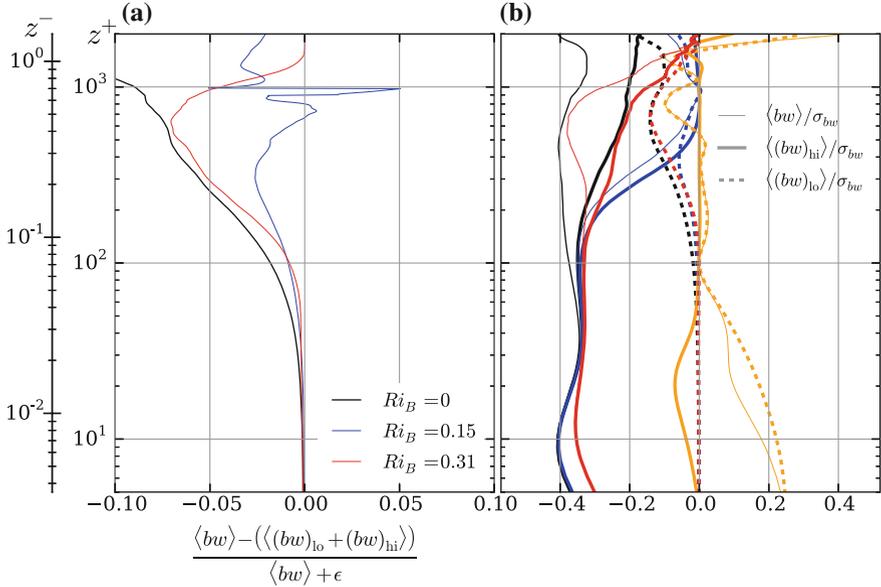
Fig. 8.10 a Residual of the flux $\langle bw \rangle$ in the term combining large-scale and small-scale motions as a fraction of the total flux. **b** Flux in the raw field $\langle bw \rangle$, the high-pass filtered field $\langle (bw)_{\mathrm{hi}} \rangle$ and in the low-pass filtered field $\langle (bw)_{\mathrm{lo}} \rangle$ normalized by $\sigma_{bw} := \sqrt{\langle bb \rangle \langle ww \rangle}$. *Coloring* indicated in panel (**a**) is as in previous figures. The second vertical axis (z^-) is valid for neutral stratification only

$$\langle bw \rangle \simeq \langle b_{\mathrm{lo}} w_{\mathrm{lo}} \rangle + \langle b_{\mathrm{hi}} w_{\mathrm{hi}} \rangle \qquad (8.8)$$

within very small deviations (2 % within the boundary layer, 5–10 % around $z = \delta$ where the flux is very small, Fig. 8.10). In the surface layer of the neutrally and weakly stratified cases, the buoyancy flux is entirely in the high-pass filtered contribution, i.e. $\langle bw \rangle \simeq \langle b_{\mathrm{hi}} w_{\mathrm{hi}} \rangle$. There, the correlation between b and w is relatively large. Only in the non-turbulent region aloft the turbulent part of the boundary layer, contributions in the large-scale signal matter (Fig. 8.10b). Here, the correlation between b and w drops by one order of magnitude indicating the change to a wave-dominated regime. Under strong stratification (case I620LH), the turbulence is extinguished, and nearly all the flux resides in large-scale contributions. This flux is, however, characterized by a very small—sometimes even negative—correlation coefficient between b and w. In fact, the net transport $\int \langle bw \rangle \mathrm{d}t$ is very close to zero (not shown) in the non-turbulent region aloft the turbulent part of the boundary layer. Such a small or no correlation between b and w is a feature of wave motions whereas turbulent motion is characterized by non-zero correlation between b and w (Sutherland 2010). This behavior of the correlation coefficient between b and w suggests that the filter operation based on the length scale δ—as anticipated above—constitutes a decomposition of the flow into wave and turbulence modes.

8.4 Conditional Statistics

The capability to detect global intermittency allows to compute conditional statistics that do not mix up the effects of a decreased intensity of turbulence on the one hand and a partial re-laminarization of the flow on the other hand. This allows for new insight into turbulence under strong stratification.

8.4.1 Concentration of Dissipative Flow Structures

It remains unclear, how strong the structure of turbulence changes under very stable stratification. When considering the flow as a whole, the effect of stratification in the strongly stable case is tremendous. This might make one expect that the turbulent eddies are fundamentally different from those in the neutrally stratified flow. A tracer of turbulence is the dissipation of TKE (Fig. 8.11b). In the cases I620LH and I310LH the dissipation in the entire flow is decreased by about 50 % respectively 90 %. If, however, solely the turbulent sub-volumes are considered, the dissipation is reduced by less than 10 % with respect to the neutrally stratified flow (Fig. 8.11a). This finding is consistent with the spectral analysis (Fig. 8.4) and flow visualizations
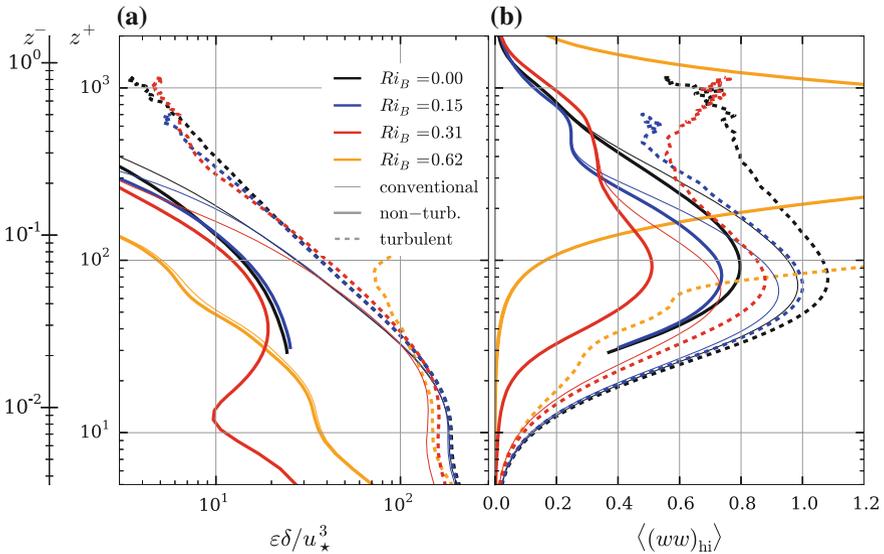
Fig. 8.11 a Viscous dissipation rate of TKE of the field **u** (*solid*) and conditioned to the turbulent (*dashed*, *opaque*) and laminar (*solid*, *opaque*) volume fraction. **b** Vertical component of TKE, $\langle ww \rangle$, conditioned as panel (**a**). The second vertical axis (z^-) is valid for neutral stratification only

(Figs. 8.2 and 8.7) which already suggest that the morphology of the flow inside a turbulent patch is very similar to that under neutral stratification.

The concentration of dissipative flow structures into the turbulent patches of the flow that is illustrated by the conditioned dissipation rate of TKE is also found in terms of $\langle ww \rangle$ (Fig. 8.11b), but less clearly. The reason for this less clear distinction between the turbulent and non-turbulent partition are the large-scale structures discussed in Sect. 8.1. These large-scale structures are more prominent in terms of absolute velocity than they are in terms of velocity derivatives. Hence the much higher sensitivity of TKE to such motions which is the reason for a less clear distinction between the TKE conditioned to the turbulent and non-turbulent flow partition.

The concentration of dissipative structures into a small volume fraction of the flow has consequences for resolution requirements under stable stratification. A common assumption when simulating stably stratified flows is that due to a reduced level of (mean) dissipation the resolution required for a corresponding simulation without the impact of stratification is always sufficient to study the stable case. In a globally intermittent flow, the dissipation is, however, not distributed homogeneously on a large scale and the reduction of the dissipation rate on average must not be mistaken for an indicator of less strict resolution requirements. A globally intermittent flow hence requires higher resolution than in a flow with the same averaged dissipation rate that is turbulent-throughout but with reduced turbulence intensity of individual turbulent structures. The concentration of turbulence dissipation into sub-volumes of the flow where turbulence acts vigorously over a relatively short amount of time may in fact demand an even higher resolution than necessary in a neutrally stratified flow.

8.4.2 Structural Interpretation

Turbulent and non-turbulent sub-volumes of flow can be attributed to their source region by analyzing the conditional statistics of buoyancy and velocity. Inside turbulent sub-volumes, the vertical velocity is positive. The streamwise velocity in the buffer layer is higher and in the rest of the surface layer lower with respect to the non-turbulent sub-volumes (Fig. 8.12a, b, d, e). This negative–positive combination of the signal implies decreased shear in the turbulent flow partition. In terms of a quadrant analysis this shows that turbulent sub-volumes in the surface layer mainly contribute to stress in the second quadrant ($u' < 0$, $w' > 0$) while the non-turbulent sub-volumes contribute to stress in the fourth quadrant ($u' > 0$, $w' < 0$). Buoyancy behaves very similar to the streamwise velocity and reduces in turbulent sub-volumes with respect to their non-turbulent counter-parts (Fig. 8.12c, f). This is a manifestation of the character of turbulence events as it is suggested by a structural approach to wall-bounded turbulence (Adrian 2007): Turbulence is sustained by ejections from below, and the fluid inside these sub-volumes originates from the wall. The fluid in the non-turbulent partition is entrained from the outer non-turbulent region aloft.
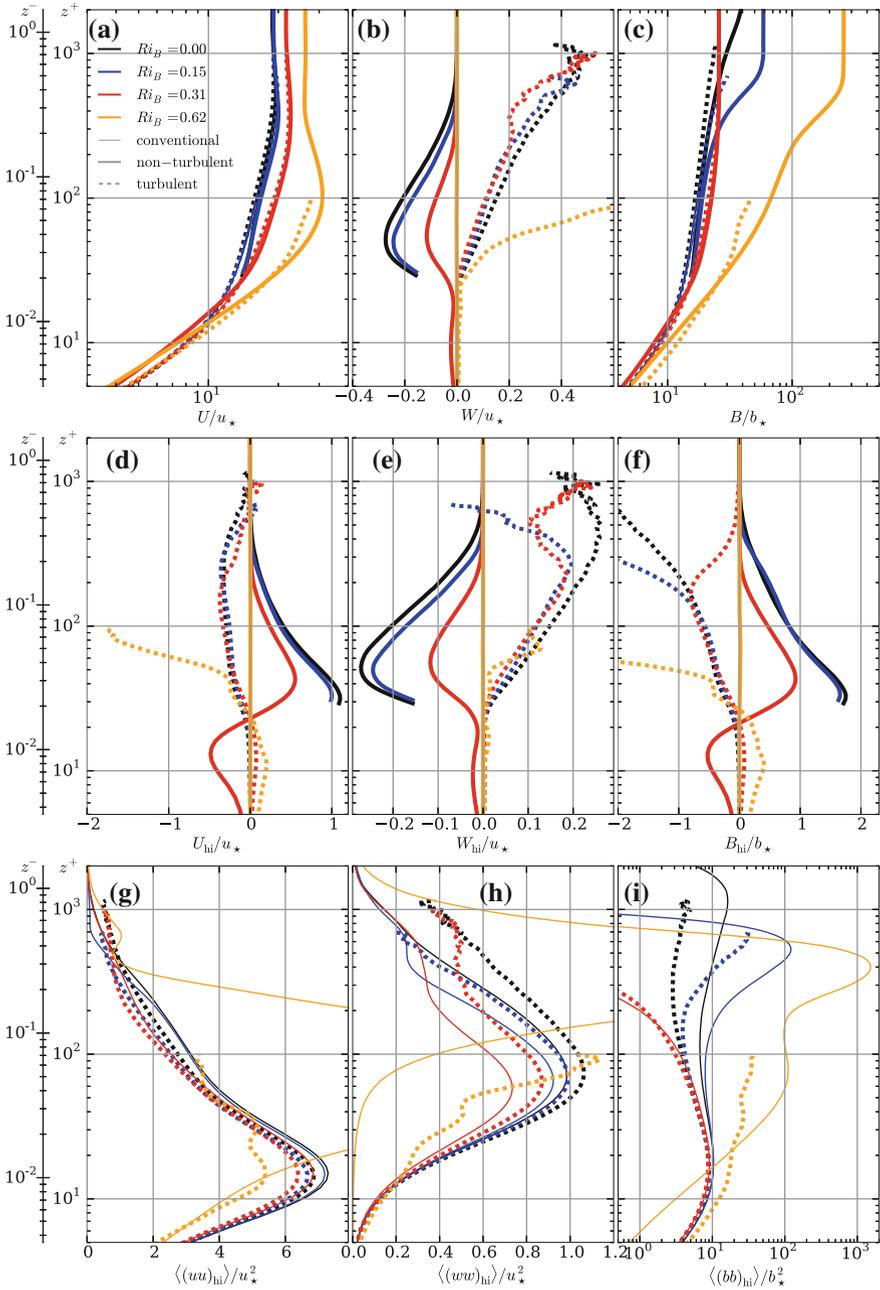
Fig. 8.12 Vertical profiles of filtered and unfiltered variables conditioned to non-turbulent and turbulent sub-volumes of the flow. The lines are drawn if the area fraction contributing to a partition exceeds 1 %. The second vertical axis (z^-) is valid for the neutrally stratified case only

This holds also for the scalar and velocity variances (Fig. 8.12g–i): their change inside the turbulent regions is very small when compared to changes in the total signal. When considering the second moment of streamwise velocity inside the buffer layer, the total variance in the turbulent field of the cases with $Ri_B \leq 0.31$ is up to 10 % larger than the variance inside turbulent and non-turbulent patches. Here, the contribution of variance from a different mean inside each of the patches is relevant.

A relatively small impact of stratification on the turbulent signal inside turbulent patches when compared to the impact of stratification on the total signal is consistent with the concentration of dissipation into the turbulent volume fraction. The nature of the turbulent signal does not depend on the stratification too strongly, but it is the intermittent fraction which governs the order-one decrease in turbulent dissipation, and fluctuation velocities when the flow is exposed to strong stratification.

8.5 Summary

In this chapter, the partial collapse of turbulence in the form of global intermittency is studied. The flow's large-scale organization is shown to scale with the outer scale δ, and not with the wall unit. The localized collapse of turbulence provoking the presence of these large-scale structures in the buffer and surface layers of the flow is, however, a surface-layer process and as such governed by inner scalings, namely the Obukhov length expressed in wall units L_O^+.

A conditioning method based on the vorticity of high-pass filtered velocity fields is developed, and I demonstrate its capability to detect global intermittency in a stratified Ekman flow over a wide range of stratifications. Under neutral stratification, the modified method yields results identical to those of the standard method based on the velocity of the full field. In addition, the modified method provides a spectral decomposition of the flow, and there is evidence that this decomposition is one into turbulence and wave modes. While this work only examines one particular case where rotation and strongly stable stratification interact, the concept put forward here—subject to a tuning of the filter wavelength and the vorticity threshold—also applies to wall-bounded flow with other stabilizing body forces such as magneto-hydrodynamic flows. Similarly, the present concept applies to stably stratified shear layers or rotating flows without density stratification.

The new partitioning method developed here allows for the first time to partition globally intermittent flow to turbulent and non-turbulent regions and yields new insight into the dynamics of turbulence under strong stratification: The main impact of stratification on turbulence is not a change in the dynamics of turbulence in the regions where the flow is turbulent, but it is rather a confinement of the turbulent area fraction which is quantified by the intermittency factor that can now be determined with the above partitioning method. This finding is consistent with the analysis of flow visualizations, spectra and probability density functions.

References

Adrian, R. J. (2007). Hairpin vortex organization in wall turbulence. *Physics of Fluids*, *19*, 041301–1–041301-16. doi:10.1063/1.2717527.

Brethouwer, G., Duguet, Y., & Schlatter, P. (2012). Turbulent-laminar coexistence in wall flows with Coriolis, buoyancy or Lorentz forces. *Journal of Fluid Mechanics*, *704*, 137–172.

Corrsin, S., Kistler, A. L. (1955). Free-stream boundaries of turbulent flows. *Technical Report TR1244-3133*, John Hopkins University, Washington DC, doi:10.1088/1468-5248/5/1/013.

Deusebio, E. (2015). The intermittency boundary in plane couette flow. *Submitted to: Journal of Fluid Mechanics*, 781, 298–329. doi:10.1017/jfm.2015.497.

Di Prima, R. C., & Swinney, H. L. (1981). Instabilities and transition in flow between concentric rotating cylinders. In H. L. Swinney & J. P. Gollub (Eds.), *Hydrodynamic instabilities and the transition to turbulence*. Berlin: Springer.

Fernando, H. (1991). Turbulent mixing in stratified fluids. *Annual Review of Fluid Mechanics*, *23*, 455–493.

Flores, O., & Riley, J. J. (2011). Analysis of turbulence collapse in the stably stratified surface layer using direct numerical simulation. *Boundary-Layer Meteorology*, *139*(2), 241–259. doi:10.1007/s10546-011-9588-2.

Hof, B., de Lozar, A., Avila, M., et al. (2010). Eliminating turbulence in spatially intermittent flows. *Science (New York, NY)*, *327*(5972), 1491–1494. doi:10.1126/science.1186091.

Lilly, D. K. (1966). On the instability of Ekman boundary layer flow. *Journal of the Atmospheric Sciences*, *23*, 481–494.

Mahrt, L. (2014). Stably stratified atmospheric boundary layers. *Annual Review of Fluid Mechanics*, *46*, 23–45.

Maslowe, S. A. (1981). Shear flow instabilities and transition. In H. L. Swinney & J. P. Gollub (Eds.), *Hydrodynamic instabilities and the transition to turbulence*. Berlin: Springer.

Nieuwstadt, F. T. (2005). Direct numerical simulation of stable channel flow at large stability. *Boundary-Layer Meteorology*, *116*(2), 277–299. doi:10.1007/s10546-004-2818-0.

Pope, S. B. (2000). *Turbulent flows*. New York: Cambridge Univ Press.

Rayleigh, L. (1880). On the stability, or instability, of certain fluid motions. *Proceedings of the London Mathematical Society*, *11*, 57–70.

Steeneveld, G.-J. (2014). Current challenges in understanding and forecasting stable boundary layers over land and ice. *Frontiers in Environmental Science*, *2*, 1–6. doi:10.3389/fenvs.2014.00041.

Sutherland, B. R. (2010). *Internal gravity waves* (1 ed.). Cambridge University Press.

Taylor, G. I. (1923). Stability of a viscous liquid contained between two rotating cylinders. *Philosophical Transactions of the Royal Society of London A: Mathematical, Physical and Engineering Sciences*, *223*, 289–343.

Tritton, D. J., & Davies, P. A. (1981). Instabilities in geophysical fluid dynamics. In H. L. Swinney & J. P. Gollub (Eds.), *Hydrodynamic instabilities and the transition to turbulence*. Berlin: Springer.

van de Wiel, B. J. H., Moene, A. F., Jonker, H. J. J., et al. (2012). The minimum wind speed for sustainable turbulence in the nocturnal boundary layer. *Journal of the Atmospheric Sciences*, *69*(11), 3116–3127. doi:10.1175/JAS-D-12-0107.1.

Part IV
Concluding Remarks

Chapter 9
Implications for the Study
# of the Atmospheric Boundary Layer
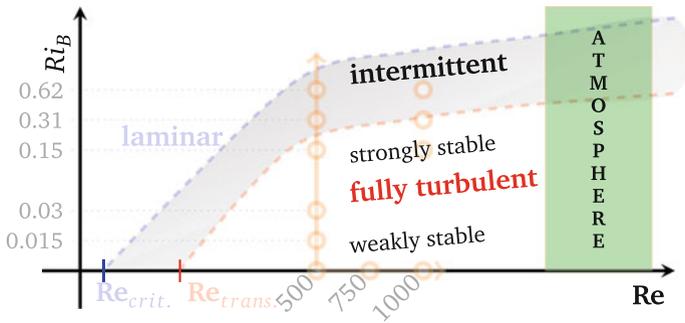
This work is motivated by a lack of process-level understanding in the SBL
(Chap. 1)—a meteorological problem at its core. The direct simulation of a tur-
bulent flow is relatively new in a meteorological context, and the technical framing
of this work is borrowed from an engineering context where DNS as a tool in tur-
bulence research is widely used since decades (Moin and Mahesh 1998). In fact,
part III of this book studies Ekman flow as a fluid-mechanics problem. In the present
chapter, the key findings of this work are outlined in a more applied context, and
their implications for work on the SBL are discussed.

9.1 The Rough-Wall Problem and the Wall Unit

A fundamental difference of the set-up used here with respect to a real boundary
layer is the character of the wall. In the present simulations, it is infinitely aerody-
namically smooth, and the local dissipation, set by the kinematic viscosity ν, governs
the extent of the smallest length scale relevant to the flow. This length scale is the

Fig. 9.1 Vertical profile of the Kolmogorov scale η calculated from the dissipation rate of turbulent kinetic energy ε at each height
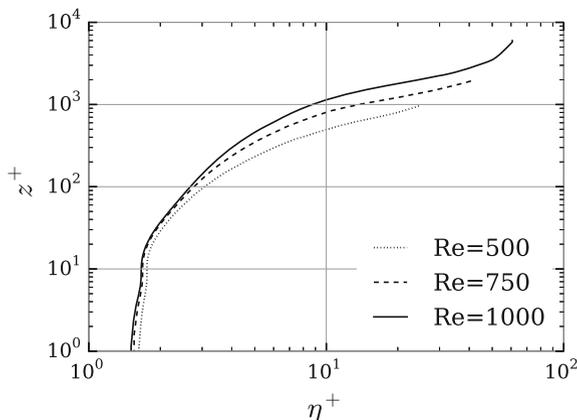
Kolmogorov scale η and was originally introduced for homogeneous isotropic turbulence by Kolmogorov (1941). In the present inhomogeneous anisotropic case, η is not single-valued, but described by a profile—a reflection of the changing character of turbulence across the depth of the PBL. For $z^+ < 15$, that is, in the viscous and buffer layers, $\eta^+ \simeq 1.5$ independent of height (Fig. 9.1).

The idealization of an infinitely smooth wall is not even attainable in laboratories, and a length scale z_r related to the roughness of the surface enters in the set of parameters of the problem. The presence of roughness affects the range of scales available for turbulent motion: local boundary layers with different dynamics form in the rough region, and if z_r becomes sufficiently large, the smallest scale relevant to the turbulent PBL as a whole is no longer η, but z_r. Provided the roughness is homogeneously distributed and $z_r \ll \delta$, it has been demonstrated that the scaling laws for smooth walls also hold over rough surface when η is replaced by an appropriate roughness length z_r (Monin and Yaglom 1975; Jiménez 2004). Hence, all vertical profiles shown in this dissertation in terms of the wall unit may as well be read in terms of the roughness length. Not only applies this to vertical profiles, but also to the range of critical stability $200 < L_O^+ < 800$. This alternative interpretation explains why global intermittency is frequently found in atmospheric flow even if the surface heat flux is rarely large enough for $L_O^+ = L_O u_\star / \nu$ to become as small as 800 when expressed in terms of the viscous wall unit: L_O/z_r may be orders of magnitude smaller. This illustrates an important role of roughness for the effective stability of an atmospheric flow: While so far roughness is often seen as a potential trigger of turbulence, the increased level of mixing near the surface may deem the flow over a rough wall more sensitive to static stability than it would be over a smooth wall.

The presence of roughness does not change the Reynolds number $Re = GD/\nu$ (cf. Chap. 2) of the flow or the Kolmogorov scale η, but it does affect the range of scales available to turbulent motion in the immediate vicinity of the surface. This means, the effective Reynolds number (measuring the range of scales available in the buffer layer) for a PBL over a rough surface is potentially much lower than $Re_\tau = \delta^+ = u_\star \delta / \nu$; it may in fact be expressed by δ/z_r.

9.2 Convergence of a Flux Measurement Based on a Single-Point Probe

In Sect. 6.2 the impact of coherent motion on estimates of mean profiles and turbulent fluxes in the surface layer is quantified. It is found that it may be as large as 10 % when averaging over less than a tenth of the inertial period. Such turbulent motions at very large scales have been investigated before, but their impact on tower measurements in boundary layers has so far not been quantified. This quantification of the flux-underestimation due to large-scale turbulent processes is possible as a consequence of the complete control over the physical set-up when investigating the flow numerically.

No conclusive statement on the question, Do the largest scales of the turbulent spectrum (at length scales of the order of several δ) persist when the symmetry of the set-up is broken by external processes and forcing such as topography or synoptic effects? is possible. The present results, however, provide a limit in the homogeneous case, and as such are of great utility for conceptual studies and idealized numerical simulations of the problem. Moreover, they imply contributions to the turbulent signal from scales that would actually be counted as belonging to the meso-scale regime even though no source of meso-scale motion exists in the present set-up. These large-scale motions may affect observations as well as turbulence-resolving and Reynolds-averaged simulations:

- In field campaigns turbulent fluxes are often averaged over rather short periods of time (much less than an hour) to avoid effects of synoptic or day-time non-stationarity; they likely miss out significant contributions from the large scales. Charuchittipan et al. (2014) discuss the impact of such errors on the long-standing problem of the surface energy-balance closure.
- Given a good turbulence representation at the small scales, LES can be expected to cover the large-scale end of the turbulent spectrum reasonably well, and represent these very-large-scale motions if the memory in the small scales is resolved properly.
- In Reynolds-averaged flow simulations, where all turbulence is parameterized, the neglect of these significant contributions may also have an effect, and it may be one reason why enhanced-diffusivity schemes are still needed, and also recently decreases in artificial diffusion have been found to be detrimental for the performance skill of large-scale weather prediction models (Sandu et al. 2013).

9.3 Relation to Monin–Obukhov Similarity Theory

When the surface layer of the SBL is considered, the law of the wall $\partial_z \langle u^+ \rangle = (\kappa z^+)^{-1}$ is not strictly valid any more since stratification enters the scaling. In Monin–Obukhov similarity theory, the impact of stratification is considered via a non-dimensional stability correction function based on the height $\zeta := z/L_O$ (Obukhov 1971). A common formulation for the gradient of velocity in the stratified surface layer is

$$\frac{\kappa z^+}{u_\star}\frac{\partial U}{\partial z^+} = \Phi_M. \tag{9.1a}$$

Assuming a stability correction function $\Phi_M(\zeta) := 1 + \beta\zeta$, it is

$$\int_{z_0}^{z} \Phi_M \frac{\partial z'^+}{z'^+} = \int_{z_0}^{z} \mathrm{d}\ln(z'^+) + \Phi_M - 1 - \beta\frac{z_0}{L_O}. \tag{9.1b}$$

The term $\beta z_0/L_O$ is the stability correction at $z = z_0$, the lower end of the surface layer, and one may assume $\Phi_M(z = L_O) = 0$. Hence, using the common assumption $z_0^+ = 1$,

$$\Phi_M - 1 = \kappa\left(U^+(z) - \kappa^{-1}\ln z^+\right) = \beta\zeta. \tag{9.1c}$$

Equation (9.1a) assumes a logarithmic velocity profile in the neutral reference case. In Chap. 6 it is shown that the velocity profile under neutral stratification fits a logarithmic law much better when the effect of external intermittency is taken into account and only the velocity from turbulent regions is considered for the averages; the reference profile used here is that conditioned to turbulent regions, i.e.

$$\Phi_M - 1 = \kappa\left(U^+(z) - U^+_{\mathrm{neutral,turb}}(z)\right) \tag{9.1d}$$

with the von-Kármán constant $\kappa = 0.4$.

When data in the range $20 < z^+ < 50$ and conditioned to the turbulent regions of the flow are considered, the stability correction estimated from the simulation (full circles in Fig. 9.2) agrees well with the least-squares fit $\Phi_M - 1 = 5.8\zeta - 1/40$. As in the case of neutral stratification, this is not the case when only the laminar patches are considered, and the data fit worse when the whole average is used, and not only the turbulent partition. The small offset $1/40$ of $\Phi_M - 1$, can be explained by the neglect of the lower boundary condition $\beta z_0/L_O$. The fit explains 98.5 % of the variance in the data conditioned to the turbulent partition. This agrees well with data obtained from atmospheric measurements ($\beta = 5.3$; Högström 1996) and channel-flow DNS ($\beta = 4.5$; van de Wiel et al. 2008). Agreement of the numerical simulations with Monin–Obukhov similarity theory supports their relevance for atmospheric conditions—despite the difference in Re.

9.4 Global Intermittency and Turbulence Collapse

In agreement with previous work on the SBL and canonical flow studies under stable stratification, the present results show that the absence of turbulence in extended regions of flow, even close to the surface, is a ubiquitous phenomenon under very strong stratification (Chaps. 7 and 8). Once turbulence cannot be fully sustained, the intermittency function (i.e. the turbulent area fraction and the relative size of the
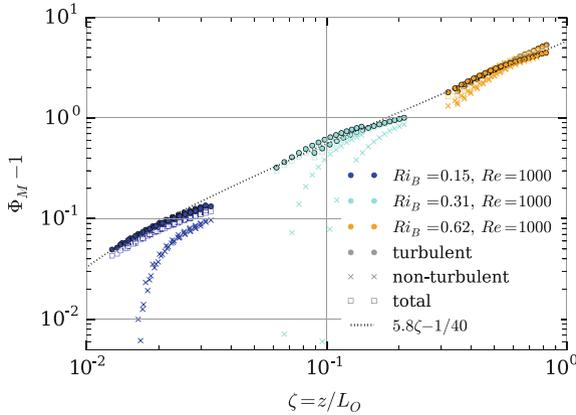
Fig. 9.2 Stability correction function $\Phi_M - 1$ for heights $20 < z^+ < 50$ conditioned to turbulent (*filled circles*) and non-turbulent (*crosses*) parts of the flow for the three cases I150LH (*blue*), I310LH (*cyan*), I620LH (*orange*). *Squares* show data for the full field. The stability correction is calculated with respect to the corresponding partition from the neutrally stratified flow. Height and Obukhov length are normalized respectively calculated with global instantaneous values of the wall friction $u_\star$

non-turbulent region) is determined by the Obukhov length expressed in wall units L_O^+, a surface property of the system that relates to the surface heat flux (Sect. 8.2). Thus, it is demonstrated that global intermittency can arise from a global constraint on the flow, for instance the exceedance of the maximum sustainable heat flux as suggested in the literature (van de Wiel et al. 2012; van de Wiel and Moene 2012). Local perturbations, such as surface heterogeneities—or large-scale dynamics as in the present case—, simply determine the spatio-temporal distribution of global intermittency (Sun et al. 2012; Acevedo and Fitzjarrald 2003; Sun et al. 2004), but they are not necessary as a trigger.

The relevance of $L_O^+ = u_\star^3/(b_\star \nu)$ for the collapse of turbulence that this dissertation provides strong evidence for, is consistent with a cubic dependency of the threshold for a turbulence breakdown found in an observational study by van de Wiel et al. (2012). The quantitative dependency of the proposed mechanism on Re can be elucidated in future work. Nonetheless, this simplified set-up is suited to study dynamics of the stably and very stably stratified PBL. This analogy over a cascade of complexity—ranging from the canonical-flow problem of stable channel flow via rotating Couette and stable Ekman flow to the PBL—encourages further investigation of the fundamental aspects of stably stratified turbulence in rotating reference frames.

Owing to the absence of heterogeneities in the numerical set-up, the spatio-temporal pattern of global intermittency close to the surface is caused by a large-scale structure in the outer layer of the flow. The characteristic length scale of these large-scale motions is found here to scale with the boundary-layer depth scale δ, and it is on the order of 1–2δ (Sect. 8.1). A very similar phenomenon is observed

Fig. 9.3 Simplified and idealized parameter space for stably stratified Ekman flow studied in terms of the Normalized Obukhov length L_O^+ and Friction Reynolds number Re_τ
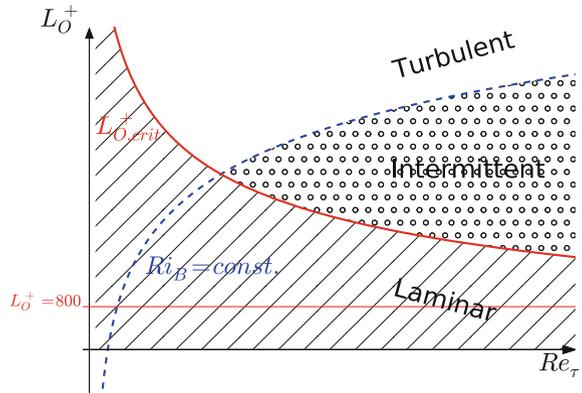
in homogeneously stratified shear turbulence and rotating Couette flow (Chung and Matheou 2012; Brethouwer et al. 2012), in both of which no local or coherent perturbations are present. This agreement among a number of different flow configurations suggests there is a very general mechanism behind what is recently called 'weak turbulence' in an atmospheric context (Mahrt 2014). And it furthermore suggests relevance of the global-intermittency mechanism at atmospheric scale.

In terms of the two-dimensional parameter space spanned by Ri_B and Re (introduced in Chap. 2), the parameter governing stratification should be replaced by L_O^+ when global intermittency is considered. This compensates for a dependency of the stratification at the surface on both Ri_B and Re. When the characterization of the problem in terms of external parameters is not the primary objective, it is further useful to employ $Re_\tau = u_\star\delta/\nu$ as the governing Reynolds number (Fig. 9.3). In the simplified set-up spanned by the two non-dimensional parameters L_O^+ and Re_τ, the use of the normalized Obukhov length L_O^+ compensates for the viscid dependency of Ri_B. Given the above findings, we suppose that there is a boundary in this phase space beyond which turbulence cannot be sustained; the larger Re_τ the smaller is the L_O^+ (and the larger is $1/L_O^+$) for which this is the case. This boundary is qualitatively illustrated by the red dashed line in Fig. 9.3. For large Re_τ, we would assume that the critical L_O^+ converges towards a finite non-zero limit on the order of 800 (solid red line). The exact Reynolds-number dependency of this phase boundary cannot be elucidated with the data available here.

A second finding is the occurrence of global intermittency in the flow, and one may ask, For which part of the parameter space does this global intermittency occur? The qualitative agreement of the occurrence and character of global intermittency with other canonical flows points towards a general mechanism which may be similar to the one observed in pipe flow where a similar type of intermittency occurs due to a non-linear instability in a linearly stable flow. Following Richardson's straightforward argumentation (Richardson 1920), linear stability is established once Ri_B exceeds a particular threshold. From the definitions of L_O^+, Re_τ and Ri_B it follows that

$$\frac{1}{L_O^+} \propto \frac{1}{Re_\tau} \text{ for } Ri_B = const. \tag{9.2}$$

This implies a widening intermittent region in the $L_O^+ - Re_\tau$ parameter space for increasing Re_τ (cf. Fig. 9.3). This widening does not contradict physical intuition but is a consequence of the strong correlation between L_O^+ and Re_τ. In particular, it does not mean that at fixed stratification a turbulent flow may become laminar when the scale separation changes because that would imply a change of L_O^+ as well.

There are two ways in which a transition from turbulent to laminar might happen: Either through stronger stratification, that is changing only L_O^+, or via a decrease in Re_τ. Once in the fully turbulent regime, it is unlikely that the fundamental character of this transition changes—whether it occurs by changing L_O^+ or Re_τ. Such a change in the character of transition would require high-Re turbulence in the SBL to be caused by a different instability than in the numerical simulations at intermediate Reynolds number. Such a mechanism is theoretically possible as a consequence of a series of bifurcations at high Reynolds number. The agreement of numerical results which is demonstrated within this dissertation (and also at other places), however, deems the occurrence of such additional instability mechanisms at atmospheric scale highly unlikely. While it is shown in this work that this transition is governed by the parameter L_O^+, and occurs in the range $200 < L_O^+ < 800$, the exact properties of this transition may depend on Re similarly to $u_\star$ and α (Chap. 6) and as observed in stably stratified shear and channel flow (Jacobitz et al. 1997; Flores and Riley 2011).

References

Acevedo, O. C., & Fitzjarrald, D. R. (2003). In the core of the night-effects of intermittent mixing on a horizontally heterogeneous surface. *Boundary-Layer Meteorology*, *106*(1), 1–33. doi:10.1023/A:1020824109575.

Brethouwer, G., Duguet, Y., & Schlatter, P. (2012). Turbulent-laminar coexistence in wall flows with coriolis, buoyancy or Lorentz forces. *Journal of Fluid Mechanics*, *704*, 137–172.

Charuchittipan, D., Babel, W., Mauder, M., et al. (2014). Extension of the averaging time in eddy-covariance measurements and its effect on the energy balance closure. *Boundary-Layer Meteorology*, *152*, 303–327. doi:10.1007/s10546-014-9922-6.

Chung, D., & Matheou, G. (2012). Direct numerical simulation of stationary homogeneous stratified sheared turbulence. *Journal of Fluid Mechanics*, *696*(410), 434.

Flores, O., & Riley, J. J. (2011). Analysis of turbulence collapse in the stably stratified surface layer using direct numerical simulation. *Boundary-Layer Meteorology*, *139*(2), 241–259. doi:10.1007/s10546-011-9588-2.

Högström, U. (1996). Review of some basic characteristics of the atmospheric surface layer. *Boundary-Layer Meteorology*, *78*(3–4), 215–246. doi:10.1007/BF00120937.

Jacobitz, F. G., Sarkar, S., & van Atta, C. W. (1997). Direct numerical simulations of the turbulence evolution in a uniformly sheared and stably stratified flow. *Journal of Fluid Mechanics*, *342*, 231–261. doi:10.1017/S0022112097005478.

Jiménez, J. (2004). Turbulent flows over rough walls. *Annual Review of Fluid Mechanics*, *36*, 173–196.

Kolmogorov, A. N. (1941). Dissipation of energy in locally isotropic turbulence. *Dokl Akad Nauk SSSR*, *434*(1890), 15–17.

Mahrt, L. (2014). Stably stratified atmospheric boundary layers. *Annual Review of Fluid Mechanics*, *46*, 23–45.

Moin, P., & Mahesh, K. (1998). Direct numerical simulation: A tool in turbulence research. *Annual Review of Fluid Mechanics*, *30*, 539–578.

Monin, A. S., & Yaglom, A. M. (1975). Statistical fluid mechanics. In *Mechanics of Turbulence* (Vol. I). Dover Publications, Inc.

Obukhov, A. M. (1971). Turbulence in an atmosphere with a non-uniform temperature. *Boundary-Layer Meteorology*, *2*(1), 7–29.

Richardson, L. F. (1920). The supply of energy from and to atmospheric eddies. *Proceedings of the Royal Society of London Series a-Containing Papers of a Mathematical and Physical Character*, *97*(686), 354–373.

Sandu, I., Beljaars, A. C. M., Bechtold, P., et al. (2013). Why is it so difficult to represent stably stratified conditions in numerical weather prediction (NWP) models? *Journal of Advances in Modeling Earth Systems*, *5*(2), 117–133. doi:10.1002/jame.20013.

Sun, J., Lenschow, D. H., Burns, S. P., et al. (2004). Atmospheric disturbances that generate intermittent turbulence in nocturnal boundary layers. *Boundary-Layer Meteorology*, *110*(2), 255–279.

Sun, J., Mahrt, L., Banta, R. M., et al. (2012). Turbulence regimes and turbulence intermittency in the stable boundary layer during CASES-99. *Journal of the Atmospheric Sciences*, *69*(1), 338–351. doi:10.1175/JAS-D-11-082.1.

van de Wiel, B. J. H., Moene, A. F., De Ronde, W. H., et al. (2008). Local similarity in the stable boundary layer and mixing-length approaches: consistency of concepts. *Boundary-Layer Meteorology*, *128*(1), 103–116. doi:10.1007/s10546-008-9277-y.

van de Wiel, B. J. H., Moene, A. F., Jonker, H. J. J., et al. (2012). The minimum wind speed for sustainable turbulence in the nocturnal boundary layer. *Journal of the Atmospheric Sciences*, *69*(11), 3116–3127. doi:10.1175/JAS-D-12-0107.1.

van de Wiel, B. J. H., & Moene, A. F. (2012). The cessation of continuous turbulence as precursor of the very stable nocturnal boundary layer. *Journal of the Atmospheric Sciences*. doi:10.1175/JAS-D-12-064.1.

Chapter 10
Résumé

The stably stratified boundary layer was early recognized as a fluid-mechanics problem of fundamental interest. Nonetheless, the study of stratified turbulence and the stable boundary layer have taken different paths: Stratified turbulence is mostly studied as a canonical-flow problem in fluid mechanical engineering. On the contrary, the stably stratified boundary layer is commonly investigated as a parameterization problem—motivated by the need for a working turbulence closure in general circulation and numerical weather prediction models. This gave rise to a number of fixes in turbulence closures which are motivated by a large-scale point of view. Still recently, a lack of fundamental understanding in stratified turbulence is identified as a pertinent challenge in understanding the boundary layer. These two paths are consolidated here applying systematically the direct numerical simulation of a turbulent flow, a tool widely used in fluid mechanical engineering, to study the stably stratified boundary layer.

When stratification in the boundary layer becomes strong enough to cause the—in time and space localized—absence of turbulence, the calculation of motions over the full spectrum of turbulence is a great advantage. A well-defined and easily-controllable set-up, namely Ekman flow over a smooth surface at a fixed temperature, is introduced as a virtual laboratory to study aspects of turbulence under strong stability. The utility of DNS in studying this problem lies in the absence of a turbulence closure, and it allows to draw conclusions unaffected by assumptions of turbulence closures or the like. This enables a study of detailed aspects of the collapse of turbulence under strong stratification and yields new insight into long-standing questions with regard to stable density stratification:

- L_O^+, the Obukhov length normalized with an appropriate length scale for the surface layer, is identified as the governing parameters for the occurrence of global intermittency.
- A method is developed to identify global intermittency, and to condition fields on its existence.

- The regulating impact of global intermittency on the velocities, turbulence kinetic energy and dissipation in the surface layer of a strongly stratified flow is quantified. Global intermittency is shown to be the main mechanism in reducing the turbulence intensity while the actual level of turbulence inside turbulent patches is not affected. This is consistent with the impact of external intermittency in the neutrally stratified flow: A controversy on the logarithmic law for the mean velocity and associated constants is shown in this work to result from the neglect of external intermittency in previous work.

A significant contribution of this dissertation is the solution of the Navier–Stokes equations in the Boussinesq limit for the particular, physically relevant set of boundary conditions corresponding to Ekman flow. This requires utilization of cutting-edge computational resources and programming paradigms as laid out in Part II. An algorithm that efficiently overlaps the communication and computation of data is developed in Chap. 4; this algorithm utilizes the supercomputer `juqueen` efficiently with up to 256,000 threads. From a fluid mechanics point of view, the solutions of the Navier–Stokes equations which had not been obtained before for such a large domain of Ekman flow, is a great value. It allows to study large-scale temporal and spatial modes in the flow that were not observed before. Another technical innovation of this dissertation is the dual availability of data at high resolution in both time *and* space facilitating a better comparison between field measurement and simulation data.

While the focus of this work is the stably stratified boundary layer, new insight also results into Ekman flow under neutral stratification (Chap. 6). I extend the analogy of Ekman and channel flow beyond mean profiles and identify limitations. In the surface layer, the turbulence-kinetic energy budget is shown to be very similar to that of channel flow at similar Reynolds number. External intermittency is found to be an important mode of large-scale motion in the flow; its occurrence is quantified, and I show that the impact of external intermittency in the surface layer is significant. A mean velocity that does not take into account the externally intermittent regions of the flow is shown to exhibit a logarithmic scaling over a three-times broader range of heights than the conventional mean.

The relevance of channel flow for the turbulent Ekman layer extends beyond neutral stratification. The re-laminarization process under very strong stratification is shown to be governed by surface-layer dynamics. The threshold of critical stability for the turbulence collapse is—in accordance with recent work on pipe flow and the study of minimal flow units in channel flow—most appropriately expressed in terms of an inner scale, namely the Obukhov length L_O^+. A consistent study of this very delicate regime of turbulence is possible in this work due to the absence of a turbulence closure, since the assumptions underlying turbulence closures employed in Reynolds-averaged and Large-Eddy simulations of similar set-ups fail in the very stable regime. Hence, this work is the first to study turbulence in all regimes of static stability without a break in the underlying paradigms.

The explicit calculation of the turbulence collapse as part of the direct numerical simulation allows an analysis of the associated mechanisms. I show that global intermittency, i.e. the localized (in space and time) absence of turbulence in rather large

regions close to the surface, is a process intrinsic to Ekman flow under the impact of a stable density stratification: Global intermittency also occurs if the triggers commonly assumed a prerequisite (orographic disturbances, solitary waves, upside-down boundary layers) are absent. Occurrence of global intermittency is governed by L_O^+, and global intermittency is observed over the range $200 < L_O^+ < 800$, which is potentially relevant to the atmospheric boundary layer when the wall unit is replaced by a roughness length scale.

In the globally intermittent flow, conventional averages are less indicative, and no method existed to condition a wall-bounded flow on the occurrence of external intermittency. The vorticity-based detection of external intermittency is extended here by a high-pass filter operation, and this approach is shown to detect global intermittency also in the vicinity of the wall. Statistics conditioned on the occurrence of global intermittency can now be computed. Such conditioned statistics confirm quantitatively the visual impression that the morphology of turbulence inside turbulent regions does not significantly differ from that under neutral stratification. Order-of-one changes in turbulent quantities under strong stratification are rather governed by a confinement of the turbulent area fraction than they are by a change of turbulence dynamics inside turbulent regions of the flow: Turbulent quantities inside the turbulent regions of flow do not change by more than 20–30 %, even under very strong stratification, whereas the intermittency factor varies between zero and one.

This new understanding of global intermittency has implications for turbulence models applied under very stable stratification: First, global intermittency effects could be incorporated into turbulence closures for large-scale models. For this, the dependency of global intermittency (expressed in terms of the turbulent flow fraction) on the external parameters (the Richardson and Reynolds numbers) and L_O^+ needs to be quantified. Effects of global intermittency might then be consistently incorporated into turbulence closures without depending strongly on the local details of the flow such as surface heterogeneities or other forcings previously considered—these would rather determine the particular place and time of occurrence than the turbulent area fraction itself. Second, new light is shed on the term 'weak turbulence' that is used recently to describe atmospheric turbulence under strong stratification: While certainly appropriate in a bulk sense, this work shows that when applied on the level of individual turbulence elements, the term might be misleading.

This work has embarked on the direct numerical simulation of a stably stratified boundary layer. While the tool of direct numerical simulation dates back to the 1970s and is well-established to study canonical problems in fluid mechanics, only recently computers became powerful enough to allow for the simulation of an external boundary layer at sufficient scale separation to study idealized geophysical problems. Hence, this approach is relatively new in the geophysical context, and it was not applied systematically to study problems of the stratified boundary layer from a meteorological perspective. Despite a low Reynolds number $Re = GD/\nu$ when compared to atmospheric values, many processes and dynamics observed here do occur in the atmosphere—and even a quantitative comparison with boundary-layer measurements in terms of the Monin–Obukhov stability correction yields very good agreement. The reason for this is not only the well-established concept of

Reynolds-number similarity in a turbulent flow. Also, roughness elements orders of magnitude larger than the wall unit $\nu/u_\star$ affect the small scales of turbulent motion in the surface layer over a rough wall. Enhanced mixing in the vicinity of such roughness elements may deem the scale range available for free turbulent motion in the PBL much smaller than what is suggested by commonly assumed Reynolds numbers around $Re = 10^5$ for atmospheric flow.

Epilogue

Neither is the endeavor of completing a dissertation possible without professionally maintained technical equipment nor without a strong network of mentors, colleagues and friends. Prima facea, I would like to express my sincere gratitude to my advisor *Juan Pedro Mellado* for his enduring support throughout my master and doctoral studies–for his kind understanding, patient teaching and immense knowledge. His guidance and support were a pillar of strength in completing this dissertation. Continuous meetings of the *TMP Group* under his lead, in particular the comments by *Chiel van Heerwaarden* and *Alberto de Lozar*, were a unique forum and crucial for the birth and exchange of Ideas.

Besides my advisor, I also thank the committee members: *Prof. Martin Claußen*, *Prof. Jens Struckmeier* and *Jun.-Prof. Gualtiero Badin* for their involvement in the evaluation of the dissertation and disputation. My sincere thanks go to the committee chair *Prof. Felix Ament* whose unbureaucratic and friendly kind together with his great commitment turned out to be essential for a timely defense of the dissertation. I thank *Prof. Bas van de Wiel* (TU Delft) who was appointed as external referee for his in-depth revision of the dissertation.

For his enduring support along the work and insightful discussions on the topic I am indebted to *Prof. Evgeni Fedorovich* at the University of Oklahoma. I wish to thank *Prof. Jörg Schumacher* (TU Ilmenau), *Prof. Petra Klein* (University of Oklahoma) and *Dmitrii Mironov* (Deutscher Wetterdienst) for inspiring discussions.

Florian Ziemen is thanked for the most useful and entertaining distraction I could think of along working on a dissertation, two *Schülerakademien*, many more coffees and even more fun–even in the most forlorn moments. *Thomas Keitzl* was the greatest companion to do a PhD with and I cannot imagine surviving the years in Hamburg without his fun and open comments on research and life in general. The *Sölden-Crew* was a key to keeping the work-life balance a balance. And *Astrid Eichhorn*: Thank you for the music! *Katharina Weinert* provided strong support in the beginning compilation of this work.

I thank *my parents* who taught me questioning things deeply and supported my education at all times and *Robert Ansorge* who was always on the spot. And I thank Anna who immortally stepped into my life and opened up a new horizon.

Appendix A
Analytical Study of the Inertial Oscillation

The quasi-laminar, stationary Ekman layer. For reference, Ekman's classical solution of the laminar case is reproduced, where $w = \bar{w} = 0$, and it is extended here to a temporally evolving case. Assuming the absence of ageostrophic pressure gradients and turbulent fluxes, the RANS equations in the Boussinesq limit in non-dimensional form reduce to

$$\frac{\partial U}{\partial t} = V + Re^{-1}\frac{\partial^2 U}{\partial z^2} \tag{A.1a}$$

$$\frac{\partial V}{\partial t} = -(U - 1) + Re^{-1}\frac{\partial^2 V}{\partial z^2}, \tag{A.1b}$$

where U and V are non-dimensionalized with the geostrophic wind G, and the length scale $D \equiv \sqrt{2\nu/f}$, such that

$$Re \equiv \frac{GD}{\nu} = \sqrt{2\frac{G\Lambda_{Ro}}{\nu}} \tag{A.1c}$$

with the Rossby Radius $\Lambda_{Ro} = G/f$. The Reynolds number Re hence measures the scale separation between the Rossby radius of deformation and the viscous length scale $D = \sqrt{2\nu/f}$.

The stationary solution of this problem was derived by Ekman in 1905, and in non-dimensionalized form reads as

$$(U_\infty - 1) = -e^{-z}\cos z \quad \text{and} \quad V_\infty = e^{-z}\sin z. \tag{A.1d}$$

This concept, strictly valid only in a laminar flow, is commonly extended to quasi-laminar boundary layers where the molecular viscosity is replaced by an eddy-viscosity ν_E. If $\nu_E(z) = const.$, the quasi-laminar case discussed by Ekman (1905) is recovered.

Perturbation of the quasi-laminar system. Once the Ekman solution (A.1d) is known, one can write any horizontally homogeneous velocity field as $V(z,t) = V_\infty(z) + V'(z,t)$ and analogously for $U(z,t)$ with $(U_\infty(z), V_\infty(z))$ from Eq. (A.1d). Applying this decomposition to $\xi := U + iV$ with the imaginary unit $i := \sqrt{-1}$ leads to the linear PDE

$$\frac{\partial \xi'}{\partial t} = -i\xi' + Re^{-1}\frac{\partial^2 \xi'}{\partial z^2}. \tag{A.2a}$$

A non-trivial solution for perturbation of the form of the first derivative of a Gaussian is

$$\begin{aligned} U(t,z) - 1 &= -e^{-z}\cos z \; -A_0\cos t \exp\left(-\frac{z^2}{4\tau}\right)\frac{z}{2\tau^{3/2}} \\ V(t,z) &= +e^{-z}\sin z \; +A_0\sin t \exp\left(-\frac{z^2}{4\tau}\right)\frac{z}{2\tau^{3/2}} \end{aligned} \tag{A.2b}$$

with $\tau = t/Re + \tau_0$. $A_0, \tau \in \mathbb{R}_+$; A_0 defines the strength of the perturbation and τ_0 the initial width of the perturbation at. For $\sigma_0 > 0$ and $t \to \infty$, the first member of the family of solution approaches the quasi-laminar steady-state solution (U_∞, V_∞). Once σ_0 is specified, the level where the perturbation profile has its maximum depends on time as $z_{max}/D = \sqrt{\tau} = \sqrt{t/Re + \tau_0}$. Perturbations propagate upwards and their magnitude is damped.

Despite its simplicity, this simple and exact analytical model for a quasi-laminar boundary layer features the main characteristics of inertial oscillations. It is moreover relevant for the fully turbulent problem in the sense that if such modes are present, at least locally, this mechanism will be at work until they become affected by other processes. Note that by scaling the initial perturbation strength with the parameter τ_0 and eventually by using higher modes, a variety of perturbations exist for which this mechanism is relevant.

Vertical momentum budget—constraint for the pressure. I turn now to the turbulent problem, and first consider the vertical momentum equation to show that no horizontal ageostrophic pressure gradients can exist, even in turbulent Ekman flow. In the general form, the vertical momentum budget of Ekman flow reads as

$$\frac{\partial W}{\partial t} = -\frac{\partial \overline{ww}}{\partial z} - \frac{\partial \Pi}{\partial z} + \frac{1}{Re}\frac{\partial^2 W}{\partial z^2}. \tag{A.3a}$$

Using the symmetries of the problem equation (A.3a) becomes

$$0 = -\frac{\partial \overline{ww}}{\partial z} - \frac{\partial \Pi}{\partial z} \Rightarrow \Pi_\infty - \Pi_0 = 0, \tag{A.3b}$$

or more general: $\Pi(z) = \Pi(0) - \overline{ww}(z)$. Hence, there do not exist ageostrophic pressure gradients in the mean flow at any height if it is statistically homogeneous in the horizontal directions.

Integral formulation. Using the fact that the ageostrophic pressure gradients are zero at any height, and integrating the horizontal momentum budgets vertically, I obtain

$$\int_0^\infty \partial_t(U-1)\mathrm{d}z - \int_0^\infty V\,dz = -\left.\overline{uw}\right|_0^\infty + \frac{1}{Re}\left.\frac{\partial U}{\partial z}\right|_0^\infty = -\frac{1}{Re}\left.\frac{\partial U}{\partial z}\right|_0 \quad \text{(A.4a)}$$

$$\int_0^\infty \partial_t V\,\mathrm{d}z + \int_0^\infty (U-1)dz = -\left.\overline{vw}\right|_0^\infty + \frac{1}{Re}\left.\frac{\partial V}{\partial z}\right|_0^\infty = -\frac{1}{Re}\left.\frac{\partial V}{\partial z}\right|_0 \quad \text{(A.4b)}$$

For notational convenience, let

$$\mathscr{U} := \int_0^\infty (U-1)\mathrm{d}(z)$$

$$\mathscr{V} := \int_0^\infty (V)\mathrm{d}(z)$$

$$u_\star^2 := \frac{1}{Re}\sqrt{\partial_z(U)^2 + \partial_z(V)^2}\big|_0;$$

$$\tan\alpha := (\partial_z V|_0)/(\partial_z U|_0)$$

$$f_x := u_\star^2 \cos\alpha$$

$$f_y := u_\star^2 \sin\alpha$$

to arrive at the following system describing the inertial oscillator:

$$\partial_t \mathscr{U} = \mathscr{V} - f_x \quad \text{and} \quad \partial_t \mathscr{V} = -\mathscr{U} - f_y \quad \text{(A.4c)}$$

A steady-state solution of this system is given by

$$\mathscr{U}_\infty = -f_{y,\infty} = -u_{\star,\infty}^2 \sin\alpha_\infty \quad \text{and} \quad \mathscr{V}_\infty = f_{x,\infty} = u_{\star,\infty}^2 \cos\alpha_\infty. \quad \text{(A.4d)}$$

The perturbed system. It remains unclear, how the perturbed system (A.4c) behaves. In particular, it is unclear what determines the damping of the inertial oscillation—if there is any.

Let $\mathscr{U} = \mathscr{U}' + \mathscr{U}_\infty$ and analogous for $\mathscr{V}$, f_x and f_y. Using the equilibrium solution from above, one arrives at a system of ODEs for the perturbations $\mathscr{U}'$ and $\mathscr{V}'$.

$$\frac{\partial \mathscr{U}'}{\partial t} = \mathscr{V}' + f_x' \text{ with } f_x' = u_\star^2 \cos\alpha - u_{\star,\infty}^2 \cos\alpha_\infty$$

$$\frac{\partial \mathscr{V}'}{\partial t} = -\mathscr{U}' + f_y' \text{ with } f_y' = u_\star^2 \sin\alpha - u_{\star,\infty}^2 \sin\alpha_\infty$$

$$\text{(A.4e)}$$

From this, the two oscillator equations

$$\frac{\partial^2 \mathscr{U}'}{\partial t^2} = \qquad -\mathscr{U}' + f_y' + \frac{\partial f_x'}{\partial t} \tag{A.5a}$$

$$\frac{\partial^2 \mathscr{V}'}{\partial t^2} = \qquad -\mathscr{V}' - f_x' + \frac{\partial f_y'}{\partial t}. \tag{A.5b}$$

follow. These equations are an immediate consequence of the Navier–Stokes equations in the Boussinesq limit, and no further assumptions are necessary for their derivation.

The oscillator equations under quasi-laminar conditions. I employ now the quasi-laminar solution to illustrate the role of the terms in the oscillator equation and rule out the main damping mechanism, at least under quasi-laminar and laminar conditions. The quantities $\mathscr{U}'$ and $\mathscr{V}'$ evaluate to

$$\mathscr{U}'(t) = -\frac{A_0}{\sqrt{\tau}} \cos t; \quad \mathscr{V}'(t) = +\frac{A_0}{\sqrt{\tau}} \sin t, \tag{A.6a}$$

$$\Rightarrow \begin{cases} \dfrac{\partial \mathscr{U}'}{\partial t} = A_0 \left(\dfrac{\sin t}{\sqrt{\tau}} + \dfrac{1}{2Re} \dfrac{\cos t}{\tau^{3/2}} \right); \\[2ex] \dfrac{\partial \mathscr{V}'}{\partial t} = A_0 \left(\dfrac{\cos t}{\sqrt{\tau}} - \dfrac{1}{2Re} \dfrac{\sin t}{\tau^{3/2}} \right) \end{cases} \tag{A.6b}$$

$$\Rightarrow \begin{cases} \dfrac{\partial^2 \mathscr{U}'}{\partial t^2} = A_0 \left(\dfrac{\cos t}{\sqrt{\tau}} - \dfrac{1}{Re} \dfrac{\sin t}{\tau^{3/2}} - \dfrac{3}{4Re^2} \dfrac{\cos t}{\tau^{5/2}} \right); \\[2ex] \dfrac{\partial^2 \mathscr{V}'}{\partial t^2} = A_0 \left(-\dfrac{\sin t}{\sqrt{\tau}} - \dfrac{1}{Re} \dfrac{\cos t}{\tau^{3/2}} + \dfrac{3}{4Re^2} \dfrac{\sin t}{\tau^{5/2}} \right) \end{cases} \tag{A.6c}$$

where it is reminded that $\tau = \mu_0 + t/Re$. Other terms of interest are

$$f_x' = -\frac{A_0}{2Re} \frac{\cos t}{\tau^{3/2}} \Rightarrow \frac{\partial f_x'}{\partial t} = \frac{A_0}{2Re \cdot \tau^{5/2}} \left(\tau \sin t + \frac{3}{2Re} \cos t \right) \tag{A.6d}$$

$$f_y' = +\frac{A_0}{2Re} \frac{\sin t}{\tau^{3/2}} \Rightarrow \frac{\partial f_y'}{\partial t} = \frac{A_0}{2Re \cdot \tau^{5/2}} \left(\tau \cos t - \frac{3}{2Re} \sin t \right) \tag{A.6e}$$

One can now write

$$\begin{aligned} f_y' + \frac{\partial f_x'}{\partial t} &= \frac{A_0 \sin t}{Re \cdot \tau^{3/2}} + \frac{3A_0}{4Re^2 \tau^{5/2}} \cos t = \frac{1}{Re \cdot \tau} \frac{\partial \mathscr{U}'}{\partial t} + \frac{1}{4Re^2 \tau^{5/2}} \cos t \\ &= \frac{1}{Re \cdot \tau} \frac{\partial \mathscr{U}'}{\partial t} - \frac{1}{4Re^2 \tau^2} \mathscr{U}' \\ f_x' + \frac{\partial f_y'}{\partial t} &= \frac{A_0 \cos t}{Re \cdot \tau^{3/2}} - \frac{3A_0}{4Re^2 \tau^{5/2}} \sin t = \frac{1}{Re \cdot \tau} \frac{\partial \mathscr{V}'}{\partial t} - \frac{1}{4Re^2 \tau^{5/2}} \sin t \\ &= \frac{1}{Re \cdot \tau} \frac{\partial \mathscr{V}'}{\partial t} - \frac{1}{4Re^2 \tau^2} \mathscr{V}'. \end{aligned} \tag{A.6f}$$

Hence, the oscillator equations (A.5) can be rewritten as

$$\frac{\partial^2 \mathscr{U}'}{\partial t^2} = \qquad -\left(1 + \frac{1}{4Re^2 \cdot \tau^2}\right)\mathscr{U}' + \frac{1}{Re \cdot \tau}\frac{\partial \mathscr{U}'}{\partial t} \qquad\qquad \text{(A.7a)}$$

$$\frac{\partial^2 \mathscr{V}'}{\partial t^2} = \qquad -\left(1 + \frac{1}{4Re^2 \cdot \tau^2}\right)\mathscr{V}' + \frac{1}{Re \cdot \tau}\frac{\partial \mathscr{V}'}{\partial t}. \qquad\qquad \text{(A.7b)}$$

Appendix B
High-Frequency Oscillation Under Stable Stratification

Under very stable stratification ($Ri_B = 0.62$), a high-frequency oscillation in the vertical velocity variance, the buoyancy variance and the buoyancy flux is observed. The transport equations for these quantities are shown in Table B.1.

Second-order closure. Now, simplify above equations which are complete and exact for a Boussinesq flow to a simple model that explains the main mechanism at work in the flow under consideration. First, molecular diffusion is small when comapred to turbulent mixing, and the corresponding terms $\nu\partial_{zz}\langle b'b'\rangle$, $\nu\partial_{zz}\langle w'b'\rangle$, $\nu\partial_{zz}\langle w'w'\rangle$ can be neglected. The triple-correlation terms are parameterized with the following down-gradient model

$$\partial_z\langle u'u'w'\rangle \simeq u'w'\partial_z U \qquad \partial_z\langle v'v'w'\rangle \simeq v'w'\partial_z V \qquad \partial_z\langle w'w'w'\rangle \simeq 0$$
$$\partial_z\langle u'w'w'\rangle \simeq w'w'\partial_z U \qquad \partial_z\langle v'w'w'\rangle \simeq w'w'\partial_z V \qquad \partial_z\langle v'w'w'\rangle \simeq u'w'\partial_z U + v'w'\partial_z V$$
$$\partial_z\langle b'w'b'\rangle \simeq \langle b'w'\rangle N^2 \qquad \partial_z\langle w'w'b'\rangle \simeq \langle w'w'\rangle N^2$$

[1] where $N := \sqrt{\partial B/\partial z}$ is the Brunt–Väisälä frequency. Dissipation is assumed to be proportional to the fluctuation intensity of a quantity, i.e.

$$\nu\left\langle\frac{\partial\xi_1'}{\partial x_j}\frac{\partial\xi_2'}{\partial x_j}\right\rangle \propto \tau_{\xi_2\xi_2}\langle\xi_1'\xi_2'\rangle \tag{B.2}$$

where $\tau_{\xi_1\xi_2}$ is a time scale for the turbulent dissipation of the quantity $\langle\xi_1\xi_2\rangle$. Regarding the Reynolds stresses, let $\tau_{u_iu_j} = \tau_{u_iu_i} = \tau_\epsilon$, and the dissipation of buoyancy variance is parameterized similarly: $\tau_{bb} = \tau_\epsilon$. For the pressure-strain term, a return-to-isotropy model can be employed (Rotta 1951). In terms of the scalar, this implies

---

[1]An alternative parameterization for the triple correlation in the buoyancy-flux transport equation would be $\partial_z\langle b'w'w'\rangle \simeq \langle b'w'\rangle\partial_z W = 0$. If this approach is taken, however, the equation for $\partial_{tt}\langle w'w'\rangle$ would be structurally different from that for $\partial_{tt}\langle b'b'\rangle$ whereas oscillations at identical magnitude and frequency are observed.

Table B.1 Second-order equations

$$\frac{\partial \langle u'u'\rangle}{\partial t} = -\frac{\partial}{\partial z}\left[\langle u'^2 w'\rangle - \nu\frac{\partial \langle u'u'\rangle}{\partial z}\right] - 2\nu\left\langle\left(\frac{\partial u'}{\partial x_j}\right)^2\right\rangle - \langle u'\partial_x p'\rangle - 2\langle u'w'\rangle\partial_z U + 2f\langle u'v'\rangle \tag{B.1a}$$

$$\frac{\partial \langle v'v'\rangle}{\partial t} = -\frac{\partial}{\partial z}\left[\langle v'^2 w'\rangle - \nu\frac{\partial \langle v'v'\rangle}{\partial z}\right] - 2\nu\left\langle\left(\frac{\partial v'}{\partial x_j}\right)^2\right\rangle - \langle v'\partial_y p'\rangle - 2\langle v'w'\rangle\partial_z V - 2f\langle u'v'\rangle \tag{B.1b}$$

$$\frac{\partial \langle u'v'\rangle}{\partial t} = -\frac{\partial}{\partial z}\left[\langle u'v'w'\rangle - \nu\frac{\partial \langle u'v'\rangle}{\partial z}\right] - 2\nu\left\langle\frac{\partial u'}{\partial x_j}\frac{\partial v'}{\partial x_j}\right\rangle - \langle v'\partial_x p' + u'\partial_y p'\rangle - \langle u'w'\rangle\partial_z U - \langle v'w'\rangle\partial_z V + f\left(\langle v'v'\rangle - \langle u'u'\rangle\right) \tag{B.1c}$$

$$\frac{\partial \langle u'w'\rangle}{\partial t} = -\frac{\partial}{\partial z}\left[\langle u'w'w'\rangle - \nu\frac{\partial \langle u'w'\rangle}{\partial z}\right] - 2\nu\left\langle\frac{\partial u'}{\partial x_j}\frac{\partial w'}{\partial x_j}\right\rangle - \langle w'\partial_x p' + u'\partial_z p'\rangle - \langle u'w'\rangle\partial_z U + f\langle v'w'\rangle + \langle u'b'\rangle \tag{B.1d}$$

$$\frac{\partial \langle v'w'\rangle}{\partial t} = -\frac{\partial}{\partial z}\left[\langle v'w'w'\rangle - \nu\frac{\partial \langle v'w'\rangle}{\partial z}\right] - 2\nu\left\langle\frac{\partial v'}{\partial x_j}\frac{\partial w'}{\partial x_j}\right\rangle - \langle w'\partial_y p' + v'\partial_z p'\rangle - \langle v'w'\rangle\partial_z V - f\langle u'w'\rangle + \langle v'b'\rangle \tag{B.1e}$$

$$\frac{\partial \langle u'b'\rangle}{\partial t} = -\frac{\partial}{\partial z}\left[\langle u'b'w'\rangle - \nu\frac{\partial \langle u'b'\rangle}{\partial z}\right] - 2\nu\left\langle\frac{\partial u'}{\partial x_j}\frac{\partial b'}{\partial x_j}\right\rangle - \langle b'\frac{\partial p'}{\partial x}\rangle - \langle b'w'\rangle\frac{\partial U}{\partial z} - \langle u'w'\rangle\frac{\partial B}{\partial z} + f\langle v'b'\rangle \tag{B.1f}$$

$$\frac{\partial \langle v'b'\rangle}{\partial t} = -\frac{\partial}{\partial z}\left[\langle v'b'w'\rangle - \nu\frac{\partial \langle v'b'\rangle}{\partial z}\right] - 2\nu\left\langle\frac{\partial v'}{\partial x_j}\frac{\partial b'}{\partial x_j}\right\rangle - \langle b'\frac{\partial p'}{\partial y}\rangle - \langle b'w'\rangle\frac{\partial V}{\partial z} - \langle v'w'\rangle\frac{\partial B}{\partial z} - f\langle u'b'\rangle \tag{B.1g}$$

$$\frac{\partial \langle w'w'\rangle}{\partial t} = -\frac{\partial}{\partial z}\left[\langle w'^2 w'\rangle - \nu\frac{\partial \langle w'w'\rangle}{\partial z}\right] - 2\nu\left\langle\left(\frac{\partial w'}{\partial x_j}\right)^2\right\rangle - 2\langle w'\partial_z p'\rangle + 2\langle w'b'\rangle \tag{B.1h}$$

$$\frac{\partial \langle b'b'\rangle}{\partial t} = -\frac{\partial}{\partial z}\left[\langle w'b'^2\rangle - \nu\frac{\partial \langle b'b'\rangle}{\partial z}\right] - 2\nu\left\langle\left(\frac{\partial b'}{\partial x_j}\right)^2\right\rangle - 2\langle w'b'\rangle N^2 \tag{B.1i}$$

$$\frac{\partial \langle b'w'\rangle}{\partial t} = -\frac{\partial}{\partial z}\left[\langle w'^2 b'\rangle - \nu\frac{\partial \langle b'w'\rangle}{\partial z}\right] - 2\nu\left\langle\frac{\partial b'}{\partial x_j}\frac{\partial w'}{\partial x_j}\right\rangle + \langle b'\partial_z p'\rangle + \langle b'b'\rangle - \langle w'w'\rangle N^2. \tag{B.1j}$$

$$\left\langle b' \frac{\partial p'}{\partial x_j} \right\rangle = \frac{\partial \langle p'b' \rangle}{\partial x_j} - \left\langle p' \frac{\partial b'}{\partial x_j} \right\rangle = \frac{\langle u'_j b' \rangle}{\tau_{\text{iso}}}. \tag{B.3}$$

With these closure assumptions Equations (B.1) simplify to the following set of second-order equations (parameterized terms are marked by red font).

$$\frac{1}{2} \frac{\partial \langle u'u' \rangle}{\partial t} = - \langle u'w' \rangle \frac{\partial U}{\partial z} + f \langle u'v' \rangle - \frac{\langle u'u' \rangle}{\tau_\epsilon} + \text{Rotta} \tag{B.4a}$$

$$\frac{1}{2} \frac{\partial \langle v'v' \rangle}{\partial t} = - \langle v'w' \rangle \frac{\partial V}{\partial z} - f \langle u'v' \rangle - \frac{\langle v'v' \rangle}{\tau_\epsilon} + \text{Rotta} \tag{B.4b}$$

$$\frac{\partial \langle u'v' \rangle}{\partial t} = - \langle u'w' \rangle \frac{\partial U}{\partial z} - \langle v'w' \rangle \frac{\partial V}{\partial z} + f(\langle v'v' \rangle - \langle u'u' \rangle) + \langle u'b' \rangle - \frac{\langle u'w' \rangle}{\tau_\epsilon} + \text{Rotta} \tag{B.4c}$$

$$\frac{\partial \langle u'w' \rangle}{\partial t} = - \langle w'w' \rangle \frac{\partial U}{\partial z} + f \langle v'w' \rangle + \langle u'b' \rangle - \frac{\langle u'w' \rangle}{\tau_\epsilon} + \text{Rotta} \tag{B.4d}$$

$$\frac{\partial \langle v'w' \rangle}{\partial t} = - \langle w'w' \rangle \frac{\partial V}{\partial z} - f \langle u'w' \rangle - \frac{\langle v'w' \rangle}{\tau_\epsilon} + \text{Rotta} \tag{B.4e}$$

$$\frac{1}{2} \frac{\partial \langle w'w' \rangle}{\partial t} = \langle b'w' \rangle - \frac{\langle w'w' \rangle}{\tau_\epsilon} + \text{Rotta} \tag{B.4f}$$

$$\frac{1}{2} \frac{\partial \langle b'b' \rangle}{\partial t} = - \langle b'w' \rangle N^2 \left(1 + \frac{1}{2}\right) - \frac{\langle b'b' \rangle}{\tau_\epsilon} \tag{B.4g}$$

$$\frac{\partial \langle b'w' \rangle}{\partial t} = \left[\langle b'b' \rangle - \langle w'w' \rangle N^2 \left(1 + \frac{1}{2}\right) \right] - \langle b'w' \rangle \left(\frac{1}{\tau_{wb}} + \frac{1}{\tau_{\text{iso}}} \right). \tag{B.4h}$$

This system constitutes a second-order closure for the turbulent flow with down-gradient closure for the triple correlation, a relaxation time scale for dissipation of turbulent stress and the Rotta-Model for the pressure–velocity correlation terms. For time scales small compared with the return-to-isotropy time τ_{iso} of the Rotta parameterization, the system falls apart into the two independent sub-systems Eqs. (B.4a–B.4e) and (B.4f–B.4h). The first sub-system is the one containing the horizontal components of TKE and the off-diagonal Reynolds stresses. This sub-system is strongly coupled, not only through the return-to-isotropy terms of Rotta's model but also due to the production terms involving the vertical momentum fluxes $\langle u'w' \rangle$ and $\langle v'w' \rangle$ in the equation for $\langle u'u' \rangle$ and $\langle v'v' \rangle$ respectively. The second sub-system is relevant under stable stratification where it describes the interaction between buoyancy variance $\langle b'b' \rangle$, the mean buoyancy gradient N^2 and the vertical velocity perturbations—the only component of velocity that is directly influenced by stratification.

Inertia—gravity oscillation. The second sub-system can be understood as a damped harmonic oscillator when considering the perturbation energy defined as

$$e := \left(\frac{3}{2} N^2 \langle w'w' \rangle + \langle b'b' \rangle \right). \tag{B.5}$$

The above closure equation (B.1) implies dissipation of fluctuations such that energy decays exponentially as $\partial_t e = -e/\tau_\epsilon$. Regarding the buoyancy flux, one can derive an oscillator equation that reads as

$$\frac{1}{2} \frac{\partial^2 \langle b'w' \rangle}{\partial t^2} = -\frac{1}{2} \left(\frac{5}{2} N^2 \langle b'w' \rangle \right) + \frac{1}{\tau_\epsilon} \left(-\langle b'b' \rangle + \frac{3}{2} N^2 \langle w'w' \rangle \right) - \frac{1}{2} \frac{1}{\tau_{\text{eff}}} \frac{\partial \langle b'w' \rangle}{\partial t} \tag{B.6}$$

with $\tau_{\text{eff}}^{-1} = \tau_{wb}^{-1} + \tau_{\text{iso}}^{-1}$. The term $3/2 N^2 \langle w'w' \rangle - \langle b'b' \rangle$ can be substituted according to equation (B.1j) yielding

$$\frac{1}{2} \frac{\partial^2 \langle b'w' \rangle}{\partial t^2} = -\frac{1}{2} \left(\frac{5}{2} N^2 \right) \langle b'w' \rangle + \frac{1}{\tau_\epsilon} \left(-2 \frac{\partial \langle b'w' \rangle}{\partial t} + \frac{1}{\tau_{\text{eff}}} \langle b'w' \rangle \right) - \frac{1}{2} \frac{1}{\tau_{\text{eff}}} \frac{\partial \langle b'w' \rangle}{\partial t} \tag{B.7}$$

$$\Rightarrow \frac{\partial^2 \langle b'w' \rangle}{\partial t^2} = -\omega_{bw}^2 \langle b'w' \rangle - \alpha_{bw} \frac{\partial \langle b'w' \rangle}{\partial t}$$

$$\text{with } \omega_{bw} = \sqrt{\left(\frac{5}{2} N^2 - \frac{2}{\tau_{\text{eff}} \tau_\epsilon} \right)} \quad \text{and} \quad \alpha_{bw} = \left(\frac{1}{\tau_{\text{eff}}} - \frac{4}{\tau_\epsilon} \right) \tag{B.8}$$

In this equation it is required for physical stability that

$$\tau_{\text{eff}} = \frac{\tau_{\text{iso}} \tau_{wb}}{\tau_{\text{iso}} + \tau_{wb}} < \frac{1}{4} \tau_\epsilon. \tag{B.9}$$

Similar oscillator equations can be derived for $\langle b'b' \rangle$ and $\langle w'w' \rangle$:

$$\frac{1}{2} \frac{\partial^2 \langle w'w' \rangle}{\partial t^2} = \frac{\partial \langle b'w' \rangle}{\partial t} - \frac{1}{\tau_\epsilon} \frac{\partial \langle w'w' \rangle}{\partial t}$$

$$= \langle b'b' \rangle - \frac{3}{2} N^2 \langle w'w' \rangle - \frac{1}{\tau_{\text{eff}}} \langle b'w' \rangle - \frac{1}{\tau_\epsilon} \frac{\partial \langle w'w' \rangle}{\partial t} \tag{B.10}$$

$$\frac{1}{2}\frac{\partial^2}{\partial t^2}\left[\langle w'w'\rangle + \frac{2}{5N^2}e\right] = -\frac{5}{2}N^2\left(\langle w'w'\rangle + \frac{2}{5N^2}e\right) - \frac{\langle b'w'\rangle}{\tau_{\text{eff}}}$$
$$- \frac{1}{\tau_\epsilon}\frac{\partial\left(\langle w'w'\rangle + 2/(5N^2)e\right)}{\partial t} \tag{B.11}$$

$$\begin{aligned}
\frac{1}{2}\frac{\partial^2\langle b'b'\rangle}{\partial t^2} &= -\frac{3}{2}N^2\frac{\partial\langle b'w'\rangle}{\partial t} - \frac{1}{\tau_\epsilon}\frac{\partial\langle b'b'\rangle}{\partial t}\\
&= -\frac{3}{2}N^2\left[\langle b'b'\rangle - \frac{3}{2}N^2\langle w'w'\rangle + \frac{\langle b'w'\rangle}{\tau_{\text{eff}}}\right] - \frac{1}{\tau_\epsilon}\frac{\langle b'b'\rangle}{\partial t}\\
&= -\frac{5}{2}N^2\left(\langle b'b'\rangle - \frac{2}{5N^2}e\right) + \frac{\langle b'w'\rangle}{\tau_{\text{eff}}} - \frac{1}{\tau_\epsilon}\frac{\partial\langle b'b'\rangle}{\partial t}
\end{aligned}$$
$$\tag{B.12}$$

$$\Rightarrow \begin{aligned}
\frac{1}{2}\ddot\sigma_w &= -\frac{5N^2}{2}\sigma_w - \frac{1}{\tau_\epsilon}\dot\sigma_w - \frac{\langle b'w'\rangle}{\tau_{\text{eff}}}\\
\frac{1}{2}\ddot\sigma_b &= -\frac{5N^2}{2}\sigma_b - \frac{1}{\tau_\epsilon}\dot\sigma_b + \frac{\langle b'w'\rangle}{\tau_{\text{eff}}}
\end{aligned} \tag{B.13}$$

where $\sigma_w = \langle w'w'\rangle + \frac{2}{5N^2}e$ and $\sigma_b = \langle b'b'\rangle - \frac{2}{5N^2}e$.

Reference

Rotta, J. C. (1951). Statistische Theorie Nichthomogener Turbulenz. 1. *Zeitschrift Fur Physik*, *129*(6), 547–572.

Index